Electronic Structure and Chemical Bonding in Novel Lanthanide and Actinide Compounds: A Comprehensive Theoretical Study

By

Meenakshi Joshi

(CHEM01201504005)

Bhabha Atomic Research Centre, Mumbai

A thesis submitted to the

Board of Studies in Chemical Sciences

In partial fulfillment of requirements

for the Degree of

DOCTOR OF PHILOSOPHY

of

HOMI BHABHA NATIONAL INSTITUTE

May, 2020

Homi Bhabha National Institute[1]

Recommendations of the Viva Voce Committee

As members of the Viva Voce Committee, we certify that we have read the dissertation prepared by **Ms. Meenakshi Joshi** entitled **"Electronic Structure and Chemical Bonding in Novel Lanthanide and Actinide Compounds: A Comprehensive Theoretical Study"** and recommend that it may be accepted as fulfilling the thesis requirement for the award of Degree of Doctor of Philosophy.

Chairman – **Prof. Alok K. Samanta**		**Date:** 14/09/2020
Guide / Convener – **Prof. Tapan K. Ghanty**	Tapan kr Ghanty	**Date:** 14/09/2020
Examiner – **Prof. Swapan K. Pati**		**Date:** 14/9/2020
Member 1 – **Prof. Chandra N. Patra**		**Date:** 14-09-2020
Member 2 – **Prof. Ashok Arya**		**Date:** 14/09/2020
Member 3 – **Prof. Arunasis Bhattacharyya**		**Date:** 14.09.2020
The Technology Adviser – **Prof. Neetika Rawat**	Neetika Rawat	**Date:** 14.09.20

Final approval and acceptance of this thesis is contingent upon the candidate's submission of the final copies of the thesis to HBNI.

I hereby certify that I have read this thesis prepared under my direction and recommend that it may be accepted as fulfilling the thesis requirement.

Tapan kr Ghanty

Date: 14th **September, 2020**
Place: Mumbai

Prof. Tapan K. Ghanty
Guide

---

[1] This page is to be included only for final submission after successful completion of viva voce.

STATEMENT BY AUTHOR

This dissertation has been submitted in partial fulfillment of requirements for an advanced degree at Homi Bhabha National Institute (HBNI) and is deposited in the Library to be made available to borrowers under rules of the HBNI.

Brief quotations from this dissertation are allowable without special permission, provided that accurate acknowledgement of source is made. Requests for permission for extended quotation from or reproduction of this manuscript in whole or in part may be granted by the Competent Authority of HBNI when in his or her judgment the proposed use of the material is in the interests of scholarship. In all other instances, however, permission must be obtained from the author.

Meenakshi

Meenakshi Joshi

DECLARATION

I, hereby declare that the investigation presented in the thesis has been carried out by me. The work is original and has not been submitted earlier as a whole or in part for a degree / diploma at this or any other Institution / University.

Meenakshi

Meenakshi Joshi

List of Publications arising from the thesis

Journal

1. “Atom- and Ion-Centered Icosahedral Subnanometer-Sized Clusters of Molecular Hydrogen”, **M. Joshi**, A. Ghosh and T. K. Ghanty, *J. Phys. Chem. C*, **2017**, *121*, 15036−15048.

2. “Theoretical Investigation of $M@Pb_{12}^{2-}$ and $M@Sn_{12}^{2-}$ Zintl Clusters ($M = Lr^{n+}$, Lu^{n+}, La^{3+}, Ac^{3+} and $n = 0, 1, 2, 3$)”, **M. Joshi**, A. Chandrasekar and T. K. Ghanty, *Phys. Chem. Chem. Phys.,* **2018**, *20*, 15253–15272.

3. “Counter-Intuitive Stability in Actinide-Encapsulated Metalloid Clusters with Broken Aromaticity”, **M. Joshi**, A. Ghosh, A. Chandrasekar and T. K. Ghanty, *J. Phys. Chem. C*, **2018**, *122*, 22469−22479.

4. “Predicted $M(H_2)_{12}^{n+}$ (M = Ac, Th, Pa, U, La and n = 3, 4) Complexes with Twenty Four Hydrogen Atoms Bound to the Metal Ion”, **M. Joshi** and T. K. Ghanty, *Chem. Commu.*, **2019**, *55*, 7788−7791.

5. “Prediction of a Nine-Membered Aromatic Heterocyclic Ligand, 1,4,7-triazacyclononatetraenyl and its Sandwich Complexes with Divalent Lanthanides”, **M. Joshi** and T. K. Ghanty, *ChemistySelect,* **2019**, *4*, 9940−9946.

6. “Lanthanide and Actinide Doped $B_{12}H_{12}^{2-}$ and $Al_{12}H_{12}^{2-}$ Clusters: New Magnetic Superatoms with f-block Elements”, **M. Joshi** and T. K. Ghanty, *Phys. Chem. Chem. Phys.*, **2019**, *21*, 23720−23732.

7. “On the Position of La, Lu, Ac and Lr in the Periodic Table: a Perspective”, A. Chandrasekar, **M. Joshi** and T. K. Ghanty, *J. Chem. Sci.*, **2019**, *131*, 122.

Conferences

1. “Theoretical Investigations of Complexation of Trivalent Lanthanides and Actinides using 1, 10-Phenanthroline 2, 9-Dicarboxylic Acid Based Ligands”, **M. Joshi** and T. K. Ghanty, 6th Interdisciplinary Symposium on Materials Chemistry (ISMC−2016), December 6–10, **2016**.

2. “Dynamical Behaviour of Noble Gas Encapsulated Zintl Clusters in the Ultra-fast Time Domain”, **M. Joshi**, P. Sekhar, A. Ghosh and T. K. Ghanty, 14th DAE BRNS Biennial Trombay Symposium on Radiation and Photochemistry (TSRP−2018), January 3−7, **2018**.

3. “Fluorescent Characteristics of Th and Ce Complexes from the Ground State Electronic Structures”, **M. Joshi**, A. Chandrasekar and T. K. Ghanty, 8th Emerging Trends in Separation Science and Technology (SESTEC−2018), May 23–26, **2018**.

4. “Molecular Hydrogen Clusters in the Condensed State”, **M. Joshi**, A. Ghosh and T. K. Ghanty, 7th Interdisciplinary Symposium on Materials Chemistry (ISMC−2018), December 4–8, **2018**.

5. “Separation of Trivalent Americium from Trivalent Europium using Octadentate Picolinic Acid Based Ligand”, **M. Joshi** and T. K. Ghanty, 14th Biennial DAE−BRNS Symposium on Nuclear and Radiochemistry (NUCAR−2019), January 15−19, **2019**.

6. “Optical Absorption Spectra of Molecular Hydrogen Clusters in the Condensed State”, **M. Joshi** and T. K. Ghanty, 13th National Symposium on Radiation and Photochemistry (NSRP−2019), February 6−9, **2019**.

7. “Stability of Metal Doped Metalloid Clusters with Broken Aromaticity”, **M. Joshi**, A. Ghosh, A. Chandrasekar and T. K. Ghanty, 16th Theoretical Chemistry Symposium (TCS−2019), February 13−16, **2019**.

8. “Implications of Hybrid Organic-Inorganic Functionalised Dodecaborane Dianions in Lithium and Magnesium Ion Batteries”, **M. Joshi** and T. K. Ghanty, Ninth

Conference of the Asia-Pacific Association of Theoretical and Computational Chemists (APATCC−2019), September 30–October 3, **2019**.

Other Publications (not included in the Thesis)

1. "Noble Gas Encapsulated Endohedral Zintl Ions $Ng@Pb_{12}^{2-}$ and $Ng@Sn_{12}^{2-}$ (Ng = He, Ne, Ar, and Kr): A Theoretical Investigation", P. Sekhar, A. Ghosh, **M. Joshi** and T. K. Ghanty, *J. Phys. Chem. C,* **2017**, *121*, 11932−11949.

2. "Hybrid Organic-Inorganic Functionalized Dodecaboranes and their Potential Role in Lithium and Magnesium Ion Batteries", **M. Joshi** and T. K. Ghanty, *J. Phys. Chem. C,* **2018**, *122*, 27947−27954.

3. "Quantum Chemical Prediction of a Superelectrophilic Dianion and its Binding with Noble Gas Atoms", **M. Joshi** and T. K. Ghanty, *Chem. Commun.*, **2019**, *55*, 14379−14382.

4. "Highly Selective Separations of U(VI) from a Th(IV) Matrix by Branched Butyl Phosphates: Insights from Solvent Extractions, Chromatography and Quantum Chemical Calculations", A. Chandrasekar, A. Suresh, **M. Joshi**, M. Sundararajan, T. K. Ghanty and N. Sivaraman, *Sep. Puri. Technol.,* **2019**, *210*, 182−194.

5. "Synthesis and Characterization of Some BODIPY Based Substituted Salicylaldimine Schiff Bases", N. Kushwah, S. Mula, A. P. Wadawale, **M. Joshi**, G. Kedarnath, M. Kumar, T. K. Ghanty, S. K. Nayak and V. K. Jain, *J. of Heterocyclic Chemistry*, **2019**, *56*, 2499−2507.

6. "A Combined Experimental and Quantum Chemical Studies on the Structure and Binding Preferences of Picolinamide Based Ligands with Uranyl Nitrate", D. Das, **M. Joshi**, S. Kannan, M. Kumar, T. K. Ghanty, T. Vincent, S. Manohar and C. P. Kaushik, *Polyhedron,* **2019,** *171*, 486−492.

7. "Unprecedented Stability Enhancement of Multiply Charged Anions through Decoration with Negative Electron Affinity Noble Gases", **M. Joshi** and T. K. Ghanty, *Phys. Chem. Chem. Phys.,* **2020**, *22*, 13368−13372.

Meenakshi

Meenakshi Joshi

Dedicated

to

My Beloved Parents

ACKNOWLEDGEMENTS

First of all, I would like to acknowledge my deepest gratitude to my Ph.D. supervisor Prof. Tapan K. Ghanty for his guidance, thoughtful advice, motivation, constant encouragement, and valuable suggestions throughout my research tenure. I am deeply indebted to him for sharing his knowledge with me.

It gives me immense pleasure to thank all the members of my doctoral committee Prof. A. K. Samanta (Chairman), Prof. C. N. Patra (Member), Prof. Ashok Arya (Member), Prof. Arunasis Bhattacharyya (Member) and Prof. Neetika Rawat (Technology Advisor) for their critical review and suggestions during the progress review and pre−synopsis viva voce.

It is my pleasure to express sincere thanks to all the members of Theoretical Chemistry Section for their help and support. I express my sincere thanks to Dr. Ayan Ghosh and Dr. Aditi Chandrasekar for their scientific help in my PhD work.

I sincerely acknowledge the Department of Atomic Energy for providing the fellowship and the supercomputing facility of Bhabha Atomic Research Centre for providing the computational facilities to perform my research work.

I express my deep sense of gratitude and indebtedness to my family for their love, blessings and constant support that helped me to achieve what I am today. I also wish to thank my all friends especially, Dr. Arjun Sharma, Ms. Pragya Chopra, Ms. Bhawana Saklani, Mrs. Seema Belal, Mrs. Deepti Singh, Ms. Reema Chaudhury, Ms. Pooja dhorge and all well−wishers for their love and support.

Meenakshi

Meenakshi Joshi

CONTENTS

LIST OF FIGURES

LIST OF TABLES

CHAPTER 8

Summary and Conclusion

In this chapter, we summarize all the works discussed throughout the thesis as well as possible future perspectives of the work. In the present thesis, we have studied the effect of doping of an isoelectronic series of lanthanide and actinide atom/ion on the structure, electronic and magnetic properties of a host cluster. Besides we have investigated the position of lanthanides and actinides in the periodic table. Also, we have analyzed how the chemical bonding of f–elements with various chemical species changes across the f–block.

All the work presented in this thesis has been mainly carried out by using density functional theory (DFT) and dispersion corrected DFT. In addition, we have also used post–Hartree–Fock based methods such as MP2 and CCSD(T) as discussed in Chapter 2.

At first in Chapter 3 we investigated the position of La, Ac, Lu and Lr elements in the periodic table by modeling their chemical behaviour in the Lu^{n+}, Lr^{n+}, La^{3+} and Ac^{3+} (n = 0, 1, 2, 3) doped Pb_{12}^{2-} and Sn_{12}^{2-} icosahedral symmetry clusters as these clusters can provide a spherical atom−like environment to the doped ion. Despite having different valence electronic configuration, both Lu^{n+} and Lr^{n+} (n = 0, 1, 2, 3) doped clusters show exactly similar structure, bonding, HOMO–LUMO energy gap and charge distribution, which indicates the similar behaviour of Lr and Lu in their different oxidation states (n = 0–3). Among all the studied Lu^{n+} and Lr^{n+} (n = 0, 1, 2, 3) doped clusters, the Lu^{3+} and Lr^{3+} doped clusters have maintained icosahedral symmetry of the parent cluster and possess higher HOMO–LUMO energy gap, high binding energy which indicate higher stability of Lu^{3+} and Lr^{3+} doped clusters. Moreover, 18–electron principle is fulfilled around the Lu/Lr atom in the Lu^{3+} and Lr^{3+} doped clusters corresponding to $s^2p^6d^{10}$ configuration rather than the 32–electron rule as their highly shielded f–orbitals could not involve in the bonding with the cage atoms. Similar to Lu^{3+} and Lr^{3+} ion, the La^{3+} and Ac^{3+} doped Pb_{12}^{2-} and Sn_{12}^{2-} clusters also possess icosahedral geometry, high HOMO–LUMO energy gap, high binding energy and follow 18–electron rule indicating the exactly similar behaviour of La, Ac, Lu and Lr elements. Therefore, from our results we suggest to place all lanthanide (La–Lu) and actinide (Ac–Lr) elements in the 15–elements f–blocks, which is in agreement with the IUPAC accepted periodic table.

Then we studied the isoelectronic series of Ln = La^{3+}, Ce^{4+}, Pr^{5+}, Nd^{6+} and An = Th^{4+}, Pa^{5+}, U^{6+}, Np^{7+} doped metalloid clusters, viz., $M@(Sb_4^{2-})_3$ and $M@(Bi_4^{2-})_3$ (M = Ln and An) in Chapter 4. We have found that as we move from La^{3+} to Nd^{6+} and Th^{4+} to Np^{7+} doped systems, the bonding of Ln/An with the E_4^{2-} (E= Sb, Bi) ring increases and binding energy also increases along the same. Thus, the stability of $M@(Sb_4^{2-})_3$ and $M@(Bi_4^{2-})_3$ systems increases along the same. However, along the same the non–planarity of the E_4^{2-} (E = Sb/Bi) rings increases indicating lose in the aromaticity of E_4^{2-} rings. To understand this counterintuitive increase in the stability despite the ring losing their aromaticity, we have analyzed the molecular orbital pictures of these clusters and find out that no f–orbital of La and Th involved in bonding with the ring, however, as we move across the f–block, the involvement of f–orbitals in bonding with ring increases which lead to the fulfillment of 32–electron count in the $M@(Sb_4^{2-})_3$ and in $M@(Bi_4^{2-})_3$ systems and provides very high stability to these systems.

Furthermore, we have also studied an isoelectronic series of Ln = Pm^{+}, Sm^{2+}, Eu^{3+} and An = Np^{+}, Pu^{2+}, Am^{3+} doped exohedral $B_{12}H_{12}^{2-}$ and exohedral as well as endohedral $Al_{12}H_{12}^{2-}$ clusters in Chapter 5. As the ground state of the chosen Ln/An ions is associated with a high spin state, therefore, we have optimized these Ln/An doped $E_{12}H_{12}^{2-}$ (E = B, Al) clusters in different possible spin states. Among all spins, the septet spin Ln/An doped exohedral clusters are the most stable. It is noteworthy to mention that in all the systems the spin density of Ln/An remains intact, which can provide magnetic characteristics to these clusters. It is very interesting to observe that the spin population of Am^{3+}/Eu^{3+} ion is enhanced after doping in the $E_{12}H_{12}^{2-}$ clusters (E = B, Al). In $M@E_{12}H_{12}^{2-}$ (M = Ln, An and E = B, Al) clusters the bonding of f–orbital with cage increases as we move across the f–block from Pm^{+} to Eu^{3+} and Np^{+} to Am^{3+}. Moreover, in the septet spin endohedral $An@Al_{12}H_{12}^{2-}$ (An = Pu^{2+} and Am^{3+}) clusters the 32–electron count is fulfilled around the An ion corresponding to $s^2p^6d^{10}f^{14}$ configuration. Thus, in the present thesis, we have predicted the magnetic superatomic $M@Al_{12}H_{12}^{2-}$ clusters which are quite rare to observe.

Besides we have designed nine–membered aromatic novel heterocyclic 1,4,7−triazacyclononatetraenyl anion, $C_6H_6N_3^{-}$, and its sandwich complexes with divalent lanthanide cation, viz., $Ln(C_6H_6N_3)_2$ (Ln = Nd(II), Pm(II), Sm(II), Eu(II), Tm(II), Yb(II)) as discussed in Chapter 6. In these sandwich complexes, the spin population of Ln ion is almost equivalent to their atomic spin. Thus, Ln sandwich complexes with high spin population will possess high magnetic moment. These predicted sandwich complexes with a high spin population may also find application as a single ion magnet. Moreover, the designed $Ln(C_6H_6N_3)_2$ sandwich complexes possess comparable stability with the experimentally synthesized $Ln(C_9H_9)_2$ complexes, which indicates a possible synthesis of the predicted complexes.

In Chapter 7, we have studied the coordination behaviour of An (Ac^{3+}, Th^{3+}, Th^{4+}, Pa^{4+}, U^{4+}) and Ln (La^{3+}) ion toward H_2 molecules. The $An^{3+/4+}$ and Ln^{3+} ion is found to form side on η^2 type of non–classical 3–centered 2–electron (3c–2e) bond ($M–H_2$) with the H_2 molecules where bonded electrons of H–H bond are involved in bonding with the metal ion. It is noteworthy to mention that the An (Ac^{3+}, Th^{3+}, Th^{4+}, Pa^{4+}, U^{4+}) and Ln (La^{3+}) ions are capable to form bonds with a maximum of 24 hydrogen atoms of $12H_2$ molecules in its first coordination sphere which is the highest number recorded till date. In addition 18–electron count is fulfilled around Ac ion corresponding to $s^2p^6d^{10}$ configuration in few of the $Ac(H_2)_n^{3+}$ (n = 9–12) systems.

Over all we can conclude that our work will not only motivate experimentalists to synthesize these predicted systems but also encourage for discovering various new systems with intriguing properties by just doping single atom or ion in a cluster.

Summary

Lanthanides (Ln) and actinides (An) have attracted immense attention of scientists due to their complex electronic structure and bonding, and their various applications. These ions can be used in designing new magnetic materials, nanomaterials as well as single molecule magnet (SMM). Therefore, in the present thesis, we have studied the effect of doping of an isoelectronic series of lanthanide and actinide atom/ion on the structure, electronic and magnetic properties of a host cluster. Moreover, we have made an attempt to settle down the on-going debate on the position of La, Ac, Lr and Lu in the periodic table using computational techniques. With the help of doping of Ln/An ion in Pb_{12}^{2-} and Sn_{12}^{2-} clusters, we have shown that La^{3+}, Ac^{3+}, Lr^{3+} and Lu^{3+} doped Pb_{12}^{2-} and Sn_{12}^{2-} clusters possess exactly similar structural, bonding, electronic and energetic behaviour. Thus, we proposed to place all these four elements in the 15−elements f−blocks which supports the IUPAC accepted periodic table.

For designing novel clusters, we have chosen host clusters made up of p−block elements, viz., Pb_{12}^{2-}, Sn_{12}^{2-}, $(Sb_4^{2-})_3$, $(Bi_4^{2-})_3$, $B_{12}H_{12}^{2-}$ and $Al_{12}H_{12}^{2-}$. The chosen host clusters are highly stable closed−shell clusters with highly symmetric icosahedral geometry except for $(Sb_4^{2-})_3$ and $(Bi_4^{2-})_3$. In the present thesis, we have predicted highly stable 18−electron count following $M@Pb_{12}^{2-}$ and $M@Sn_{12}^{2-}$ ($M = Lr^{3+}, Lu^{3+}, La^{3+}, Ac^{3+}$) clusters associated with 18 valence-electron around the central metal ion. Also, we have predicted $M@(E_4^{2-})_3$ ($M = La^{3+}, Th^{4+}$) and $M@(E_4^{2-})_3$ ($M = Pa^{5+}, U^{6+}, Np^{7+}$; E = Sb, Bi) clusters, which follow 26−electron and 32−electron principles, respectively.

Moreover, using the structural parameters, electron counting rule and energetics, we have shown that the highly unstable $(E_4^{2-})_3$ (E = Sb or Bi) clusters are significantly stabilized after doping with the iso−electronic series of lanthanide and actinide ion even though the

aromatic Sb_4^{2-} and Bi_4^{2-} rings lose their planarity in $M@(E_4^{2-})_3$ (M = Ln, An) clusters.

Furthermore, we have predicted magnetic $M@B_{12}H_{12}^{2-}$ and $M@Al_{12}H_{12}^{2-}$ clusters (M = Pm^+, Sm^{2+}, Eu^{3+}; Np^+, Pu^{2+}, Am^{3+}) with the high spin population. It is noteworthy to mention that the septet spin endohedral $M@Al_{12}H_{12}^{2-}$ (M = Sm^{2+}, Eu^{3+}; Pu^{2+}, Am^{3+}) clusters follow 32−electron principle which is very rare to observe in case of open−shell clusters.

Besides we have predicted novel aromatic nine−membered heterocyclic ligand 1,4,7−triazacyclononatetraenyl ion and its sandwich complexes with the divalent lanthanide (Ln = Nd(II), Pm(II), Sm(II), Eu(II), Tm(II) and Yb(II)). These predicted lanthanide sandwich complexes possess high spin population and might be considered as single-ion magnet.

Furthermore, we have shown that the Ln (La^{3+}) and An (Ac^{3+}, Th^{3+}, Th^{4+}, Pa^{4+}, U^{4+}) ion can hold a maximum of 24 hydrogen atoms in its first coordination sphere in $M(H_2)_{12}^{3+/4+}$ (M = La, An) clusters via side on 3−center−2−electron bond with H_2 molecules, which is the highest recorded coordination number till date.

In the studied systems, it has been found that as we move across the iso−electronic series of lanthanide and actinide doped ion, the bonding of Ln and An ions with the host clusters increases due to a greater involvement of their f−orbital in the bonding, which leads to an increase in the stability of doped clusters across the same. Thus, the present work reveals that for the clusters of the size in the range of sub-nano to nanometer, even presence of one f-block atom/ion can make a difference in their properties. We have shown that the structural, electronic, energetic and magnetic properties of the clusters can be modified by just doping a single lanthanide and actinide atom/ion. We believe that our results will motivate scientists to synthesize these predicted lanthanide and actinide doped clusters and compounds as well as to find new metal atom or ion doped clusters with novel properties as these clusters might be used as building blocks for new materials.

CHAPTER 1

Introduction

1.1 General introduction of actinides and lanthanides

In the periodic table the elements from lanthanum (La) to lutetium (Lu) with atomic number 57 to 71 are known as lanthanides while the elements from actinium (Ac) to lawrencium (Lr) with the atomic number 89 to 103 are known as actinides. The phrases “lanthanides” and “actinides” are derived from the first element of their respective series, which is lanthanum and actinium. In general, the chemical symbol Ln and An is used for representing the elements of lanthanide and actinide series. There are total 15−elements in each Ln and An series. However, in some periodic table, the elements lanthanum (La) and actinium (Ac) have been labeled as group 3 elements of the d block, while in some other periodic table lutetium (Lu) and lawrencium (Lr) are labeled as d block elements of group 3, but most often all these four elements are included in the general discussion of the lanthanide and actinide elements chemistry.[1-6] In the periodic table, the Ln and the An can be seen in two additional rows underneath the main body of the table, either with empty space or with a particular single element of each series (either lanthanum and actinium, or lutetium and lawrencium) present in a particular cell in the d−block of the main table in group 3 below scandium and yttrium.[1-6] Still today the position of these four elements (La, Ac, Lu, and Lr) in the periodic table is in controversy.[7-8] One of the chapters of this thesis is fully dedicated to the chemical bonding of La, Ac, Lu, and Lr elements and their position in the periodic table. While the other chapters of the thesis deal with the chemical bonding of other lanthanide and actinide elements with various chemical species.

1.2 Chemical properties of Ln and An

The electronic configurations of lanthanides and actinides are [Xe] $4f^{0-14}5d^{0-1}6s^2$ and [Rn] $5f^{0-14}6d^{0-1}7s^2$, respectively. Thus in the lanthanides, the valence electrons are distributed in the 4f, 5d, and 6s orbitals. The most common oxidation state of Ln is +3 while few of the lanthanides can also show +2 and +4 oxidation states as listed in Table 1.1. After the removal of three electrons from the valence 5d and 6s orbitals of the Ln, the 4f orbitals become highly stabilized due to the increased effective nuclear charge. Thus, it becomes very difficult to remove the electrons from their 4f orbitals. Therefore, almost all the lanthanides prefer +3 oxidation state except in few exceptional cases when the f orbitals gain half−filled (f^7) or full−filled (f^{14}) electronic configuration.[9-10]

Table 1.1: The Ground State Electronic Configuration of the Lanthanides and their Variable Oxidation State[9].

Element	**Symbol**	**Atomic Number**	**Electronic Configuration**	**Oxidation State**
Lanthanum	La	57	[Xe] $5d^1 6s^2$	+3
Cerium	Ce	58	[Xe] $4f^1 5d^1 6s^2$	+3,+4
Praseodymium	Pr	59	[Xe] $4f^3 6s^2$	+3
Neodymium	Nd	60	[Xe] $4f^4 6s^2$	+2,+3
Promethium	Pm	61	[Xe] $4f^5 6s^2$	+2,+3
Samarium	Sm	62	[Xe] $4f^6 6s^2$	+2,+3
Europium	Eu	63	[Xe] $4f^7 6s^2$	+2,+3
Gadolinium	Gd	64	[Xe] $4f^7 5d^1 6s^2$	+3
Terbium	Tb	65	[Xe] $4f^9 6s^2$	+3
Dysprosium	Dy	66	[Xe] $4f^{10} 6s^2$	+3
Holmium	Ho	67	[Xe] $4f^{11} 6s^2$	+3
Erbium	Er	68	[Xe] $4f^{12} 6s^2$	+3
Thulium	Tm	69	[Xe] $4f^{13} 6s^2$	+3
Ytterbium	Yb	70	[Xe] $4f^{14} 6s^2$	+2,+3
Lutetium	Lu	71	[Xe] $4f^{14} 5d^1 6s^2$	+3

However, the corresponding actinides show variable oxidation states (Table 1.2) in the range of +2 to +7 after the removal of electrons from their valence 5f, 6d and 7s orbitals, which indicates that the 5f orbitals of An are relatively more diffuse as compared to the 4f orbitals of Ln.

Table 1.2: The Ground State Electronic Configuration of the Actinides and their Variable Oxidation State[9].

Element	**Symbol**	**Atomic Number**	**Electronic Configuration**	**Oxidation State**
Actinium	Ac	89	[Rn] $6d^1 7s^2$	+3
Thorium	Th	90	[Rn] $6d^2\ 7s^2$	+4
Protactinium	Pa	91	[Rn] $5f^2 6d^1 7s^2$	+4, +5
Uranium	U	92	[Rn] $5f^3 6d^1 7s^2$	+3,+4,+5,+6
Neptunium	Np	93	[Rn] $5f^4 6d^1 7s^2$	+3,+4,+5,+6,+7
Plutonium	Pu	94	[Rn] $5f^6\ 7s^2$	+3,+4,+5,+6,+7
Americium	Am	95	[Rn] $5f^7\ 7s^2$	+2,+3,+4,+5,+6
Curium	Cm	96	[Rn] $5f^7 6d^1 7s^2$	+3,+4,
Berkelium	Bk	97	[Rn] $5f^9\ 7s^2$	+3,+4,
Californium	Cf	98	[Rn] $5f^{10} 7s^2$	+3
Einsteinium	Es	99	[Rn] $5f^{11} 7s^2$	+3
Fermium	Fm	100	[Rn] $5f^{12} 7s^2$	+3
Mendelevium	Md	101	[Rn] $5f^{13}\ 7s^2$	+3
Nobelium	No	102	[Rn] $5f^{14}\ 7s^2$	+2,+3
Lawrencium	Lr	103	[Rn] $5f^{14} 6d^1 7s^2$	+3

Therefore, the 5f orbitals of An are more radially extended and participate in chemical bond formation as compared to that of the 4f orbitals of Ln. The radial extension of the 4f/5f atomic orbitals decreases across the Ln/An series. On moving across the lanthanide and actinide series both nuclear charge as well as intervening electrons in f–orbitals increases, however, due to the poor nuclear shielding power of the f electrons, the effective nuclear charge felt by all valence electrons increases, which leads to the contraction of the atomic and ionic radii of the Ln and An atoms or ions. This effect is called as actinide and lanthanide contraction for the actinides and lanthanides series, respectively. Thus, as we move across the An series, the 5f orbitals of actinide behave much like the lanthanide 4f orbitals.[9-10] Similarly, in the periodic table as we move across the period from left to right, the atom/ion size decreases due to the same effect as for the lanthanides. However, due to the lanthanide contraction the size of 5d elements (post-lanthanide) remains almost the same as that of the 4d elements; hence the post-lanthanide elements in the periodic table are greatly influenced by the lanthanide contraction. In fact the radii of the period-6 transition metals are very similar to the radii of the period-5 transition metals. In this regard the lanthanide contraction could be considered as an exotic effect.

The similarities and differences in the chemical bonding of the lanthanides and actinides with various species have been of considerable research interests[11-13] due to their applications in various fields including the field of nuclear science.

1.3 Role of Ln and An elements in nuclear energy and related applications

Actinides play a very important role in the nuclear power generation because actinides especially uranium and plutonium are used as nuclear fuels in a nuclear reactor, which releases energy through nuclear fission to generate heat, which is then converted into electricity using steam turbines in a nuclear power plant. In most of the nuclear reactors, the electricity is produced by nuclear fission of uranium and plutonium. The uranium−233, uranium−235, and plutonium−239 are the three most relevant fissile isotopes. In the nuclear fission process, the unstable nuclei of these fissile isotopes absorb neutron and split into two lighter daughter nuclei and produce two, three or more neutrons. These produced neutrons further split more nuclei, which created a self−sustaining chain reaction. The use of nuclear power for electricity generation is increasing day by day. In the year 2017, nuclear power has provided about 10% of the worldwide electricity (2,488 terawatt−hours) and became the second largest environment−friendly energy source after the hydroelectricity.[14]

Although nuclear energy is a clean source of energy but the management of the radioactive nuclear waste and spent nuclear fuel (unused fuel) is a very difficult task because of the presence of highly radiotoxic actinides such as uranium and plutonium, with small amounts of long−lived minor actinides, namely, neptunium, americium, curium, and fission products including lanthanides and transition metals. Therefore, at first, the spent nuclear fuel is reprocessed to separate uranium and plutonium, which are again used in the nuclear reactor to produce nuclear energy. Partitioning and transmutation is another strategy of waste management in which long−lived minor actinides are transmuted into stable elements or short−lived nuclides via neutron fission and is considered an effective method to reduce the long−term radiotoxicity of the nuclear waste. Lanthanides are neutron poisonous and can hinder the transmutation process, therefore, to increase the efficiency of the transmutation process lanthanides must be separated from the minor actinides.[15] However, the separation of trivalent lanthanides from minor actinides remains a great challenge due to their very similar physical and chemical properties.[16] In this regard, the ligands with soft donor atoms (N or S) are found to be highly promising as they can distinguish the difference between actinides and lanthanides and forms relatively stronger covalent bond with the more diffuse 5f orbitals of actinides. Therefore, a large number of soft donor containing ligands have been designed for the selective separation of trivalent actinides over lanthanides.[17-19] In the recent past, it has been found that in the presence of softer donor atoms, even hard donor atoms of the ligand can selectivity bind with softer actinides over harder lanthanides.[20-23] Several methods have been proposed for the separation of the radioactive nuclides from the nuclear waste, such as Plutonium URanium EXtraction process (PUREX)[24], a process to selectively extract plutonium and uranium into an organic phase using tri−butyl phosphate (TBP) ligand, TRans

Uranic Extraction process (TRUEX)[25], a process in which Am and Cm minor actinide are selectively extracted from the nuclear waste, DIAMide EXtraction (DIAMEX) process[26], in which minor actinides are selectively extracted using malondiamide as extractant. Similarly, Selective ActiNide EXtraction process (SANEX)[27] is also used to separate minor actinides from the lanthanides. The remaining radioactive wastes are disposed off in deep geological repositories.

Apart from the electricity production, radioisotopes such as ^{60}Co, ^{131}I, ^{137}Cs, ^{90}Sr, and ^{32}P are widely used in cancer therapy, medical diagnosis and imaging, storage of food items, and equipment sterilization.[28-30]

As discussed above the actinides play a very important role in the nuclear fuel cycle, but due to the high radioactivity of these elements, their experimental handling becomes very difficult. Therefore, working with actinides is very challenging from the perspective of an experimentalist. However, it is desirable to have knowledge of Ln/An chemistry as it is very important in the context of nuclear waste management and spent fuel reprocessing. In this regard, computational chemistry plays an extremely important role in studying the chemistry of lanthanide and actinide compounds as compared to that for the compounds of any other elements of the periodic table.[31-32] Thus, with the help of computational studies, we can investigate the actinide properties, which are hard to quantify experimentally. Nevertheless, the computational study of lanthanide and actinide compounds is unusually complex due to the large number of electronic states arising from their open f−shells, low lying and dense atomic (n−2)f and (n−1)d orbitals that are close in energy, strong electron correlation effect and large relativistic effect.[33] Most often the relativistic effects are treated using relativistic effective core potential (RECP), however, for some applications all of the electrons are treated using relativistic Hamiltonian. Different theoretical approaches have been proposed to overcome the challenges and to understand the chemistry of the lanthanides and actinides.

Among all the theoretical methods, the density functional theory (DFT) is the most widely used computational technique for studying chemistry of medium to large size lanthanide and actinide−containing compounds because the results produced using DFT are most often found to be in good agreement with the corresponding experimental values.

1.4 Other applications of Ln and An compounds

The lanthanide and actinide compounds have attracted significant attention of experimentalists and theoretical chemists alike due to their fascinating electronic structure, hyperactive valence electrons and their intriguing bonding via 4f (lanthanide, Ln) and 5f (actinide, An) orbitals. The actinide elements can also be used for the development of novel nanomaterials and nanomedicine due to their distinct electronic structures. In the past, the actinide encapsulated fullerenes have been investigated to understand the complex electronic structures of An and their interaction with the fullerene.[34-36] Doping with an atom, ion, or molecule in a cluster is a powerful method for modifying the chemical and physical properties of the cluster for particular applications. Sometimes doping lead to the formation of more stable doped structures than the corresponding hollow cage structures. The actinide doped gold nanoclusters may also find applications in the radio−labelling, nano−drug carrier and other biomedical applications.[37]

Moreover, f−elements, especially lanthanides can be used in the construction of single−molecule magnets (SMMs) or single−ion magnets (SIMs), which have received considerable attention due to their slow magnetic relaxation and their application in creating switchable molecular−scale devices and in quantum computing.[38-45] The interaction between a single ion electron density of f−element and the crystal field environment (ligand field environment) provides the desirable magnetic characteristics, which lead to the single−ion anisotropies required for the strong single−molecule magnets.[43] The spins on individual metal ions couple to give rise to a high−spin ground state to generate magnetism in the SMMs. The lanthanide phthalocyanine sandwich complexes, $[LnPc_2]_n$ (Ln(III) = Tb, Dy, Ho; H_2Pc = phthalocyanine; n = −1, 0, +1) display unprecedented slow magnetic relaxation behaviour.[46] The dysprosium metallocene also displays slow magnetic relaxation.[47-48] Particularly, a linear two−coordinate complex with perfect axial anisotropy excites the synthetic chemists to develop the SMMs. Although a significant amount of research has been carried out on the lanthanide−based single−molecule magnet of the highly anisotropic Dy^{3+} and Tb^{3+} ions, but studies on the lighter and non−classical lanthanides are still relatively scarce.

Furthermore, the lanthanide-nickel (Ln-Ni) alloys have attracted considerable attention of scientists in view of their potential role for reversible hydrogen storage. Moreover, the Ln-alloys are used in various portable electronic devices and electric vehicles.[49-50]

Apart from these, lanthanides or rare earth elements (REE) are widely used in the permanent magnets and these lanthanide based permanent magnets are used in the wind turbine and electric vehicles.[51,52-53] As far as the reduction of the environmental pollution is concerned, the demand of these environment-friendly electric vehicle and wind turbine generator is rapidly escalating which in turn increases the demand for REE.[54]

Furthermore, the lanthanide compounds are also used as luminophores and show wide range of applications in the telecommunications, bioanalysis, optoelectronics, lasers and biological imaging because of their unique and sharp luminescence bands that cover the entire visible and near infrared (NIR) spectral regions.[55-59] In addition, lanthanide-doped up-conversion nanoparticles play a significant role in biological applications and optical encoding.[60-61]

1.5 Properties of hollow clusters and Ln/An doped clusters

Zintl ion clusters such as Pb_{12}^{2-} and Sn_{12}^{2-} clusters have received significant attention due to their ability to form stable and hollow cage−like structures with icosahedral (I_h) symmetry.[62-63] In these clusters the valence np electrons are delocalized over the cage and forms π−bonds. Due to the spherical π−bonding the Pb_{12}^{2-} and Sn_{12}^{2-} clusters are considered as the inorganic analogues of fullerenes. The Pb_{12}^{2-} and Sn_{12}^{2-} clusters cannot be isolated in the gas phase. Therefore, these clusters are stabilized via doping with alkali metal ion, which results in the formation of exohedral $K@Pb_{12}^{-}$ or $K@Sn_{12}^{-}$ clusters. Thus, Pb_{12}^{2-} and Sn_{12}^{2-} clusters have been produced in the form of KPb_{12}^{-} ($K^{+}[Pb_{12}^{2-}]$) and KSn_{12}^{-} ($K^{+}[Sn_{12}^{2-}]$) experimentally by laser vaporization of a lead and tin target, respectively, containing ∼15% potassium (K). The formation of exohedral $K@Pb_{12}^{-}$ or $K@Sn_{12}^{-}$ clusters has been confirmed by the mass spectra and photoelectron spectroscopy. The cage diameter of Pb_{12}^{2-} (6.3 Å) and Sn_{12}^{2-} (6.1 Å) Zintl clusters is slightly smaller than the C_{60} fullerene (7.1 Å)[34] and it is large enough to accommodate a d− or f−block element. In the past, lanthanide and actinide doped fullerene have been successfully synthesized.[35-36,64] Thus similar to the fullerene, Zintl ion clusters can also be used as a model system to create new materials by doping with atom or ion or molecule. Experimentally it has been shown that the Sn_{12}^{2-} cluster can trap a transition metal atom or the f−block elements (M = Ti, V, Cr, Fe, Co, Ni, Cu, Y, Nb, Gd, Hf, Ta, Pt, Au) to form endohedral clusters with very little distortion in the icosahedral cage.[65] Till now several atom or ion have been doped or encapsulated in lead and tin clusters.[66-71] It is very interesting to observe that most of the anionic and neutral species formed after doping in the Sn_{12}^{2-} clusters are of ionic type viz., $[Sn_{12}^{2-}M^{+}]$ and $[Sn_{12}^{2-}M^{2+}]$, respectively, whereas in gold doped cluster opposite charge distribution ($Au^{\delta-}@Sn_N^{\delta+}$) has been observed.[72] The doping of actinide element can enhance the stability of a cluster and also tune its optical and magnetic properties due to the hyperactive valence electrons of the actinide elements.

The bonding pattern of the Pb_{12}^{2-} and Sn_{12}^{2-} clusters also matches with that of the valence−isoelectronic $B_{12}H_{12}^{2-}$ (borate) and $Al_{12}H_{12}^{2-}$ (alanate) clusters.[73-74] Similar to the Pb_{12}^{2-} (6.3 Å) and Sn_{12}^{2-} (6.1 Å) clusters, the $B_{12}H_{12}^{2-}$ (3.4 Å) and $Al_{12}H_{12}^{2-}$ (5.1 Å) clusters possess hollow cage−like icosahedral structures but of relatively smaller cage diameter. Through density functional calculations, it has been shown that a noble gas (Ng) atom can be doped inside and outside of the $B_{12}H_{12}^{2-}$ and $Al_{12}H_{12}^{2-}$ cages.[75] Moreover, the exohedral $M@A_{12}H_{12}^{2-}$ (M = Be^{2+}, Na^{+}, Mg^{2+},..; A = B or Al) clusters are found to be more stable than the corresponding endohedral clusters.[76] Also, it might be possible to design new superatoms through doping of lanthanide and actinide ion in the $B_{12}H_{12}^{2-}$ and $Al_{12}H_{12}^{2-}$ clusters.

In the recent past, a series of intermetalloid Pb/Bi cluster anions embedded with different Ln^{3+} ions have been synthesized.[77] Subsequently, encapsulation of an actinide ion in intermetalloid clusters viz., $[U@Bi_{12}]^{3-}$, $[U@Tl_2Bi_{11}]^{3-}$, $[U@Pb_7Bi_7]^{3-}$, and $[U@Pb_4Bi_9]^{3-}$ has also been realized experimentally.[78] An unprecedented antiferromagnetic coupling between U^{4+} site and a unique radical, Bi_{12}^{7-} shell has been observed in $[U@Bi_{12}]^{3-}$ cluster.[78] The formation of such clusters is of great interest in regard to their structural, bonding, and magnetic properties. Moreover, a series of all−metal antiaromatic anions, $[Ln(\eta^4{-}Sb_4)_3]^{3-}$ (Ln = La, Y, Ho, Er, Lu) possessing counterintuitive stability, have been synthesized.[79]

1.6 Properties of Ln and An sandwich complexes

The synthesis of highly symmetric bis(cyclo−octatetraene)uranium, $U(COT)_2$, sandwich complex also known as “uranocene” has motivated the experimentalists and theoretical chemists to discover new actinide and lanthanide sandwich complexes.[80-81] In the past it was assumed that f−orbitals of An/Ln are not involved in bonding, however, experimental and theoretical evidences of f−orbital participation in bonding in the (cyclo−octatetraene)actinides, M(COT)$_2$, convinced scientists that the f orbitals do involve in the bonding. Since then much effort has been made to discover the nature of the bonding in various other actinide complexes. In the U(C_8H_8)$_2$ complex, U^{4+} ion is sandwiched between the two aromatic $C_8H_8^{2-}$ rings and dominant covalency is observed in the system due to 5f(U)−π(C_8H_8) overlap.[82-83] Also, the sandwich complexes of divalent Ln (Eu and Yb) ion have been prepared as $(K^+)_2[Ln^{2+}(C_8H_8^{2-})_2]$ salts.[84-85] Even multiple decker sandwich complexes of $Ln_n(C_8H_8)_m$ (Ln = Ce, Nd, Eu, Ho, and Yb) have been produced experimentally by using a combination of laser vaporization and molecular beam methods.[86] The $Ln_n(C_8H_8)_m$ complexes with (n, m) = (n, n + 1) for n = 1−5 are prominently produced as magic numbers in the mass spectra. It has been found that in these magic−numbered multiple decker sandwich complexes the Ln atoms and C_8H_8 ligands are alternately arranged. Very recently, Layfield et al have synthesized perfectly linear uranium(II) metallocene.[87]

The most important application of the sandwich compounds of the rare earth elements is their use as single molecule magnets (SMMs).[88] The lanthanide based SMMs can show magnetic hysteresis at liquid nitrogen temperature.[89-91] Most of the sandwich complexes of transition metals are made up of 5 and 6−memebered rings[92-93], while the sandwich complexes of the f−block elements contain 8− to 9−membered rings.[80, 94-96] Very recently, heteroleptic sandwich complexes of Ln ion, viz., $[(\eta^9-C_9H_9)Ln(\eta^8-C_8H_8)]$ where Ln = Ce(III), Pr(III), Nd(III) and Sm(III))[96] have been synthesized which shows slow magnetic relaxation, including hysteresis loops up to 10 K for the Er(III) analogue. Thus, knowing the importance of the SMMs, significant efforts have been made to find the nanometer−scale magnets, which can operate at the temperatures higher than the cryogenic range.

1.7 Electron counting in Ln and An compounds

In chemistry the stability of atoms, molecules, and compounds is described using electron counting rule. For example, for explaining the stability of the main group elements (s and p block elements) octet rule[97-98] has been proposed which states that an atom needs to contain eight electrons in its valence ns and np shell to achieve ns^2np^6 configuration. Thus, with the help of octet principle, the stable (inert) behaviour of noble gas atoms (ns^2np^6) and highly reactive nature of alkali metals (ns^1) and halogens (ns^2np^5) can be easily understood. On the other hand, 18−electron principle[99-100] has been proposed for explaining the stability of transition metal complexes due to the presence of additional (n−1)d valence orbitals in transition metals. According to the 18−electron principle, any transition metal compound which contains 18−electrons in its valence ns, np and (n−1)d orbitals and possess $ns^2np^6(n-1)d^{10}$ configuration are stable. For example $Cr(C_6H_6)_2$ and $Fe(C_5H_5)_2$ metallocene complexes are stable as both of them satisfy 18 electrons principle. Similarly, due to the presence of additional (n−2)f valence orbitals in the f−elements, the 32−electron principle has been proposed which states that 32−electrons are needed in the valence shell to achieve stable $[ns^2np^6(n-1)d^{10}(n-2)f^{14}]$ closed-shell configuration. The $Pu@Pb_{12}^{2-}$ is the first example of a 32−electron compound of the f−element.[101]

The same electron−counting rule is used for explaining the stability of atomic and molecular clusters of various elements. The stable clusters also known as magic clusters, show extra stability as compared to its nearest neighbours. Experimentally the magic behaviour of a particular size cluster is identified by the presence of intense ion signal in the mass spectra. However, theoretically, the magic behaviour of a cluster is analyzed using higher binding energy, higher HOMO–LUMO energy gap, higher ionization potential, lower electron affinity, and electron counting rule. Apart from the electron−counting rule, the closed-shell electronic configuration and highly symmetric geometry of a cluster also governs the stability of the cluster. For example, the alkali metal cluster with 2, 8, 20, 40… number of electrons shows magic behaviour.[102] However, $2(N+1)^2$ Hirsch rule is used for icosahedral symmetry cluster according to which clusters with 2, 8, 18, 32, 50,... number of delocalized electrons are more stable compared to other clusters.[103] For example, a sharp peak has been observed in the mass spectra of $AlPb_{12}^+$ cluster while no peak was observed for neutral $AlPb_{12}$ cluster. The stability of $AlPb_{12}^+$ cluster is explained due to the fulfillment of 50−electron rule and it possesses a highly symmetric icosahedral structure.[104]

Pyykkö et al theoretically predicted a stable $W@Au_{12}$ cluster,[105] which possess the icosahedral symmetry and a closed−shell 18−electron $ns^2np^6(n-1)d^{10}$ configuration. Soon after, the structure and stability of $W@Au_{12}$ cluster have been confirmed experimentally using photoelectron spectroscopy (PES).[106] Moreover, the superheavy element doped gold clusters, $Sg@Au_{12}$ is found to be stable theoretically and follow the 18−electron principle.[107] Therefore, 18−electron principle is very promising for explaining the high stability of various transition metal doped clusters. However, the stability of actinide doped clusters, such as $Pu@Pb_{12}$,[101] $An@C_{28}$,[108-110] $[U@Si_{20}]^{6-}$,[111] $Pu@C_{24}$,[112] and lanthanide and actinide doped fullerene, $M@C_{26}$,[113] is successfully explained using 32−electron principle. On the other hand, the very early lanthanide doped gold cluster, $Ce@Au_{14}$ follow 18−electron rule because of their highly stable 4f shells.[114] Till now only uranium doped C_{28} fullerene, $U@C_{28}$, has been observed experimentally.[64]

Unlike to other compounds the stability of closo-boranes ($B_nH_n^{2-}$)[115] can be explained using Wade–Mingos rule.[116-117] According to this rule closo-borane with n vertices will be stable if it possesses 2n+2 electrons or n+1 pairs of skeletal electrons (where n = no of vertices). The $B_{12}H_{12}^{2-}$ is the most stable member of borane family because the 26−electron (12−electrons from B_{12} cage + 12−electrons from 12H atoms and 2−electrons from negative charge) are available for bonding in $B_{12}H_{12}^{2-}$, which is equivalent to the required 2n+2 electrons (n = 12) needed to satisfy Wade–Mingos rule. A unified electron−counting rule for boranes has also been proposed by Jemmis *et al.*[118]

1.8 Scope of the present thesis

Of late scientists have shown that the quantum chemical techniques are very successful in unraveling the nature of bonding in the lanthanide (Ln) and actinide (An) compounds. The applications of lanthanide encapsulated fullerenes[119-121] in nano−materials and nano−medicine have stimulated a new field of f−block element doped compounds. Moreover, application of actinide and lanthanide doped compounds or cluster in spintronics and in the design of novel materials with magnetic properties have further motivated the scientists to explore such compounds. Motivated by the aforementioned applications in various fields, in the present thesis, we have investigated the bonding of Ln and An ions with various chemical species with an objective to find highly stable clusters with intriguing electronic and magnetic properties using density functional theory. Besides, we have also investigated the variation in the chemical bonding of the isoelectronic series of Ln/An with the various chemical species across the f−block.

The complex electronic structure and presence of relativistic effect make the computational investigation of Ln and An chemistry very challenging. For example, the valence electronic configuration of Lr calculated using relativistic correction is $f^{14}p^1s^2$, which is more stable than the previously predicted $f^{14}d^1s^2$ configuration, thereby raising a question whether Lr ($f^{14}p^1s^2$) will still show similarity with Lu ($f^{14}d^1s^2$) or not?[122-127] The complexity in the chemistry of Ln and An elements can also be analyzed from the fact that even in the 150th year of the periodic table it is not clear whether the elements La, Lu, Ac and Lr belong to d−block or f−block. Because in few periodic tables Lu, Lr are placed in d−blocks while in other periodic tables La, Ac are located in d−blocks. On the contrary a third version of the periodic table contains all of these four elements in f blocks. [1-6, 127]

Therefore, the first objective of the present thesis is to investigate the properties of La, Lu, Ac and Lr elements to settle down the on−going debate on their position in the periodic table. For this purpose, we have investigated the La, Lu, Ac and Lr doped Pb_{12}^{2-} and Sn_{12}^{2-} Zintl ion clusters and compared the chemical bonding and electronic behaviour of these metal−doped clusters in each oxidation states of doped Lu^{n+} and Lr^{n+} ($n = 0, 1, 2, 3$) ion. In this study, we have found that Lr^{n+} doped clusters show similarity with the corresponding Lu^{n+} doped clusters despite having different valence electronic configuration. Among all the doped clusters, the M^{3+} (M = La, Lu, Ac and Lr) doped clusters are the most stable clusters due to their highly symmetric icosahedral geometry and electronic shell closing corresponding to $ns^2np^6(n-1)d^{10}$ configuration around M^{3+} ion. Unlike to other actinides and lanthanides, the f−orbitals of La, Ac, Lr and Lu do not involve in bonding with the cluster, therefore, all these M^{3+} doped clusters form 18−electron system rather than 32−electron systems. Thus, due to the similarity in the structure, bonding and electronic properties of La, Lu, Ac and Lr ions doped clusters, we have proposed to place all the four La, Ac, Lr and Lu elements in the 15−element f−blocks.

The second objective of the thesis is to predict new lanthanide and actinide doped compounds, which possess high stability and follow the electron−counting rule as well as possess intriguing electronic and magnetic properties. In this context, we predicted new Ln and An containing metalloid clusters, viz, $[An@(E_4^{2-})_3]$ and $[Ln@(E_4^{2-})_3]$ (An = Th^{4+}– Pa^{5+}– U^{6+}– Np^{7+}; Ln = La^{3+}, Ce^{4+}, Pr^{5+}, Nd^{6+} and E = Sb, Bi) which possess unusually high stability, although the aromaticity of rings in these clusters decrease after binding with the Ln/An ion. As we move across the f−block, the involvement of the f−orbitals of these An (to a lesser extent of Ln) in bonding with the E_4^{2-} rings increases which lead to the fulfillment of

32−electron count in these systems. Therefore, the fulfillment of 32−electrons condition and stronger bonding in the actinide and lanthanide containing systems, viz., $[An@(E_4^{2-})_3]$ (An = U^{6+}, Np^{7+}) and $[Ln@(E_4^{2-})_3]$ (Ln = Nd^{6+}), are responsible for the very high stability of these clusters.

Furthermore, we have predicted another isoelectronic series of lanthanide and actinide doped borate ($B_{12}H_{12}^{2-}$) and alanate ($Al_{12}H_{12}^{2-}$) clusters. The predicted exohedral− and endohedral−$Ln@E_{12}H_{12}^{2-}$ and $An@E_{12}H_{12}^{2-}$ (Ln = Pm^+, Sm^{2+}, Eu^{3+}; An = Np^+, Pu^{2+}, Am^{3+}; E = B or Al) clusters are stable and possess high spin population. In the endohedral $M@Al_{12}H_{12}^{2-}$ (M = Ln, An) clusters, the f−orbitals of actinides and to a lesser extent of lanthanides are involved in the bonding with the parent cluster, which lead to the fulfillment of 32−electrons around the An ion corresponding to $ns^2np^6(n-1)d^{10}(n-2)f^{14}$ configuration. Thus, the present study provides a new example of endohedral $An@Al_{12}H_{12}^{2-}$ (An = Pu^{2+}, Am^{3+}) magnetic superatomic clusters.

Besides, we have made an attempt to predict a nine−membered novel aromatic heterocyclic anionic ligand, viz., 1,4,7−triazacyclononatetraenyl ion, $C_6H_6N_3^-$ (tacn) and their linear sandwich complexes with divalent lanthanide ion (Ln = Nd(II), Pm(II), Sm(II), Eu(II), Tm(II) and Yb(II)) using dispersion corrected density functional theory. It is noteworthy to mention that in $Ln(tacn)_2$ complex all the spin density of the complex is centered on the Ln(II) ion. Moreover, the highest occupied molecular spinor (HOMS) of $Eu(tacn)_2$ complex shows a significant electronic delocalization in the metal centered orbitals, originated mainly from the 4f orbitals of Eu(II) ion. Therefore, the $Eu(tacn)_2$ complex might have application as a single molecule magnet (SMM). Furthermore, the comparable stability of the predicted $C_6H_6N_3^-$ ligand and its $Ln(C_6H_6N_3)_2$ complexes with that of the recently synthesized $C_9H_9^-$ ligand and $Ln(C_9H_9)_2$ complexes[95] favours the feasibility of the predicted ligand and its Ln−sandwich complexes.

Finally, we have predicted another class of closed-shell $An(H_2)_n^{3+}$ and $La(H_2)_n^{3+}$ (n = 1−12) clusters. Though for a long time it was known that the actinide and lanthanide can show high coordination number in their complexes due to their large size, in this work we have shown that an An (Ac^{3+}, Th^{3+}, Th^{4+}, Pa^{4+}, U^{4+}) and Ln (La^{3+}) ion is able to coordinate directly with the 24 H atoms of $12H_2$ molecules via 3−centered 2−electron (3c−2e) $M-\eta^2(H_2)$ bonds, which is the highest recorded coordination behaviour of any metal ion towards H_2 molecules till date. The predicted $Ac(H_2)_n^{3+}$ (n = 9−12) clusters follow the 18−electron rule. Thus, with this study, we have added another stable member in the 18−electron family.

CHAPTER 2

Computational and Theoretical Methodologies

2.1 Introduction

Theoretical chemistry is a branch of chemistry that defines the chemical concepts using mathematical equations. The well−developed mathematical equations or theoretical methods have been incorporated in the computer programs to solve various chemical problems such as stability, energetics, electronic properties, reaction path for chemical reactions etc. The computational results not only support the information obtained by the experiments but also assist in understanding and visualizing the experimental data, which sometimes cannot be analyzed directly from the experimental results. The computational chemistry can also predict the possibility of entirely unknown molecules as well as new chemical phenomena. It also plays an extremely important role in the design of new materials, ligands, and drugs. The most popular theoretical methods such as Hartree-Fock (HF), Post Hartree-Fock, coupled-cluster, density functional, semi−empirical and molecular mechanics have been discussed in great detail in numerous books.[128-130] A brief discussion of the theoretical methods is given here to understand the use of computational techniques in chemistry.

(a) ***Ab initio*****:** *Ab initio* means from the first principle and without empirical parameters. Quantum mechanical methods such as Hartree−Fock, coupled-cluster, Møller−Plesset perturbation theory (MP), configuration interaction (CI), etc are *ab initio* methods. All these methods are wave function based methods. On the other hand, density functional theory (DFT) is based on electron density. Sometimes it is referred as an *ab initio* method though it is a matter of controversy because of the unavailability of the exchange-correlation energy density functional for a system with inhomogeneous electron density distributions, such as atoms, molecules etc.

(b) Semi−empirical methods: Semi−empirical methods use experimental data or the results of *ab initio* calculations to determine some of the required matrix elements or integrals to find properties of the systems.

(c) Molecular mechanics: Unlike other theoretical methods, molecular mechanics uses classical mechanics to model the molecular systems.

The computational chemistry provides meaningful insights into the various chemical systems and processes. Among all the methods, *ab initio* methods provide the most accurate results; however, the computational cost of these methods is very high and even increases with the size of the system. Moreover, the most accurate *ab initio* method viz., coupled-cluster with single and double with perturbative triple excitations [CCSD(T)], also known as a gold standard method is limited to only small size systems. Therefore, for the computational chemists, the selection of accurate method is very important. Among all the available theoretical methods, the density functional theory (DFT) is the most popular as well as most frequently used computational methods for medium to large size molecular systems because of its lower cost and reasonably good accuracy. Therefore, in the present thesis, we have used mostly DFT and to a certain extent second order Møller−Plesset perturbation theory (MP2) and CCSD(T) to investigate various chemical systems.

2.2 Theoretical methodologies

The wave function, Ψ, (known as the heart of the quantum mechanics) contains all the information about the system. It can be obtained by solving the Schrödinger equation and hence all the properties of the systems can be calculated using the wave function. It is to be noted that in the quantum mechanics we use basis set to represent the electronic wave function or to model the electronic behaviour of a system.

2.2.1 Basis set

The basis set is a set of mathematical functions, which is used to represent the electronic wave function in computational chemistry. The basis set is made up of a linear combination of the atomic orbitals (LCAOs) with the coefficient to be determined.

$$\phi_i = \sum_{\mu=1}^{K} C_{\mu i}\chi_\mu \tag{2.1}$$

where $C_{\mu i}$ is expansion coefficient and χ_μ represents a set of a basis functions for the μ^{th} orbital.

For the accurate description of the wave function, basis set should be made up of the infinite number of basis functions. However, due to the computational limitation, a finite number of basis functions are used in most of the quantum chemical calculations. The error associated with the size of the basis set is known as truncation error. Therefore, in general, large size basis set is preferred for the accurate calculations. Moreover, if the finite basis function is expanded towards an infinite complete set of functions, then the calculations using such basis sets are said to approach the basis set limit.

In the present study two types of orbitals, namely, Gaussian−type orbitals or Slater−type orbitals have been used for the construction of the basis functions.

(a) Slater type orbital (STO)

The mathematical form of STO matches with that of the hydrogenic orbital.[131] The mathematical representation of STO in polar coordinates is,

$$\chi_{\xi,n,l,m}(r,\theta,\phi) = Nr^{n-1}e^{-\xi r}Y_{l,m}(\theta,\phi) \tag{2.2}$$

where (r, θ, ϕ) are the spherical coordinates, $Y_{l,m}$ is the spherical harmonics, N is the normalization constant and ξ is the Slater orbital exponent. Since STO has a cusp at the nucleus, therefore, electrons near the nucleus are nicely described by the STOs. The disadvantage of using STO is that the three- and four-centre two-electron integrals cannot be calculated analytically.

(b) Gaussian type orbital (GTO)

The mathematical representation of GTO[132] in polar coordinates is defined as,

$$\chi_{\xi,n,l,m}(r,\theta,\phi) = Nr^{2n-2-l}e^{-\xi r^2}Y_{l,m}(\theta,\phi) \tag{2.3}$$

where the exponent ξ controls the width of the GTO.

At the nucleus a GTO has no cusp, consequently GTOs have problems in representing the proper behaviour near the nucleus. Moreover, due to exponential in r^2 the decay of GTOs is too fast, therefore it poorly describes the behaviour of electrons present at the larger distance from the nucleus. However, calculation of four−index integral can be performed analytically using GTOs.

The limitations of GTO can be overcome by constructing the basis functions as a linear combination of several GTOs to give as good fit as possible to the Slater orbitals. Such basis function is known as a contracted Gaussian−type basis function (CGTF) while the individual Gaussians involved to construct the controlled basis function is known as Gaussian primitives. The CGTF is a good compromise between speed and accuracy.[133]

2.2.2 The Schrödinger equation

In 1926 Erwin Schrödinger postulated a partial differential equation to describe the wave function or state function of a quantum−mechanical system, known as Schrödinger equation.[134] The ground state properties of a system can be described by using the time−independent Schrödinger equation,

$$\hat{H}\ \Psi = E\ \Psi \tag{2.4}$$

For many body systems the time−independent Schrödinger equation can be written as,

$$\hat{H}\ \psi_i\ (r_1, \dots, r_N, R_1, \dots, R_N) = E_i\ \psi_i\ (r_1, \dots, r_N, R_1, \dots, R_N) \tag{2.5}$$

where $\hat{H}$ is the Hamiltonian operator, ψ_i is the wave function of electron and nuclear coordinates and E_i is the eigenvalue of the i^{th} state. The total energy operator "Hamiltonian" in the atomic units can be represented as,

$$\hat{\mathrm{H}} = -\frac{1}{2}\sum_{i=1}^{N} \nabla_i^2 - \frac{1}{2}\sum_{A=1}^{M} \nabla_A^2 - \sum_{i=1}^{N}\sum_{A=1}^{M}\frac{Z_A}{r_{iA}} + \sum_{i=1}^{N}\sum_{j>1}^{N}\frac{1}{r_{ij}} + \sum_{A=1}^{M}\sum_{B>A}^{M}\frac{Z_A Z_B}{R_{AB}} \tag{2.6}$$

where, $r_{iA} = |r_i - R_A|$ is the distance between the i^{th} electron and the A^{th} nucleus, $r_{ij} = |r_i - r_j|$ is the distance between the i^{th} and the j^{th} electrons and R_{AB} is the distance between A and B nuclei. The first and second terms in the equation (2.6) are the kinetic energy for the electrons and nucleus, respectively, third term is potential energy of electron due to its interaction with nucleus, fourth and last terms are the electron−electron and nuclear−nuclear repulsive interactions, respectively.

For an N-electron system, the wave function is a function of 3N spatial variables and N spin variables. Moreover, the total wave function is a function of electronic and nuclear coordinates, therefore it is very difficult to get the exact solution of the Schrödinger equation. Fortunately, Born Oppenheimer (BO) approximation simplifies the Schrödinger equation by decoupling the nuclear and electronic degrees of freedom. According to BO approximation[135] the kinetic energy of nuclei can be neglected from the Hamiltonian and the nuclear repulsion term is kept constant at a fixed nuclear position, because nuclei move much slower than the electron due to its larger mass, therefore, nuclei are considered to be in rest with respect to electronic motion.

Thus, according to the BO approximation, the total wave function of the molecule can be represented as the product of electronic and nuclear wave function.

$$\psi_{total}(r, R) = \psi_{electronic}(r; R) \times \psi_{nuclear}(R) \tag{2.7}$$

and the Schrödinger equation now can be written as,

$$(\hat{H}_{el} + V_N)\ \psi_{el} = E_{el}\ \psi_{el} \tag{2.8}$$

$$\hat{H}_{el} = T_e + V_{eN} + V_{ee} \tag{2.9}$$

Thus, the total energy of the system can be represented as a sum of electronic energy and nuclear energy,

$$E_{total} = E_{el} + E_{nucl} \tag{2.10}$$

Although the BO approximation is generally considered in almost all the theoretical calculations, the solution of the Schrödinger equation is still very difficult due to the presence of electron−electron repulsion term in the many-electron systems. The exact solution of the Schrödinger equation is possible for only the hydrogen (H) atom or H like atoms. But the presence of electron−electron repulsion term prevents the reduction of a many-electron problem to an effective single electron problem (like H atom).

2.2.3 The Variational principle

Infinite numbers of solutions are possible for the electronic Schrödinger equation. However, the accurate solution is the one which minimizes the energy of the system, i.e. which provides the lowest energy solution to the Schrödinger equation. Thus, the real goal of the quantum mechanics is to find a wave function, which provides the ground state energy of the system.

The variational principle states that for any normalized trial wave function Φ_{trial} (that satisfies the appropriate boundary conditions), the expectation value of the Hamiltonian represents an upper bound to the exact ground state energy. In other words, any trial wave function cannot provide energy lower than the ground state energy (ε_0) of the system.

$$\varepsilon_0 \leq \langle \Phi_{trial} | \hat{H} | \Phi_{trial} \rangle \tag{2.11}$$

where ε_0 is the true ground state energy of the system.

The trial or guess wave function, Φ_{trial}, can be constructed as a linear combination of the actual eigenfunctions of the Hamiltonian

$$\Phi_{trial} = \sum_n C_n \Psi_n \tag{2.12}$$

In quantum mechanics, the wave function of a multi−fermionic system is represented as a Slater determinant because it satisfies anti−symmetry requirements, and consequently the Pauli principle. In the following section, we will discuss the brief outline of the Slater determinant as well as the different approximations that have been proposed for solving the Schrödinger equation.

2.2.4 Hartree−Fock approximation

Soon after the introduction of the Schrödinger equation, Hartree in 1928 proposed[136] that the electronic wave function could be approximated in such a way that the individual electrons could be decoupled similar to the decoupling of nucleus and electron in the BO approximation. Thus, the many−electron wave function would be a product of one−electron wave functions as shown in equation (2.13).

$$\psi(\mathbf{r}_1, \mathbf{r}_2, \ldots\ldots, \mathbf{r}_n) = \Phi(\mathbf{r}_1)\Phi(\mathbf{r}_2) \ldots\ldots \Phi(\mathbf{r}_n) \tag{2.13}$$

This wave function completely ignores the instantaneous electron−electron repulsion. To account for this, Hartree assumed that each electron experience an average field created by all other electrons and nuclei in the molecule. This average potential is called mean−field potential (V_i^{eff}) or Hartree potential. Thus, the Schrödinger equation can be written as,

$$\left(-\frac{1}{2}\nabla_{\mathrm{i}}{}^{2}-\sum_{i}^{n}\frac{Z_A}{r_{iA}}+\ V_i^{eff}\right)\phi_i=E_i\ \phi_i \tag{2.14}$$

The Hartree product wave function violates the Pauli Exclusion Principle and does not fulfill the antisymmetry requirement. In 1930 Fock and Slater expressed the wave function as a Slater determinant to incorporate the antisymmetry requirement and the Pauli Exclusion Principle in the wave function.[128]

(a) Slater determinant

According to the antisymmetry principle wave function must change sign on interchange of the positions of any two particles as shown in equation (2.15).

$$\Phi\,(x_1, \dots, x_i, \dots, x_j, \dots, x_N) = -\ \Phi\,(x_1, \dots, x_j, \dots, x_i, \dots, x_N) \tag{2.15}$$

The two−particle wave function can be represented as product of two one−particle wave functions as follows,

$$\Phi_{12}\,(x_1, x_2) = \chi_i\,(x_1)\,\chi_j\,(x_2) \tag{2.16}$$

If we interchange the position of electrons by placing electron one in χ_j and electron two in χ_i, we will have,

$$\Phi_{21}\,(x_1, x_2) = \chi_i\,(x_2)\,\chi_j\,(x_1) \tag{2.17}$$

Thus, the actual wave function can be written as a linear combination of these two functions by simply adding or subtracting these functions. The wave function that is created by subtracting the right−hand side of Equation (2.17) from the right−hand side of Equation (2.16) has the desired anti-symmetric behaviour,

$$\Phi\,(x_1, x_2) = \frac{1}{\sqrt{2}}\,(\chi_i\,(x_1)\,\chi_j\,(x_2) - \chi_i\,(x_2)\,\chi_j\,(x_1)) \tag{2.18}$$

where, the factor $\frac{1}{\sqrt{2}}$ is known as 'normalization factor'.

This equation can be rewritten in determinant form as shown below,

$$\Phi(x_1, x_2) = \frac{1}{\sqrt{2}} \begin{vmatrix} \chi_i(x_1) & \chi_j(x_1) \\ \chi_i(x_2) & \chi_j(x_2) \end{vmatrix} \tag{2.19}$$

This determinant is known as 'Slater determinant'.[137] Similarly, for N−electrons system, the Slater determinant can be written as,

$$\Phi(x_1, x_2, \dots, x_N) = \frac{1}{\sqrt{N!}} \begin{vmatrix} \chi_i(x_1) & \chi_j(x_1) & \dots & \chi_k(x_1) \\ \chi_i(x_2) & \chi_j(x_2) & \dots & \chi_k(x_2) \\ \vdots & \vdots & \dots & \vdots \\ \chi_i(x_N) & \chi_j(x_N) & & \chi_k(x_N) \end{vmatrix} \tag{2.20}$$

In the Slater determinant on going from one row to another row, the electronic coordinates change while on going from one column to the next column the spin−orbital changes. The Slater determinant fulfills the anti-symmetry requirement of the wave function as interchanging the coordinates of two electrons (equivalent to the interchange of two rows) will change the sign of the determinant. Moreover, the determinant will vanish if two electrons occupy the same spin−orbital, which is equivalent to two identical columns of the determinant.

(b) Electron correlation

In Hartree−Fock approximation, the antisymmetric wave function is approximated by a single Slater determinant which does not take into account Coulomb correlation, leading to total electronic energy different from the exact solution of the non−relativistic Schrödinger equation. This energy difference is known as the correlation energy, E_{corr} as shown in equation (2.21), where E_0 and E_{HF} are the exact non-relativistic energy and the Hartree-Fock energy, respectively. However, a certain amount of electron correlation is always present within the HF approximation in the electron exchange term describing the correlation between electrons with parallel spin, which prevents the two parallel spin electrons from being found at the same point in the space known as the Fermi correlation. However, the correlation between the spatial positions of electrons due to Coulomb repulsion (known as Coulomb correlation) is missing in the HF approximation.

$$E_{corr} = E_0 - E_{HF} \tag{2.21}$$

There are two types of electron correlation namely, dynamic and static (nondynamic). The dynamic correlation arises due to the failure of the HF method to account for the instantaneous correlation between the motions of electrons. Whereas, the static correlation arises in those situations when single-Slater-determinant HF wave function provides poor representation of the system's state. The solution of the HF method is discussed as follows.

Considering the simplest case, one−electron hydrogen−like atoms, it is easy to be convinced that the solutions are atomic orbitals (AOs). However, for many electron systems first simple guess is to construct the molecular orbitals (MOs) ϕ_i from the AOs χ_μ (basis functions).

$$\phi_i = \sum_{\mu=1}^{K} C_{\mu i}\chi_\mu \tag{2.22}$$

The Hartree−Fock energy of a Slater determinant can be obtained from the following equation,

$$E_{HF} = \langle \Phi | \hat{H} | \Phi \rangle = \sum_{i}^{N} (i\,|\hat{h}|\,i) + \frac{1}{2}\sum_{i}^{N}\sum_{j}^{N} (ii \mid jj) - (ij \mid ji) \tag{2.23}$$

where the first term of equation (2.23) is,

$$(i\,|\hat{h}|\,i) = \int \chi_i^{*}\vec{x}_1 \left\{ -\frac{1}{2}\nabla^2 - \sum_{A}^{M} \frac{Z_A}{r_{1A}} \right\} \chi_i(\vec{x}_1)\, d\vec{x}_1 \tag{2.24}$$

Equation 2.24, defines the contribution due to the kinetic energy and the electron−nucleus attraction.

The second term of equation (2.23) can be expressed as,

$$\hat{J}_j(i) = (ii \mid jj) = \int\int \left|\chi_i(\vec{x}_1)\right|^2 \frac{1}{r_{12}} \left|\chi_j(\vec{x}_2)\right|^2 d\vec{x}_1 d\vec{x}_2 \tag{2.25}$$

$$\hat{K}_j(i) = (ij \mid ji) = \int\int \chi_i(\vec{x}_1)\chi_j^*(\vec{x}_1) \frac{1}{r_{12}} \chi_j(\vec{x}_2)\chi_i^*(\vec{x}_2) d\vec{x}_1 d\vec{x}_2 \tag{2.26}$$

Here, $\hat{J}_j$ and $\hat{K}_j$ are 'Coulomb' and 'Exchange' operator, respectively. The variational principle is applied for minimizing the Hartree−Fock Energy (E_{HF}). The resulting Hartree−Fock equations can be written as,

$$\hat{F}_i\chi_i = \varepsilon_i\chi_i \qquad (i = 1, 2, 3, \dots, N) \tag{2.27}$$

where $\hat{F}_i = \hat{h}_i + \sum_j^N(\hat{J}_j(i) - \hat{K}_j(i))$ and $\hat{h}_i = -\frac{1}{2}\nabla_\mathrm{i}{}^2 - \sum_i^n \frac{Z_A}{r_{iA}}$ is a one electron Hamiltonian.

In the above expression in equation (2.27), $\hat{F}$ is the Fock operator and ε_i are the Lagrangian multipliers which possesses the physical representation as the orbital energies. In the HF method electron correlation part is missing due to which HF wave function cannot account for the electron correlation (~1% of the total energy), which is very important for describing chemical phenomena. Various post−HF methods improve the Hartree−Fock energy by taking into account the effect of the electron correlation.

2.2.5 Post Hartree−Fock methods

(a) Configuration interaction method

In the configuration interaction (CI) method the trial wave function is written as a linear combination of determinants with the expansion coefficients to be determined by variationally minimizing the energy.[129] If we consider all possible excited configurations that can be generated from the HF determinant, we will have a full CI as shown in equation (2.28).

$$\Psi = a_0\Psi_{HF} + \sum_{i}^{occ.}\sum_{r}^{vir.} a_i^r\Psi_i^r + \sum_{i<j}^{occ.}\sum_{r<s}^{vir.} a_{ij}^{rs}\Psi_{ij}^{rs} + \cdots \tag{2.28}$$

where *i, j*,.. are occupied MOs and *r, s*,.. are virtual MOs in the HF wave function. The first term in the r.h.s of equation (2.28) is the ground state HF wave function. The second and third terms appearing in the equation (2.28) are generated by exciting an electron from the occupied orbital(s) into the virtual orbital(s). Thus, the second and third terms in equation (2.28) represents all possible single electronic excitations and all possible double excitations, respectively, and so on.

The energies *E* of *N* different CI wave functions can be determined from the *N* roots of the CI secular equation,

$$\begin{vmatrix} H_{11}-E & H_{12} & \dots & H_{1N} \\ H_{21} & H_{22}-E & \dots & H_{2N} \\ \vdots & \vdots & \dots & \vdots \\ H_{N1} & H_{N2} & & H_{NN} \end{vmatrix} = 0 \tag{2.29}$$

where $H_{mn} = \langle\Psi_m|H|\Psi_n\rangle$

Solving the secular equations is equivalent to diagonalizing the CI matrix. The CI energy is obtained as the lowest eigenvalue of the CI matrix, and the corresponding eigenvector contains the a_i coefficients in front of the determinants in equation (2.28). The configuration interaction method (CI) recovers the static correlation.

In order to develop a computationally affordable model, the number of excited determinants in the CI expansion (equation (2.28)) must be reduced. Since all matrix elements between the HF wave function and singly excited determinants are zero (Brillouin’s theorem), truncating the excitation level at single excitation (CI with Singles (CIS)) does not give any improvement over the HF method. Only doubly excited determinants have nonzero matrix elements with the HF wave function, thus the lowest CI level that gives an improvement over the HF result is to include only doubly excited states, yielding the CI with Doubles (CID) model. Similarly, CI can be truncated at single and double excitations which gives rise to CISD method.

(b) Møller−Plesset Perturbation theory

The Møller−Plesset (MP) perturbation theory proposed by Møller and Plesset in 1934, treats the electron correlation in a perturbative way by considering the electronic correlation effects as a small perturbation to the basic Hartree−Fock (HF) calculation.[138] This form of many-body perturbation (MBPT) is called as Møller-Plesset (MP) perturbation theory.

The MP unperturbed Hamiltonian is a sum of the one-electron Fock operator ($\hat{f}$) as shown in following equation (2.30),

$$\widehat{H}^0 \equiv \sum_{m=1}^{n} \hat{f}\,(m) \tag{2.30}$$

The ground state HF wave function $\mathit{\Phi}_0$ is a Slater determinant of n spin-orbitals u_i. Thus,

$$\widehat{H}^0 \mathit{\Phi}_0 \equiv \left(\sum_{m=1}^{n} \varepsilon_m\right) \mathit{\Phi}_0 = E^{(0)} \mathit{\Phi}_0 \tag{2.31}$$

The HF ground-state function $\mathit{\Phi}_0$ is one of the zeroth-order wave function of the unperturbed Hamiltonian $\widehat{H}^0$ and $E^{(0)}$ is zeroth order energy of unperturbed Hamiltonian. Thus, the zeroth order eigenfunction ($\mathit{\Phi}_0$) of $\widehat{H}^0$ (using equation (2.31)) has the eigenvalue $\sum_{m=1}^{n} \varepsilon_m$.

Therefore, $$E(MP0) = E_0^{(0)} = \langle \mathit{\Phi}_0 | \widehat{H} | \mathit{\Phi}_0 \rangle = \sum_{m=1}^{n} \varepsilon_m \tag{2.32}$$

The difference between the true molecular electronic Hamiltonian ($\widehat{H}$) and unperturbed Hamiltonian ($\widehat{H}^0$) is defined as perturbed Hamiltonian ($\widehat{H}'$) as shown in equation (2.33).

$$\hat{H}' = \hat{H} - \hat{H}^0 = \sum_{l}\sum_{m>l}\frac{1}{r_{lm}} - \sum_{m=1}^{n}\sum_{j=1}^{n}\left[\hat{J}_j(m) - \hat{K}_j(m)\right] \tag{2.33}$$

where $\hat{H}'$ is the difference between true interelectronic repulsion and the HF average interelectronic repulsion potential. The $\hat{J}_j(m)$ and $\hat{K}_j(m)$ are the same as defined in equations 2.25 and 2.26. The r_{lm} is the distance between the l^{th} and the m^{th} electrons.

The Møller-Plesset first order correction to the ground state energy ($E_0^{(1)}$) can be obtained using following equation (2.34),

$$E_0^{(1)} = \langle \psi_0^{(0)} | \hat{H}' | \psi_0^{(0)} \rangle = \langle \Phi_0 | \hat{H}' | \Phi_0 \rangle \tag{2.34}$$

where subscript 0 denotes the ground state while superscript 0 denotes the zeroth-order (unperturbed) correction. Thus, on adding zeorth and first order corrected energy of the ground state we get,

$$E_0^{(0)} + E_0^{(1)} = \langle \psi_0^{(0)} | \hat{H}^0 | \psi_0^{(0)} \rangle + \langle \Phi_0 | \hat{H}' | \Phi_0 \rangle = \langle \Phi_0 | \hat{H}^0 + \hat{H}' | \Phi_0 \rangle = \langle \Phi_0 | \hat{H} | \Phi_0 \rangle \tag{2.35}$$

Since $\langle \Phi_0 | \hat{H} | \Phi_0 \rangle$ is an expectation value of HF Hamiltonian over HF ground state wave function Φ_0, it equals to the HF energy, E_{HF}. Hence,

$$E(MP1) = E_0^{(0)} + E_0^{(1)} = E_{HF} \tag{2.36}$$

The Hartree-Fock energy can be further improved by including the second order energy correction $E_0^{(2)}$ which is as follows,

$$E_0^{(2)} = \sum_{s \neq 0} \frac{|\langle \psi_s^{(0)} | \hat{H}' | \Phi_0 \rangle|^2}{E_0^{(0)} - E_s^{(0)}} \tag{2.37}$$

where the $\psi_s^{(0)}$ states are all possible Slater determinants made from n different spin-orbitals. Let us consider *i, j, k, l, ...* are the occupied spin-orbitals in the ground state HF wave function Φ_0 and *a, b, c, d, ...* are the unoccupied (also known virtual) spin-orbitals in the HF wave function. Each unperturbed wave function can be categorized by a number of excitation level or virtual spin-orbitals. The singly excited determinant (Φ_i^a) can be formed from Φ_0 by replacing the occupied spin-orbital (u_i) by virtual spin-orbital (u_a) while the doubly excited determinant (Φ_{ij}^{ab}) are formed from Φ_0 by replacing occupied spin orbitals u_i, and u_j by virtual spin orbitals u_a and u_b, and so on.

According to Brillouin's theorem, the value of $\langle \psi_s^{(0)} | \hat{H}' | \Phi_0 \rangle = 0$, for all singly excited $\psi_s^{(0)}$ states and according to Condon-Slater rule $\langle \psi_s^{(0)} | \hat{H}' | \Phi_0 \rangle$ vanishes for $\psi_s^{(0)}$ states whose excitation level is three or higher. Hence we only need doubly excited $\psi_s^{(0)}$ states to find $E_0^{(2)}$ using the following equation (2.38),

$$E(MP2) = E_0^{(2)} = \sum_{b=a+1}^{\infty} \sum_{a=n+1}^{\infty} \sum_{i=j+1}^{n} \sum_{j=1}^{n-1} \frac{|\langle ab\, | r_{12}^{-1} | \, ij \rangle - \langle ab\, | r_{12}^{-1} | \, ji \rangle|^2}{\varepsilon_i + \varepsilon_j - \varepsilon_a - \varepsilon_b} \tag{2.38}$$

where n is the number of electrons and

$$\langle ab\, | r_{12}^{-1} | \, ij \rangle = \int \int u_a^*(1) u_b^*(2) r_{12}^{-1} u_i(1) u_j(2) d\tau_1 d\tau_2 \tag{2.39}$$

The above integrals over the spin orbitals can be calculated in terms of the electron repulsion integrals. The inclusion of all the doubly substituted $\psi_s^{(0)}$ states leads to the summation over a, b, i, and j in equation (2.39).

The more accurate molecular energy can obtained by incorporating the second order correction in the Hartree-Fock energy (E_{HF}), which is designated as MP2 or MBPT(2) as shown in equation (2.40).

$$E(MP2) = E_{HF} + E_0^{(2)} = E_0^{(0)} + E_0^{(1)} + E_0^{(2)} \tag{2.40}$$

The single reference Møller–Plesset perturbation theory (MPn) recovers primarily the dynamic correlation. In the present thesis for a few systems we have performed calculations using the MP2 method.

(c) Coupled cluster method

The coupled cluster (CC) method incorporate the electron correlation using cluster operator.[139] In the CC method wave function can be described as,

$$\Psi_{\mathrm{CC}} = e^{\hat{T}}\Psi_{HF} \tag{2.41}$$

where the cluster operator $e^{\hat{T}}$ is defined by the Taylor series expansion as,

$$e^{\hat{T}} \equiv 1 + \hat{T} + \frac{\hat{T}^2}{2!} + \frac{\hat{T}^3}{3!} + \cdots = \sum_{k=0}^{\infty} \frac{\hat{T}^k}{k!} \tag{2.42}$$

and $\hat{T}$ is defined as,

$$\hat{T} \equiv \hat{T}_1 + \hat{T}_2 + \cdots + \hat{T}_n \tag{2.43}$$

where n is the number of electrons in the molecule and $\hat{T}_1$ is the 'one particle excitation operator' and $\hat{T}_2$ is the 'two particle excitation operator' expressed as,

$$\hat{T}_1\Phi_0 \equiv \sum_{a=n+1}^{\infty}\sum_{i=1}^{n} t_i^a \Phi_i^a \tag{2.44}$$

$$\hat{T}_2\Phi_0 \equiv \sum_{b=a+1}^{\infty}\sum_{a=n+1}^{\infty}\sum_{j=i+1}^{n}\sum_{i=1}^{n-1} t_{ij}^{ab}\Phi_{ij}^{ab} \tag{2.45}$$

where Φ_i^a is the singly excited Slater determinant formed by replacing occupied i^{th} spin-orbital u_i by virtual a^{th} spin-orbital u_a in Φ_0 and the value of numerical coefficient t_i^a depends on i and a. The $\hat{T}_1$ operator on operating on the determinant Φ_0 ($\Phi_0 = |u_1 \cdots u_n|$) converts it into a linear combination of all possible singly excited Slater determinants. On the other hand, (Φ_{ij}^{ab}) is the doubly excited Slater determinant created by replacing occupied spin-orbitals u_i and u_j by virtual spin-orbitals u_a and u_b, respectively. Similar explanation holds for $\hat{T}_3$, ..., $\hat{T}_n$.

In coupled cluster theory the computational problem is to find out the coefficients t_i^a, t_{ij}^{ab}, t_{ijk}^{abc}, ... for all i, j, k, ... , and all a, b, c, ... for all of the operators included in the particular approximation. In the standard application, we can find their values by left-multiplying the Schrödinger equation by trial wave functions expressed as determinants of the HF orbitals. This generates a set of coupled, nonlinear equations in the amplitudes which must be solved, usually by some iterative technique.

With the amplitudes in hand, the coupled-cluster energy is computed as,

$$\langle\Psi|\hat{H}|e^{\hat{T}}\Psi_{HF}\rangle = E_{CC}$$

If cluster operator ($\hat{T}$) expansion is cut off after two terms, the coupled cluster singles and doubles (CCSD) method is created. Using CCSD method it is possible to obtain very good results at a slightly higher computational cost than CI. If couple cluster singles and doubles (CCSD) includes the triple excitations through perturbation then the method is called CCSD(T). The problem is that the formal scaling of these methods is N^4 for regular HF theory to N^8 or higher for the most accurate methods such as CCSD(T), where N is the number of basis functions to describe a system. In the present thesis for a few small size systems we have performed calculations using the CCSD(T) method.

2.3 Density based methods

Density functional theory (DFT) uses density instead of the wave function to investigate the electronic properties of the many-body systems. The use of electron density instead of wave function reduces the 3N variable problem into three variables problem as the electron density is a function of only three variables. It is to be noted that the square of the wave function is physically observable (also known as electron density, ρ ($\vec{\mathrm{r}}$)) and can be defined as the probability of finding an electron in the volume element d$\overrightarrow{r_1}$, whereas wave function itself has no physical significance.

The mathematical representation of electron probability density is,

$$\rho(\vec{r}) = N\int\cdots\int|\psi(\vec{x}_1,\vec{x}_2,\dots,\vec{x}_N)|^2 ds_1 d\vec{x}_2 \dots d\vec{x}_N \qquad (2.46)$$

The electron density, $\rho(\vec{r})$, is a non−negative function of only the three spatial variables which vanishes at infinity and integrates to the total number of electrons,

$$\rho(\vec{r} \rightarrow \infty) = 0 \tag{2.47}$$

$$\int \rho(\vec{r}) d\vec{r}_1 = N \tag{2.48}$$

2.3.1 The Thomas−Fermi model

Thomas and Fermi were the first to introduce the use of density instead of wave function to solve many body problems. In this model, a functional form of the kinetic energy of non−interacting uniform electron gas is derived from the quantum statistical theory.[140-141] However, the electron−nucleus and electron−electron interactions treated classically. The significance of this simple Thomas−Fermi model is that the energy can be determined purely using the electron density. The kinetic energy functional of the electrons is defined as,

$$T[\rho] = C_F \int \rho^{\frac{5}{3}}(\vec{r}) d\vec{r} \tag{2.49}$$

where
$$C_F = \frac{3}{10}(3\pi^2)^{\frac{2}{3}} \tag{2.50}$$

The total energy in terms of electron density is represented as,

$$E[\rho] = C_F \int \rho^{\frac{5}{3}}(\vec{r}) d\vec{r} - Z \int \frac{\rho(\vec{r})}{\vec{r}} d\vec{r} + \frac{1}{2} \iint \frac{\rho(\vec{r}_1)\rho(\vec{r}_2)}{|\vec{r}_1 - \vec{r}_2|} d\vec{r}_1 d\vec{r}_2 \tag{2.51}$$

While this kinetic energy expression is correct for uniform electron gas, it is not obvious if this relation will hold for inhomogeneous electron gas (real systems). In the above equation, the first term represents the kinetic energy; second and third terms are the electron−nucleus and electron−electron interactions energy, respectively.

2.3.2 The Hohenberg−Kohn theorems

Although Thomas–Fermi have first proposed the density functional theory for the electronic structure of materials, the DFT was first put on a firm theoretical basis by Walter Kohn and Pierre Hohenberg in 1964 in the framework of the two Hohenberg–Kohn theorems (HK). The original HK theorems held only for non−degenerate ground states. The HK theorems relate to any system consisting of electrons moving under the influence of an external potential.[142]

Theorem 1: The first HK theorem states that the ground−state properties of the many−electron systems are uniquely determined by an electron density ($\rho(\vec{r})$) that depends on only three spatial coordinates. Moreover, the ground state density ($\rho(\vec{r})$) uniquely determines the potential and thus all properties of the system, including the many−body wave function.

Theorem 2: The second HK theorem defines an energy functional for a system and demonstrates that the correct ground state density for a system is the one that minimizes the total energy through the functional E[$\rho(\vec{r})$]. Thus, the true ground state density of the system gives the lowest energy.

For any positive integer N and external potential V_{Ne}, a density functional $F[\rho]$ exists such that,

$$E[\rho] = (F[\rho] + \int \rho(\vec{r})V_{Ne}d\vec{r}) \tag{2.52}$$

While the ground state energy of any atomic or molecular system can be expressed as,

$$E_0[\rho] = \min_{\rho \to N}(F[\rho] + \int \rho(\vec{r})V_{Ne}d\vec{r}) \tag{2.53}$$

where $$F[\rho(\vec{r})] = T[\rho(\vec{r})] + J[\rho(\vec{r})] + E_{ncl}[\rho(\vec{r})] \tag{2.54}$$

The first term $T[\rho(\vec{r})]$ denotes kinetic energy; second term $J[\rho(\vec{r})]$ is a classical Coulomb interaction and the third term $E_{ncl}[\rho(\vec{r})]$ is a non−classical term, which contains a self−interaction correction, exchange and electron correlation effects. The HK theorems cannot explain how to find the energy from the density since functional F$[\rho]$ in the equation 2.52 is unknown. Also, the HK theorems do not tell how to find the density without first finding the wave function. In 1965 Kohn and Sham devised a practical method for finding the density and energy from the density.

2.3.3 The Kohn−Sham method

The Kohn–Sham (KS) equation is the one−electron Schrödinger equation of a fictitious system of non−interacting electrons that generate the same density as that of the any given system of interacting electrons.[143] The Kohn–Sham equation is defined by a local effective (fictitious) external potential in which the non−interacting particles move, typically denoted as $v_{eff,}$ and known as Kohn–Sham potential. As the particles in the Kohn–Sham system are non−interacting fermions, the Kohn–Sham wave function is a single Slater determinant constructed from a set of orbitals that are the lowest energy solutions,

$$\left(-\frac{1}{2}\nabla^2 + v(\vec{r}) + \int \frac{\rho(\vec{r}\,')}{|\vec{r}-\vec{r}\,'|}d\vec{r}\,' + v_{xc}(\vec{r})\right)\phi_i = \varepsilon\phi_i \tag{2.55}$$

Here the first term is kinetic energy, second term is external potential, third term is Hartree potential and the last term is the exchange−correlation potential, respectively. Here, ε is the orbital energy of the corresponding Kohn–Sham orbital, ϕ_i, and the density for an N−particle system is expressed by,

$$\rho(\vec{r}) = \sum_i^N |\phi_i|^2 \tag{2.56}$$

The exchange−correlation potential is given by,

$$v_{xc}(\vec{r}) = \frac{\delta E_{xc}[\rho]}{\delta \rho(\vec{r})} \tag{2.57}$$

$$\text{and } E_{xc}[\rho] = (T[\rho] - T_s[\rho]) + (E_{ee}[\rho] - E_H[\rho]) \tag{2.58}$$

where $T[\rho]$ and $E_{ee}[\rho]$ are the exact kinetic energy and electron–electron repulsion energy, while $T_s[\rho]$ and $E_H[\rho]$ are approximated kinetic energy and electron–electron repulsion energy.

Thus, the effective potential can be defines as,

$$v_{eff} = v(\vec{r}) + \int \frac{\delta \rho(\vec{r})}{|\vec{r} - \vec{r}\,'|} d\vec{r}\,' + v_{xc}(\vec{r}) \tag{2.59}$$

Therefore, the equation (2.55) can be rewritten in a more compact form as,

$$\left(-\frac{1}{2}\nabla^2 + v_{eff}\right)\phi_i = \varepsilon \phi_i \tag{2.60}$$

From the above expression, it is clearly evident that the KS equation is like a Hartree–Fock single particle equation, which needs to be solved iteratively. The total energy can be determined from the resulting density through the following equation,

$$E = \sum_{i}^{N} \varepsilon_i - \frac{1}{2}\iint \frac{\rho(\vec{r})\rho(\vec{r}\,')}{|\vec{r} - \vec{r}\,'|} d\vec{r} d\vec{r}\,' + E_{XC}[\rho] - \int v_{xc}(\vec{r})\rho(\vec{r})d\vec{r} \tag{2.61}$$

Equations (2.55) and (2.60) are the distinguished Kohn–Sham equations. Since v_{eff} depends on $\rho(\vec{r})$ through the equation (2.59), therefore, the Kohn–Sham equation is solved self–consistently. In KS method at first we have to make a guess of electron density, which is used in the construction of v_{eff} using the equation (2.59). Using this v_{eff}, KS equation (2.60) is solved to get the Kohn–Sham orbitals. Based on these orbitals, a new density is calculated from equation (2.56) and the process is repeated until the convergence is achieved.

Finally, the total energy of the system is calculated from equation (2.61) with the final electron density. If each term in the Kohn–Sham energy functional was known, we would be able to obtain the exact ground state density and the total energy. Unfortunately, there is one unknown term, the exchange−correlation (XC) functional (E_{XC}). The E_{XC} includes the non−classical aspects of the electron−electron interaction along with the component of the kinetic energy of the real system, which is different from the fictitious non−interacting system. Since E_{XC} is not known exactly, it is necessary to approximate it. Therefore, since the birth of DFT, a large number of approximations for E_{XC} have been proposed.[130]

(a) Local density approximation

The local density approximation (LDA) is the simplest approximation for constructing exchange−correlation (XC) functional, which assumes a fictitious uniform electron gas model for calculating the exchange−correlation energy. Thus in the LDA, XC functionals depend only on the local value of the electron density.

In general, the LDA expression for XC energy is written as,

$$E_{XC}^{LDA}[\rho] = \int \rho(\vec{\boldsymbol{r}})\varepsilon_{XC}\big(\rho(\vec{\boldsymbol{r}})\big)d\boldsymbol{r} \tag{2.62}$$

Evaluating the integral, using a uniform gas produces,

$$\varepsilon_X = C_X \int \rho^{4/3}\ (\boldsymbol{r})d\boldsymbol{r} \tag{2.63}$$

$$C_X = -\frac{3}{4}\left(\frac{3}{\pi}\right)^{1/3} \tag{2.64}$$

The analytic form of exchange term is simple for the homogenous electron gas model. However, only limiting expressions for the correlation density are known exactly, leading to numerous different approximations for correlation energy, ε_c. The high−level quantum Monte Carlo simulations provide accurate values of the correlation energy density. The Vosko−Wilk−Nusair (VWN) and Perdew−Wang (PW92) are LDA's for the correlation functional.

For spin−polarized systems local spin−density approximation (LSDA) is used instead of LDA. The spin polarized system in DFT possess two density, ρ_α and ρ_β for the up and down spins, with $\rho = \rho_\alpha + \rho_\beta$

$$E_{XC}^{LDA}[\rho_\alpha, \rho_\beta] = \int \rho(\boldsymbol{r})\varepsilon_{XC}(\rho_\alpha, \rho_\beta)d\boldsymbol{r} \tag{2.65}$$

LDA has been widely used for band structure calculations, however, their performance is less impressive for molecular calculations.

(b) Generalized gradient approximation

The LDA is appropriate model for a system with uniform electron density. However, in the real system the electron density is not as uniform as considered in LDA approach. Therefore, apart from the density, the exchange−correlation functionals in GGA contain the first derivative of the electron density to take into account the non−homogeneity of the true electron density, which includes information about the immediate neighbourhood of the point under consideration. There are various functionals using the GGA approach in use, and they can be semi−empirical or non−empirical. BLYP is an example of a semi−empirical GGA functional, which is dependent upon a parameter fitted to experimental data. The PBE is a popular non−empirical GGA functional.

$$E_{XC}^{GGA}[\rho(r)] = \int \rho^{4/3}(\boldsymbol{r})f\big(X(r)\big)dx \tag{2.66}$$

$$X(r) = \frac{\nabla\rho(r)}{\rho^{4/3}(r)} \tag{2.67}$$

GGA provides very good results for molecular geometries and ground−state energies. The PW86, B88 ("b"), PBE[144] and PW91 are the examples of exchange and either PW91 or PBE or LYP is correlation in GGA. The exchange energy of B88 can be written as,

$$E_X^{B88}[\rho] = E_X^{LDA}[\rho] - \beta\rho^{1/3}\frac{X^2}{1 + 6\beta\sinh^{-1}X} \tag{2.68}$$

$$X = \frac{|\nabla\rho|}{\rho^{4/3}} \tag{2.69}$$

The B86 and PBE functionals contains no empirical parameters.

The next level of improvement over GGA is the meta−GGA. These functionals are dependent on the second derivatives of the electron density (the Laplacian) or on kinetic energy density. TPSS is a popular example of a meta−GGA functional. The GGA’s tend to improve total energies, atomization energies, energy barriers and structural energy differences. The M06 suite of functionals[145] is a set of meta−hybrid GGA and meta−GGA DFT functionals. The M06 suite gives good results for systems containing dispersion forces.

(c) Hybrid exchange−correlation functionals

The exchange-correlation energy with a LDA or a GGA functional incorporates an unphysical self-interaction error (SIE). In contrast the Hartree-Fock (HF) theory explicitly accounts for the self-interaction correction but correlation effect is not included in the HF method which is important in larger molecules and solids for describing the chemical bonding accurately. As these correlation effects are captured well within the local exchange-correlation functionals, Becke[132] rationalized an intermixture of local exchange-correlation functionals with HF exchange known as hybrid functionals. The popular B3LYP exchange−correlation functional is an example of a semi−empirical hybrid functional containing exact exchange, LDA and GGA exchange (with the latter coming from the B88 functional), plus LDA and GGA correlation (with the latter coming from the LYP functional). The B3LYP functional[146-147] is defined in equation (2.70),

$$E_{XC}^{B3LYP} = E_X^{LDA} + a_0(E_X^{HF} - E_X^{LDA}) + a_x(E_X^{GGA} - E_X^{LDA}) + E_C^{LDA} + a_c(E_C^{GGA} - E_C^{LDA}) \quad (2.70)$$

where the parameters a_0 = 0.20, a_x = 0.72 and a_c = 0.81. These parameters are specified by fitting the functional's predictions to experimental or accurately calculated thermochemical data.

PBE0 functional is another hybrid functional.[148-149] The PBE0 functional mixes the Hartree−Fock exchange with exchange obtained from the Perdew–Burke−Ernzerhof (PBE) functional in 1:3 ratio as shown in equation (2.71).

$$E_{XC}^{B3LYP} = \frac{1}{4}E_X^{HF} + \frac{3}{4}E_X^{PBE} + E_C^{PBE} \quad (2.71)$$

The hybrid functionals further improves the performance in the calculation of many molecular properties, such as atomization energies, bond lengths, and vibration frequencies.

2.4 Computational details

All the theoretical calculations have been performed using the TURBOMOLE[150] and ADF[151-153] programs. Bare as well as metal encapsulated clusters have been optimized using PBE, PBE0, B3LYP, BHLYP and M06−2X functionals.[144-149, 154-155] Moreover, in weakly interacting systems we have added Grimme's D3−dispersion correction.[156-157] For most of the calculations we have used Gaussian type basis set, however, for fewer calculations Slater type basis set has been used. Apart from DFT, for few systems we have also used wave function based methods such as MP2[138, 158] and CCSD(T)[159]. The def−TZVP and def−TZVPP basis sets[160] have been used along with a relativistic effective core potential (RECP) for all the heavier elements.[161-164] The CCSD(T) calculations are performed using MOLPRO2012[165] software. Frequency calculations have been carried out in order to obtain the true minima on their respective potential energy surfaces (PES). Charges on the metal atoms or ions have been calculated using natural population analysis with def-TZVP and def-TZVPP basis sets[166]. Besides, Voronoi deformation density (VDD) method[167] has also been used for the charge calculation using Slater type basis set as implemented in ADF software. Furthermore, the atoms–in–molecules (AIM) analysis[168-169] has been adopted to understand the nature of bonding that exists between the lanthanide or actinide elements with the elements present in the host cluster. The Multiwfn[170] software has been used for analyzing the electron density based on Bader's quantum theory of atoms in molecules (QTAIM).[168-169] The bond critical point (BCP) and the electron localization function (ELF)[171] have been analyzed using Boggs criteria[169] of bonding to get information about the nature of the bonding between the central metal ion and cage atoms. The missing core electron density on heavy atoms is modeled by using the tightly localized electron density function (EDF) as proposed by Keith and Frisch.[172] Since the results of electron density analysis by using the ECP based wave function augmented with EDF are nearly identical to the corresponding all electron wave function derived results,[172] therefore we have calculated all the bond critical point properties by using the EDF augmented electron density as implemented in the Multiwfn software. Furthermore, to obtain the interaction energies between the fragments in the doped cluster, energy decomposition analysis (EDA)[173-175] has been performed using scalar relativistic zeroth order regular approximation(ZORA)[176-177] with ADF software. The TZ2P basis set[178] has been used along with the zeroth−order regular approximation (ZORA) for the incorporation of scalar relativistic effect. Furthermore, spin orbit coupling effect has also been studied using ZORA approach as implemented in ADF software.[179] Throughout the thesis, the molecular orbital pictures are plotted with an electron density cutoff of 0.02 eÅ^{-3}.

CHAPTER 3

Position of Lanthanides and Actinides in the Periodic Table: A Theoretical Study

3.1 Introduction

For the past three decades there has been a heated debate with reference to the position of lawrencium (Lr) and lutetium (Lu) in the periodic table. In 1983 Jensen suggested that Lu should be placed in the third group of the periodic table below scandium (Sc) and yttrium (Y) due to the absence of empty f−orbitals in Lu and its similarities with Sc and Y for various atomic properties such as atomic radii, the sum of the first two ionization potentials, the melting point, and electronegativity. However, Jensen placed Lr in group 3 below Lu solely on the basis of their similar properties.[1-2] This placement resulted in fourteen−element rows, La–Yb and Ac–No for the f−block elements, is now also chosen by Wikipedia. Later calculations which incorporated the relativistic effect, found the ground state of Lr to be [Rn]$5f^{14}7s^{2}7p^{1}$ instead of [Rn]$5f^{14}6d^{1}7s^{2}$.[122-124] On this basis, Lavelle in 2008 claimed that Lr and Lu should not be placed in the d block, but instead La ([Xe]$5d^{1}6s^{2}$) and Ac ([Rn]$6d^{1}7s^{2}$) be placed in the d block as both have their last electron in a d orbital.[3-5] Lavelle maintained that Lu and Lr must remain in the f block consisting of fourteen−element rows, Ce–Lu and Th–Lr.[3-5] The placement of Lr and Lu in the f−block and La and Ac in the d block as suggested by Lavelle is accepted by the Royal Society of Chemistry and the American Chemical Society. However, Lavelle’s view is solely based on the electronic configuration which is not reasonable and acceptable due to the presence of exceptional electronic configurations. For example Cr ($s^{1}d^{5}$) follows V ($s^{2}d^{3}$) and Cu ($s^{1}d^{10}$) follows Ni ($s^{2}d^{8}$) in the periodic table even though there is no continuity in the electronic configuration. If we only focus on the electronic configuration, then we will be forced to place Lr ($f^{14}s^2p^1$) in p block rather than in d or f block.

Apart from various electronic properties of atoms considered by Jensen[1-2], electric response property, mainly, the polarizability trends[180] also favours the placement of Lu in the group 3 of the periodic table. However, the polarizability of Lr is extremely large as compared to that of the group 3 elements and f-elements.[181] Later, Scerri has used XIX-century semi-quantitative reasoning to show that the elements Y, Lu, Lr form an atomic number triad, whereas the same is not true for Y, La and Ac which supports the Jensen's view.[182] In addition, Scerri has given various other contributions to the periodic table.[183-186] In 2015, Jensen has reconfirmed his initial suggestions[187] and maintained the placement of Lu and Lr in d-block. Recently Cao *et al.*[188] have also supported the Jensen's view by showing that the Lu and Lr have f^{14} shell in their lanthanoid- and actinoid-contracted atomic core and they are found to be more similar to the d elements than the La and Ac, respectively. Thus, in the periodic table elements are arranged in such a way that one may easily find similarity in the properties as they go down the group and elements are separated in the periodic table with systematic filling of electrons in s, p, d, … shells.[189]

The experimentally determined and theoretically calculated, exceptionally low value of the first ionization potential of Lr (4.96 eV) clearly shows the importance of the relativistic effect in the heavy elements.[125] Recent studies in 2016 by Srivastava *et al.* uncovered that the Lr@C_{60} cluster shows similar behaviour to the alkali metal encapsulated Li@C_{60} cluster.[126] This finding and a very low value of ionization potential of Lr again raises a query concerning the position of Lr in the periodic table. Employing the relativistic electronic configuration of Lr ([Rn]$5f^{14}7s^27p^1$), Pyykkö *et al.* in 2016 studied the effect of the ground state configuration of Lr on its chemical behaviour and concluded that though they have different ground state configurations, both Lr and Lu show the same chemical behaviour, whereas Tl and Lr show quite different properties, in spite of having similar ground state electronic configurations. Thus, Pyykkö *et al.* advocated the placement of all lanthanides (La–Lu) and actinides (Ac–Lr) in the f block[6] consisting of 15 elements with configurations of f^0 to f^{14}. This placement has now been adopted in the modern periodic table and by IUPAC.[190] Therefore, to date the position of Lr, Lu, La, Ac elements in the periodic table is in controversy and this has motivated us to investigate the chemical as well as the electronic behaviour of Lr and Lu and compare their properties with those of La and Ac.

To settle down the ongoing controversy we have looked into this issue from a new perspective, which involves encapsulation of these four elements into Zintl ion clusters, Sn_{12}^{2-} (stannaspherene)[62] and Pb_{12}^{2-} (plumbaspherene)[63] followed by determination of structural, thermodynamic and electronic properties of these endohedral $M@Pb_{12}^{2-}$ and $M@Sn_{12}^{2-}$ clusters (M = Lr^{n+}, Lu^{n+}, La^{3+}, Ac^{3+} with n = 0, 1, 2, 3) using density functional theory (DFT). We have doped Lr and Lu element in their different oxidation states (0 to +3) in a cluster due to their different valence electronic configuration while La and Ac are studied in their most stable +3 oxidation state. All the results discussed in this chapter have been obtained by using PBE[144] and B3LYP functionals[146-147] with def−TZVP basis set along with a relativistic effective core potential (RECP) for heavy elements by using Turbomole[150], ADF[151, 153] and Multiwfn[170] programs. The PBE results are discussed throughout the chapter unless otherwise stated. Detail computational methodologies have been discussed in Chapter 2 of this thesis.

3.2 Results and discussions

3.2.1 Structural stability analysis

The bare Sn_{12}^{2-} and Pb_{12}^{2-} cages possess icosahedral geometry as the minimum energy structure. In the recent past a number of transition metal as well as lanthanide encapsulated Pb_{12}^{2-} and Sn_{12}^{2-} clusters have been investigated experimentally as well as theoretically owing to their large diameter.[66-67, 191-194] Moreover, we have calculated the ionization potential (IP) of Pb_{12}^{2-} and Sn_{12}^{2-} which came out to be 0.14 and 0.15 eV, respectively. The positive value of IP suggests that these dianions are stable in the gas phase and would not show auto-detachment of excess electron in the gas phase. Both the Pb_{12}^{2-} and Sn_{12}^{2-} clusters are found to be stabilized due to the substantial delocalization of excess two electrons in such a large size systems. Therefore, in the present work we have modeled the chemical behaviour of Ln (La, Lu) and An (Ac, Lr) atom or ion by doping them in Pb_{12}^{2-} and Sn_{12}^{2-} clusters and compared the similarity and differences in the various properties of La, Ac, Lu and Lr doped clusters.

To start with we have considered icosahedral geometry as the initial geometry of $M@Pb_{12}^{2-}$ and $M@Sn_{12}^{2-}$ ($M = Lr^{n+}$, Lu^{n+}, La^{3+}, Ac^{3+} and n = 0, 1, 2, 3) clusters. However, only Lr^{3+}, Lu^{3+}, La^{3+} and Ac^{3+} encapsulated Sn_{12}^{2-} and Pb_{12}^{2-} clusters with closed-shell configurations are optimized with all real frequency values in the icosahedral geometry, while all the other $M@Pb_{12}^{2-}$ and $M@Sn_{12}^{2-}$ clusters ($M = Lr^{n+}$, Lu^{n+} and n = 0, 1, 2) are associated with imaginary frequency values. Therefore, to obtain the minimum energy structures we have again optimized the clusters by displacing their coordinates along the imaginary frequency modes. We repeated this process several times until we obtained the lowest energy structure associated with real frequency values for all the endohedral clusters. The most stable geometry of each metal encapsulated cluster is discussed below in detail.

3.2.2 Endohedral Lr^{n+} and Lu^{n+} doped clusters

(a) Lr^{3+} and Lu^{3+} clusters

First we have considered Lr^{3+} and Lu^{3+} encapsulated Pb_{12}^{2-} and Sn_{12}^{2-} cages, which result in $Lr@Pb_{12}^{+}$, $Lu@Pb_{12}^{+}$, $Lr@Sn_{12}^{+}$ and $Lu@Sn_{12}^{+}$ clusters. The structures of all these clusters have been optimized in I_h, O_h and D_{5h} geometries to obtain the energetically most stable structures and these geometries are represented as Str1(I_h), Str2(O_h) and Str3(D_{5h}) respectively (Figure 3.1). The calculated values of the relative energy of the M@Pb_{12}^+ and M@Sn_{12}^+ (M = Lr and Lu) clusters are reported in Table 3.1. From Table 3.1 one can see that both the lower symmetry geometries viz., Str2(O_h) and Str3(D_{5h}) of the M@E_{12}^+ (M = Lr and Lu, E = Pb, Sn) clusters are less stable (by 1.83−2.86 eV) than the corresponding highly symmetric icosahedral geometry, Str1(I_h). Frequency calculations subsequently carried out on the optimized structures result in Str1(I_h) with all real frequencies, while both Str2(O_h) and Str3(D_{5h}) possess imaginary frequency modes. Therefore, to obtain the true minimum structure, we have displaced the coordinates along the imaginary frequency mode and subsequently re−optimized these structures with and without any symmetry constraints. Interestingly, all the optimized geometries (with and without any symmetry) are found to have the same icosahedral structure. Thus both Lr^{3+} and Lu^{3+} encapsulated Pb_{12}^{2-} and Sn_{12}^{2-} clusters retained icosahedral geometry of the parent clusters and shows one−to−one correspondence in their geometry.

(b) Lr^{2+} and Lu^{2+} clusters

Similarly, Lr^{2+} and Lu^{2+} encapsulated Pb_{12}^{2-} and Sn_{12}^{2-} cages, viz., Lr@Pb_{12}, Lu@Pb_{12}, Lr@Sn_{12} and Lu@Sn_{12} clusters have been investigated and four different geometries, one with D_{3d} symmetry and the remaining three with C_1 symmetry, represented as Str4(D_{3d}), Str5(C_1), Str6(C_1) and Str7(C_1), respectively, are found to be optimized with all real frequency values (Figure 3.1). Their relative energies are listed in Table 3.1. For both Lr@Pb_{12} and Lu@Pb_{12} clusters, the Str4(D_{3d}) is the most stable and Str7(C_1) the least as shown in Table 3.1. Similarly, M@Sn_{12} clusters (M = Lr and Lu) have been optimized to give three different geometries: one with D_{3d} and two with C_1 symmetry, which are represented as Str4(D_{3d}), Str6(C_1) and Str7(C_1), respectively (Figure 3.1). Here again for both Lr@Sn_{12} and Lu@Sn_{12} clusters, Str4(D_{3d}) or Str6(C_1) is the most stable and Str7(C_1) is the least stable structure. Thus, one–to–one correspondence between the Lr^{2+} and Lu^{2+} ions in the Lr@Pb_{12}, Lu@Pb_{12}, Lr@Sn_{12} and Lu@Sn_{12} clusters is found to exist.

(c) Lr^+ and Lu^+ clusters

Next we have considered the mono–positive cation containing Pb_{12}^{2-} and Sn_{12}^{2-} cages, namely, Lr@Pb_{12}^-, Lu@Pb_{12}^-, Lr@Sn_{12}^- and Lu@Sn_{12}^- clusters. The geometries of all these clusters are optimized and we obtain four different structures with D_{3d}, C_1, C_1, and C_s symmetries for the M@Pb_{12}^- clusters (M = Lr and Lu). These are represented as Str4(D_{3d}), Str7(C_1), Str8(C_1) and Str9(C_s), respectively (Figure 3.1) and their relative energy is reported in Table 3.1. For both Lr@Pb_{12}^- and Lu@Pb_{12}^- clusters, the Str8(C_1) is the most stable, whereas Str7(C_1) corresponds to the least stable structure. While all the M@Sn_{12}^- clusters exist in four different geometries (Str6(C_1), Str7(C_1), Str8(C_1), and Str11(C_1)) all with C_1 symmetry. For Lr@Sn_{12}^- and Lu@Sn_{12}^- clusters also Str8(C_1) and Str7(C_1) represent the most and least stable structures, respectively (Table 3.1). All these results clearly indicate the analogous behaviour of Lr^+ and Lu^+ ions when encapsulated within the Pb_{12}^{2-} and Sn_{12}^{2-} cages.

(d) Lr and Lu clusters

Apart from the +3, +2 and +1 oxidation states of Lr and Lu as discussed above, here we discuss the encapsulation of neutral Lr and Lu atom within the Pb_{12}^{2-} and Sn_{12}^{2-} cages. In order to locate the most stable structure for the M@Pb_{12}^{2-} and M@Sn_{12}^{2-} (M = Lr, Lu) clusters, the calculations have been carried out using a number of initial geometries. However, only three structures, two with C_1 and one with C_2 symmetry (Str7(C_1), Str8(C_1)

and Str10(C_2), respectively) are found to possess real frequencies. For both Lr@Pb_{12}^{2-} and Lu@Pb_{12}^{2-} clusters, Str10(C_2) and Str8(C_1) are the most stable, while Str7(C_1) represents the least stable isomer (Table 3.1). Similarly, for both Lr@Sn_{12}^{2-} and Lu@Sn_{12}^{2-} clusters, Str8(C_1) proved to be the most stable though Str7(C_1) is the least stable (Table 3.1). Once again the calculated results suggest a close similarity between Lr and Lu even in their neutral state.

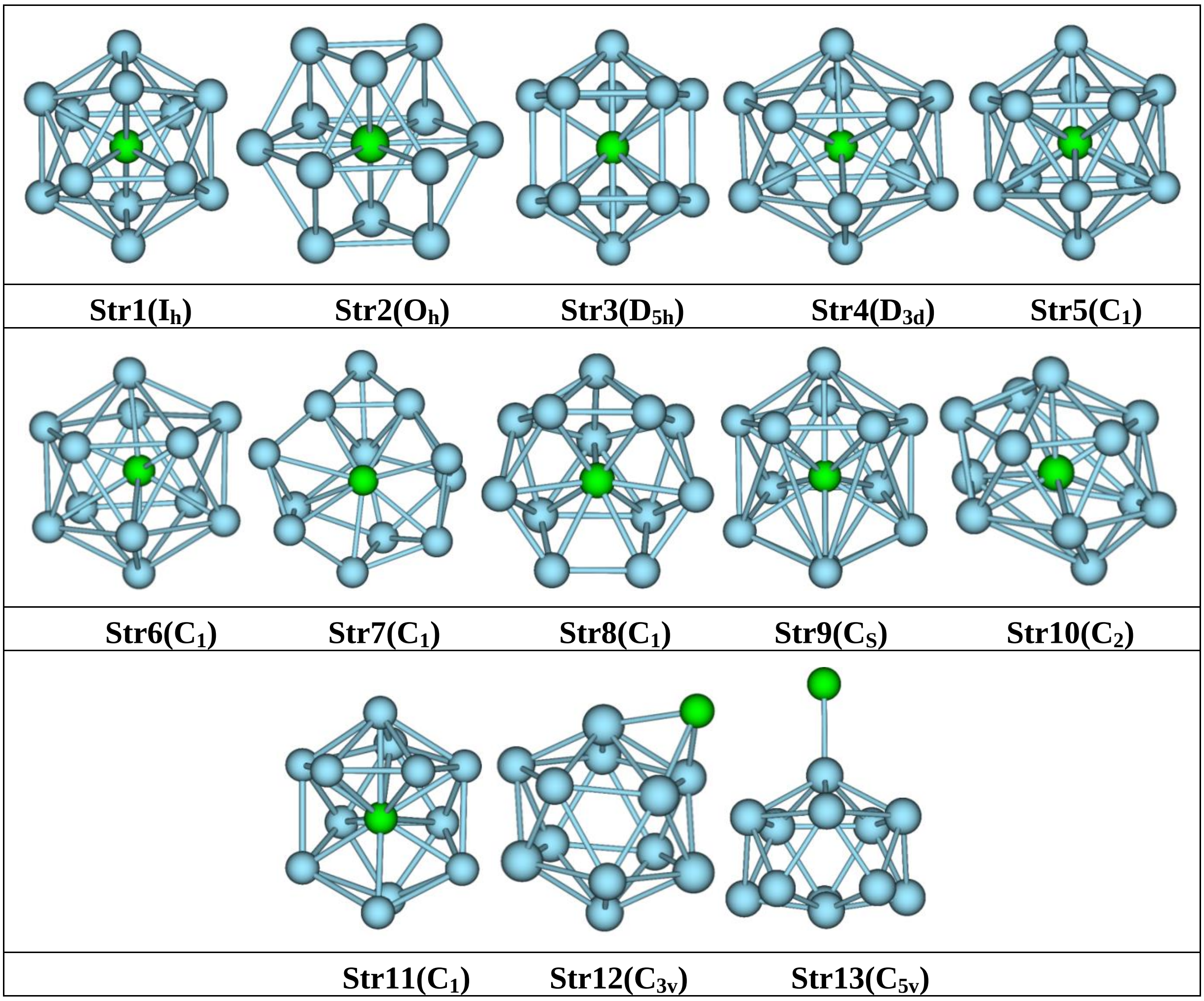

Str1(I_h) **Str2(O_h)** **Str3(D_{5h})** **Str4(D_{3d})** **Str5(C_1)**

Str6(C_1) **Str7(C_1)** **Str8(C_1)** **Str9(C_S)** **Str10(C_2)**

Str11(C_1) **Str12(C_{3v})** **Str13(C_{5v})**

Figure 3.1: Optimized structures of M@Pb_{12}^{2-} (M = Lr^{n+}, Lu^{n+} and n = 0, 1, 2, 3) clusters.

Table 3.1: Relative Energy (RE, in eV) of Different Isomers of $M^{n+}@E_{12}^{2-}$ with Respect to the Corresponding Most Stable Isomer using PBE Functional.

Geometry	**RE**		**Geometry**	**RE**	
	$Lr^n@Pb_{12}^{2-}$	**$Lu^n@Pb_{12}^{2-}$**		**$Lr^n@Sn_{12}^{2-}$**	**$Lu^n@Sn_{12}^{2-}$**
			$M@E_{12}^+$		
Str1(I_h)	0.00	0.00	**Str1(I_h)**	0.00	0.00
Str2(O_h)	2.13[a]	2.23[a]	**Str2(O_h)**	1.83[a]	1.94[a]
Str3(D_{5h})	2.76[a]	2.86[a]	**Str3(D_{5h})**	2.31[a]	2.40[a]
Str12(C_{3v})(exo)	1.33	2.10	**Str12(C_{3v})(exo)**	0.52	1.33
Str13(C_{5v})(exo)	2.06[a]	3.55[a]	**Str13(C_{5v})(exo)**	1.16[a]	2.76[a]
			$M@E_{12}$		
Str4(D_{3d})	0.00	0.00	**Str4(D_{3d})**	0.00	0.01
Str5(C_1)	0.01	0.01	**Str6(C_1)**	0.04	0.00
Str6(C_1)	0.02	0.01	**Str7(C_1)**	0.56	0.97
Str7(C_1)	1.82	1.61	**...**	...	...
			$M@E_{12}^-$		
Str8(C_1)	0.00	0.00	**Str8(C_1)**	0.00	0.00
Str9(C_s)	0.22	0.19	**Str6(C_1)**	0.72	0.55
Str4(D_{3d})	0.38	0.18	**Str11(C_1)**	0.42	0.39
Str7(C_1)	1.22	1.33	**Str7(C_1)**	1.17	0.78
			$M@E_{12}^{2-}$		
Str10(C_2)	0.00	0.00	**Str8(C_1)**	0.00	0.00
Str8(C_1)	0.01	0.01	**Str10(C_2)**	0.14	0.20
Str7(C_1)	1.21	1.32	**Str7(C_1)**	1.03	0.86

[a] Clusters are associated with imaginary frequencies.

3.2.3 Exohedral Lr^{3+} and Lu^{3+} doped clusters

Apart from endohedral metal−doped clusters, exohedrally doped Pb_{12}^{2-} or Sn_{12}^{2-} clusters with Lr^{3+} and Lu^{3+} viz., $Lr@Pb_{12}^+$, $Lu@Pb_{12}^+$, $Lr@Sn_{12}^+$ and $Lu@Sn_{12}^+$ are also investigated to compare their stability with endohedral metal doped clusters. Exohedral metal−doped clusters have been optimized and this resulted in exohedral isomers having C_{3v}

and C_{5v} symmetries. These are represented as Str12(C_{3v}) and Str13(C_{5v}), respectively (Figure 3.1). Among these, Str12(C_{3v}) is more stable and has real frequencies, whereas Str13(C_{5v}) is less stable and has imaginary frequencies. Interestingly, all the exohedral $M@Pb_{12}^{+}$ and $M@Sn_{12}^{+}$ (M = Lr and Lu) clusters are energetically less stable (by 0.52−3.55 eV) as compared to the corresponding endohedral Str1(I_h) cluster as shown in Table 3.1.

It is noteworthy to mention at this juncture, that the different geometries of the $M@Pb_{12}^{2-}$ and $M@Sn_{12}^{2-}$ clusters in their different oxidation states (M = Lr^{n+}, n = 0, 1, 2, 3) are very close to the geometries of the equivalent $M@Pb_{12}^{2-}$ and $M@Sn_{12}^{2-}$ clusters in the corresponding oxidation states of Lu^{n+} (n = 0, 1, 2, 3). Furthermore, in most of the cases the most stable geometries of Lr encapsulated clusters in their different oxidation states are the same as those of the corresponding Lu encapsulated clusters in their equivalent oxidation states, which clearly show a one to one correspondence between Lr and Lu in their respective oxidation states.

3.2.4 Optimized structural parameters

(a) Endohedral $M@Pb_{12}^{2-}$ and $M@Sn_{12}^{2-}$ clusters (M = Lr^{n+}, Lu^{n+} and n = 0, 1, 2, 3)

After obtaining the most stable geometry for all the clusters, the structural parameters of all the $M@Pb_{12}^{2-}$ or $M@Sn_{12}^{2-}$ (M = Lr^{n+}, Lu^{n+}, and n = 0, 1, 2, 3) clusters have been analyzed. The most stable metal encapsulated cluster geometries have been considered for this analysis for each oxidation state and are compared with the structural parameters obtained for the bare Pb_{12}^{2-} and Sn_{12}^{2-} cages. The cage diameter of the bare icosahedral Pb_{12}^{2-} and Sn_{12}^{2-} is calculated as 6.258 and 6.030 Å, respectively, and the Pb–Pb and Sn–Sn bond distances are 3.290 and 3.170 Å, respectively. At this juncture it is worth noting that the encapsulation of Lr^{3+} and Lu^{3+} into the bare Pb_{12}^{2-} and Sn_{12}^{2-} clusters does not alter the icosahedral geometry, Str1(I_h), however, there is a slight increase in Pb–Pb bond distances from 3.290 Å to 3.468 Å and 3.445 Å on encapsulation of a Lr^{3+} and Lu^{3+} ion, respectively. Similarly, in $M@Sn_{12}^{+}$ clusters, Sn–Sn bond distances are increased on encapsulation of a Lr^{3+} or Lu^{3+} ion (Table 3.2). Consequently, in $M@Pb_{12}^{+}$ clusters, the cage diameter expands by 0.17 Å (for Lr) and 0.15 Å (for Lu), while in $M@Sn_{12}^{+}$ clusters, a slightly larger expansion of the bare cage has been observed (0.19 Å for Lr and 0.16 Å for Lu). This difference in the extent of expansion can be attributed to the smaller size of the bare Sn_{12}^{2-} cage compared to the bare Pb_{12}^{2-} cage. A smaller cage size effectively leads to more repulsion between the cage and the encapsulated metal atom/ion. These findings are in concurrence with previously studied $Pu@Pb_{12}$ and $Pu@Sn_{12}$ clusters in which the cage diameter of Pb_{12}^{2-} and Sn_{12}^{2-} clusters is expanded by 0.18 and 0.19 Å, respectively.[101] The Lr–Pb (Lr−Sn) and Lu–Pb (Lu−Sn) bond distances are calculated to be 3.298 (3.209) and 3.276 (3.176) Å in $M@Pb_{12}^{+}$ ($M@Sn_{12}^{+}$) clusters, respectively. The Lr–Pb/Sn and Lu−Pb/Sn bond distances are slightly differ in values due to the smaller size of Lu^{3+} ion compared to Lr^{3+} ion. Similar results are obtained using B3LYP functional as reported in Table 3.2. However, encapsulation of other Lr^{n+} or Lu^{n+} (n = 0, 1, 2) ion inside the Pb_{12}^{2-} or Sn_{12}^{2-} clusters has distorted the icosahedral geometry of their parent Pb_{12}^{2-} or Sn_{12}^{2-} clusters and the corresponding M−Pb/Sn and Pb−Pb/Sn−Sn bond distances of these clusters are reported in Table 3.2. It can be seen from Table 3.2 that trend in the structural parameters viz. bond lengths of M–Pb/Sn and Pb–Pb/Sn–Sn of Lr^{n+} encapsulated clusters (where n = 0, 1, 2 and 3) shows a striking similarity with that of the corresponding Lu^{n+} encapsulated clusters (n = 0, 1, 2 and 3).

(b) Endohedral $M@Pb_{12}^{2-}$ and $M@Sn_{12}^{2-}$ clusters (M = La^{3+}, Ac^{3+})

In addition to the Lr and Lu encapsulated Zintl ion clusters, the structures of La^{3+} or Ac^{3+} encapsulated Pb_{12}^{2-} or Sn_{12}^{2-} clusters have also been investigated to elucidate the structural similarity/differences between La^{3+} or Ac^{3+} ions and the smaller sized Lu^{3+} and

Lr^{3+} ions. Similar to Lu^{3+} and Lr^{3+} ions, encapsulation of La^{3+} or Ac^{3+} into Pb_{12}^{2-} clusters does not alter the I_h geometry of the parent Pb_{12}^{2-} cluster and the geometry contains real frequencies. However, because of the larger size of the La^{3+} and Ac^{3+} ions and the comparatively smaller cage size of the Sn_{12}^{2-} cluster, the $M@Sn_{12}^{+}$ clusters show small imaginary frequency values using PBE functional. The M–Pb and Pb–Pb bond distances are calculated to be 3.384, 3.559 Å, respectively in the $La@Pb_{12}^{+}$ cluster and 3.432, 3.609 Å, respectively, in the $Ac@Pb_{12}^{+}$ cluster. The M–Pb/Sn and Pb–Pb/Sn–Sn bond distances calculated by using the PBE/def-TZVP and B3LYP/def-TZVP methods are found to be very close as reported in Table 3.2. Due to the large size of La and Ac ion, the cage diameter in the $La@Pb_{12}^{+}$ and $Ac@Pb_{12}^{+}$ clusters expands even more than for Lr^{3+} and Lu^{3+} (0.51 and 0.61 Å, respectively whereas for Lr^{3+} and Lu^{3+} this expansion is 0.17 and 0.15 Å, respectively).

3.2.5 Binding energy estimation

The binding energy is an important parameter for determining the stability of clusters. The encapsulation of the metal atom or ion into the Pb_{12}^{2-} or Sn_{12}^{2-} clusters can be represented by the following reaction.

$$M^{n+} + E_{12}^{2-} \rightarrow (M@E_{12})^{n-2} \qquad (3.1)$$

$$BE = [E(M@E_{12})^{n-2} - E(M^{n+}) - E(E_{12}^{2-})] \qquad (3.2)$$

where M = Lr^{n+}, Lu^{n+}, La^{3+}, Ac^{3+}, E = Pb, Sn, and n = 0, 1, 2, 3 and negative value of binding energy implies that the cluster is stable with respect to its fragments.

The binding energies of all the lawrencium and lutetium encapsulated Pb_{12}^{2-} and Sn_{12}^{2-} clusters are negative indicating that they are energetically stable. However, among all the clusters, Str1(I_h) of the $M@Pb_{12}^{+}$ and $M@Sn_{12}^{+}$ (M = Lr and Lu) clusters are observed to be the most stable having most negative values of the binding energy (−37.19 and −37.90 eV for $Lr@Pb_{12}^{+}$ and $Lu@Pb_{12}^{+}$, respectively, and −36.23 and −37.03 eV, for $Lr@Sn_{12}^{+}$ and

$Lu@Sn_{12}^{+}$ respectively) as reported in Table 3.2. They also possess the highest symmetry, which is an added advantage when it comes to their stable energetics. For the other Lr^{n+} or Lu^{n+} (n = 0, 1, 2) doped clusters, the binding energy corresponding to their most stable structure is less negative compared to Lr^{3+} and Lu^{3+} encapsulated Pb_{12}^{2-} and Sn_{12}^{2-} clusters (Table 3.2), which implies their relatively lower stability. In all the clusters, binding energies decrease with a decrease in the charge on the encapsulated atom or ion (Table 3.2). Thus, more positive charge on the encapsulated metal ion increases the interaction between the cage and the encapsulated atom (ion). Furthermore, despite their size difference, the binding energies of Lr^{n+} encapsulated clusters in their different oxidation states (n = 0, 1, 2, 3) are found to be very close to the corresponding binding energies of Lu^{n+} encapsulated clusters in their corresponding oxidation states (Table 3.2). It may be noted that the $M@Pb_{12}^{+}$ and $M@Sn_{12}^{+}$ (M = Lr, Lu) clusters are found to be energetically more stable than the previously studied $Pu@Pb_{12}$ and $Pu@Sn_{12}$ clusters which have comparatively less negative binding energies of −26.76 and −26.19 eV, respectively.[101]

Moving to the La and Ac clusters, their binding energy is observed to be relatively smaller (−31.36 and −28.88 eV, respectively, for $La@Pb_{12}^{+}$ and $Ac@Pb_{12}^{+}$ clusters) as compared to that of the $Lu@Pb_{12}^{+}$ and $Lr@Pb_{12}^{+}$ clusters, but nonetheless higher than the $Pu@Pb_{12}$ cluster[101] (−26.76 eV). Similarly, binding energy values of the $La@Sn_{12}^{+}$ and $Ac@Sn_{12}^{+}$ clusters are −30.04 and −27.47 eV, respectively, which are also smaller than the corresponding values for the $Lu@Sn_{12}^{+}$ and $Lr@Sn_{12}^{+}$ clusters (Table 3.2). This trend shows that larger metal ion (La^{3+} or Ac^{3+}) encapsulated Pb_{12}^{2-} or Sn_{12}^{2-} clusters are less stable compared to smaller metal ion (Lu^{3+} and Lr^{3+}) encapsulated clusters. The B3LYP/def-TZVP calculated binding energy values follow exactly the same stability trend as we discussed above using the PBE/def-TZVP method (Table 3.2).

Table 3.2: Calculated Values of Average Bond Distance ($R_{(M-Pb/M-Sn)}$ and $R_{(Pb-Pb/Sn-Sn)}$, in Å), Binding Energy (BE, in eV) and HOMO−LUMO Energy Gap (ΔE_{Gap}, in eV) using PBE (B3LYP) Functionals.

Cluster	**Geometry**	$\mathbf{R_{(M-Pb/M-Sn)}}$	$\mathbf{R_{(Pb-Pb/Sn-Sn)}}$	**BE**	$\mathbf{\Delta E_{Gap}}$
Pb_{12}^{2-}	I_h	3.129 (3.151)	3.290 (3.314)	**…**	2.28 (3.05)
Sn_{12}^{2-}	I_h	3.015 (3.030)	3.170 (3.186)	**…**	1.87 (2.72)
$Lr@Pb_{12}^{+}$	Str1(I_h)	3.298 (3.326)	3.468 (3.497)	−37.19 (−36.54)	1.81 (2.69)
$Lu@Pb_{12}^{+}$	Str1(I_h)	3.276 (3.302)	3.445 (3.472)	−37.90 (−37.20)	1.87 (2.79)
$Lr@Sn_{12}^{+}$	Str1(I_h)	3.209 (3.219)	3.375 (3.385)	−36.23 (−35.43)	1.62 (2.57)
$Lu@Sn_{12}^{+}$	Str1(I_h)	3.176 (3.196)	3.339 (3.360)	−37.03 (−36.21)	1.70 (2.69)
$La@Pb_{12}^{+}$	Str1(I_h)	3.384 (3.413)	3.559 (3.589)	−31.36 (−30.79)	1.26 (2.17)
$Ac@Pb_{12}^{+}$	Str1(I_h)	3.432 (3.464)	3.609 (3.642)	−28.88 (−28.28)	1.22 (2.11)
$La@Sn_{12}^{+}$	Str1(I_h)	3.293 (3.317)	3.462 (3.488)	−30.04 (−29.35)	1.06 (2.03)
$Ac@Sn_{12}^{+}$	Str1(I_h)	3.342 (3.371)	3.513 (3.544)	−27.47 (−26.71)	1.02 (1.96)
$Lr@Pb_{12}$	Str4(D_{3d})	3.291 (3.320)	3.460 (3.531)	−20.03 (−19.17)	0.25 (0.96)
$Lu@Pb_{12}$	Str4(D_{3d})	3.269(3.305)	3.437 (3.499)	−21.61 (−20.69)	0.25 (0.99)
$Lr@Sn_{12}$	Str4(D_{3d})	3.190 (3.266)	3.353 (3.437)	−19.57 (−18.57)	0.24 (0.99)
$Lu@Sn_{12}$	Str6(C_1)	3.169 (3.190)	3.331 (3.343)	−21.16 (−20.17)	0.25 (1.02)
$Lr@Pb_{12}^{-}$	Str8(C_1)	3.462 (3.536)	3.373 (3.416)	−8.00 (−7.16)	0.99 (1.86)
$Lu@Pb_{12}^{-}$	Str8(C_1)	3.435 (3.460)	3.358 (3.388)	−9.84 (−8.95)	0.98 (1.87)
$Lr@Sn_{12}^{-}$	Str8(C_1)	3.356 (3.385)	3.294 (3.297)	−8.30 (−7.37)	0.80 (1.71)
$Lu@Sn_{12}^{-}$	Str8(C_1)	3.346 (3.344)	3.301 (3.266)	−10.21 (−9.24)	0.82 (1.73)
$Lr@Pb_{12}^{2-}$	Str10(C_2)	3.478 (3.530)	3.380 (3.434)	−2.79 (−1.99)	0.27 (1.00)
$Lu@Pb_{12}^{2-}$	Str10(C_2)	3.420 (3.423)	3.471 (3.447)	−3.67 (−2.82)	0.27 (1.01)
$Lr@Sn_{12}^{2-}$	Str8(C_1)	3.333 (3.378)	3.267 (3.369)	−3.37 (−2.50)	0.27 (1.06)
$Lu@Sn_{12}^{2-}$	Str8(C_1)	3.310 (3.328)	3.253 (3.326)	−4.32 (−3.45)	0.27 (1.07)

3.2.6 Molecular orbitals analysis

Molecular orbital (MO) energy level diagrams of Lr^{3+} and Lu^{3+} metal ion encapsulated Pb_{12}^{2-} and Sn_{12}^{2-} clusters as obtained using the B3LYP/def-TZVP method are represented in Figure 3.2. In Pb_{12}^{2-} the HOMO and lowest unoccupied molecular orbital (LUMO) correspond to the $2t_{1u}$ and $1g_g$ levels, respectively, while in the Sn_{12}^{2-} clusters the HOMO and LUMO are of $2h_g$ and $1g_g$ symmetries, respectively, with the corresponding HOMO–LUMO energy gaps of 3.05 and 2.72 eV. The HOMO–LUMO energy gap of all these clusters calculated by using the PBE/def-TZVP method are relatively smaller (cf. 2.28 and 1.87 eV, for Pb_{12}^{2-} and Sn_{12}^{2-}, respectively) than the B3LYP/def-TZVP method calculated values (Table 3.2).

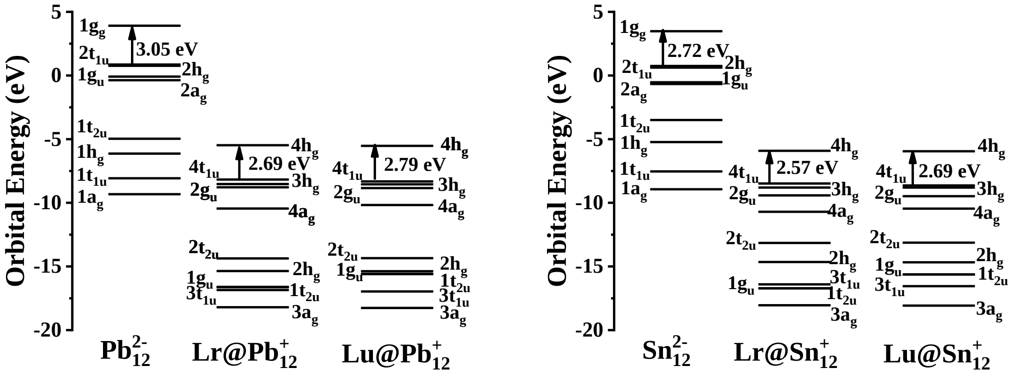

Figure 3.2: MOs energy level diagrams of E_{12}^{2-} and $M@E_{12}^{+}$ (M = Lr, Lu and E = Pb, Sn) clusters using B3LYP functional.

In the bare cage the occupied MOs corresponding to $2t_{1u}$, $2h_g$, $1g_u$ and $2a_g$ symmetry are associated with the valence electrons of the cage atoms and form stable 26−electrons systems,[62-63] while the remaining occupied MOs ($1t_{2u}$, $1h_g$, $1t_{1u}$ and $1a_g$ symmetries) contain only the inner s electrons of the cage atoms (Pb and Sn) and do not have any role in the reactivity of the system. For $M@Pb_{12}^{+}$ clusters (M = Lr and Lu), the HOMO and LUMO are found to be of $4t_{1u}$ and $4h_g$ symmetries, respectively, with the HOMO–LUMO energy gap values of 2.69 (1.81) eV and 2.79 (1.87) eV, respectively, using the B3LYP (PBE) functionals. These values are slightly smaller than that of the bare cluster. In the case of the Lr@Sn_{12}^{+} and Lu@Sn_{12}^{+} clusters the HOMO–LUMO energy gaps of 2.57 (1.62) and 2.69 (1.70) eV, respectively, calculated using the B3LYP (PBE) functionals are also closer to the corresponding value of the bare cluster, however, slightly smaller relative to the corresponding M@Pb_{12}^{+} clusters. The calculated HOMO–LUMO energy gap of Lr^{3+} or Lu^{3+} encapsulated clusters are fairly large, indicating that these clusters are chemically stable, while for other charged Lr^{n+} and Lu^{n+} (n = 0, 1, 2) encapsulated Pb_{12}^{2-} and Sn_{12}^{2-} clusters the HOMO–LUMO gap is small (Table 3.2).

Now it is worthwhile to discuss about the valence electron count of the cage in the presence of the central atom/ion, and around the central atom/ion. It is to be noted that in the presence of the metal atom/ion (Lr, Lu, La and Ac), the cage possesses 26 electrons in the t_{1u}, h_g, g_u and a_g MOs in the M@Pb_{12}^{+} clusters. This behaviour is exactly identical to the 26−electron count in the bare cage. However, unlike in the bare cage, the t_{1u}, h_g, and a_g MOs in the M@Pb_{12}^{+} clusters are formed by the hybridization of the s, p, d valence orbitals of the central atom/ion and the p orbitals of the cage atoms, while the g_u orbital corresponds to the pure cage orbital. In the Lr@Pb_{12}^{+} cluster, $4t_{1u}$, $3h_g$, $2g_u$, $4a_g$, $2t_{2u}$, $1g_u$, $1t_{2u}$, $2h_g$, $3t_{1u}$, and $3a_g$ MOs correspond to occupied MOs. From Figure 3.2, one can see that the energy separation between the $4a_g$ and $2t_{2u}$ orbitals is very large. Therefore, only $4t_{1u}$, $3h_g$, $2g_u$ and $4a_g$ orbitals are considered as the outer valence MOs of the Lr@Pb_{12}^{+} cluster. Among these valence MOs, the $2g_u$ orbital corresponds to the pure cage orbital as it does not interact with the central atom, while the remaining $4t_{1u}$, $3h_g$ and $4a_g$ MOs are formed by the overlapping of the 7s, 7p, 6d orbitals of Lr with the cage orbitals (Figure 3.3) with a cumulative electron count of 18. Therefore, the Lr@Pb_{12}^{+} cluster satisfies the 18−electron principle and can be considered as a new example of an 18−electron system[99-100, 107, 114] corresponding to shell−closing around the central metal atom with an $s^2p^6d^{10}$ electronic configuration.

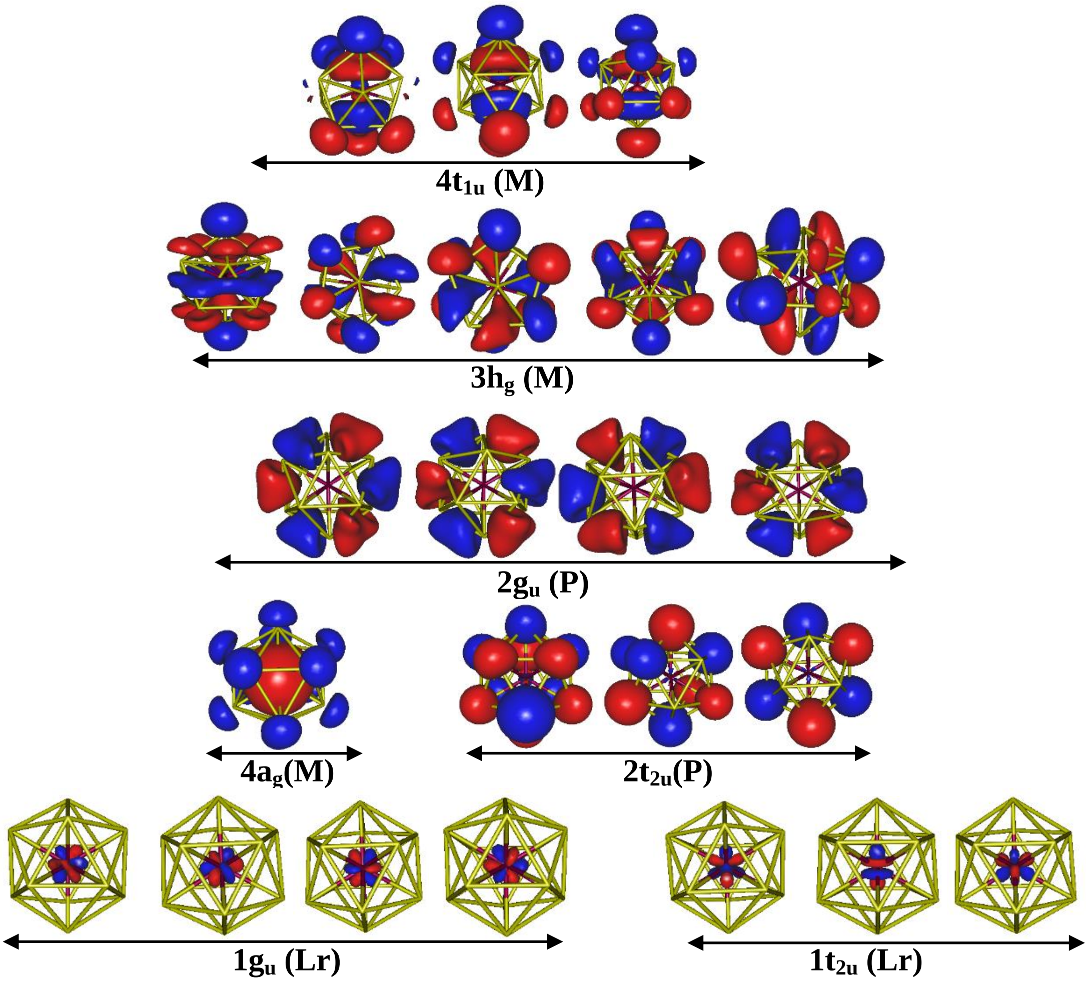

Figure 3.3: MO pictures of $Lr@Pb_{12}^+$ cluster using B3LYP functional. Here, '(M)' stands for mixed Lr−cage atoms MOs and '(P)' stands for pure cage atoms MOs and '(Lr)' represents pure Lr MOs.

Similarly, the $Lu@Pb_{12}^+$ system also forms a very stable 18−electron system corresponding to completely filled $4t_{1u}$, $3h_g$ and $4a_g$ hybridized MOs as shown in Figure 3.4. In the same way, the $Lr@Sn_{12}^+$ and $Lu@Sn_{12}^+$ clusters are also obey the 18−electron principle.

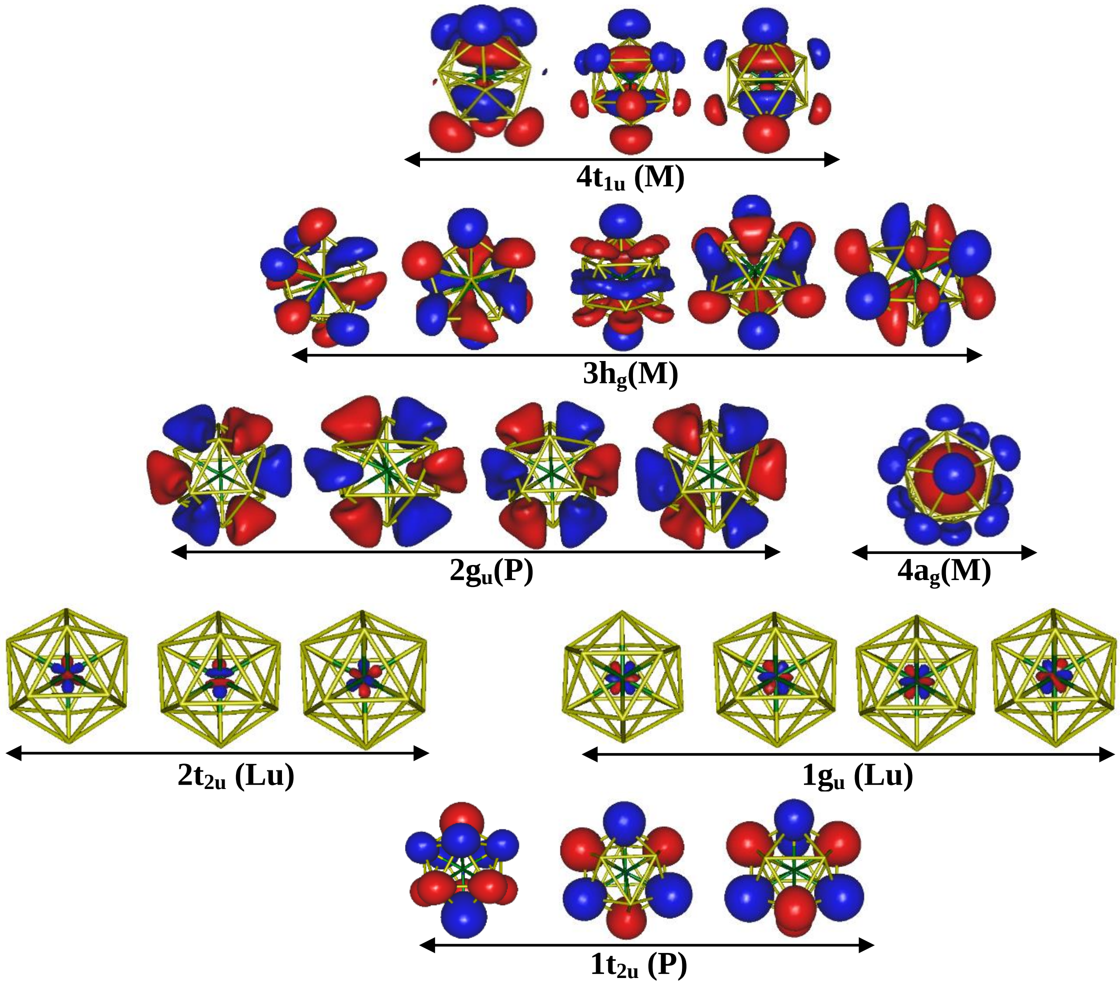

Figure 3.4: MO pictures of Lu@Pb_{12}^{+} cluster using B3LYP functional. Here, '(M)' stands for mixed Lu−cage atoms MOs and '(P)' stands for pure cage atoms MOs and '(Lu)' represents pure Lu MOs.

The MO pictures of the La^{3+} and Ac^{3+} encapsulated clusters are depicted in Figures 3.5 and 3.6, respectively. Similar to Lr^{3+} and Lu^{3+} encapsulated clusters, the La@Pb_{12}^{+} (Ac@Pb_{12}^{+}) cluster also forms a stable 18−electron system corresponding to mixed $3t_{1u}$, $2h_g$, $3a_g$ ($4t_{1u}$, $3h_g$, $4a_g$) MOs with $s^2p^6d^{10}$ configuration around La (Ac) ion. It is to be noted that the HOMO–LUMO energy gaps (Table 3.2) of La^{3+} and Ac^{3+} encapsulated Pb_{12}^{2-} clusters is 2.17 (1.26) and 2.11 (1.22) eV, respectively, calculated using the B3LYP (PBE) functionals are relatively smaller than those for Lr^{3+} and Lu^{3+} encapsulated Pb_{12}^{2-} clusters. The same is true for La^{3+} and Ac^{3+} encapsulated Sn_{12}^{2-} clusters.

Thus, in the M@Pb_{12}^{+} (M = La, Lu, Ac and Lr) clusters magic properties are satisfied individually with respect to the central metal atom and the cage. The central metal atom is found to satisfy shell closing with 18−bonding electrons around the central atom. On the other hand, the cage satisfies the 26−electron magic number through MOs involving pure cage orbitals and cage−central atom mixed orbitals.

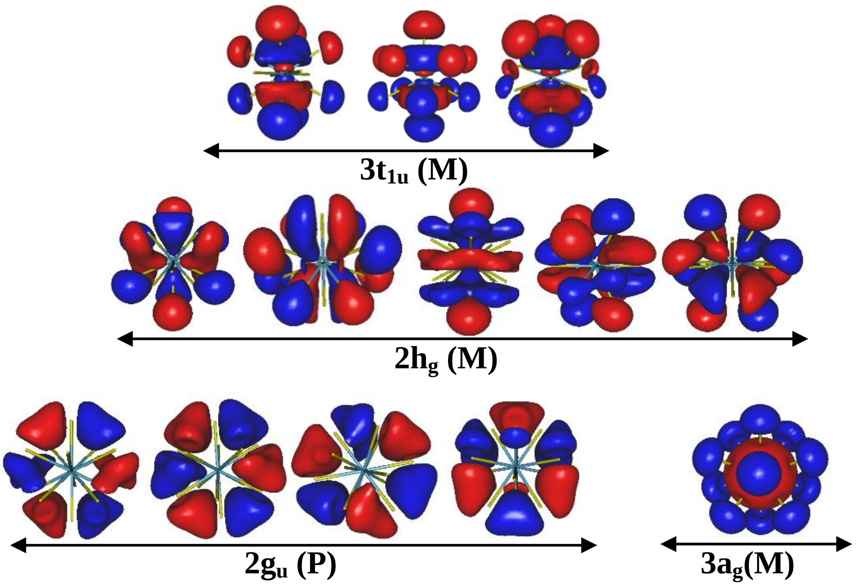

Figure 3.5: MO pictures of La@Pb_{12}^{+} cluster using B3LYP functional. Here, '(M)' stands for mixed La−cage atoms MOs and '(P)' stands for pure cage atoms MOs.

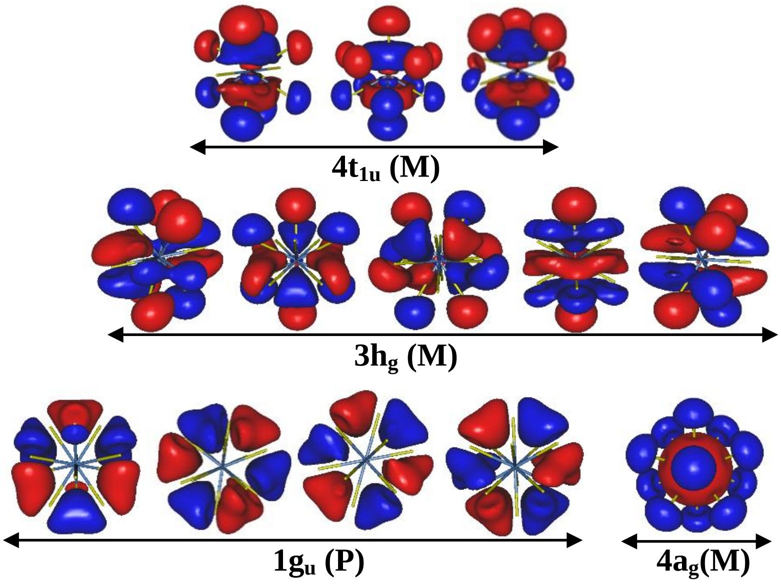

Figure 3.6: MO pictures of Ac@Pb_{12}^{+} cluster using B3LYP functional. Here, '(M)' stands for mixed Ac−cage atoms MOs and '(P)' stands for pure cage atoms MOs.

Now, it is interesting to compare the 32−electron shell−closing in U or Pu containing clusters reported recently with the present systems. Unlike mid lanthanide or actinide encapsulated clusters, namely, Pu@Pb_{12},[101] [U@Si_{20}]$^{6-}$,[111] M@C_{26},[113] (M = lanthanide/actinide), Pu@C_{24},[112] and U@C_{28},[110] in the M@Pb_{12}^{+} cluster, the participation of the highly shielded 4f/5f orbitals of the Lu/Lr is negligible in the bonding with the cage atoms. Since the 4f/5f orbital of Lu/Lr does not participate in bonding with the cage (Pb_{12}^{2-} and Sn_{12}^{2-}), therefore the Lr@Pb_{12}^{+}, Lu@Pb_{12}^{+}, Lr@Sn_{12}^{+} and Lu@Sn_{12}^{+} systems behave like an 18−electron system rather than a 32−electron system, though the total number electron (including the 14 non-bonding electrons) around the Lr or Lu in the M@Pb_{12}^{+} clusters are found to be 32. Nevertheless, as far as the fulfillment of electron counting rule is concerned, normally the number of bonding electrons are considered, accordingly Lr and Lu containing systems better be described as 18-electron systems.

3.2.7 Density of states analysis

The density of states (DOS) plots for bare Pb_{12}^{2-} cluster as well as of endohedral M@Pb_{12}^{+} (M = Lr and Lu) clusters are shown in Figure 3.7, which reveals that the Fermi level moves down in energy upon complexation with Lu^{3+}/Lr^{3+} ion (pointed by green arrow) due to the stabilization of ligand’s (i.e. cage’s) orbitals in the field of Ln^{3+}/An^{3+} cation. Figure 3.7 represents the DOS corresponding to the clusters molecular orbitals (MOs), and the composition of each of the valence occupied MOs is discussed in the molecular orbital analysis section. Intense bands are observed for the bare Pb_{12}^{2-} clusters, which correspond to their valence 6s and 6p orbitals. Similar intense bands have been observed for M@Pb_{12}^{+} clusters. However, the DOS of the M@Pb_{12}^{+} clusters are slightly red shifted compared to the corresponding peaks for the bare Pb_{12}^{2-} cluster. The deeper energy bands corresponding to the 4f or 5f valence orbitals of the Lu^{3+} or Lr^{3+} metal ion in the Lu@Pb_{12}^{+} and Lr@Pb_{12}^{+}

clusters is indicative that these 4f or 5f orbitals of the central metal ions are highly shielded by their intervening electrons, and therefore act as inert/core orbitals and do not participate in bonding with the cage atoms. Both Lu^{3+} and Lr^{3+} ion encapsulated Pb_{12}^{2-} clusters show almost similar energy shifts (Figure 3.7). Similar DOS is observed for Sn_{12}^{2-} and $M@Sn_{12}^{+}$ clusters.

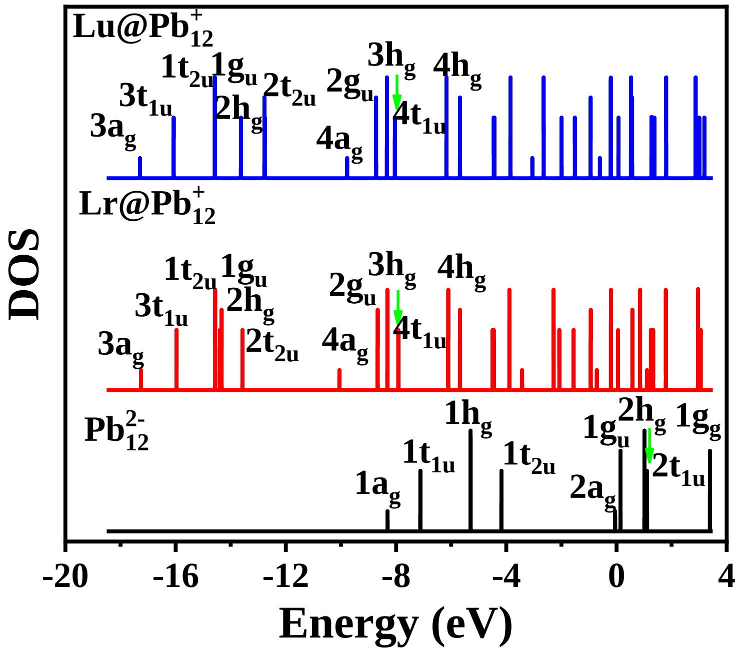

Figure 3.7: Variation of DOS of Pb_{12}^{2-} and $M@Pb_{12}^{+}$ (M = Lr and Lu) clusters as a function of MOs energy using PBE functional. (Vertical green arrow is pointing toward HOMO).

3.2.8 Charge distribution analysis

The charges on the central atoms calculated by natural population analysis (NPA)[166] at PBE/def-TZVP level of theory are found to be very high, indicative of ionic bonding between the central atom and the cage atoms (Table 3.3). Therefore, we have performed Voronoi charge density (VDD)[167] analysis at PBE/TZ2P level to calculate the Voronoi charge. The VDD charges are highly useful in calculating the amount of electronic density that flows to or from a certain atom due to bond formation and thereby provide a chemically meaningful charge distribution.

Table 3.3: Calculated Values of VDD and NPA Charges[1] using PBE Functional.

Cluster	**Geometry**	**q_{M} (NPA)**	**$q_{Sn/Pb}$ (NPA)**	**q_{M} (VDD)**	**$q_{Sn/Pb}$ (VDD)**
Pb_{12}^{2-}	I_h	…	−0.17	…	−0.17
Sn_{12}^{2-}	I_h	…	−0.17	…	−0.17
Lr@Pb_{12}^{+}	Str1(I_h)	–3.63	0.39	0.10	0.08
Lu@Pb_{12}^{+}	Str1(I_h)	–2.50	0.29	0.07	0.08
Lr@Sn_{12}^{+}	Str1(I_h)	–3.93	0.41	0.11	0.08
Lu@Sn_{12}^{+}	Str1(I_h)	–2.83	0.32	0.08	0.08
La@Pb_{12}^{+}	Str1(I_h)	–3.48	0.37	–0.11	0.09
Ac@Pb_{12}^{+}	Str1(I_h)	–6.86	0.66	–0.04	0.09
La@Sn_{12}^{+}	Str1(I_h)	–3.46	0.37	–0.12	0.09
Ac@Sn_{12}^{+}	Str1(I_h)	–6.51	0.63	–0.05	0.09
Lr@Pb_{12}	Str4(D_{3d})	−3.52	0.29	0.08	–0.01
Lu@Pb_{12}	Str4(D_{3d})	−2.42	0.20	0.05	–0.01
Lr@Sn_{12}	Str4(D_{3d})	−3.82	0.32	0.09	–0.01
Lu@Sn_{12}	Str6(C_1)	−2.73	0.23	0.05	–0.01
Lr@Pb_{12}^{-}	Str8(C_1)	−2.03	0.09	0.17	–0.10
Lu@Pb_{12}^{-}	Str8(C_1)	−1.31	0.03	0.14	–0.10
Lr@Sn_{12}^{-}	Str8(C_1)	−2.32	0.11	0.17	–0.10
Lu@Sn_{12}^{-}	Str8(C_1)	−1.56	0.05	0.13	–0.09
Lr@Pb_{12}^{2-}	Str10(C_2)	−1.88	−0.05	0.17	–0.18
Lu@Pb_{12}^{2-}	Str10(C_2)	−1.32	−0.01	0.13	–0.18
Lr@Sn_{12}^{2-}	Str8(C_1)	−2.20	0.02	0.17	–0.18
Lu@Sn_{12}^{2-}	Str8(C_1)	−1.44	−0.05	0.14	–0.18

[1] Average charge ($q_{Sn/Pb}$) for Sn/Pb atoms is reported.

The VDD charges on Lr and the cage atom are calculated to be 0.10 (0.11) and 0.08 (0.08), respectively, in the $Lr@Pb_{12}^{+}$ ($Lr@Sn_{12}^{+}$) clusters, which are very different from the initial charges on Lr (+3) and the cage (−2). Similarly, the charges on Lu and the cage atom are calculated to be 0.07 (0.08) and 0.08 (0.08), respectively, in the $Lu@Pb_{12}^{+}$ ($Lu@Sn_{12}^{+}$) clusters. Thus an increase in the electron density around the central atom and a decrease in the electron density around the cage clearly indicate that some electron density has been transferred to the valence orbitals of the central atoms from the valence orbitals of the cage atoms. Further similar charges on Lr and Lu once again indicate that both Lr and Lu are forming a similar kind of bond with the cage atoms. The nature of the charges on the metal and cage atoms in $M@Pb_{12}^{2-}$ and $M@Sn_{12}^{2-}$ ($M = Lr^{n+}$ and Lu^{n+} and n = 0, 1, 2, 3) clusters clearly signifies a very weak covalent or electrostatic interaction between the cage atoms and the encapsulated central atom.

Since ligand field is expected to be different on different subshells, therefore, we have calculated the orbital population in the s, p, d, and f orbitals for the central metal atom of $M@Pb_{12}^{2-}$ ($M = La^{3+}$, Lu^{3+}, Lr^{n+}, Lu^{n+}, n = 0, 1, 2, 3) clusters using NPA scheme and the corresponding values are reported in Table 3.4. The atomic population analysis confirms that Lu and Lr have their f^{14} shell in their lanthanoid- or actinioid-contracted atomic cores, respectively, which is also revealed from the molecular orbital pictures depicted in Figures 3.3 and 3.4. The n(p) population on Lr is 1 unit higher than that on Lu as Lr has $7p^1$ configuration while n(d) population is ~ 0.5 unit higher on Lu in $M@Pb_{12}^{2-}$ clusters. It is to be noted that only n(d) population on Lr and Lu changes considerably with the change in the oxidation state of Lr and Lu in $M@Pb_{12}^{2-}$ ($M = Lr^{n+}$, Lu^{n+}, n = 0, 1, 2, 3) clusters. Furthermore, the d orbital of La, Lu, Ac and Lr in the studied clusters are found to be partially filled with electrons.

Table 3.4: Calculated Values of Atomic Population on the Central Metal Atom in $M@Pb_{12}^{2-}$ ($M = Lr^{n+}$, Lu^{n+}, La^{3+}, Ac^{3+} and n = 0, 1, 2, 3) using NPA with PBE Functional.

Cluster	n(s)	n(p)	n(d)	n(f)
$Lr@Pb_{12}^{+}$	4.6	13.8	14.3	14.0
$Lr@Pb_{12}$	4.6	13.6	14.3	14.0
$Lr@Pb_{12}^{-}$	4.6	13.1	13.3	14.0
$Lr@Pb_{12}^{2-}$	4.6	13.1	13.2	14.0
$Lu@Pb_{12}^{+}$	4.5	12.2	14.8	14.0
$Lu@Pb_{12}$	4.5	12.1	14.8	14.0
$Lu@Pb_{12}^{-}$	4.4	12.1	13.8	14.0
$Lu@Pb_{12}^{2-}$	4.5	12.0	13.8	14.0
$Ac@Pb_{12}^{+}$	4.5	12.0	15.5	3.8
$La@Pb_{12}^{+}$	2.6	6.0	5.8	0.1

3.2.9 Analysis of topological properties

For further understanding the nature of the M–Pb/Sn and Pb–Pb/Sn–Sn bonds in $M@Pb_{12}^{+}$ (M = Lr, Lu, La and Ac) and $M@Sn_{12}^{+}$ (M = Lr and Lu) clusters, the bond critical point (BCP) properties of the M–Pb and Pb–Pb bonds have been calculated using quantum theory of atoms in molecules (QTAIM) analysis.[168, 172] The BCP properties viz., the electron density (ρ), the Laplacian of the electron density ($\nabla^2\rho$), the Lagrangian kinetic energy G(r), the potential energy density V(r), the local electron energy density $E_d(r)$, ratio of local electron kinetic energy density and electron density ($G(r)/\rho$ in au) and ELF Values at M−Pb, Pb−Pb and Sn−Sn bonds are reported in Table 3.5.

Generally, the value of the electron density and the Laplacian of the electron density at the BCP are used to distinguish between covalent [large electron density ($\rho > 0.1$) and $\nabla^2\rho(r) < 0$] and non−covalent [small electron density ($\rho < 0.1$) and $\nabla^2\rho(r) > 0$] interactions. However, according to Boggs[169], sometimes the use of $\nabla^2\rho(r)$ can produce conflicting results regarding the nature of bonding at a critical point (r). According to Boggs, if $E_d < 0$ or $|E_d| <$

0.005 and G(r)/ρ(r) < 1, the interaction possesses some degree of covalency even if the value of $\nabla^2\rho(r) > 0$. In the present work for M–Pb/M−Sn and Pb–Pb/Sn−Sn bonds, the value of $\nabla^2\rho(r) > 0$, however the value of $E_d(r) < 0$, $G(r)/\rho(r) < 1$ and $|E_d(r)| < 0.005$ at the BCP satisfy Bogg's criteria of weak covalent interaction of type C and type D in $M@Pb_{12}^+$ and $M@Sn_{12}^+$ (M = Lr, Lu) clusters (Table 3.5). Therefore, the M−Pb/M−Sn and Pb−Pb/Sn−Sn bonds are not truly covalent in nature; however, these bonds possess only a small degree of covalent interaction, which is in the agreement with the results of the VDD charge distribution analysis.

Table 3.5: BCP Properties at M−Pb/M−Sn and Pb−Pb/Sn−Sn Bonds using PBE Functional along with Small Core RECP Employed with EDF.

Cluster	Bond	ρ	$\nabla^2\rho$	G(r)	V(r)	$E_d(r)$	G(r)/ρ	Type	ELF
$Lr@Pb_{12}^+$	Lr−Pb	0.023	0.04	0.01	–0.02	–0.003	0.54	C, D	0.16
	Pb–Pb	0.023	0.02	0.01	–0.01	–0.002	0.32	C, D	0.34
$Lu@Pb_{12}^+$	Lu–Pb	0.022	0.04	0.01	–0.02	–0.003	0.54	C, D	0.15
	Pb–Pb	0.023	0.02	0.01	–0.01	–0.002	0.32	C, D	0.34
$Lr@Sn_{12}^+$	Lr–Sn	0.026	0.04	0.01	–0.02	–0.004	0.54	C, D	0.18
	Sn–Sn	0.025	0.02	0.01	–0.01	–0.003	0.27	C, D	0.46
$Lu@Sn_{12}^+$	Lu–Sn	0.024	0.04	0.01	–0.02	–0.003	0.56	C, D	0.16
	Sn–Sn	0.026	0.02	0.01	–0.01	–0.003	0.28	C, D	0.45
$La@Pb_{12}^+$	La−Pb	0.022	0.05	0.01	–0.02	–0.001	0.65	C, D	0.11
	Pb–Pb	0.022	0.02	0.01	–0.01	–0.002	0.29	C, D	0.39
$Ac@Pb_{12}^+$	Ac−Pb	0.021	0.04	0.01	–0.01	–0.001	0.61	C, D	0.11
	Pb–Pb	0.020	0.02	0.01	–0.01	–0.002	0.26	C, D	0.40

Moreover, we have calculated the electron localization function (ELF)[171] values for M−Pb/Sn and Pb−Pb/Sn−Sn bond as it is an important parameter for understanding the nature of bonding between the constituent atoms. In general high value of the ELF (close to 1) implies a covalent bonding between the constituent atoms, while a small value of ELF (< 0.5) indicate ionic or a very weak covalent interaction between the constituent atoms. For all the studied systems the calculated value of ELF is less than 0.5 (Table 3.5) which primarily suggests an ionic behaviour of M−Pb/M−Sn and Pb−Pb/Sn−Sn bonds in $M@Pb_{12}^{+}$ and $M@Sn_{12}^{+}$ clusters (M = Lr, Lu, La and Ac).

3.2.10 Energy decomposition analysis

To analysis the nature of interaction between the fragments of a molecular system, energy decomposition analysis (EDA) has been performed using Morokuma-type[173, 175] energy decomposition method as implemented in ADF program. For EDA, the $M^{n+}@Pb_{12}^{2-}$ and $M^{n+}@Sn_{12}^{2-}$ clusters (M = Lr, Lu and n = 0, +1, +2, +3) have been decomposed into two fragments, viz., $M^{n+} + Pb_{12}^{2-}$ and $M^{n+} + Sn_{12}^{2-}$, respectively. In the EDA method, the total interaction energy between the separated fragments (ΔE^{int}) can be divided into the Pauli repulsion (ΔE^{Pauli}), electrostatic interaction (ΔE^{elec}), and orbital interaction (ΔE^{orb}) terms as shown in equation (3.3) and corresponding values are reported in Table 3.6.

$$\Delta E^{int} = \Delta E^{Pauli} + \Delta E^{elec} + \Delta E^{orb} \qquad (3.3)$$

where, ΔE^{orb} is the stabilizing orbital interaction term which consists of a polarization term and a covalency factor due to the overlap between the metal and cage orbitals, ΔE^{elec} and ΔE^{Pauli} denote the electrostatic interaction energy and the Pauli repulsion energy, respectively, between the fragments.

Table 3.6: EDA at PBE/TZ2P Level of Theory. Percentage Contribution of Energy Components to the Total Interaction Energy (in eV) is Provided within the Parenthesis.

Cluster	**ΔE^{Pauli}**	**ΔE^{elec}**	**ΔE^{orb}**	**ΔE^{int}**
(a) Cationic clusters (+1 charge)				
Lr@Pb$_{12}^{+}$ (I_h)	13.62	−27.01 (52.1)	−24.88 (47.9)	−38.35
Lu@Pb$_{12}^{+}$ (I_h)	11.11	−25.27 (50.1)	−24.60 (49.3)	−38.76
Lr@Sn$_{12}^{+}$ (I_h)	14.38	−26.68 (51.9)	−24.72 (48.1)	−37.16
Lu@Sn$_{12}^{+}$ (I_h)	12.07	−25.02 (50.3)	−24.68 (49.7)	−37.62
(b) Neutral clusters				
Lr@Pb$_{12}$ (D_{3d})	20.91	−23.57 (56.0)	−18.53 (44.0)	−21.22
Lu@Pb$_{12}$ (D_{3d})	18.94	−22.05 (54.0)	−18.81 (46.0)	−21.93
Lr@Sn$_{12}$ (D_{3d})	22.15	−23.50 (55.1)	−19.16 (44.9)	−20.52
Lu@Sn$_{12}$ (D_{3d})	20.48	−22.16 (53.1)	−19.57 (46.9)	−21.27
Lu@Sn$_{12}$ (C_1)	19.97	−21.97 (52.8)	−19.66 (47.2)	−21.66
(c) Anionic clusters (−1 charge)				
Lr@Pb$_{12}^{-}$ (C_1)	20.82	−17.60 (54.8)	−14.50 (45.2)	−11.28
Lu@Pb$_{12}^{-}$ (C_1)	20.40	−17.13 (52.5)	−15.48 (47.5)	−12.22
Lr@Sn$_{12}^{-}$ (C_1)	22.39	−18.05 (54.1)	−15.32 (45.9)	−10.98
Lu@Sn$_{12}^{-}$ (C_1)	21.94	−17.65 (51.9)	−16.35 (48.1)	−12.06
(d) Anionic clusters (−2 charge)				
Lr@Pb$_{12}^{2-}$ (C_2)	52.62	−19.82 (34.1)	−38.24 (65.9)	−5.43
Lu@Pb$_{12}^{2-}$ (C_2)	46.78	−19.26 (36.7)	−33.20 (63.3)	−5.68
Lr@Sn$_{12}^{2-}$ (C_1)	45.50	−19.73 (38.0)	−32.16 (62.0)	−6.39
Lu@Sn$_{12}^{2-}$ (C_1)	40.90	−18.85 (39.6)	−28.81 (60.4)	−6.77

Table 3.6 shows the contribution from electrostatic, Pauli and orbital interactions to the total interaction energy for the lowest energy isomer for each oxidation state of the metal in M@Pb$_{12}^{2-}$ and M@Sn$_{12}^{2-}$ clusters (M = Lr^{n+} and Lu^{n+} and n = 0, 1, 2, 3). Based on their charge, the clusters are grouped (a) to (d) in Table 3.6. In all the clusters, the total interaction energy between fragments decreases with a decrease in the charge on the encapsulated atom

or ion as shown in Table 3.6. Slightly higher contribution of ΔE^{elec} term to the ΔE^{int} once again confirms a stronger electrostatic and weaker covalent interaction in these systems. Each energy components of Lr^{n+} doped clusters matches with the corresponding component of Lu^{n+} doped cluster, which indicate very similar bonding behaviour of Lr and Lu ion with the cluster.

3.2.11 Spin orbit coupling effect

Since the spin orbit (SO) coupling effect is very important for systems containing a heavy atom, the effect of spin orbit coupling has therefore been investigated for the bare clusters (Pb_{12}^{2-} and Sn_{12}^{2-}) and $Lr@Pb_{12}^{+}$, $Lu@Pb_{12}^{+}$, $Lr@Sn_{12}^{+}$ and $Lu@Sn_{12}^{+}$ clusters using the ZORA approach at the PBE/TZ2P level. The optimized bond lengths calculated using the spin orbit ZORA approach are found to be very close to those of the optimized bond lengths calculated using the scalar ZORA approach as reported in Table 3.7, which clearly shows a negligible effect of spin orbit coupling on the optimized geometrical parameters of these clusters. It is interesting to note that the geometrical parameters obtained using the RECP approach (Table 3.2) are very close to those reported in Table 3.7, indicating the suitability of the RECP approach in determining the structural properties of the clusters reported in this work. However, the HOMO–LUMO energy gap is slightly lowered (by 0.1−0.6 eV) after incorporating the spin–orbit coupling. The effect of spin orbit coupling can be noticed from the splitting of the various energy levels (g_u, h_g and t_u) as shown in Figure 3.8, plotted using the B3LYP/TZ2P results. At the B3LYP/TZ2P level, the splitting of various energy levels (g_u, h_g and t_u) is slightly higher than the splitting at the PBE/TZ2P level.

In the $Lr@Pb_{12}^{+}$ and $Lu@Pb_{12}^{+}$ clusters the splitting of the g_u orbital is slightly higher (in the range of 0.58–0.56 eV) as compared to h_g (0.43–0.53 eV) and t_u (0.06–0.35 eV) orbitals. In the $Lr@Sn_{12}^{+}$ and $Lu@Sn_{12}^{+}$ clusters the extent of splitting of g_u (in the range of

0.20–0.23 eV), h_g (0.14–0.19eV) and t_u (0.04–0.25eV) is relatively smaller than that in the $Lr@Pb_{12}^{+}$ and $Lu@Pb_{12}^{+}$ clusters. Due to the spin–orbit coupling, the HOMO (t_u) of the $M@Pb_{12}^{+}$ and $M@Sn_{12}^{+}$ clusters is splitted into $g_{3/2u}$ and $e_{1/2u}$ orbitals. Because of this splitting, the HOMO is destabilized (either of the $g_{3/2u}$ or $e_{1/2u}$ orbital), resulting in a decrease of the HOMO–LUMO gaps of the bare cage as well as of the $Lr@Pb_{12}^{+}$, $Lu@Pb_{12}^{+}$, $Lr@Sn_{12}^{+}$, $Lu@Sn_{12}^{+}$ clusters after the incorporation of the spin–orbit effect. Since in all the studied clusters the effect of spin–orbit coupling is rather small, the spin orbit coupling is therefore not significant enough to affect their electronic and structural properties.

Table 3.7: Calculated Bond Distances ($R_{(M-Pb/M-Sn)}$ and $R_{(Pb-Pb/Sn-Sn)}$, in Å), and HOMO−LUMO Energy Gap (ΔE_{Gap}, in eV) at PBE/TZ2P Level of Theory. B3LYP Calculated ΔE_{Gap} Values are Provided in the Parenthesis.

Cluster	**$R_{(M-Pb/M-Sn)}$**		**$R_{(Pb-Pb/Sn-Sn)}$**		**ΔE_{Gap}**	
	Scalar	**SO**	**Scalar**	**SO**	**Scalar**	**SO**
Pb_{12}^{2-}	3.106	3.052	3.266	3.226	2.11 (2.93)	1.89 (2.59)
Sn_{12}^{2-}	3.031	3.030	3.187	3.186	1.96 (2.75)	1.84 (2.61)
$Lr@Pb_{12}^{+}$	3.273	3.261	3.443	3.429	1.68 (2.54)	1.28 (2.06)
$Lu@Pb_{12}^{+}$	3.264	3.283	3.433	3.438	1.66 (2.61)	1.13 (1.99)
$Lr@Sn_{12}^{+}$	3.217	3.211	3.382	3.377	1.57 (2.42)	1.25 (2.10)
$Lu@Sn_{12}^{+}$	3.199	3.199	3.363	3.363	1.55 (2.52)	1.35 (2.31)

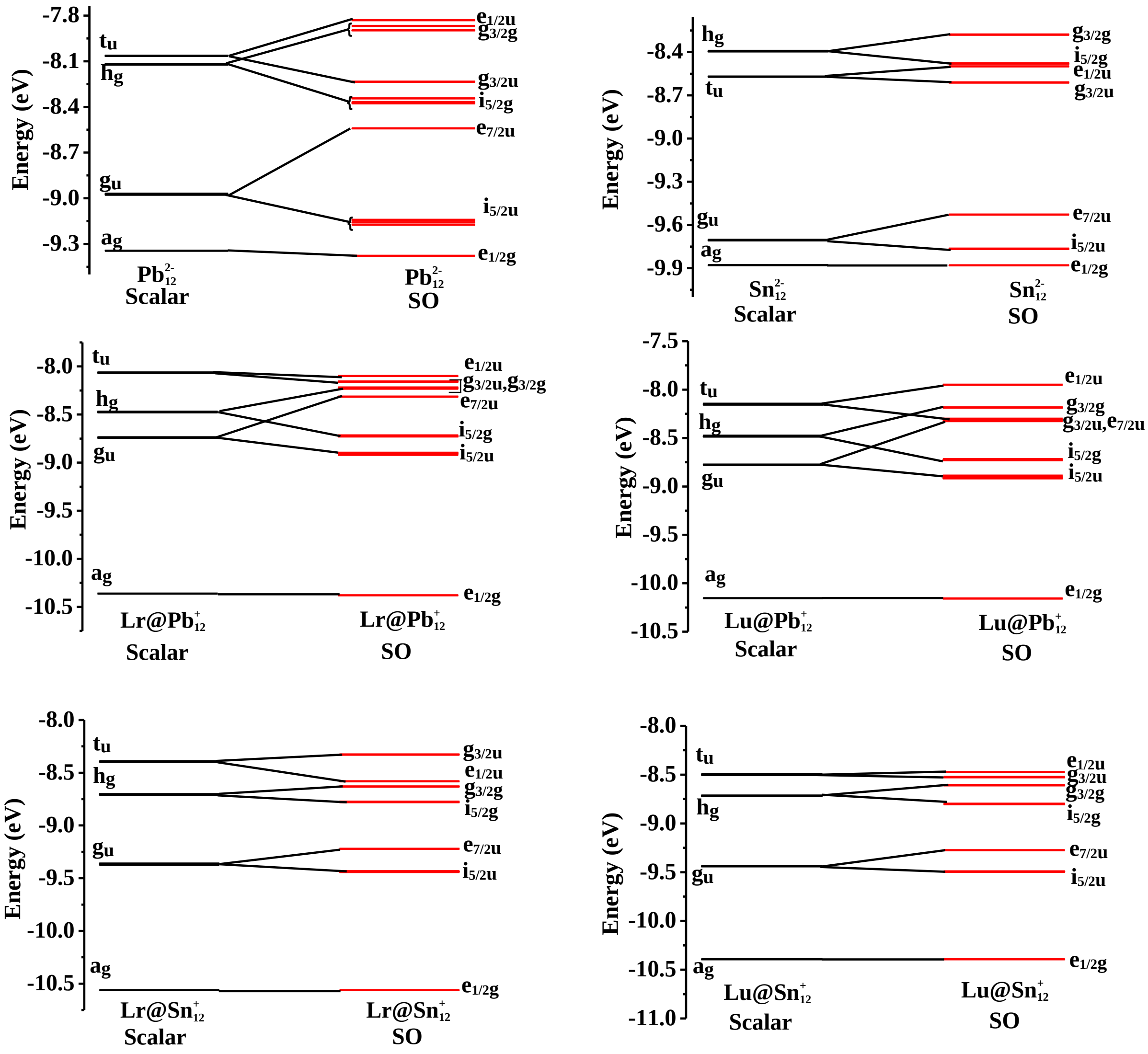

Figure 3.8: Scalar relativistic and spin orbit (SO) splitting of the valence MO energy levels at B3LYP/TZ2P level of theory.

3.3 Conclusion

In light of the positions of the elements Lr, Lu, La and Ac in the periodic table, these elemental atom and ion encapsulated Sn_{12}^{2-} and Pb_{12}^{2-} clusters have been constructed and studied. We have found remarkable similarities in the various properties viz. geometrical stability, structural properties, the binding energy and HOMO–LUMO energy gap and electronic distributions of the different oxidation states of Lr^{n+} (n = 0, 1, 2, 3) encapsulated clusters with those of the corresponding Lu^{n+} (n = 0, 1, 2, 3) encapsulated clusters, indicating that Lr in all its oxidation states possesses similarity with the corresponding oxidation states of Lu in spite of their different atomic ground state valence electronic configurations.

Among all the M^{n+} doped clusters (M = Lr, Lu, and n = 0, 1, 2, 3), only Lr^{3+} or Lu^{3+} ion encapsulated Pb_{12}^{2-} and Sn_{12}^{2-} clusters retained the icosahedral geometry and also displayed the highest energetic stability. Moreover, these $M@Pb_{12}^{+}$ and $M@Sn_{12}^{+}$ clusters form stable magic clusters with shell-closing corresponding to 18−bonding electrons around the central metal ion. Similarly, La^{3+} or Ac^{3+} encapsulated clusters also possess icosahedral geometry with high negative binding energy values and form highly stable 18−electron systems. The similarity further extends to the formation of similar HOMOs and LUMOs in the case of all the four elements in question. All the Lr^{3+}, Lu^{3+}, La^{3+}, and Ac^{3+} doped clusters follow 18-electron rule corresponding to $s^2p^6d^{10}$ configuration around the doped metal ion and also the doped metal atom or ion possess partially filled d orbital (similar to transition metal complex). Altogether, Lr^{3+}, Lu^{3+}, La^{3+}, and Ac^{3+} show the same kind of electronic, energetic as well as geometric behavior, convincing us to recommend that all four of these elements to be placed in a same block in the periodic table.[190] Therefore, among all the three periodic table we choose the IUPAC accepted periodic table where all the lanthanides and actinides (La to Lu and Ac to Lr) are placed in a 15-element f block. Moreover, in the 15-elements f block the behaviour at the two ends is found to be quite similar, which supports 15−member Ln and An rows.

CHAPTER 4

Electronic Structure and Chemical Bonding in Lanthanide and Actinide doped Sb_4^{2-} and Bi_4^{2-} Rings

4.1 Introduction

In the previous chapter (Chapter 3), we have investigated the position of lanthanide (Ln) and actinide (An) elements in the periodic table and predicted early and late Ln/An (La, Ac, Lr, Lu) atom or ion doped highly stable Zintl ion clusters, which follow 18–electron principle. However, highly stable 32–electron system could be produced with the doping of mid Ln/An atom or ion in a cluster. Recently in the work done by Mitzinger and co–workers,[195] an attempt has been made to comprehend the formation mechanism of ligand–free inorganic chemical compounds containing Zintl ions and it has attracted the attention of scientists in this advancing field of research. A large number of studies have been carried out in the past on a range of multi–metallic clusters doped with transition–metal atoms or ions.[196-202] Rare–earth–doped metalloid clusters, $[Ln@Pb_6Bi_8]^{3-}$, $[Ln@Pb_3Bi_{10}]^{3-}$, $[Ln@Pb_7Bi_7]^{4-}$, $[Ln@Pb_4Bi_9]^{4-}$, and so forth, have also been studied experimentally as well as quantum mechanically.[77, 203-205] Recently, U–doped metalloid clusters $[U@Bi_{12}]^{3-}$, $[U@Tl_2Bi_{11}]^{3-}$, $[U@Pb_7Bi_7]^{3-}$, and $[U@Pb_4Bi_9]^{3-}$ have been synthesized and characterized experimentally as well as theoretically and have been shown to have unique antiferromagnetic coupling between the metal–actinide atoms.[78] Apart from the uranium–doped clusters, lanthanide–doped metalloids clusters, $[Ln@(Sb_4)_3]^{3-}$ (Ln = La, Y, Ho, Er, Lu) have also been synthesized by Min *et al.* and isolated as the K([2.2.2]crypt) salts and characterized by single–crystal X–ray diffraction techniques.[79] Very recently Rookes *et al.* have synthesized and characterized the $[An(Tren^{DMBS})(Pn(SiMe_3)_2)]$ and $[An(Tren^{TIPS})(Pn(SiMe_3)_2)]$ systems, and investigated the thermal and photolytic reactivity of U–Pn and Th–Pn (Pn = Pnictogen) bonds.[206]

Although the ligand–free inorganic chemical compound containing lanthanum, $[La@(Sb_4)_3]^{3-}$ is synthesized and characterized experimentally as well as studied theoretically,[79] encapsulation of actinide (Th^{4+}, Pa^{5+}, U^{6+} and Np^{7+}) ions in the negatively charged antimony $(Sb_4^{2-})_3$ and bismuth $(Bi_4^{2-})_3$ clusters have not been reported before. Also we have made an attempt to predict new stable 32–electron[108, 110-113] systems by doping iso–electronic series of early to mid Ln and An ion in the metalloid clusters. Thus, the present work not only attempts to provide a thorough analysis on the stability of the experimentally observed $[La@(Sb_4)_3]^{3-}$ cluster[79] within the framework of electronic shell closing principles but also to predict the highly stable closed-shell actinide–centered clusters, $[An@(E_4^{2-})_3]$ (An = Th^{4+}, Pa^{5+}, U^{6+} and Np^{7+}), and other valence isoelectronic lanthanide–centered clusters, $[Ln@(E_4^{2-})_3]$ (Ln = La^{3+}, Ce^{4+}, Pr^{5+} and Nd^{6+}), through quantum chemical calculations. Another interesting feature in this work is to study the dependence of charge on the metal ion toward the extent of nonplanarity of the E_4^{2-} rings in the $[M@(E_4^{2-})_3]$ complexes. The encapsulated forms denoted as $[Ln@(E_4^{2-})_3]$ and $[An@(E_4^{2-})_3]$, have been examined with respect to their stability order with variation of the central metal ion in different metalloid $[(Sb_4^{2-})_3$ and $(Bi_4^{2-})_3]$ clusters. In the present theoretical study, metal atom or ion–encapsulated clusters have been rendered stable in spite of losing the aromaticity of their parent E_4^{2-} (E = Bi, Sb) rings. The concept of aromaticity and antiaromaticity plays an important role in guiding experimental synthesis and rationalizing geometrical and electronic structures of some Zintl clusters.[207] Thus, it is of immense interest to explore the reasons behind the unusually high stability of these clusters, notwithstanding their conversion into what is expected to be a less stable antiaromatic cluster.

All the results discussed in this chapter have been obtained by using PBE[144] and B3LYP functionals[146-147] with def–TZVPP basis set along with a relativistic effective core potential (RECP) for heavier elements by using Turbomole[150], ADF[151, 153] and Multiwfn[170] programs. Detail computational methodologies have been discussed in Chapter 2 of this thesis.

4.2 Results and discussions

4.2.1 Bare $(E_4^{2-})_3$ systems

Both bare metalloid Zintl ion clusters, $(E_4^{2-})_3$ (E = Sb and Bi) are made up of three aromatic E_4^{2-} rings. Individual Sb_4^{2-} and Bi_4^{2-} rings are found to optimize in D_{4h} symmetry with all real frequencies. The ionization potential (IP) of Sb_4^{2-} and Bi_4^{2-} rings are calculated to be negative (−1.8 and −1.7 eV, respectively) in the vacuum. However, the potassium-cryptand salts of the Sb_4^{2-} and Bi_4^{2-} have already been prepared in the past.[208-210] The pictorial representation of the E_4^{2-} ring is shown in Figure 4.1. The bare $(E_4^{2-})_3$ systems are found to be highly unstable because of the weak interactions among the neighbouring E_4^{2-} units in the absence of any metal ion. In these Zintl clusters $(E_4^{2-})_3$, two types of bonding is possible, one is intra–ring bonding (R_{intra}), that is bonding within the E_4^{2-} ring and the second is inter–ring bonding (R_{inter}), that is bonding between the neighbouring rings (E_4^{2-}–E_4^{2-}). In both $(Sb_4^{2-})_3$ and $(Bi_4^{2-})_3$ clusters, R_{intra} bonds are found to be much stronger, whereas R_{inter} bonds are observed to be extremely weak which clearly represents the highly stable and less reactive nature of the aromatic Sb_4^{2-} and Bi_4^{2-} rings.

4.2.2 Optimized structure of $M@(E_4^{2-})_3$ systems

To begin with, we optimized the experimentally observed $[U@(Bi_4)_3]^{3-}$ and $[La@(Sb_4)_3]^{3-}$ clusters using def–TZVPP (represented as DEF) basis set. For comparison purpose both the systems are also optimized with small–core ECP using def2–TZVPP basis set for Sb, Bi and Stuttgart basis set for La[211-212] (represented as DEF2). The calculated bond lengths of $[U@(Bi_4)_3]^{3-}$ and $[La@(Sb_4)_3]^{3-}$ clusters are reported in Table 4.1. In the optimized structure of the $[M@(E_4^{2-})_3]$ (M = Ln, An) clusters, six atoms (E = Sb or Bi) of the $(E_4^{2-})_3$ clusters are in the plane (represented as "eq" atom) while for the remaining six atoms, three atoms are above the plane and three lie below the plane (represented as "ax" atom) as shown in Figure 4.1.

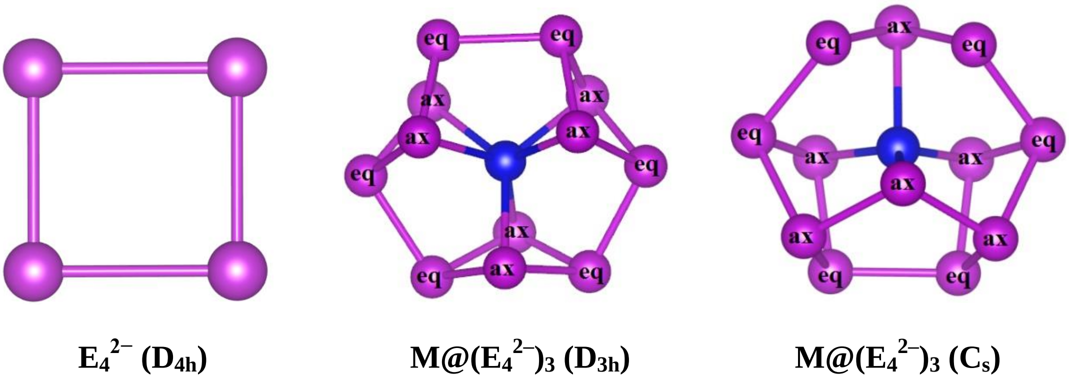

Figure 4.1: Optimized structures of E_4^{2-} and $M@(E_4^{2-})_3$ (M = Ln, An) systems.

In addition to R_{intra} and R_{inter} bond distances, metal–doped clusters also possess two other types of bonding: one is the bonding of central metal atom with the six in–plane atoms of $(E_4^{2-})_3$ cluster known as equatorial bonding (R_{eq}) and the second is the bonding of central metal ion with the six out–of–plane atoms of the $(E_4^{2-})_3$ cluster, which is mentioned as axial bonding (R_{ax}) throughout the paper. It is noteworthy to mention that for $[La@(Sb_4)_3]^{3-}$ and $[U@(Bi_4)_3]^{3-}$, the R_{ax} and R_{eq} corresponding to M–E (M = La, U) bond as well as R_{inter} and R_{intra}, corresponding to E–E (E = Sb, Bi) bond calculated using PBE/DEF and PBE/DEF2 methods are somewhat close to the corresponding experimental values (Table 4.1).[78-79] However, the B3LYP calculated R_{ax}, R_{eq}, R_{inter}, and R_{intra} values in $[La@(Sb_4)_3]^{3-}$ and $[U@(Bi_4)_3]^{3-}$ clusters are significantly different from the corresponding reported experimental values. Further, from Table 4.1, it can be seen that the results calculated using PBE/DEF and PBE/DEF2 methods are very close. Therefore, we have investigated the various properties of all of the clusters using the PBE/DEF method and corresponding results have been discussed throughout this chapter unless otherwise mentioned.

Table 4.1: Calculated Bond Distances (in Å) in $[U@(Bi_4)_3]^{3-}$ and $[La@(Sb_4)_3]^{3-}$ Clusters using PBE (B3LYP) Functionals.

Systems	**Method**	$\mathbf{R_{eq}}$	$\mathbf{R_{ax}}$	$\mathbf{R_{intra}}$	$\mathbf{R_{inter}}$
$\mathbf{[U@(Bi_4)_3]^{3-}}$	**Expt**	3.463 − 3.545	3.119 − 3.167	3.051 − 3.109	3.018 − 3.046
	DEF	3.567 (3.664)	3.133 (3.236)	3.100 (3.073)	3.006 (3.085)
	DEF2	3.592 (3.693)	3.158 (3.261)	3.107 (3.076)	3.020 (3.105)
$\mathbf{[La@(Sb_4)_3]^{3-}}$	**Expt**	3.434 − 3.474	3.239 − 3.263	2.809 − 2.826	3.018 − 3.052
	DEF	3.542 (3.588)	3.334 (3.384)	2.865 (2.865)	3.136 (3.168)
	DEF2	3.529 (3.583)	3.310 (3.365)	2.870 (2.872)	3.121 (3.150)

After performing the benchmark study for $[U@(Bi_4)_3]^{3-}$ and $[La@(Sb_4)_3]^{3-}$ clusters, which are known experimentally, all of the lanthanide– and actinide–doped metalloid clusters, viz., $[Ln@(E_4^{2-})_3]$ and $[An@(E_4^{2-})_3]$ (Ln = La^{3+}, Ce^{4+}, Pr^{5+}, Nd^{6+}; An = Th^{4+}, Pa^{5+}, U^{6+}, Np^{7+}; E = Sb, Bi) are optimized in D_{3h} symmetry (Figure 4.1) with all real frequency values. In addition to the D_{3h} symmetry, all of the $[Ln@(E_4^{2-})_3]$ and $[An@(E_4^{2-})_3]$ clusters except the $[Nd@(Bi_4)_3]$ cluster are optimized in C_s symmetry (Figure 4.1) with all real frequencies. However, this particular geometry with C_s symmetry is energetically less stable (7–16 kcal mol^{-1}) as compared to the corresponding D_{3h} geometry isomer. Also, we have made an attempt to optimize the $[Ln@(E_4^{2-})_3]$ and $[An@(E_4^{2-})_3]$ clusters using icosahedral geometry without any symmetry constrain. However, they are optimized in distorted icosahedral structure. Furthermore, these distorted icosahedral geometries for all of the $[Ln@(E_4^{2-})_3]$ and $[An@(E_4^{2-})_3]$ clusters are found to be energetically less stable (by 0.05–1.6

eV) as compared to their corresponding D_{3h} isomer, which is consistent with the experimentally observed D_{3h} structure of $[Ln@(Sb_4)_3]^{3-}$ clusters[79] reported recently. Therefore, the D_{3h} geometry represents the true minimum structure for all of the $[Ln@(E_4^{2-})_3]$ and $[An@(E_4^{2-})_3]$ clusters.

In general, the intra–ring bond distances (R_{intra}) are found to be smaller than the inter–ring bond distances (R_{inter}), indicating a stronger intra–ring bonding as compared to inter–ring bonding in most of the metalloid systems (Table 4.2). This trend is in agreement with the intra– and inter–ring bond distances for the K([2.2.2]crypt) salts of $[Ln@(Sb_4)_3]^{3-}$ (Ln = La, Y, Ho, Er, Lu) systems, which have been synthesized and characterized recently.[79] However, in the presently studied $[U@(Bi_4)_3]$, $[Np@(Bi_4)_3]^+$, $[Np@(Sb_4)_3]^+$, and $[Nd@(Bi_4)_3]$ clusters, the R_{inter} bonding turns out to be stronger than the R_{intra}, indicating a greater extent of interaction among the three neighbouring E_4^{2-} rings in the presence of U^{6+}, Np^{7+}, and Nd^{6+} metal ions. This alternative trend has also been found in the recently synthesized[78] K([2.2.2]crypt) salts of $[U@(Bi_4)_3]^{3-}$.

Furthermore, on moving from Ln = La^{3+} to Nd^{6+} and An = Th^{4+} to Np^{7+} ion in $[Ln@(E_4^{2-})_3]$ and $[An@(E_4^{2-})_3]$ clusters, respectively, bonding of An/Ln ion with ring atoms (R_{ax} and R_{eq}) increases monotonically. It is also interesting to observe that as we move from La^{3+} to Nd^{6+} and Th^{4+} to Np^{7+} in $[Ln@(E_4^{2-})_3]$ and $[An@(E_4^{2-})_3]$ clusters the bonding between the neighbouring rings (R_{inter}) is progressively increases whereas the bonding within the rings (R_{intra}) decreases and finally R_{inter} bond becomes stronger than R_{intra} bond. The variation of the R_{ax}, R_{eq}, R_{intra}, and R_{inter} are reported in Table 4.2. These bond length values clearly indicate that the central metal ion plays a vital role to stabilize these clusters.

Table 4.2: Optimized Bond Length (in Å) in [Ln@(E_4^{2-})$_3$] and [An@(E_4^{2-})$_3$] Clusters using PBE Functional.

Systems	R_{eq}	R_{ax}	R_{intra}	R_{inter}
[Th@(Bi$_4$)$_3$]$^{2-}$	3.553	3.259	3.040	3.138
[Pa@(Bi$_4$)$_3$]$^{-}$	3.457	3.151	3.053	3.074
[U@(Bi$_4$)$_3$]	3.426	3.110	3.056	3.054
[Np@(Bi$_4$)$_3$]$^{+}$	3.419	3.099	3.064	3.054
[Th@(Sb$_4$)$_3$]$^{2-}$	3.456	3.218	2.872	3.053
[Pa@(Sb$_4$)$_3$]$^{-}$	3.340	3.085	2.893	2.955
[U@(Sb$_4$)$_3$]	3.295	3.029	2.902	2.914
[Np@(Sb$_4$)$_3$]$^{+}$	3.283	3.012	2.908	2.903
[La@(Bi$_4$)$_3$]$^{3-}$	3.655	3.380	3.030	3.209
[Ce@(Bi$_4$)$_3$]$^{2-}$	3.498	3.187	3.052	3.104
[Pr@(Bi$_4$)$_3$]$^{-}$	3.449	3.137	3.061	3.074
[Nd@(Bi$_4$)$_3$]	3.427	3.121	3.068	3.065
[La@(Sb$_4$)$_3$]$^{3-}$	3.542	3.334	2.865	3.136
[Ce@(Sb$_4$)$_3$]$^{2-}$	3.398	3.146	2.880	3.003
[Pr@(Sb$_4$)$_3$]$^{-}$	3.328	3.070	2.899	2.944
[Nd@(Sb$_4$)$_3$]	3.297	3.041	2.909	2.920

4.2.3 Binding energy estimation

The stability of the [Ln@(E_4^{2-})$_3$] (Ln = La^{3+}, Ce^{4+}, Pr^{5+}, Nd^{6+}) and [An@(E_4^{2-})$_3$] (An = Th^{4+}, Pa^{5+}, U^{6+}, Np^{7+}) (E = Sb, Bi) systems can be determined based on their BE values, which are calculated by using the following pathway (path1).

$$M^{n+} + 3\,[E_4^{2-}] \rightarrow [M@(E_4)_3]^{n-6} \tag{4.1}$$

$$BE = E\,([M@(E_4)_3]^{n-6}) - E\,(M^{n+}) - 3E\,(E_4^{2-}) \tag{4.2}$$

All of the encapsulations are found to be exothermic in nature with negative BE values, which is indicative of the feasibility of bond formation between the central metal atom with the E_4^{2-} rings atoms, thus favouring the formation of all [Ln@(E_4^{2-})$_3$] and [An@(E_4^{2-})$_3$] clusters. For all of the systems, calculated binding energies are very high as shown in Table 4.3. The two set of values of BE for [M@(Sb_4^{2-})$_3$] and [M@(Bi_4^{2-})$_3$] (M = Ln, An) are very close to each other, indicating that for a particular central metal ion, the BE value remains almost the same with change in the Zintl ion ligand from Sb_4^{2-} to Bi_4^{2-}. However, for a particular ligand, there is an enormous change in the BE value along the La^{3+}, Ce^{4+}, Pr^{5+}, Nd^{6+} series, which is consistent with the calculated structural trends.

For the neutral [U@(Sb_4)$_3$], [U@(Bi_4)$_3$], [Nd@(Sb_4)$_3$], and [Nd@(Bi_4)$_3$] systems, we again calculated the BE by taking neutral fragments pathway (path2) that is shown below:

$$M + 3\,[E_4] \rightarrow [M@(E_4)_3] \tag{4.3}$$

$$BE = E\,[M@(E_4)_3] - E\,(M) - 3E\,(E_4) \tag{4.4}$$

The BE values calculated using path2 are −13.84 and −13.89 eV for [U@(Bi_4)$_3$] and [U@(Sb_4)$_3$] systems, respectively. In addition, for [Nd@(Bi_4)$_3$] and [Nd@(Sb_4)$_3$] systems, binding energies are −8.75 and −8.47 eV, respectively. These values clearly indicate that the BE values are overestimated in case of highly charged fragments (path1). We anticipate higher BE by following the path1 as we are separating the highly charged species in the gas phase. However, we have not used path2 for other systems because defining neutral fragments for path2 becomes difficult for the charged systems studied here.

In the present study, initially three planar and aromatic E_4^{2-} rings (E = Sb and Bi) are considered to interact with each other and with the central metal ion to form [Ln@(E_4^{2-})$_3$] and [An@(E_4^{2-})$_3$] clusters. However, three rings (E_4^{2-} unit) deviate considerably from their planarity in the corresponding [Ln@(E_4^{2-})$_3$] and [An@(E_4^{2-})$_3$] clusters similar to the experimentally reported [La@(Sb_4)$_3$]$^{3-}$ system.[79] It is worthwhile to mention that the stability of metal–doped clusters has been significantly affected by the nonplanarity of the three E_4^{2-} rings present in their respective [M@(E_4^{2-})$_3$] clusters. On−going from [La@(E_4)$_3$]$^{3-}$ to [Nd@(E_4)$_3$] and [Th@(E_4)$_3$]$^{2-}$ to [Np@(E_4)$_3$]$^{+}$ clusters, the extent of nonplanarity of each metalloid rings (E_4^{2-}) in their corresponding systems tend to increase considerably, where the dihedral angle (DA) varies from 12.9 to 24.3° and 17.2 to 27.9° for each of the Sb_4^{2-} and Bi_4^{2-} units in the corresponding complexes, as reported in Table 4.3. Thus, it is revealed that an increase in the DA on going from valence–isoelectronic La^{3+} to Nd^{6+} and Th^{4+} to Np^{7+} doped Zintl ion clusters is associated with an increase in the strength of inter–ring bonding (R_{inter}) and bonding of central metal atom with the ring atoms (R_{ax} and R_{eq}), which in turn enhance the stability of these metalloid clusters. Consequently, all of the clusters studied in this work are stable even after losing the aromaticity of their parent E_4^{2-} rings, similar to the experimentally observed $[Ln@(Sb_4)_3]^{3-}$ (Ln = La, Y, Ho, Er, Lu) clusters.[79]

Table 4.3: Binding Energy (BE, in eV), HOMO−LUMO Energy Gap (ΔE_{Gap}, in eV), and Dihedral Angle of Ring (DA, in degree) of $M@(E_4^{2-})_3$ Systems using PBE Functional.

Systems	**BE**	**ΔE_{Gap}**	**DA**	**Systems**	**BE**	**ΔE_{Gap}**	**DA**
$[Th@(Bi_4)_3]^{2-}$	−82.58	1.21	21.8	**$[Th@(Sb_4)_3]^{2-}$**	−82.36	1.50	17.0
$[Pa@(Bi_4)_3]^{-}$	−131.53	1.31	26.1	**$[Pa@(Sb_4)_3]^{-}$**	−131.23	1.47	22.2
$[U@(Bi_4)_3]$	−196.51	0.99	27.7	**$[U@(Sb_4)_3]$**	−196.02	1.00	24.4
$[Np@(Bi_4)_3]^{+}$	−279.53	0.71	28.5	**$[Np@(Sb_4)_3]^{+}$**	−278.65	0.73	25.2
$[U@(Bi_4)_3]^{3-}$	−40.17	0.20	25.7	…	….	…	…
$[La@(Bi_4)_3]^{3-}$	−46.93	1.10	17.2	**$[La@(Sb_4)_3]^{3-}$**	−46.64	1.17	12.9
$[Ce@(Bi_4)_3]^{2-}$	−90.37	0.98	24.9	**$[Ce@(Sb_4)_3]^{2-}$**	−90.02	0.99	19.7
$[Pr@(Bi_4)_3]^{-}$	−152.27	0.74	27.0	**$[Pr@(Sb_4)_3]^{-}$**	−151.74	0.69	22.9
$[Nd@(Bi_4)_3]$	−235.60	0.69	27.9	**$[Nd@(Sb_4)_3]$**	−234.76	0.70	24.3

4.2.4 Molecular orbital and charge distribution analyses

The molecular orbital (MO) energy level diagram of $[An@(Sb_4^{2-})_3]$ clusters is shown in Figure 4.2. The sufficiently large HOMO–LUMO energy gap (Table 4.3) value points to the chemical stability of all the studied clusters. It is to be noted that in all the An– and Ln–doped clusters the energy difference between the 6s/5s orbital and the 6p/5p orbitals of Bi/Sb atom is very large; therefore, only 6p/5p orbitals are considered as outer valence orbitals for bonding with doped metal atom in the Figure 4.2. The Th^{4+}– and La^{3+}–doped Zintl ion clusters alone behave differently in comparison to the remaining An (An = Pa^{5+}, U^{6+} and Np^{7+}) and Ln (Ln = Ce^{4+}, Pr^{5+} and Nd^{6+}) doped clusters, as no f–atomic orbitals of Th and La atom are involved in bonding with the valence atomic orbitals of ring atoms.

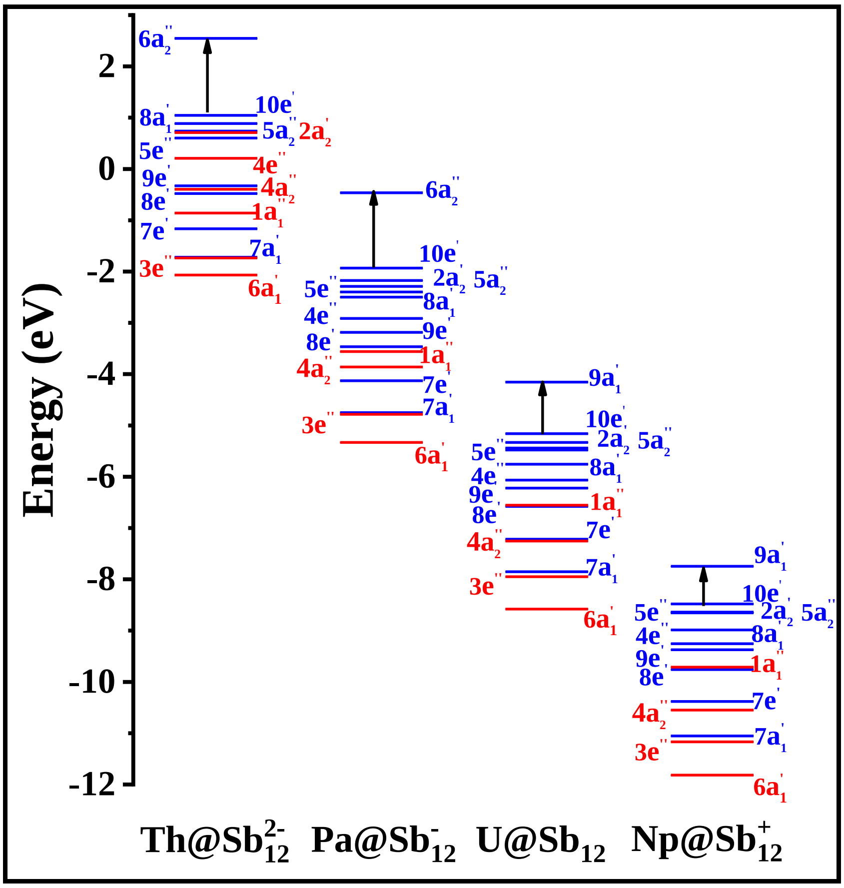

Figure 4.2: MO energy level diagram of $[An@(Sb_4^{2-})_3]$ clusters using PBE functional. Here blue lines stands for mixed An–ring atoms MOs and red for the pure ring atoms MOs.

From Figure 4.3, one can see the participation of the valence 7s, 7p, 6d orbitals of Th in bonding with the 5p orbitals of ring atoms in $10e'$, $8a_1'$, $5a_2''$, $5e''$, $9e'$, $8e'$, $7e'$, and $7a_1'$ mixed Th-Sb MOs. As a consequence, these hybrid MOs fulfill the 26–electron count around the Th. Similarly, the $[La@(Sb_4)_3]^{3-}$ cluster forms a stable 26–electron system corresponding to completely filled $6a_1'$, $8e'$, $4e''$, $4a_2''$, $7e'$, $6e'$, $5e'$, and $5a_1'$ mixed La-Sb MOs, which are formed by the overlapping of the valence orbitals of La (6s, 6p, 5d) and the valence orbitals of ring (5p) atoms. However, the remaining occupied MOs in both clusters are due to the pure ring orbitals. Unlike in the case of Th^{4+} and La^{3+}, the f orbitals of remaining An (Pa^{5+}, U^{6+} and Np^{7+}) and Ln (Ce^{4+}, Pr^{5+}, Nd^{6+}) are involved in bonding with the valence np orbitals of the rings.

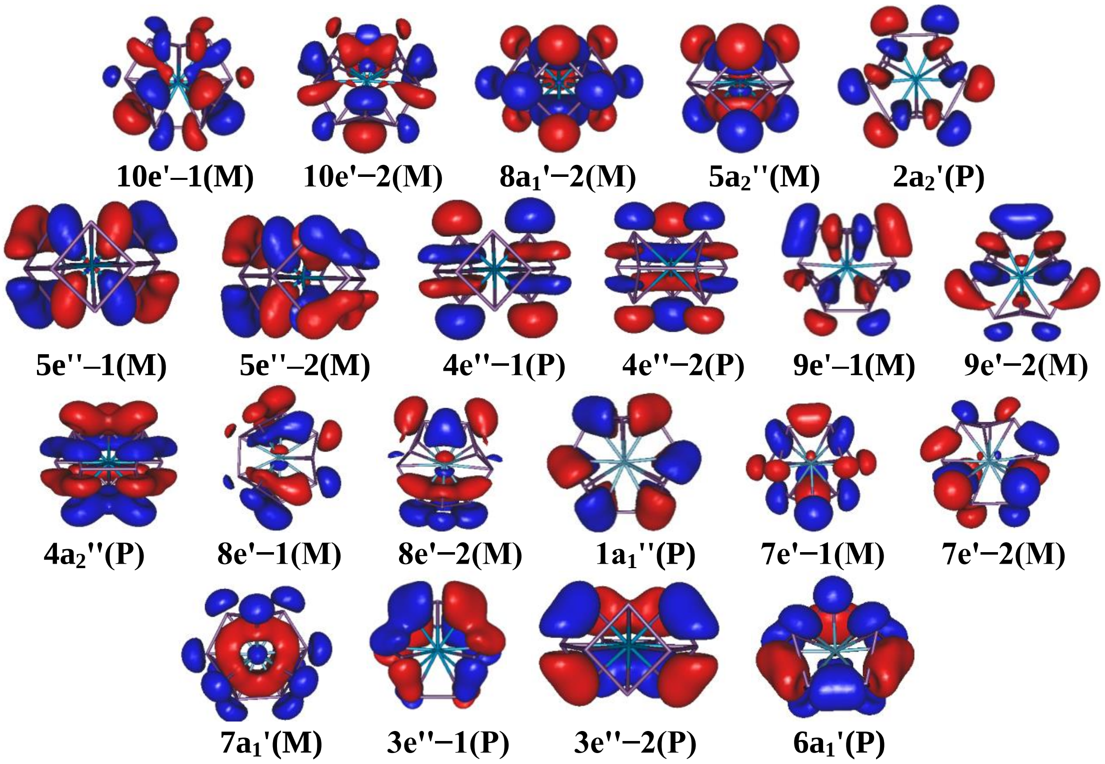

Figure 4.3: MO pictures of $[Th@(Sb_4)_3]^{2-}$ cluster using PBE functional. Here '(M)' stands for mixed Th–ring atoms MOs and '(P)' stands for pure ring atoms MOs.

In $U@(Sb_4)_3$ cluster (Figure 4.4), the 7s, 7p, 6d, and 5f orbitals of U overlap with the 5p orbitals of Sb atoms to form a stable 32–electron system[108, 110-113] corresponding to completely filled 10e′, $5a_2''$, $2a_2'$, $8a_1'$, 5e″, 9e′, 4e″, 8e′, 7e′ and $7a_1'$ mixed U-Sb MOs. However, in the Ln–doped clusters the central atom–ring mixing in 4e″ orbital is small. In all of the $[An@(Sb_4^{2-})_3]$ and $[Ln@(Sb_4^{2-})_3]$ clusters, $1a_1''$, $4a_2''$, 3e″, and $6a_1'$ MOs correspond to the 5p orbitals of ring atoms do not contribute to the bonding with the central atom. In the same way, An– and Ln–doped Bi clusters also fulfill the 26–electron count around Th and La, and 32–electron count around the remaining An (Pa^{5+}, U^{6+} and Np^{7+}) and Ln (Ce^{4+}, Pr^{5+}, Nd^{6+}) ion in their respective clusters. Thus, the absence of the involvement of the f–orbitals in the bonding with the ring atoms causes the difference of six electrons in the total electron count of Th^{4+} and La^{3+} containing [(E$_4^{2-}$)$_3$] systems. Therefore, larger involvement of the f–orbitals of An (U^{6+} and Np^{7+}) and of Ln (Nd^{6+}) in bonding with the ring atoms is responsible for the stronger inter–ring bonding as compared to the intra–ring bonding in [Np@(Sb$_4$)$_3$]$^+$, [U@(Bi$_4$)$_3$], [Np@(Bi$_4$)$_3$]$^+$ and [Nd@(Bi$_4$)$_3$] systems, which clearly shows the impact of f–orbitals of An and Ln on the geometrical parameters of these systems.

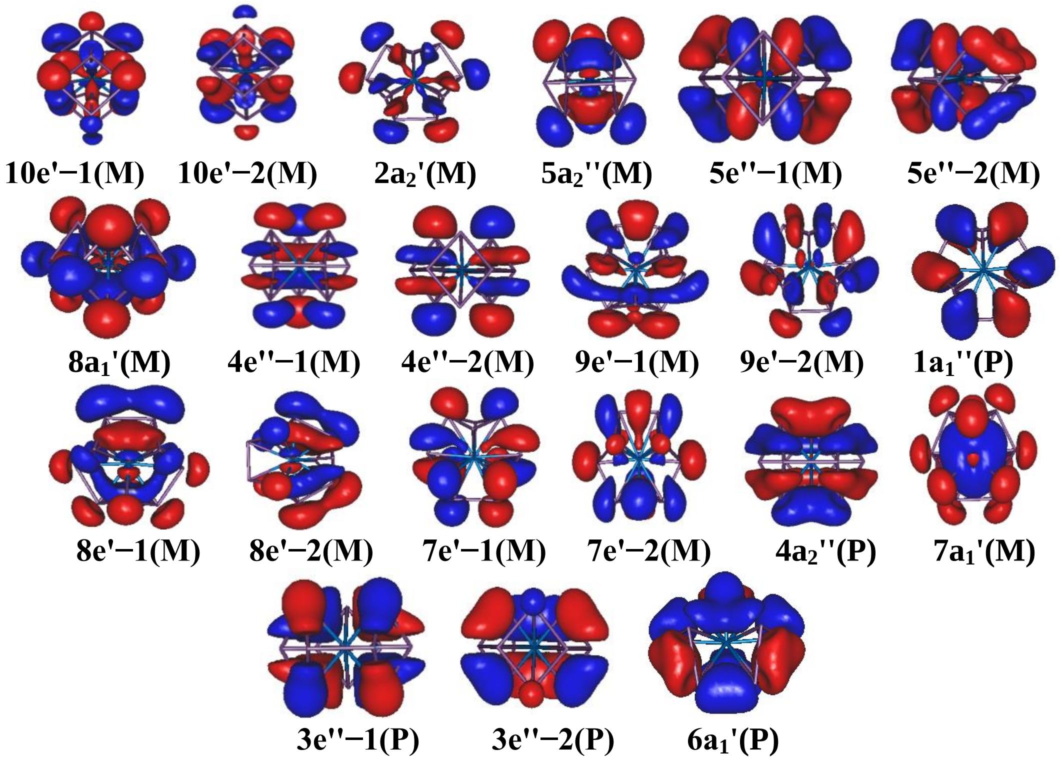

10e'−1(M) **10e'−2(M)** **2a$_2$'(M)** **5a$_2$''(M)** **5e''−1(M)** **5e''−2(M)**

8a$_1$'(M) **4e''−1(M)** **4e''−2(M)** **9e'−1(M)** **9e'−2(M)** **1a$_1$''(P)**

8e'−1(M) **8e'−2(M)** **7e'−1(M)** **7e'−2(M)** **4a$_2$''(P)** **7a$_1$'(M)**

3e''−1(P) **3e''−2(P)** **6a$_1$'(P)**

Figure 4.4: MO pictures of [U@(Sb$_4$)$_3$] cluster using PBE functional. Here ‘(M)’ stands for mixed U–ring atoms MOs and ‘(P)’ stands for pure ring atoms MOs.

Further, the VDD[167] charges on central atoms as well as on the ring atoms of $[Ln@(E_4^{2-})_3]$ and $[An@(E_4^{2-})_3]$ clusters are calculated using PBE/TZ2P method and corresponding values are reported in Table 4.4. The calculated VDD charges on the central atoms are in the range of 0.01 to −0.07 for An (Th^{4+} to Np^{7+}) and −0.05 to −0.06 for Ln (La^{3+} to Nd^{6+}), which is significantly smaller than the initial charge on the central atoms (i.e., +3 to +7). On the other hand, the overall negative charge of ring (i.e., −6) has been reduced to the range of −2.95 to 0.06, from La^{3+}– to Nd^{6+}–doped clusters and −2.01 to 1.07 from Th^{4+}– to Np^{7+}–doped clusters. Thus, in the $[An@(E_4^{2-})_3]$ and $[Ln@(E_4^{2-})_3]$ clusters, the charge density of the doped ion (Ln/An) is increased, whereas the charge density of the ring atoms (E_4^{2-}, E = Sb/Bi) is decreased. This clearly represents that the charge transfer takes place from the rings atoms (E_4^{2-}) to the doped metal ion. Moreover, the magnitude of charge transfer from the rings atoms to the doped ion is slightly increased along the actinide and the lanthanide series, An = $Th^{4+} - Pa^{5+} - U^{6+} - Np^{7+}$ and Ln = $La^{3+} - Ce^{4+} - Pr^{5+} - Nd^{6+}$ in the $[An@(E_4^{2-})_3]$ and $[Ln@(E_4^{2-})_3]$ clusters as shown in Table 4.4. Further, the population of the valence s, p, d, and f orbitals of the central atom in all metal–doped clusters are calculated using the NPA[166] scheme. On moving from Th^{4+} to Np^{7+} and La^{3+} to Nd^{6+} metal ions, it has been found that s and p populations on central atom are more or less similar while there is a significant variation in its f population for both lanthanide– and actinide–doped clusters as shown in Table 4.4.

Table 4.4: VDD Charges[1] at PBE/TZ2P Level (q_{eq}, q_{ax}, q_{ring}, and q_M) and f–Population of Ln/An (f_M) using NPA at PBE/DEF Level.

Systems	q_{eq}	q_{ax}	q_{ring}	q_M	f_M
[Th@(Bi$_4$)$_3$]$^{2-}$	−0.12	−0.21	−2.01	0.01	3.48
[Pa@(Bi$_4$)$_3$]$^{-}$	−0.05	−0.12	−1.05	0.05	3.50
[U@(Bi$_4$)$_3$]	0.03	−0.03	0.02	−0.02	4.07
[Np@(Bi$_4$)$_3$]$^{+}$	0.11	0.07	1.07	−0.07	5.04
[Th@(Sb$_4$)$_3$]$^{2-}$	−0.15	−0.22	−2.03	0.03	3.30
[Pa@(Sb$_4$)$_3$]$^{-}$	−0.04	−0.13	−1.07	0.07	3.69
[U@(Sb$_4$)$_3$]	0.04	−0.03	0.01	−0.01	4.29
[Np@(Sb$_4$)$_3$]$^{+}$	0.12	0.06	1.06	−0.06	5.23
[La@(Bi$_4$)$_3$]$^{3-}$	−0.19	−0.30	−2.95	−0.05	0.00
[Ce@(Bi$_4$)$_3$]$^{2-}$	−0.12	−0.19	−1.85	−0.15	1.23
[Pr@(Bi$_4$)$_3$]$^{-}$	−0.05	−0.11	−0.95	−0.04	2.40
[Nd@(Bi$_4$)$_3$]	0.03	−0.02	0.06	−0.06	3.54
[La@(Sb$_4$)$_3$]$^{3-}$	−0.19	−0.31	−2.97	−0.03	0.00
[Ce@(Sb$_4$)$_3$]$^{2-}$	−0.11	−0.21	−1.87	−0.12	1.19
[Pr@(Sb$_4$)$_3$]$^{-}$	−0.04	−0.12	−0.99	−0.02	2.40
[Nd@(Sb$_4$)$_3$]	0.04	−0.03	0.05	−0.05	3.56

[1] Average charge (q_{eq} and q_{ax}) for equatorial and axial Sb/Bi atoms is reported.

4.2.5 Density of states analysis

Density of states (DOS) plots for the [Ln@(E_4^{2-})$_3$] and [An@(E_4^{2-})$_3$] (E = Sb, Bi) clusters are represented in Figure 4.5. All of the bands appearing at the right side of the HOMO (HOMO is pointed by the vertical arrow) correspond to the unoccupied MOs. Whereas the bands appearing at the left side of the HOMO correspond to the mixed occupied MOs [associated with the valence orbital of central atom (s, p, d and f) as well as ring atomic orbitals (p)] and pure occupied MOs (associated with the ring atomic orbital only). It is to be noted that the DOS are shifted deeper in energy from Th^{4+}–Np^{7+} and La^{3+}–Nd^{6+}–doped clusters, indicative of the increasing extent of hybridization of central atom with ring atoms. Furthermore, as compared to the actinide–doped systems, the lanthanide–doped [Ln@(E$_4^{2-}$)$_3$] systems are shifted less deep in energy because of the slightly smaller mixing of their less diffuse 4f/5d orbitals with the valence np orbitals of Sb/Bi as compared to that of the 5f/6d orbitals of actinides.

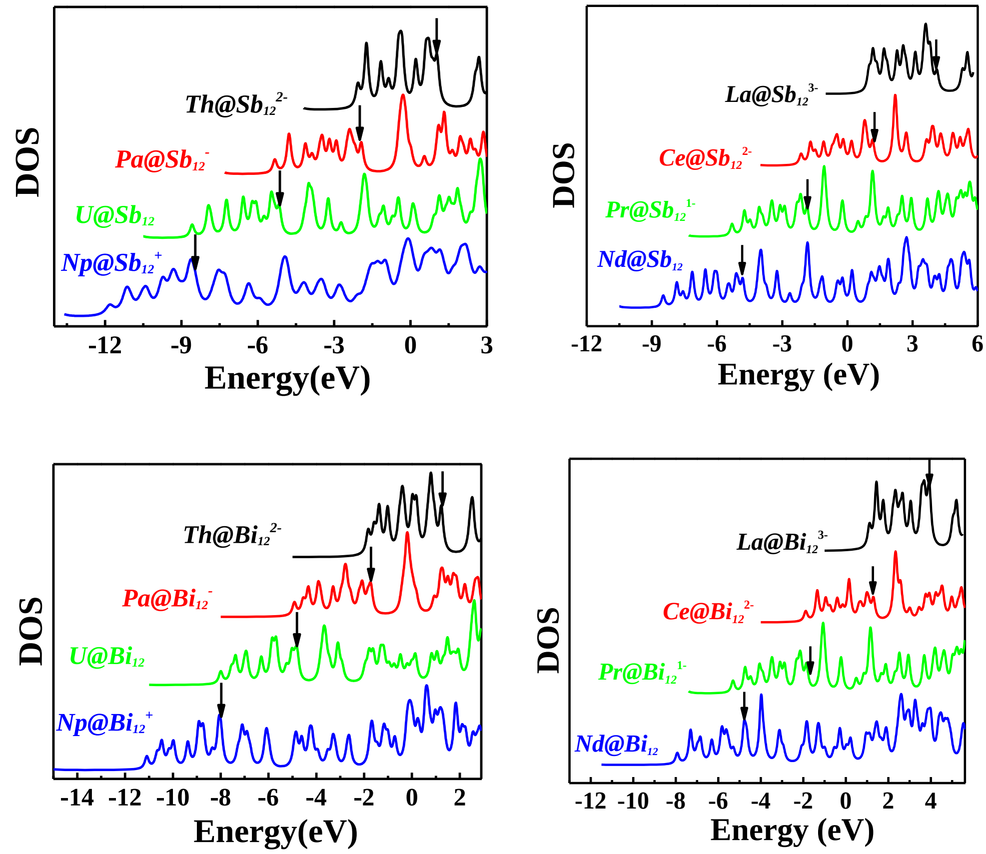

Figure 4.5: DOS plots of [An@(E$_4^{2-}$)$_3$] and [Ln@(E$_4^{2-}$)$_3$] clusters using PBE functional. (Black arrows are showing peak corresponding to HOMO).

4.2.6 Analysis of topological properties

To analyze the nature of chemical bonding between the ring atoms as well as between the central metal atom (Ln/An) and ring atoms (Sb/Bi) in [Ln@(E$_4^{2-}$)$_3$] and [An@(E$_4^{2-}$)$_3$] clusters, bond critical point (BCP) properties have been calculated using Bader’s quantum theory of atoms in molecules (QTAIM)[168, 172] with small core ECP augmented with EDF using the PBE/DEF2 method. Using Boggs[169], criteria of bonding (as discussed in Chapter 3) we have found that the R_{ax} and R_{eq} bonds as well as inter– and intra–ring bonding are not true covalent bond. However, at BCP the value of $E_d(r) < 0$ (~–0.01) and $G(r)/\rho(r) < 1$ (~0.3–0.5), suggests a very small amount of covalent character in all the four type of bonds.[169]

4.2.7 Energy decomposition analysis

In Energy decomposition analysis (EDA), the total interaction energy (ΔE^{int}) is decomposed into Pauli repulsion (ΔE^{Pauli}), electrostatic interaction (ΔE^{elec}) and orbital interaction (ΔE^{orb}) terms. Thus, the total interaction energy, ΔE^{int}, can be represented as,

$$\Delta E^{int} = \Delta E^{Pauli} + \Delta E^{elec} + \Delta E^{orb} \tag{4.5}$$

where the ΔE^{elec} and ΔE^{orb} are attractive energy (stabilizing) terms, whereas the ΔE^{Pauli} is repulsive energy (destabilizing) term.

Since the three planar E_4^{2-} rings become highly non-planar in the $[M@(E_4^{2-})_3]$ clusters so lots of deformation from the equilibrium structure of the E_4^{2-} ring, hence it is important here to consider the contribution of the deformation energy of rings in the total interaction energy as shown in equation (4.6).

$$\Delta E^{int} = \Delta E^{Pauli} + \Delta E^{elec} + \Delta E^{orb} + \Delta E^{prep} \tag{4.6}$$

where the ΔE^{prep} is the preparatory energy term (also known as deformation energy of E_4^{2-} rings in the presence of doped metal ion), which is calculated by taking the energy difference between the distorted rings ($3E_4^{2-}$ units) of $[M@(E_4^{2-})_3]$ with the relaxed bare $3E_4^{2-}$ rings.

For EDA calculations, $[M@(E_4^{2-})_3]$ clusters are partitioned into four fragments viz., central ion (M) and three identical E_4^{2-} rings (E = Sb, Bi). From Table 4.5, we can see that the ΔE^{prep} term increases as we move from Th^{4+} to Np^{7+} and La^{3+} to Nd^{6+} centered $(E_4^{2-})_3$ clusters, which is in agreement with DA variation (Table 4.3). Thus, E_4^{2-} rings of the

$[M@(E_4^{2-})_3]$ get more distorted as we move from Th^{4+} to Np^{7+} and La^{3+} to Nd^{6+} centered $[(E_4^{2-})_3]$ clusters. It is to be noted that the ΔE^{int} of all the $[Ln@(E_4^{2-})_3]$ and $[An@(E_4^{2-})_3]$ clusters is strongly affected by the nature and type of central metal atom; however, an insignificant effect of ring type (Sb_4^{2-} or Bi_4^{2-}) has been observed in the interaction energies of all clusters.

Table 4.5: EDA of $[M@(E_4^{2-})_3]$ Clusters at PBE/TZ2P Level. Percentage Contribution of Stabilizing Energy to the Total Interaction Energy (in eV) is Provided within Parenthesis.

Cluster	ΔE^{Pauli}	ΔE^{elec}	ΔE^{orb}	ΔE^{prep}	ΔE^{int}
$[Th@(Bi_4)_3]^{2-}$	56.16	−92.12 (66.30)	−46.82 (33.70)	0.91	−81.87
$[Pa@(Bi_4)_3]^{-}$	73.91	−123.44 (59.83)	−82.87 (40.17)	1.48	−130.92
$[U@(Bi_4)_3]$	83.47	−150.01 (53.28)	−131.52 (46.72)	1.71	−196.35
$[Np@(Bi_4)_3]^{+}$	88.51	−174.14 (47.04)	−196.02 (52.96)	1.84	−279.81
$[Th@(Sb_4)_3]^{2-}$	47.65	−86.43 (66.62)	−43.30 (33.38)	0.52	−81.56
$[Pa@(Sb_4)_3]^{-}$	67.31	−119.05 (59.92)	−79.63 (40.08)	1.18	−130.19
$[U@(Sb_4)_3]$	79.48	−147.70 (53.46)	−128.56 (46.54)	1.53	−195.25
$[Np@(Sb_4)_3]^{+}$	85.39	−173.13 (47.40)	−192.15 (52.60)	1.65	−278.24
$[La@(Bi_4)_3]^{3-}$	39.05	−61.64 (71.14)	−25.00 (28.86)	0.48	−47.11
$[Ce@(Bi_4)_3]^{2-}$	61.02	−96.06 (61.75)	−59.50 (38.25)	1.29	−93.25
$[Pr@(Bi_4)_3]^{-}$	71.78	−123.79 (52.25)	−113.15 (47.75)	1.62	−163.54
$[Nd@(Bi_4)_3]$	76.75	−149.16 (43.92)	−190.43 (56.08)	1.82	−261.02
$[La@(Sb_4)_3]^{3-}$	32.89	−56.91 (71.13)	−23.10 (28.87)	0.25	−46.87
$[Ce@(Sb_4)_3]^{2-}$	51.81	−89.88 (61.82)	−55.52 (38.18)	0.81	−92.78
$[Pr@(Sb_4)_3]^{-}$	65.31	−119.79 (52.20)	−109.68 (47.80)	1.29	−162.87
$[Nd@(Sb_4)_3]$	71.77	−146.79 (44.05)	−186.42 (55.95)	1.56	−259.88

In case of $[Ln@(E_4^{2-})_3]$ and $[An@(E_4^{2-})_3]$ (E = Sb, Bi) clusters, the bonding energy has been drastically increased from Th^{4+} to Np^{7+} and La^{3+} to Nd^{6+} metal–doped clusters. Note that in all of the cases the major contribution of the attractive energy components makes the overall interaction energy attractive in nature. Further, as we move from Th^{4+} to Np^{7+} and

La^{3+} to Nd^{6+} centered $[(E_4^{2-})_3]$ clusters, the percentage contribution from the electrostatic terms become smaller, while the contribution of ΔE^{orb} term is found to be increased, leading to more stability for the $[Np@(E_4)_3]^+$ and $[Nd@(E_4)_3]$ clusters as compared to the remaining clusters. The increase in the ΔE^{orb} contribution along these series is clearly due to an increase in the R_{ax}, R_{eq}, and R_{inter} bonding.

4.2.8 Spin orbit coupling effect

Finally, we have studied the effect of spin orbit coupling for four systems, namely, $[U@(Sb_4)_3]$, $[U@(Bi_4)_3]$, $[Nd@(Sb_4)_3]$, and $[Nd@(Bi_4)_3]$. The $[U@(Sb_4)_3]$ system has been optimized using spin orbit coupling and scalar relativistic effect using PBE functional and TZ2P basis set. The bond lengths calculated by incorporating the spin orbit coupling (R_{ax} = 3.082, R_{eq} = 3.372, R_{inter} = 2.968, R_{intra} = 2.960) and scalar relativistic effects (R_{ax} = 3.054, R_{eq} = 3.343, R_{inter} = 2.948, R_{intra} = 2.949) are relatively close in value, indicating a very small effect of spin orbit coupling on the structural parameter of $[U@(Sb_4)_3]$ system. Moreover, the PBE/DEF calculated bond lengths of $[U@(Sb_4)_3]$ (R_{ax} = 3.029, R_{eq} = 3.295, R_{inter} = 2.914, R_{intra} = 2.902) are relatively close to the bond lengths calculated using the scalar relativistic effects. Because the variation in the optimized bond length is not large, for the remaining systems, we have performed single–point energy calculations using scalar relativistic and spin orbit coupling by taking the optimized geometry obtained by the PBE/DEF method. We have also plotted the MO energy level diagram to see the effect of spin orbit interaction on the energy levels of all of the above–mentioned clusters. In the presence of spin orbit coupling, the HOMO–LUMO energy gap is slightly lowered in all of the systems because of splitting of the energy levels (Figure 4.6). Because of the spin orbit coupling, the MO energy levels split, although the extent of splitting of MO energy levels is very small. From Figure 4.6 one can see that the effect of spin orbit coupling on the energy levels of MOs of

$[U@(Sb_4)_3]$ is too small to affect their electronic properties. Same has been observed for $[U@(Bi_4)_3]$, $[Nd@(Sb_4)_3]$, and $[Nd@(Bi_4)_3]$ clusters.

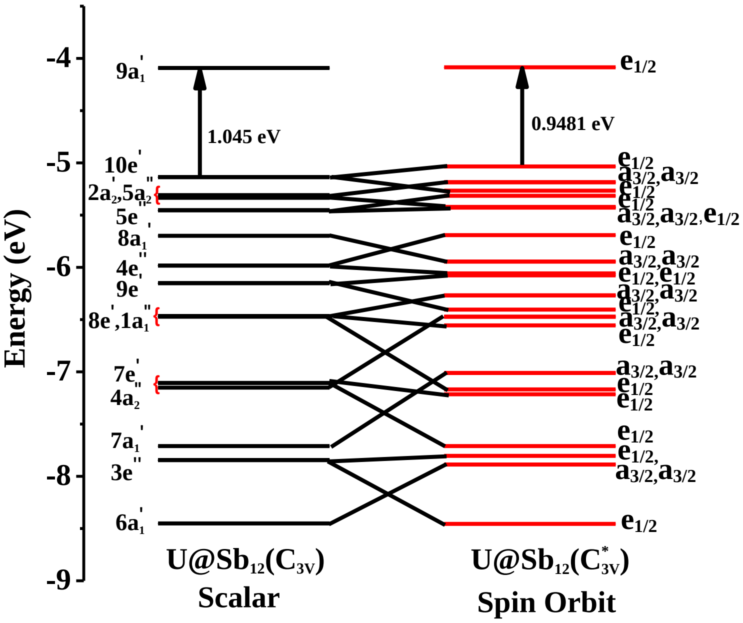

Figure 4.6: Scalar relativistic and spin orbit splitting of the valence MO energy levels of $[U@(Sb_4)_3]$ system at PBE/TZ2P level.

4.3 Conclusion

Theoretical existence of an iso–electronic series of early- to mid-lanthanide (Ln = La^{3+}, Ce^{4+}, Pr^{5+}, Nd^{6+}) and actinide (An = Th^{4+}, Pa^{5+}, U^{6+}, Np^{7+}) doped metalloid clusters, viz., $[Ln@(E_4^{2-})_3]$ and $[An@(E_4^{2-})_3]$ (E = Sb, Bi) has been comprehensively investigated in the present work using density functional theory. The stability of $[Ln@(E_4^{2-})_3]$ and $[An@(E_4^{2-})_3]$ clusters increases as we move from La^{3+} to Nd^{6+} and Th^{4+} to Np^{7+} doped clusters, although the E_4^{2-} rings lose their planarity and in turn their aromaticity along the same. Except for the La and Th, the f–orbitals of remaining Ln and An ion are involved in bonding with the ring atoms. Therefore, only 26–electron count is fulfilled in $[La@(Sb_4)_3]^{3-}$ and $[Th@(Sb_4)_3]^{2-}$ systems. Whereas, the f–orbitals of U, Np, and Nd is strongly involved in bonding with ring atoms (R_{ax} and R_{eq}) and lead to the fulfillment of 32–electron count in

$[U@(Bi_4)_3]$, $[Np@(Bi_4)_3]^+$, $[Np@(Sb_4)_3]^+$ and $[Nd@(Bi_4)_3]$ systems which is responsible for making inter–ring (R_{inter}) bond stronger as compared to that of the intra–ring (R_{inter}) bond. Thus, the formation of closed-shell 32–electron and 26–electron systems in addition to their favourable geometric as well as energetic parameters provides them with unusually high stability even though the rings are losing their aromaticity in the studied systems. Our work uncovers the reasons behind the unexpectedly high stability of lanthanide– and actinide–doped antiaromatic clusters in many aspects.

CHAPTER 5

Effect of Doping of Lanthanide and Actinide Ion in $Al_{12}H_{12}^{2-}$ and $B_{12}H_{12}^{2-}$ Clusters

5.1 Introduction

In the previous chapters (chapters 3 and 4), we have predicted highly stable lanthanide− and actinide− doped clusters, which follow 18− and 32−electron principles. In both the chapters, we have chosen Ln/An ion in their high oxidation state with f^0 configuration. Using these ions, we have tuned electronic and structural properties of the clusters, however, we have not considered the magnetic property. In order to modify the magnetic property or to induce magnetism in a cluster, one needs to dope a high spin Ln/An ion in a cluster. For this purpose, we have now chosen isoelectronic series of Ln (Pm^+, Sm^{2+}, Eu^{3+}) and An (Np^+, Pu^{2+}, Am^{3+}) ion, where all Ln/An are taken in their low oxidation state. All of the chosen Ln/An ion has f^6 configuration and possess septet spin as their ground spin state. In the present study, $B_{12}H_{12}^{2-}$ and $Al_{12}H_{12}^{2-}$ clusters have been considered as host clusters because of their highly symmetric icosahedral geometry, large cage diameter and wide range of applications.[73-74, 213-218] The $B_{12}H_{12}^{2-}$ is known experimentally but $Al_{12}H_{12}^{2-}$ has not been produced experimentally to date, although the crystal salts of the icosahedral $Al_{12}R_{12}^{2-}$ dianions with bulky substituents have been synthesized and measured in the past.[219]

Till now a large number of metal doped B_n and Al_n clusters have been investigated experimentally and theoretically,[220-226] however, only very few metal encapsulated $B_{12}H_{12}^{2-}$ and $Al_{12}H_{12}^{2-}$ clusters have been reported. In this context, noble gas doped $E_{12}H_{12}^{2-}$ (E = B, Al, Ga; Ng = He, Ne, Ar, Kr),[75] silicon doped $Al_{12}H_n$ (n = 1–14),[227] and transition metal doped $TMAl_nH_{2n}$ and $TMAl_nH_{2n+1}$ (TM = Sc, Ti, V; n = 3, 4)[228] clusters have been investigated theoretically. In addition to these studies, Charkin *et al.* have explored the exohedral and endohedral MAl_{12} and $MAl_{12}X_{12}$ (M = Li^+, Na^+, Be^{2+}, Mg^{2+}, Al^{3+}, Cu^+, Ga^+; X = H, F) clusters using density functional theory.[76, 228-230] More recently Hopkins *et al.* have investigated the transition metal doped $B_{12}X_{12}^{2-}$ (X = H, F) clusters and studied the charge transfer in these clusters.[231]

Thus, in the present work, we have investigated the isoelectronic series of actinide ion (An = Np^+, Pu^{2+} and Am^{3+}) doped $B_{12}H_{12}^{2-}$ and $Al_{12}H_{12}^{2-}$ clusters using first principles−based density functional theory. For comparison purposes, the corresponding series of lanthanide ion (Ln = Pm^+, Sm^{2+} and Eu^{3+}) doped $B_{12}H_{12}^{2-}$ and $Al_{12}H_{12}^{2-}$ clusters have also been investigated. The overall charges on these metal−doped $M^{n+}@Al_{12}H_{12}^{2-}$ and $M^{n+}@B_{12}H_{12}^{2-}$ clusters are −1, 0 and +1, respectively, for Np^+ (Pm^+), Pu^{2+} (Sm^{2+}) and Am^{3+} (Eu^{3+}) ion containing systems. The structural, energetic, electronic and magnetic properties of these actinide and lanthanide doped $B_{12}H_{12}^{2-}$ and $Al_{12}H_{12}^{2-}$ clusters have been investigated systematically. To the best of our knowledge, all these lanthanide and actinide doped $Al_{12}H_{12}^{2-}$ and $B_{12}H_{12}^{2-}$ clusters have not been reported earlier in the literature.

All the results discussed in this chapter have been obtained by using PBE[144], B3LYP[146-147], and M06−2X functionals[145] with def–TZVPP (represented as DEF) basis set along with a relativistic effective core potential (RECP) for heavier elements by using Turbomole[150], ADF[152-153] and Multiwfn[170] programs. Detail computational methodologies have been discussed in Chapter 2 of this thesis. B3LYP results are discussed throughout the chapter unless otherwise stated.

5.2 Results and discussions

5.2.1 Bare $B_{12}H_{12}^{2-}$ and $Al_{12}H_{12}^{2-}$ clusters

Both the bare $B_{12}H_{12}^{2-}$ and $Al_{12}H_{12}^{2-}$ clusters are optimized in highly symmetric icosahedral geometry (I_h) with all real frequency values. The cage diameter of $B_{12}H_{12}^{2-}$ is calculated to be small, i.e. 3.392 Å. However, the cage diameter of $Al_{12}H_{12}^{2-}$ is found to be somewhat larger (5.144 Å). Comparatively, a larger cage diameter of $Al_{12}H_{12}^{2-}$ is suitable for the encapsulation of a lanthanide or actinide ion, whereas the same is not possible with the $B_{12}H_{12}^{2-}$ cage due to its small cage diameter. Endohedral encapsulation of a lanthanide/actinide ion into $B_{12}H_{12}^{2-}$ destabilizes the cage considerably. Therefore, in the case of $B_{12}H_{12}^{2-}$, we have studied only exohedral metal−doped $B_{12}H_{12}^{2-}$ clusters ($M@B_{12}H_{12}^{2-}$), whereas for $Al_{12}H_{12}^{2-}$, we studied both exohedral as well as endohedral clusters ($M@Al_{12}H_{12}^{2-}$).

5.2.2 Endohedral and exohedral $M@Al_{12}H_{12}^{2-}$ clusters

The iso−electronic series of the actinide (An = Np^+, Pu^{2+}, Am^{3+}) and lanthanide (Ln = Pm^+, Sm^{2+}, Eu^{3+}) doped $Al_{12}H_{12}^{2-}$ clusters represented as $An@Al_{12}H_{12}^{2-}$ and $Ln@Al_{12}H_{12}^{2-}$, respectively, have been considered in this work. All the clusters are optimized in their lowest (singlet) as well as highest (septet) possible spin states. Initially, we have optimized the endohedral clusters where the metal ion is doped inside the $Al_{12}H_{12}^{2-}$ cage. All the closed−shell endohedral $An@Al_{12}H_{12}^{2-}$ and $Ln@Al_{12}H_{12}^{2-}$ clusters are optimized in the highly symmetric icosahedral symmetry (I_h) (Figure 5.1, STR1) similar to their parent $Al_{12}H_{12}^{2-}$ clusters, whereas all the corresponding open−shell endohedral clusters in septet spin state are optimized in the distorted icosahedral geometry with lower symmetry. Among all the open−shell clusters, Np^+ and Pm^+ doped clusters are optimized in highly distorted C_1 symmetry (Figure 5.1, STR2). However, the Pu^{2+} and Sm^{2+} doped $Al_{12}H_{12}^{2-}$ clusters are optimized in C_{3v} symmetry structure (Figure 5.1, STR3) as their minimum energy structure. Whereas, Am^{3+} and Eu^{3+} doped $Al_{12}H_{12}^{2-}$ clusters are optimized in the C_3 symmetry structure (Figure 5.1, STR4). Moreover, to find the true minimum energy structure we have optimized one of the endohedral systems without any symmetry constraint with different initial geometries, in which the doped ion is placed at different positions inside the cage. However, the structures obtained after the optimization are the same as we have obtained with the symmetry constraint optimization.

It is to be noted that for all the endohedral $M@Al_{12}H_{12}^{2-}$ clusters, the septet spin isomer is energetically more stable (0.3−5.7 eV) than the corresponding closed−shell cluster except for $Np@Al_{12}H_{12}^{-}$. Furthermore, the energy difference between the two different spin states (singlet and septet) is significantly larger in the case of $Ln@Al_{12}H_{12}^{2-}$ clusters as compared to that in the $An@Al_{12}H_{12}^{2-}$ clusters (Table 5.1). The 4f orbitals of Ln are deeply "buried" inside the atom and are shielded from the atom's environment by their 4d and 5p electrons. Therefore, 4f orbitals of Ln ion are not affected by the ligand field strength. Consequently, the high spin state of Ln ion remains preserved in the endohedral $Ln@Al_{12}H_{12}^{2-}$ clusters. However, the 5f orbitals of early An are much more diffused, therefore their spin state can be affected by the ligand field environment. The Np^{+} has much more diffused orbitals than Pu^{2+}, which in turn found to be more diffused than Am^{3+}. Hence, the ligand field strength will decreases in this series. As a result, Np^{+} doped endohedral cluster favours low spin state, while high spin state is preserved in Pu^{2+} and Am^{3+} doped endohedral clusters. Thus, the early actinides are very similar to the heavy 5d transition metals, while the chemistry of lanthanide differs from the transition metal elements.

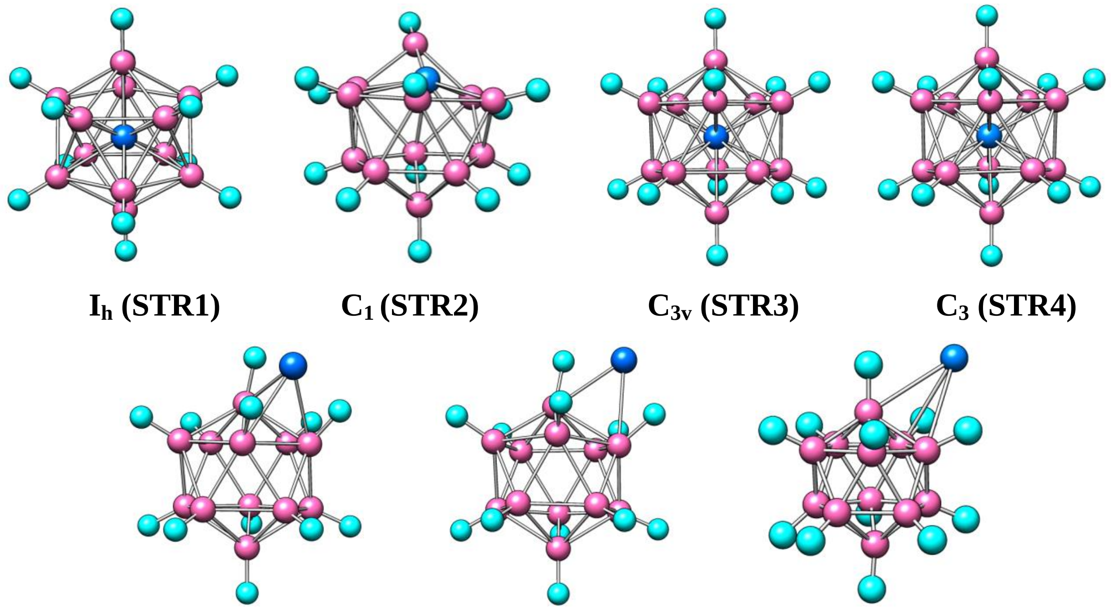

I_h (STR1) **C_1 (STR2)** **C_{3v} (STR3)** **C_3 (STR4)**

C_{3v} (STR5) **C_{2v} (STR6)** **C_1(STR7)**

Figure 5.1: Optimized structures of Ln and An doped $B_{12}H_{12}^{2-}$ and $Al_{12}H_{12}^{2-}$ clusters.

Subsequently, we have studied the exohedral An@$Al_{12}H_{12}^{2-}$ and Ln@$Al_{12}H_{12}^{2-}$ clusters where the Ln or An ion is doped at the outside region of one of the triangular faces of the $Al_{12}H_{12}^{2-}$. In all these clusters, the doped metal ion is coordinated in a tridentate manner with one of the triangular faces of $Al_{12}H_{12}^{2-}$. These exohedral clusters are also optimized in both singlet and septet spin state in C_{3v} (Figure 5.1, STR5) symmetry with the real frequency values. For exohedral clusters also, the septet spin state is found to be more stable (3.4–8.4 eV) than the corresponding singlet spin state as shown in Table 5.1. Moreover, to find out the minimum energy exohedral structure, we have optimized one of the septet spin exohedral clusters without any symmetry constraint using different initial geometries. All the different structures are finally optimized to the structure similar to the C_{3v} symmetry (Figure 5.1, STR5) where the doped metal ion is coordinated in a tridentate manner with one of the triangular faces of $Al_{12}H_{12}^{2-}$.

Table 5.1: Relative Energy (RE, in eV) of Singlet and Septet Spin Endo− and Exo−M@$Al_{12}H_{12}^{2-}$ and Exo−M@$B_{12}H_{12}^{2-}$ Cluster with Respect to Corresponding Septet Spin Exohedral Cluster using B3LYP Functional.

Cluster	**RE (M@$Al_{12}H_{12}^{2-}$)**				**RE (M@$B_{12}H_{12}^{2-}$)**	
	Endo		**Exo**		**Exo**	
	Singlet	**Septet**	**Singlet**	**Septet**	**Singlet**	**Septet**
Np@$E_{12}H_{12}^{-}$	0.86	1.27	3.38	0.00	2.92	0.00
Pu@$E_{12}H_{12}$	2.57	2.27	3.82	0.00	6.37	0.00
Am@$E_{12}H_{12}^{+}$	4.43	2.60	5.39	0.00	5.17	0.00
Pm@$E_{12}H_{12}^{-}$	6.46	2.67	5.34	0.00	5.88	0.00
Sm@$E_{12}H_{12}$	7.52	3.72	5.38	0.00	9.88	0.00
Eu@$E_{12}H_{12}^{+}$	9.72	4.01	8.44	0.00	8.25	0.00

On comparing the stability of endo− and exo− M@$Al_{12}H_{12}^{2-}$ clusters we found that the septet spin exohedral clusters are the most stable clusters as shown in Table 5.1.

Since the exohedral clusters are more stable than the corresponding endohedral clusters, therefore to find the other possible lower energy spin states for these exohedral clusters, we have optimized exohedral Pu^{2+} and Sm^{2+} doped $Al_{12}H_{12}^{2-}$ clusters in the other remaining spin states (triplet and quintet) in C_{3v} symmetry. Both the triplet and quintet spin states of Pu@$Al_{12}H_{12}$ and Sm@$Al_{12}H_{12}$ clusters are found to be energetically less stable (by 1.4–4.6 eV) as compared to the corresponding septet spin state.

To see the effect of different exchange correlation (XC) functionals on the stability of different spin states, we have also optimized exohedral as well as endohedral Pu@$Al_{12}H_{12}$ and Sm@$Al_{12}H_{12}$ clusters in different spin states with and without any symmetry constraint using PBE and M06−2X functionals. Interestingly with all different XC functionals, the septet spin state is found to be the most stable (by 0.8−10.4 eV) state.

Apart from the C_{3v} symmetry, the exohedral $Pu@Al_{12}H_{12}$ and $Sm@Al_{12}H_{12}$ clusters are also optimized in C_{2v} symmetry, where the Pu^{2+} (Sm^{2+}) ion is located at the midpoint of one of the edges of $Al_{12}H_{12}^{2-}$ and coordinated in a bidentate manner with the $Al_{12}H_{12}^{2-}$ as shown in Figure 5.1 (STR6). The optimized C_{2v} symmetry structures of $Pu@Al_{12}H_{12}$ and $Sm@Al_{12}H_{12}$ clusters possess one imaginary frequency in all the studied spin states. Moreover, all the different spin states of the C_{2v} symmetry isomer of these clusters are energetically less stable (0.6−5.9 eV) as compared to the corresponding septet spin state of the C_{3v} symmetry isomer.

5.2.3 Exohedral $M@B_{12}H_{12}^{2-}$ clusters

In $B_{12}H_{12}^{2-}$ cluster, the Ln and An ion is doped at the outside region of one of the triangular faces of the $B_{12}H_{12}^{2-}$. For this, at first, $Pu@B_{12}H_{12}$ and $Sm@B_{12}H_{12}$ clusters are optimized in both C_{3v} (STR5) and C_{2v} (STR 6) symmetry (Figure 5.1) in all the possible spin states viz., singlet, triplet, quintet, and septet. Among all the spin states of C_{3v} isomers, the septet spin isomer is energetically most stable for both the $Pu@B_{12}H_{12}$ (by 2.7–6.4 eV) and $Sm@B_{12}H_{12}$ (by 2.5–9.9 eV) clusters. The $Pu@B_{12}H_{12}$ and $Sm@B_{12}H_{12}$ clusters in C_{3v} symmetry possess all real frequencies; however, the C_{2v} symmetry isomer of $Pu@B_{12}H_{12}$ and $Sm@B_{12}H_{12}$ clusters contains one imaginary frequency value in all the studied spin states. Moreover, C_{2v} symmetry exohedral $Pu@B_{12}H_{12}$ and $Sm@B_{12}H_{12}$ clusters in the different spin states are energetically less stable (by 0.5–5.9 eV) as compared to the corresponding septet spin state of C_{3v} symmetry isomer.

In addition to the B3LYP functional, exohedral $Pu@B_{12}H_{12}$ and $Sm@B_{12}H_{12}$ clusters are optimized with PBE and M06−2X functionals in different spin states with and without any symmetry constraint. With all the different functionals, septet spin cluster is found to be the most stable (by 1.2−7.6 eV) cluster with and without symmetry constraint.

Since septet spin exohedral Pu@$B_{12}H_{12}$ and Sm@$B_{12}H_{12}$ clusters in C_{3v} symmetry are the most stable, the remaining Ln (Pm^{+}, Eu^{3+}) and An (Np^{+}, Am^{3+}) doped $B_{12}H_{12}^{2-}$ clusters are optimized in septet spin state. However, for the comparison purpose, all the clusters are also optimized in the lowest singlet spin state. All Ln and An doped $B_{12}H_{12}^{2-}$ clusters in singlet and septet spin states are optimized in C_{3v} symmetry, except for the Am^{3+} and Eu^{3+} doped $B_{12}H_{12}^{2-}$ clusters. The Am^{3+} and Eu^{3+} doped $B_{12}H_{12}^{2-}$ clusters are optimized in C_1 symmetry (Figure 5.1, STR7) with real frequency values in both the singlet and septet spin states. It is to be noted that all the exohedral An@$B_{12}H_{12}^{2-}$ (An = Np^{+}, Pu^{2+}, Am^{3+}) and Ln@$B_{12}H_{12}^{2-}$ (Ln = Pm^{+}, Sm^{2+}, Eu^{3+}) clusters in septet spin state are more stable (by 2.9–9.9 eV) than that in the corresponding singlet spin state as shown in Table 5.1.

5.2.4 Structural parameters in septet spin state

Since the C_{3v} symmetry M@$Al_{12}H_{12}^{2-}$ exohedral clusters in septet spin are the most stable clusters, we have first discussed the geometrical parameters of only these exohedral clusters. The optimized metal–cage bond distance (M–Al) is reported in Table 5.2. It is noteworthy to mention that in the metal−doped clusters, the cage diameter of the $Al_{12}H_{12}^{2-}$ is compressed (from 5.144 to 5.040 Å) along that triangular face where the metal ion is doped, whereas the cage diameter is elongated (from 5.144 to 5.271 Å) along the remaining triangular faces. The compression and elongation of the cage diameter of $Al_{12}H_{12}^{2-}$ is increased along the An = Np^{+} − Pu^{2+} − Am^{3+} and Ln = Pm^{+} − Sm^{2+}− Eu^{3+} series in the case of An@$Al_{12}H_{12}^{2-}$ and Ln@$Al_{12}H_{12}^{2-}$ clusters, respectively. Furthermore, Pu^{2+} and Sm^{2+} form the strongest bonding (metal–Al bond length of 3.070 and 3.106 Å, respectively) with the Al atoms of the triangular face followed by a stronger bonding of Am^{3+} (Eu^{3+}) and Np^{+} (Pm^{+}) ions, respectively, in An (Ln) doped $Al_{12}H_{12}^{2-}$ clusters.

Table 5.2: Calculated Bond Length Values ($R_{(M-Al/B)}$, in Å), BSSE Corrected Binding Energy (BE, in eV), HOMO−LUMO Energy Gap (ΔE_{Gap}, in eV), NPA Charge on Doped ion (q_M, in e), Total Spin Population (N_S) and $<S^2>$ value of Septet Spin Exohedral $An@E_{12}H_{12}^{2-}$ and $Ln@E_{12}H_{12}^{2-}$ (E = Al, B) Clusters using B3LYP Functional.

Cluster	**Sym**	**$R_{(M-Al/B)}$**	**q_M**	**N_S**	**ΔE_{Gap}**	**BE**	**$<S^2>$**
$Al_{12}H_{12}^{2-}$	I_h	...	...	...	3.70	...	...
$Np@Al_{12}H_{12}^{-}$	C_{3v}	3.230	0.64	5.93	1.53	−7.18	12.01
$Pu@Al_{12}H_{12}$	C_{3v}	3.070	1.20	6.17	2.21	−16.77	12.02
$Am@Al_{12}H_{12}^{+}$	C_{3v}	3.130	1.41	7.11	1.15	−33.60	13.03
$Pm@Al_{12}H_{12}^{-}$	C_{3v}	3.340	0.78	5.94	1.44	−7.00	12.01
$Sm@Al_{12}H_{12}$	C_{3v}	3.106	1.37	6.12	2.50	−16.32	12.01
$Eu@Al_{12}H_{12}^{+}$	C_{3v}	3.159	1.51	7.15	1.19	−35.42	13.02
$B_{12}H_{12}^{2-}$	I_h	...	...	...	6.57	...	...
$Np@B_{12}H_{12}^{-}$	C_{3v}	2.826	0.82	5.98	1.24	−8.53	12.00
$Pu@B_{12}H_{12}$	C_{3v}	2.636	1.60	6.11	2.08	−17.80	12.01
$Am@B_{12}H_{12}^{+}$	C_1	2.705	1.77	7.08	1.67	−33.11	13.01
$Pm@B_{12}H_{12}^{-}$	C_{3v}	2.838	0.86	5.98	1.56	−8.39	12.00
$Sm@B_{12}H_{12}$	C_{3v}	2.646	1.65	6.10	3.28	−17.48	12.01
$Eu@B_{12}H_{12}^{+}$	C_1	2.707	1.78	7.07	2.08	−35.10	13.00

Similarly we have discussed the structural parameters of the most stable C_{3v} symmetry $M@B_{12}H_{12}^{2-}$ (M = Np^{+}, Pu^{2+}, Pm^{+}, Sm^{2+}) and C_1 symmetry $M@B_{12}H_{12}^{2-}$ (M = Am^{3+}, Eu^{3+}) septet spin exohedral clusters and corresponding values are reported in Table 5.2. In septet spin exohedral $An@B_{12}H_{12}^{2-}$ (An = Np^{+}, Pu^{2+}, Am^{3+}) and $Ln@B_{12}H_{12}^{2-}$ (Ln = Pm^{+}, Sm^{2+}, Eu^{3+}) clusters, the Pu^{2+} and Sm^{2+} form the strongest bonding (metal–B bond length of 2.636 and 2.646 Å, respectively) with the B atoms present at the triangular face of the $B_{12}H_{12}^{2-}$ cluster followed by stronger bonding of Am^{3+} (Eu^{3+}) and Np^{+} (Pm^{+}) ions, in An (Ln) doped $B_{12}H_{12}^{2-}$ clusters (Table 5.2).

5.2.5 Binding energy estimation

The binding energy (BE) of the clusters is calculated by using the following equations (5.1) and (5.2),

$$M^{n+} + E_{12}H_{12}^{2-} \longrightarrow [M@E_{12}H_{12}]^{n-2} \tag{5.1}$$

$$BE = E([M@E_{12}H_{12}]^{n-2}) - E(M^{n+}) - E(E_{12}H_{12}^{2-}) \tag{5.2}$$

where, M^{n+} = Ln (Pm^{+}, Sm^{2+}, Eu^{3+}) and An (Np^{+}, Pu^{2+}, Am^{3+}), n = +1, +2, +3, respectively, and E = B and Al.

The basis set superposition error (BSSE) has been calculated using the Counterpoise (CP) method[232]. The BSSE is calculated to be in the range of 0.01–0.08 eV for exohedral clusters, whereas for endohedral clusters, the BSSE is around 0.09–0.11 eV that has been added in the B3LYP calculated BE of the exohedral and endohedral clusters and the corresponding values are reported in Tables 5.2 and 5.3. The negative BE of all the exohedral $M@Al_{12}H_{12}^{2-}$ and $M@B_{12}H_{12}^{2-}$ clusters (Table 5.2) clearly indicates high stability of these clusters. It is to be noted that the binding energy of the exohedral clusters increases along the An = $Np^{+} - Pu^{2+} - Am^{3+}$ and Ln = $Pm^{+} - Sm^{2+} - Eu^{3+}$ series in the case of An and Ln doped $Al_{12}H_{12}^{2-}$ and $B_{12}H_{12}^{2-}$ clusters as reported in Table 5.2. Such a significant increase in the binding energy (∼−7 to −35 eV) is observed due to the increase in the charge of doped An (Ln) ion from +1 to +3. However, a very small change has been observed in the binding energy with the change of the cage type from $Al_{12}H_{12}^{2-}$ to $B_{12}H_{12}^{2-}$. Continuous increase in the binding energy value of $An@E_{12}H_{12}^{2-}$ and $Ln@E_{12}H_{12}^{2-}$ (E = B, Al) clusters along the An = $Np^{+} - Pu^{2+} - Am^{3+}$ and Ln = $Pm^{+} - Sm^{2+} - Eu^{3+}$ series, shows the highest stability of Am^{3+} and Eu^{3+} doped $Al_{12}H_{12}^{2-}$ and $B_{12}H_{12}^{2-}$ clusters as compared to the remaining actinide and lanthanide ion doped clusters. Similar BE trend is observed along iso-electronic series of Ln/An doped $Al_{12}H_{12}^{2-}$ and $B_{12}H_{12}^{2-}$ clusters using PBE (BE = −8 to −36 eV) and M06−2X (−8 to −36 eV) functionals as we have discussed above with the B3LYP XC functional.

Table 5.3: Optimized Bond Lengths ($R_{(M-Al)}$, in Å), BSSE Corrected Binding Energy (BE, in eV), HOMO−LUMO Energy Gap (ΔE_{Gap}, in eV), Total Spin Population (N_S) and f−Population (nf) of An/Ln in Septet Spin Endohedral $M@Al_{12}H_{12}^{2-}$ Clusters using B3LYP Functional.

Cluster	**Sym**	**$R_{(M-Al)}$**	**N_S**	**nf**	**ΔE_{Gap}**	**BE**
$Al_{12}H_{12}^{2-}$	I_h	...	...		3.70	...
$Np@Al_{12}H_{12}^{-}$	C_1	2.846	5.02	4.03	1.20	−5.88
$Pu@Al_{12}H_{12}$	C_{3v}	2.782	5.72	5.47	2.04	−14.42
$Am@Al_{12}H_{12}^{+}$	C_3	2.789	6.48	6.15	1.53	−30.87
$Pm@Al_{12}H_{12}^{-}$	C_1	2.899	4.96	4.24	1.34	−4.28
$Sm@Al_{12}H_{12}$	C_{3v}	2.781	6.03	5.79	2.91	−12.52
$Eu@Al_{12}H_{12}^{+}$	C_3	2.798	6.95	6.60	1.41	−31.33

It is important to note here that the BE of the endohedral $M@Al_{12}H_{12}^{2-}$ clusters in the septet spin state is also negative and significantly large (−4.28 to −31.33 eV) as shown in Table 5.3, which represents high stability of these endohedral clusters. The binding energy values of all the endohedral clusters are comparatively lower (by ~2–4 eV) than that of the corresponding exohedral clusters. Nevertheless, the significantly high negative binding energy values indicate the possibility of formation of both endohedral and exohedral metal doped $Al_{12}H_{12}^{2-}$ clusters, though the formation of exohedral clusters is energetically more favourable.

5.2.6 Molecular orbital analysis

In order to explore the chemical stability of the $M@Al_{12}H_{12}^{2-}$ and $M@B_{12}H_{12}^{2-}$ clusters, we have calculated the HOMO – LUMO energy gap for the septet spin clusters (Table 5.2−5.3). For these open-shell systems, the highest energy occupied orbital is considered as HOMO (the singly occupied molecular orbital (SOMO) in our case) independent of the spin of the occupied electron and lower energy orbital among up spin LUMO and down spin LUMO is considered as LUMO. The energy difference between them is defined as the HOMO–LUMO energy gap in the present work. The HOMO–LUMO energy gap increases along An = $Np^+ < Am^{3+} < Pu^{2+}$ (1.24 to 2.08 eV) and Ln = $Pm^+ < Eu^{3+} < Sm^{2+}$ (1.56 to 3.28 eV) ion in the $An@B_{12}H_{12}^{2-}$ and $Ln@B_{12}H_{12}^{2-}$ clusters (Table 5.2). Similar HOMO–LUMO energy gap trend is observed in the endohedral $An@Al_{12}H_{12}^{2-}$ and $Ln@Al_{12}H_{12}^{2-}$ clusters in septet spin state (Table 5.3). However, in case of exohedral metal doped−$Al_{12}H_{12}^{2-}$ clusters, the HOMO–LUMO gap increases along An = $Am^{3+} < Np^+ < Pu^{2+}$ (1.15 to 2.21) and Ln = $Eu^{3+} < Pm^+ < Sm^{2+}$ (1.19 to 2.50 eV) ion doped $An@Al_{12}H_{12}^{2-}$ and $Ln@Al_{12}H_{12}^{2-}$ clusters (Table 5.2). In both the $M@Al_{12}H_{12}^{2-}$ and $M@B_{12}H_{12}^{2-}$ clusters, the HOMO–LUMO gap is the largest for the Pu^{2+} (Sm^{2+}) doped clusters. The reversal in the HOMO–LUMO energy gap trend for (Np^+, Am^{3+}) and (Eu^{3+}, Pm^+) ion pairs in exohedral $M@Al_{12}H_{12}^{2-}$ and $M@B_{12}H_{12}^{2-}$ clusters is due to the break of symmetry in $Am@B_{12}H_{12}^{+}$ and $Eu@B_{12}H_{12}^{+}$ clusters (symmetry C_1), whereas no symmetry break is observed in the corresponding $Am@Al_{12}H_{12}^{+}$ and $Eu@Al_{12}H_{12}^{+}$ clusters (symmetry C_{3v}). The sufficiently large HOMO–LUMO energy gap clearly represents the high chemical stability of these Ln and An doped clusters.

The molecular orbital energy level diagram of the empty $Al_{12}H_{12}^{2-}$ and endohedral metal−doped clusters, namely, $Pu@Al_{12}H_{12}$ and $Sm@Al_{12}H_{12}$ at the B3LYP/DEF level is shown in Figure 5.2. The HOMO of $Al_{12}H_{12}^{2-}$ cage is scaled with respect to the HOMO of the Pu@$Al_{12}H_{12}$ cluster. In the empty cage, there are a total of 50 valence electrons in the $2g_u$ (HOMO), $6h_g$, $6t_{1u}$, $5a_g$, $4t_{2u}$, $5h_g$, $5t_{1u}$ and $4a_g$ molecular orbitals (MOs). However, in the metal−doped Pu@$Al_{12}H_{12}$ cluster, six electrons are further added in the cage from the metal (f^6) ion. Therefore, in the metal−doped cluster, the electron count in the cage is 56.

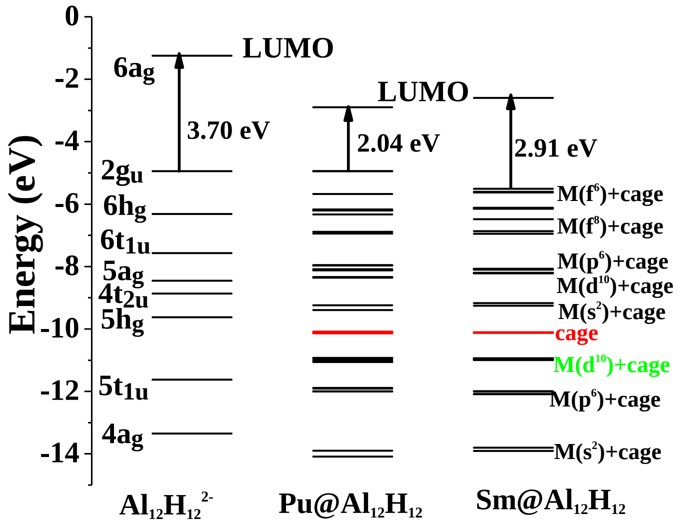

Figure 5.2: MO energy level diagram of $Al_{12}H_{12}^{2-}$ and endohedral M@$Al_{12}H_{12}^{2-}$ (M = Pu^{2+} and Sm^{2+}) clusters using B3LYP functional.

MOs pictures of Pu@$Al_{12}H_{12}$ cluster with occupation of each MOs (reported within parenthesis) is depicted in Figure 5.3 and the symmetrized fragment orbitals (SFOs) analysis obtained at the PBE/TZ2P (Table 5.4) level using the scalar relativistic ZORA approach reveal that the mixing of doped metal ion and the cage orbitals is significant for the 34e (HOMO), $6a_2$, $30a_1$, 33e, $29a_1$, $5a_2$, 32e, 31e, $28a_1$, $27a_1$, 30e, 29e and $26a_1$ MOs. Cumulatively, all these MOs account for 32 outer valence electrons. It is to be noted that among all these MOs, the initial four MOs, namely, 34e, $6a_2$, $30a_1$, 33e are SOMOs containing six unpaired electrons, while the remaining MOs are doubly occupied orbitals. The next two MOs, namely, $25a_1$ and 28e containing a total of six electrons, can be attributed to pure cage orbitals. Subsequent three MOs, $24a_1$, 27e and 26e containing ten electrons are mostly contributed by the cage atoms with virtually negligible share from the dopant metal atom. Contributions from both cage and dopant atoms are found for the next three inner MOs ($23a_1$, 25e and $22a_1$), which contain another eight electrons. After all these analysis, it may be inferred that the $Pu@Al_{12}H_{12}$ cluster contains 32 valence electrons corresponding to the metal-cage hybrid orbitals, and thus satisfies the 32−electron principle through attainment of $ns^2np^6(n-1)d^{10}(n-2)f^{14}$ electronic configuration around the central actinide atom (Pu).

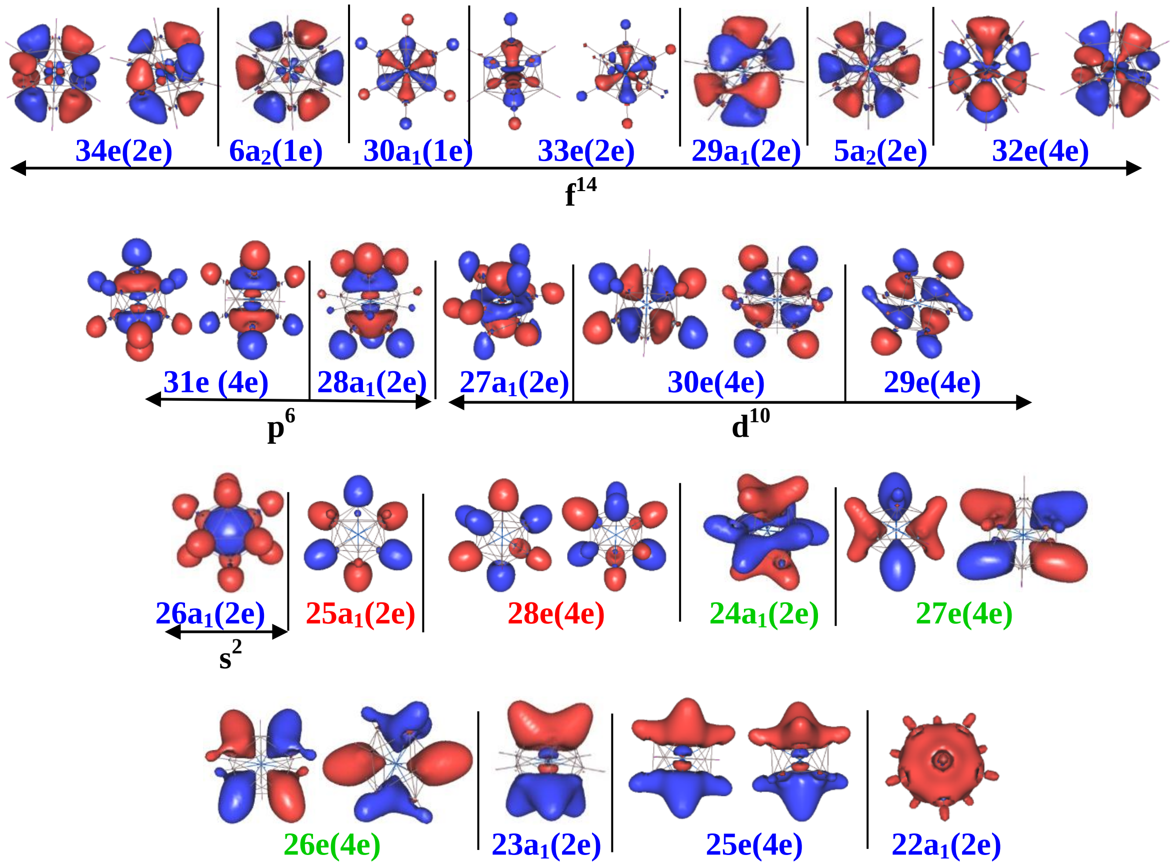

Figure 5.3: MO pictures of endohedral $Pu@Al_{12}H_{12}$ cluster using B3LYP functional. Here, Blue text represents MOs with metal−cage orbital overlap, red text represent pure cage atoms MOs, green text represent MOs with negligible metal−cage orbital mixing. Occupation of each MOs is reported within parenthesis.

Table 5.4. Symmetrized Fragment Orbitals (SFOs) Analysis and Irreducible representation (IRR) of MOs of Septet Spin Endohedral Pu@$Al_{12}H_{12}$ Cluster in D_{3d} Symmetry with PBE/TZ2P Method using ADF Software. The Corresponding IRR of MOs of Pu@$Al_{12}H_{12}$ Cluster in C_{3v} Symmetry Obtained using Turbomole software is also Reported.

IRR_SR[a]	**IRR_RECP**[b]	**Occu**[c]	**Energy (eV)**	**MO (%) metal/cage**
$10A_{1.g}$	$22a_1$	2.0	-12.9	66.6% Pu(s) + 33.0% Cage
$11E_{1.u}$:1	25e:1	2.0	-11.0	7.5% Pu(p) + 92.0% cage
$11E_{1.u}$:2	25e:2	2.0	-11.0	7.5% Pu(p) + 92.0% cage
$9A_{2.u}$	$23a_1$	2.0	-11.0	8.5% Pu(p) + 91.5% cage
$11E_{1.g}$:1	26e:1	2.0	-10.1	12.5% Pu(d_{yz}) + 87.5% cage
$11E_{1.g}$:2	26e:2	2.0	-10.1	12.5% Pu(d_{xz}) + 87.5% cage
$12E_{1.g}$:1	27e:1	2.0	-10.1	45.5% Pu(dx^2-y^2) + 54.5% cage
$12E_{1.g}$:2	27e:2	2.0	-10.1	45.5% Pu(d_{xy}) + 54.5% cage
$11A_{1.g}$	$24a_1$	2.0	-10.1	45.8% Pu(d_z^2) +54.3% cage
$12E_{1.u}$:1	28e:1	2.0	-9.2	100% cage
$12E_{1.u}$:2	28e:2	2.0	-9.2	100% cage
$10A_{2.u}$	$25a_1$	2.0	-9.1	100% cage
$12A_{1.g}$	$26a_1$	2.0	-8.5	22.0% Pu(s) +78.0% Cage
$13E_{1.g}$:1	29e:1	2.0	-7.6	18.5% Pu (d_{yz}) +81.5% Cage
$13E_{1.g}$:2	29e:2	2.0	-7.6	18.5% Pu (d_{xz}) +81.5% Cage
$13A_{1.g}$	$27a_1$	2.0	-7.6	20.0% Pu (d_z^2) + 80.0% cage
$14E_{1.g}$:1	30e:1	2.0	-7.6	18.3% Pu(dx^2-y^2) + 81.7% cage
$14E_{1.g}$:2	30e:2	2.0	-7.6	18.3% Pu(d_{xy}) + 81.7% cage
$11A_{2.u}$	$28a_1$	2.0	-7.3	14.0% Pu(p_z) + 85.9% cage
$13E_{1.u}$:1	31e:1	2.0	-7.3	13.5% Pu(p_x) + 86.5% cage
$13E_{1.u}$:2	31e:2	2.0	-7.3	13.5% Pu(p_y) + 86.5% cage
$14E_{1.u}$:1	32e:1	2.0	-6.2	24.6% Pu(f) + 75.4% cage
$14E_{1.u}$:2	32e:2	2.0	-6.2	24.6% Pu(f) + 75.4% cage
$3A_{1.u}$	$5a_2$	2.0	-6.2	24.3% Pu(f) + 75.7% cage
$12A_{2.u}$	$29a_1$	2.0	-6.1	24.3% Pu(f) + 75.7% cage
$15E_{1.u}$:1	33e:1	1.0	-5.2	75.1% Pu(f) + 24.9% cage
$15E_{1.u}$:2	33e:2	1.0	-5.2	75.1% Pu(f) + 24.9% cage
$13A_{2.u}$	$30a_1$	1.0	-5.0	70.9% Pu(f) + 29.1% cage
$16E_{1.u}$:1	34e:1	1.0	-4.0	72.0% Pu(f) + 28.0% cage
$16E_{1.u}$:2	34e:2	1.0	-4.0	72.0% Pu(f) + 28.0% cage
$4A_{1.u}$	$6a_2$	1.0	-3.9	74.1% Pu(f) + 25.9% cage-HOMO
$14A_{2.u}$	$31a_1$	0.0	-3.9	73.3% Pu(f) + 26.7% cage-LUMO

[a] IRR_SR= IRR using scalar relativistic ZORA approach with 60 electron frozen core for Pu using ADF

[b] IRR_ECP= Irreducible representation of molecular orbitals with 60 electron core ECP for Pu using Turbomole.

[c] Occu = Occupation of MO

However, consideration of inner valence electrons contained in the MOs, $23a_1$, 25e, and $22a_1$ leads to a total valence electron count of 40−electrons around the central actinide ion, which is also a magic number. Here, it is important to note that the energy gap between the set of metal−cage hybridized orbitals containing 32 electrons and the second set containing the inner 8 electrons (inner s and p orbitals) accommodated in the hybridized orbitals, $23a_1$, 25e, and $22a_1$ is quite large (~2–2.7 eV). Accordingly, the 32−electron principle is reasonably fulfilled as far as the outer valence electrons are concerned. A similar bonding is observed in the $Sm@Al_{12}H_{12}$ cluster. Moreover, 32−electron count corresponding to outer valence electrons is also found for the Am and Eu ions in the $Am@Al_{12}H_{12}^+$ and $Eu@Al_{12}H_{12}^+$ clusters.

5.2.7 Spin population and $\langle S^2 \rangle$ expectation value

It is interesting to note that the spin population as well as f−population on An and Ln ions is not significantly changed in the septet spin $M@Al_{12}H_{12}^{2-}$ and $M@B_{12}H_{12}^{2-}$ clusters (Tables 5.2–5.3). In these clusters the nf populations in Am^{3+} and Eu^{3+} ions are close to 7, which is a stable half−filled electronic configuration, whereas in the case of Pu^{2+} and Sm^{2+}, the nf populations are 6 which is equal to their atomic spins. Only in the case of Np^+ and Pm^+, the spin population of doped metal ions is partially quenched as shown in Table 5.3.

In addition, from the spin density surface pictures it can be seen that the all the spin density is localized on the doped Ln and An ions (Figure 5.4) which indicates that the Ln and An ion carry all the spin. The high spin population on doped metal ions in the metal−doped clusters favour the magnetic behaviour of the studied $M@Al_{12}H_{12}^{2-}$ and $M@B_{12}H_{12}^{2-}$ clusters. It is noteworthy to mention that for all the studied exohedral clusters, the expectation value of $\langle S^2 \rangle$ (~12.0) is found to be very close to the corresponding theoretical value [$S(S + 1) = 12$] for the septet spin state. Whereas, in the case of Am^{3+} and Eu^{3+} doped clusters, the expectation value of 〈S^2〉 (~13) differs from the theoretical value of 12 for the septet spin state as shown in Table 5.2. This deviation is observed due to the achievement of f^7 configuration of the metal ion (Am/Eu) in the doped clusters as observed from the f population of the metal ions. The 〈S^2〉 value of 12 or 13 and localized spin density on the Ln and An ion can favour a high magnetic moment for these metal−doped clusters. Therefore, all the predicted clusters can show magnetic behaviour. The same has been observed for the corresponding endohedral metal−doped clusters.

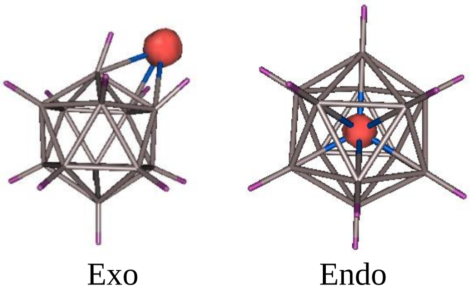

Figure 5.4: Spin density pictures of septet spin exohedral and endohedral Pu@$Al_{12}H_{12}$ clusters using B3LYP functional.

5.2.8 Natural population analysis

To analyze the nature of bonding between the doped metal ion and the cage atoms, we have performed the charge distribution analysis for all the exohedral M@$Al_{12}H_{12}^{2-}$ and M@$B_{12}H_{12}^{2-}$ clusters using natural population analysis (NPA)[166]. From Table 5.2, one can see that the positive charge of the doped metal ion is reduced significantly from its initial value, which indicates that the charge density of the doped ion is increased, whereas the charge density of the cage atom is decreased. This clearly represents that the charge transfer takes place from the cage to the doped metal ion. Moreover, the magnitude of charge transfer from the cage to the doped ion is increased along the actinide and the lanthanide series, An = $Np^+ - Pu^{2+} - Am^{3+}$ and Ln = $Pm^+ - Sm^{2+} - Eu^{3+}$ in the M@$Al_{12}H_{12}^{2-}$ (M@$B_{12}H_{12}^{2-}$) clusters as shown in Table 5.2, which is found to be in agreement with the stability trend of these clusters. The maximum charge transfer from cage to metal ion (~1.4 e) in the Am^{3+} and Eu^{3+} doped cluster is responsible for the achievement of the f^7 configuration in the doped ion. The charge transfer from the cage to the doped ion is responsible for holding the doped metal ion in these clusters. These results are also found to be in good agreement with the results of Hopkins *et al.*[231] who found a similar kind of charge transfer from the $B_{12}X_{12}^{2-}$ (X = H, F) cage to the doped transition metal using NBO analysis.

5.2.9 Energy barrier for M@$Al_{12}H_{12}$

Since the energy barrier height is an important parameter for finding the inter–conversion ability of one particular isomer to another isomer, we have calculated the energy barrier height for Pu@$Al_{12}H_{12}$ and Sm@$Al_{12}H_{12}$ clusters in septet spin state for them to go from endohedral to exohedral and vice versa. We have plotted the energy barrier height of exohedral and endohedral Pu@$Al_{12}H_{12}$ and Sm@$Al_{12}H_{12}$ clusters as shown in Figure 5.5. Barrier height for endohedral clusters is calculated by moving the Pu (Sm) atom from its equilibrium position (inside the cage) to the outside of the cage through one of the triangular faces of the Pu@$Al_{12}H_{12}$ (Sm@$Al_{12}H_{12}$) clusters. Whereas to calculate the barrier height for exohedral clusters, the Pu (Sm) atom is moved toward the centre of the cage from outside of the cage through one of the triangular faces of Pu@$Al_{12}H_{12}$ (Sm@$Al_{12}H_{12}$) clusters. In both processes, the Pu@$Al_{12}H_{12}$ (Sm@$Al_{12}H_{12}$) cluster achieves the least stable structure when the Pu (Sm) atom is placed on the surface of the triangular face of the Pu@$Al_{12}H_{12}$ (Sm@$Al_{12}H_{12}$) clusters. The energy difference between this least stable structure and the equilibrium structure is considered as the energy barrier height for endohedral and exohedral Pu@$Al_{12}H_{12}$ (Sm@$Al_{12}H_{12}$) clusters. For the endohedral Pu@$Al_{12}H_{12}$ and Sm@$Al_{12}H_{12}$ clusters, the energy required to cross the barrier height to form an exohedral cluster is calculated to be 39.87 and 34.21 eV, respectively. These extremely large barrier height values indicate that the endohedral clusters can remain stable once they are formed. Similarly, for exohedral Pu@$Al_{12}H_{12}$ and Sm@$Al_{12}H_{12}$ clusters, the energy required to cross the barrier height to form an endohedral cluster is 60.00 and 51.56 eV, respectively. It is noteworthy to mention that the barrier height for exohedral clusters is significantly large as compared to that of the corresponding endohedral clusters (by ~17–20 eV). Thus, exohedral clusters require a significantly large amount of energy to cross the barrier height to form endohedral clusters. This trend is consistent with the higher energetic stability of the exohedral isomers.

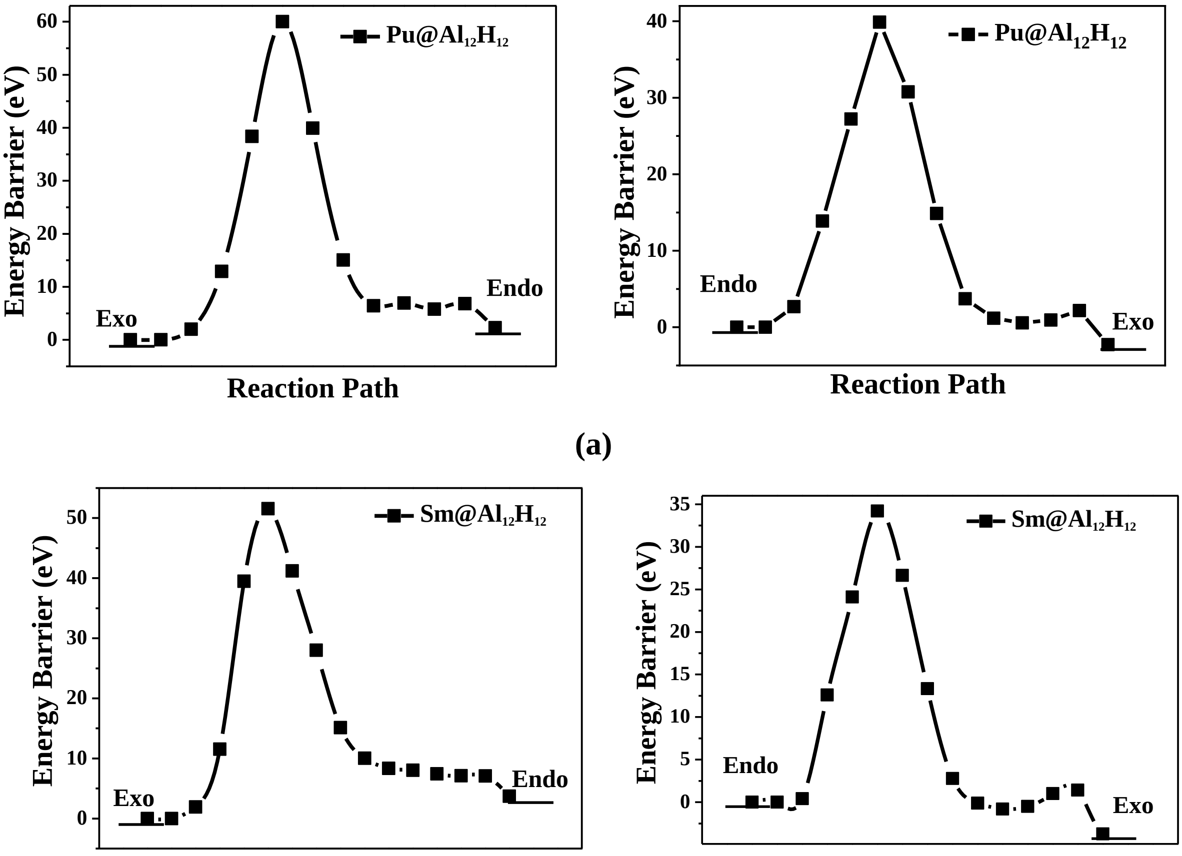

(a)

(b)

Figure 5.5: Energy barrier plots of exohedral and endohedral a) Pu@$Al_{12}H_{12}$ and b) Sm@$Al_{12}H_{12}$ clusters, using B3LYP functional.

5.2.10 Density of states analysis

We have also analyzed the density of states (DOS) plots of the exohedral lanthanide and actinide doped $B_{12}H_{12}^{2-}$ and $Al_{12}H_{12}^{2-}$ clusters in the septet spin state. The DOS plots of all these clusters as well as of the bare $B_{12}H_{12}^{2-}$ and $Al_{12}H_{12}^{2-}$ clusters are provided in Figure 5.6. From Figure 5.6, one can see that the DOS plots of exohedral metal−doped $B_{12}H_{12}^{2-}$ and $Al_{12}H_{12}^{2-}$ clusters are almost the same as those of the corresponding bare $B_{12}H_{12}^{2-}$ and $Al_{12}H_{12}^{2-}$ clusters.

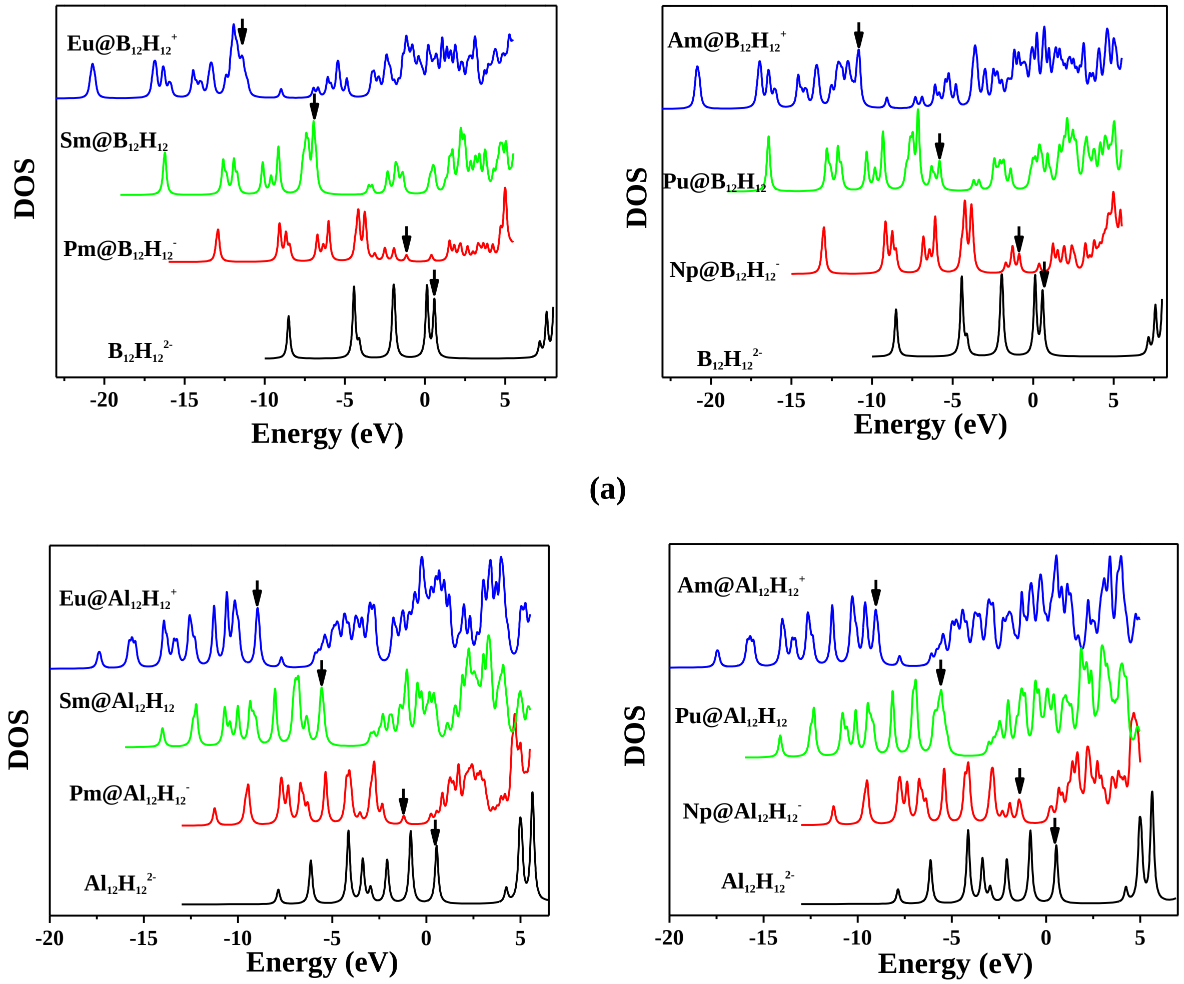

(a)

(b)

Figure 5.6: Density of states (DOS) plots of a) bare $B_{12}H_{12}^{2-}$, exohedral $M@B_{12}H_{12}^{2-}$ and b) bare $Al_{12}H_{12}^{2-}$, exohedral $M@Al_{12}H_{12}^{2-}$, (M = Ln, An) clusters using B3LYP functional.

It is to be noted that the DOS are shifted to much lower energy along Ln = Pm^{+} − Sm^{2+} − Eu^{3+} ion in $Ln@B_{12}H_{12}^{2-}$ and $Ln@Al_{12}H_{12}^{2-}$ clusters. Similarly, in the case of $An@B_{12}H_{12}^{2-}$ and $An@Al_{12}H_{12}^{2-}$ clusters, the DOS are shifted to lower energy along the An = Np^{+} − Pu^{2+} − Am^{3+} series. This energy shift in the DOS bands along the Ln = Pm^{+} − Sm^{2+} − Eu^{3+} and An = Np^{+} − Pu^{2+}− Am^{3+} series is observed due to the increase in the bonding of doped ions with the cage atoms along the two series.

5.2.11 Spin orbit coupling effect

To see the effect of spin orbit coupling, we have optimized the septet spin exohedral $Pu@B_{12}H_{12}$ cluster with spin orbit coupling (SOC) and scalar relativistic (SR) approaches using PBE and B3LYP functionals. The optimized Pu–B distance with (without) SOC is 2.646 (2.654) and 2.576 (2.585) Å using B3LYP and PBE XC functionals, respectively. However, the HOMO–LUMO gaps calculated with (without) SOC is 1.853 (1.900) and 0.014 (0.121) eV using B3LYP and PBE functionals, respectively. The optimized structure is found to be almost the same with and without the SOC. Thus, almost negligible effect of the SOC has been observed on the optimized structure; however the HOMO–LUMO energy gap is decreased by 0.05–0.1 eV due to the SOC. As shown in Figure 5.7, the SOMO to SOMO−5 of the $Pu@B_{12}H_{12}$ exohedral cluster is majorly centered on the Pu(f) orbitals. The SOMO possesses f character in both SOC and SR calculations, however, due to the change in the energy order of SOMOs due to SOC, the ordering of singly occupied f orbitals is different in SOC and SR calculations (Figure 5.7). The energy order of valence SOMO is changed in SOC due to very close lying f energy levels.

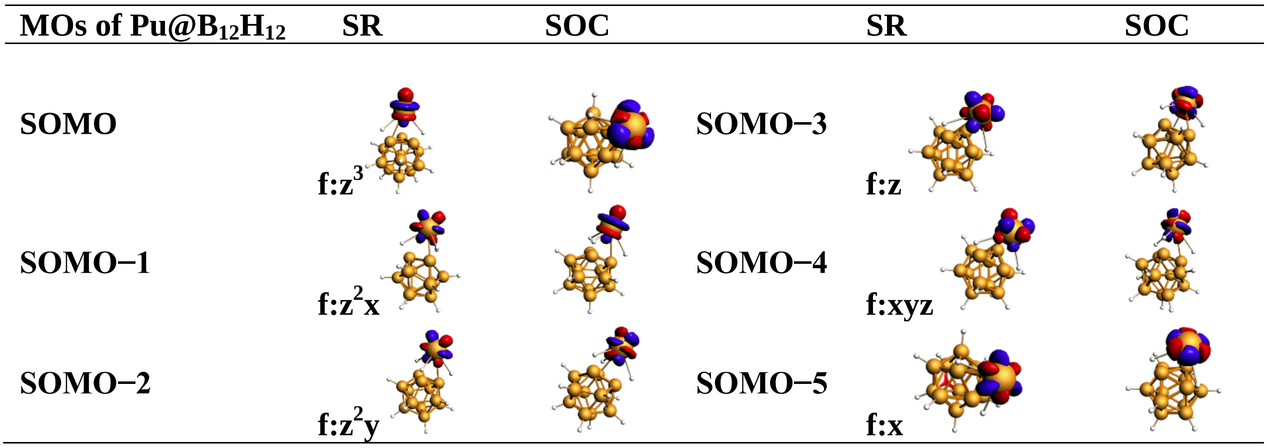

Figure 5.7: MO pictures of valence singly occupied molecular orbitals (SOMOs) of septet spin exohedral Pu@$B_{12}H_{12}$ cluster at B3LYP/TZ2P level.

5.3 Conclusion

In a nutshell, for the first time, we have predicted iso−electronic series of lanthanide (Ln = Pm^+, Sm^{2+}, Eu^{3+}) and actinide (An = Np^+, Pu^{2+}, Am^{3+}) doped exohedral and endohedral $Al_{12}H_{12}^{2-}$ clusters, whereas for $B_{12}H_{12}^{2-}$, only exohedral clusters have been investigated using density functional theory. The stabilities of all Ln and An doped clusters have been analyzed in different possible spin states. Among all the clusters, the exohedral clusters in the septet spin state are energetically the most stable. The sufficiently large HOMO–LUMO energy gap of these clusters reflects their chemically stable behaviour. Moreover, large barrier heights reveal the high kinetic stability of these clusters. All these clusters associated with high spin population on the doped metal ion in septet spin state and having a high HOMO–LUMO gap can be considered as new magnetic superatoms with f−block elements. It is to be noted that the stability of the metal doped Ln@$E_{12}H_{12}^{2-}$ and An@$E_{12}H_{12}^{2-}$ (E = Al, B) clusters increases along the Ln = Pm^+ − Sm^{2+} − Eu^{3+} and An = Np^+ − Pu^{2+} − Am^{3+} series, respectively. Additionally, the magnitude of charge transfer from the cage to the doped ion is also increased along the Ln = Pm^+ − Sm^{2+} − Eu^{3+} and An = Np^+ − Pu^{2+} − Am^{3+} series, for Ln@$E_{12}H_{12}^{2-}$ and An@$E_{12}H_{12}^{2-}$ (E = Al, B) clusters, respectively. Actinide/lanthanide ion encapsulated endohedral $Al_{12}H_{12}^{2-}$ clusters are found to fulfill the 32−electron principle corresponding to the completely filled s, p, d and f shells of the central metal atom. In the present work, we have predicted the existence of new actinide doped clusters following 32−electron principle, which are associated with open-shell electronic configuration. Among all the doped clusters, the Eu^{3+} doped cluster might be difficult to synthesize due to the highly oxidizing nature of Eu^{3+} ion.[233-235] Nevertheless, it might be possible to synthesize some of these Ln/An doped clusters with suitable experimental technique(s). Thus, the theoretical predictions of these stable lanthanide and actinide doped $B_{12}H_{12}^{2-}$ and $Al_{12}H_{12}^{2-}$ clusters could encourage experimentalists for the preparation of these metal−doped clusters.

CHAPTER 6

Neutral Sandwich complexes of Divalent Lanthanide with Novel Nine–Membered Heterocyclic Aromatic Ring: Ln($C_6H_6N_3$)$_2$

6.1 Introduction

In the previous chapters, we have shown the application of lanthanide (Ln) and actinide (An) ions in modifying the structural, electronic, and magnetic properties of clusters by doping them in a cluster. Due to the highly shielded nature of their f–orbitals, the high spin density of Ln/An ion remains unquenched as discussed in Chapter 5. Moreover, under the presence of a suitable crystal field (ligand field), the lanthanide ion with high magnetic moment shows slow magnetic relaxation as discussed in detail in Chapter 1. Therefore, lanthanide ion in the form of their sandwich complexes play a very important role in the creation of single molecule/ion magnet.[48, 89, 91, 236-238] From time to time various cyclic ligands namely benzene, cycloheptariene, cyclooctatetraene and cyclononatetraenyl are proposed for investigating different sandwich complexes.[239-247] Very recently the cyclononatetraene anion ($C_9H_9^-$) ligand has been employed to synthesize divalent lanthanide containing sandwich complexes, Ln(C_9H_9)$_2$ (Ln = Sm(II), Eu(II), Tm(II), Yb(II)).[95] Earlier the same ligand has been used to study the alkaline earth metal sandwich complexes.[94] A very few sandwich complexes with a nine–membered ring have been studied till date, however, five–, six– or eight–membered ring ligands have been widely used to form various sandwich complexes.[94-95, 245-250]

Unlike in the transition metal sandwich complexes, lanthanide ions show larger hapticity in their sandwich complexes. However, the sandwich complexes of lanthanides with a nine–membered ligand are very rare in the literature.[95] Thus, designing a new nine–membered aromatic ring is not only important for the development of novel divalent lanthanide sandwich complexes but also for the creation of magnetic coupling of metal ions along a one−dimensional chain of sandwich complexes via hybridization of the metal ion with extended π orbitals of aromatic ligand. Moreover, inclusion of heteroatoms into a ring skeleton leads to a unique electronic features and also increases the versatility of aromatic rings. For example, fully conjugated heterocyclic ring such as s−triazine, isoelectronic to benzene, and triazine based dendrimers have applications in the drug delivery and agriculture.[251-252] Therefore, various half sandwich transition metal complexes with heterocyclic ligands are synthesized in the past and shown to have biological applications such as anticancer and antibacterial properties.[253-255] Moreover, full sandwich complexes of heterocyclic ligands are also predicted in the recent past.[256-257]

Therefore, in the present chapter we have made an attempt to find a new nine−membered aromatic heterocyclic ring to form a stable novel sandwich complex with a divalent lanthanide ion. For this purpose, we have proposed a nine−membered heterocyclic 1,4,7−triazacyclononatetraenyl, $C_6H_6N_3^-$ (tacn) ligand, which is isoelectronic with the experimentally known cyclononatetraenyl $C_9H_9^-$ (cnt) ligand and associated with 10 π electrons, but possesses three hetero atoms. The electronic and structural analogy of $C_6H_6N_3^-$ with $C_9H_9^-$ ligand makes it attractive for the present study. Furthermore, we have investigated the sandwich complexes of divalent lanthanides with our newly predicted $C_6H_6N_3^-$ ligand, Ln(tacn)$_2$ (Ln = Nd(II), Pm(II), Sm(II), Eu(II), Tm(II) and Yb(II)) using dispersion corrected density functional theory (DFT).

All the results discussed in this chapter have been obtained by using PBE–D3[144, 156-157], PBE0–D3[148, 156-157] and B3LYP−D3[146-147, 156-157] functionals with def–TZVP basis set along with a relativistic effective core potential (RECP) for heavier elements by using Turbomole[150], ADF[152-153] and Multiwfn[170] programs. Detail computational methodologies have been discussed in Chapter 2 of this thesis.

6.2 Results and discussions

6.2.1 Structural and electronic properties of $C_6H_6N_3^-$ ligand

For the formation of cis and trans $C_6H_6N_3^-$ ligand, we have replaced three –CH units in each of the cis and trans isomer of $C_9H_9^-$ (cnt), with N atoms at each alternate position of –CH=CH– units which gives one cis and two different trans isomers (Trans (T) and Trans1 (T1)) as shown in Figure 6.1. In cis form, all the atoms (C, N) forms a regular ring while in the trans form one of the atoms (C or N) of ring lies inside the ring. All the three isomers of $C_6H_6N_3^-$ (tacn) ligand are optimized using PBE−D3 functional and def−TZVP basis set. For $C_6H_6N_3^-$ ligand cis isomer is more stable than the planar Trans (4.1 kcal mol^{-1}) and non−planar Trans1 (7.7 kcal mol^{-1}) isomers. It is to be noted that experimentally cis and only non–planar trans isomers of $C_9H_9^-$ ligand are observed in solution using ^1H NMR spectrum. However, theoretically cis isomer of $C_9H_9^-$ ligand is more stable than the non–planar trans isomer (11 kcal mol^{-1}). In the present study the observed energy difference between cis and trans $C_6H_6N_3^-$ ligand is even smaller (4−7 kcal mol^{-1}), which also indicates the co−existence of both the isomers of the ligand in the solution.[95]

In the gas phase the energy barrier for cis to trans isomerization process is calculated to be 8.4 and 14.0 kcal mol^{-1} for $C_6H_6N_3^-$ and $C_9H_9^-$ ligands, respectively, and hence it may be possible that the inter–conversion of cis– and trans– C_9H_9 anion and the –$C_6H_6N_3^-$ in solvent is kinetically controlled. The high HOMO−LUMO energy gap indicates the stability of $C_9H_9^-$ and $C_6H_6N_3^-$ ligands (Table 6.1). In cis $C_6H_6N_3^-$ all C−C (1.416 Å) and C−N (1.328 Å) bond distances are equal.

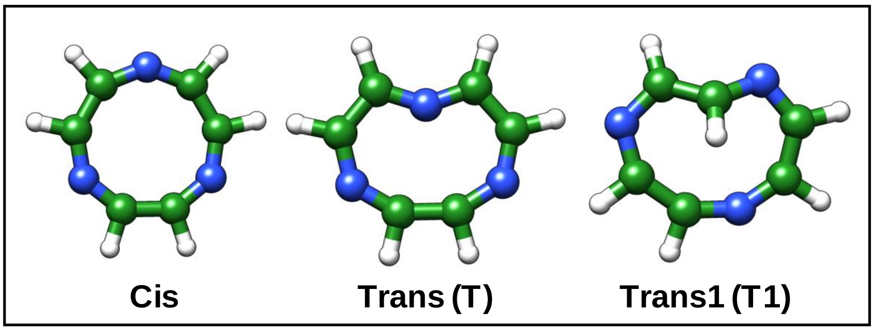

Figure 6.1: Optimized structures of cis and trans isomers of $C_6H_6N_3^-$ ligand.

Table 6.1: Shortest and Longest Bond Lengths (in Å), HOMO−LUMO Energy Gap (ΔE_{Gap}, in eV), HOMA, and NICS(0) (NICS(1)) Values Obtained using PBE–D3 Functional.

Ligand	**$R_{(C-C)}$**	**$R_{(C-N)}$**	**ΔE_{Gap}**	**HOMA**	**NICS**
$C_6H_6N_3^-$−Cis	1.416	1.328	2.675	0.93	−13.13 (−12.13)
$C_6H_6N_3^-$−Trans	1.409 1.453	1.304 1.353	3.186	0.83	...
$C_9H_9^-$−Cis	1.405	...	3.749	0.93	−13.31 (−12.02)
$C_9H_9^-$−Trans	1.389 1.433	...	3.446	0.78	...
$C_9H_9^-$−Cis (expt)	1.352 1.450	...	...	...	...
$C_9H_9^-$−Trans (expt)	1.360 1.450	...	...	...	...

6.2.2 Aromaticity of $C_6H_6N_3^-$ ligand

Aromaticity of the $C_6H_6N_3^-$ ligand is analyzed by using its structural parameters and harmonic oscillator model of aromaticity (HOMA) value. In addition, nucleus−independent chemical shift (NICS) is also calculated at the ring centre [NICS(0)] and at 1Å above the ring centre [NICS(1)]. The structural parameters, NICS and HOMA values are reported in Table 6.1. The negative NICS(0) and NICS(1) (−13.13 and −12.13) values and HOMA value (0.93) close to 1 indicate the aromaticity of cis $C_6H_6N_3^-$ ligand. To analyze the aromaticity of trans ligand HOMA value is calculated instead of NICS, as the trans ligand is not a regular ring. The unequal C−N, C−C bond lengths and relatively a smaller HOMA value of 0.83 for trans $C_6H_6N_3^-$ show a decrease in its aromaticity.

Similar NICS and HOMA values of $C_6H_6N_3^-$ and $C_9H_9^-$ ligands (Table 6.1) indicate almost similar aromaticity of both the ligands. Moreover, Hückel rule of aromaticity is also applied to check the aromaticity of the ligand. Exactly similar delocalized π molecular orbitals contributing 10π e^- shows that cis isomer of both the $C_9H_9^-$ and $C_6H_6N_3^-$ ligands follows the Hückel rule of aromaticity (Figure 6.2).

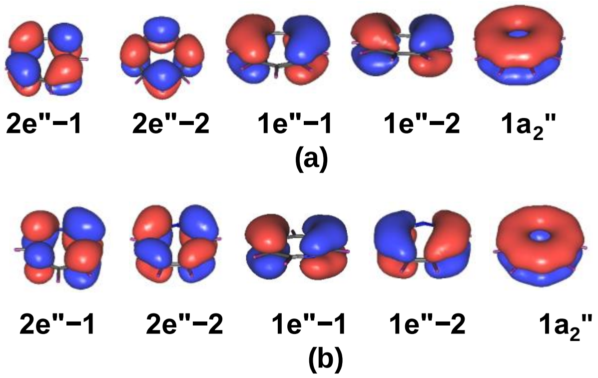

Figure 6.2: Delocalized π molecular orbital pictures of a) $C_9H_9^-$ and b) $C_6H_6N_3^-$ ligands.

6.2.3 Structural properties of $Ln(C_6H_6N_3)_2$ complexes

First of all we have optimized the experimentally observed[95] Ln(cnt−cis)$_2$, Ln(cnt−trans)$_2$ and Ln(cnt−cis)(cnt−trans) (Ln = Sm(II), Eu(II), Tm(II), Yb(II)) complexes represented as Ln(cnt−CC), Ln(cnt−TT) and Ln(cnt−CT), respectively, using PBE−D3, B3LYP−D3 and PBE0−D3 functionals. Among all the complexes, the Ln(cnt−CC) complexes are the most stable as shown in Figure 6.3.

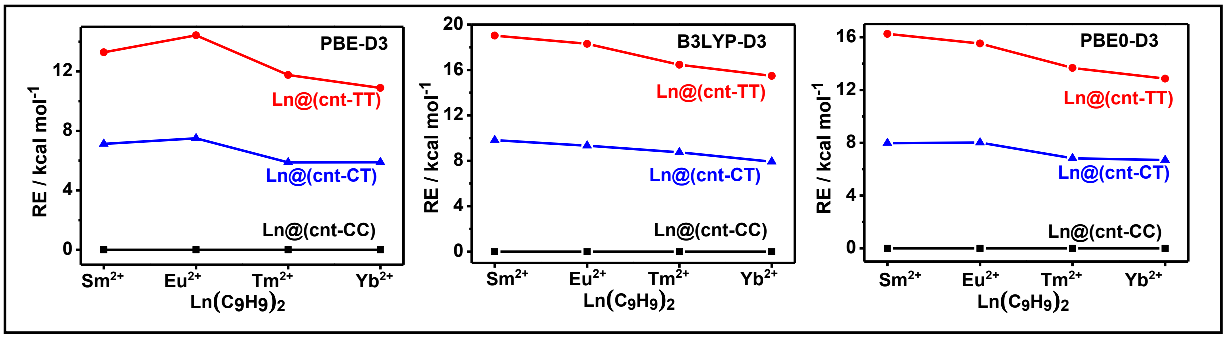

Figure 6.3: Relative energy (RE, in kcal mol^{-1}) plots of Ln(cnt−TT) and Ln(cnt−CT) complexes with respect to corresponding Ln(cnt−CC) complexes.

However, experimentally the mixture of all the three different complexes in the solution has been observed in the ^{1}H NMR spectra.[95] For the Ln(cnt)$_2$ complexes, the optimized bond lengths calculated using the PBE−D3 method are found to be in good agreement with the experimentally observed[95] values (Figure 6.4) as compared to the B3LYP−D3 and PBE0−D3 functionals.

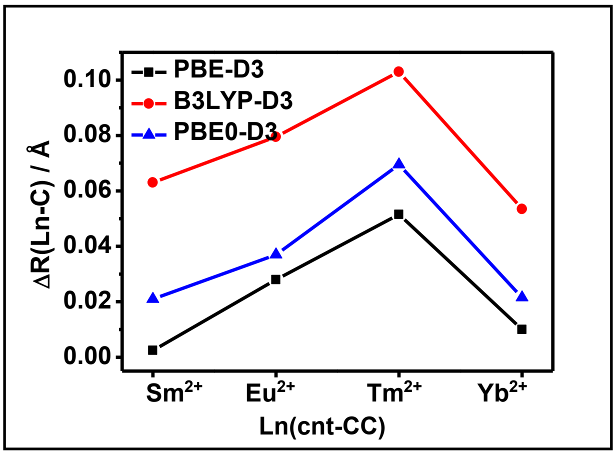

Figure 6.4: Difference between the experimental and the computed Ln–C bond lengths values (ΔR(Ln–C), in Å) in Ln(cnt−CC) complexes.

After finding a close similarity in the PBE−D3/def−TZVP and the experimental results for the $C_9H_9^-$ complexes, we have optimized the sandwich complexes of divalent Ln with cis–$C_6H_6N_3^-$ and trans–$C_6H_6N_3^-$ (tacn) ligands, viz., Ln(tacn−CC), Ln(tacn−TT) and

Ln(tacn−CT) (Figure 6.5) using the PBE−D3/def−TZVP method. Moreover, for comparison purpose, all calculations are also performed with B3LYP−D3 and PBE0–D3 functionals. The PBE–D3 results have been discussed throughout this chapter unless otherwise stated.

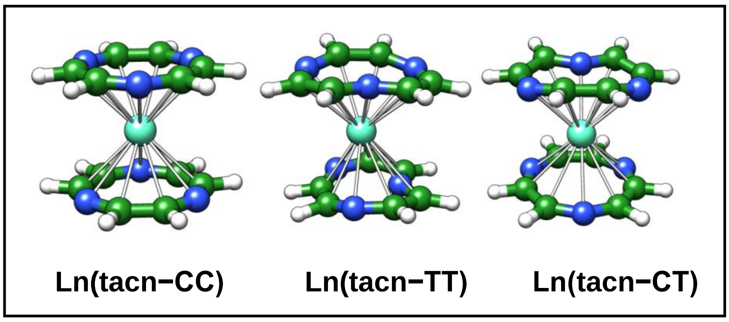

Figure 6.5: Optimized structures of staggered Ln(tacn)$_2$ complexes.

It is to be noted that non−planar $C_6H_6N_3^-$ Trans1 (T1) ligand, iso−structural with trans−$C_9H_9^-$ ligand forms less stable Ln(tacn−T1T1) and Ln(tacn−CT1) complexes (by 4 kcal mol^{-1}) as compared to the corresponding Ln(tacn−CC) complexes which is in agreement with the stability trend of the experimentally observed Ln(cnt)$_2$ complexes[95] (Figure 6.3). However, the planar $C_6H_6N_3^-$ Trans (T) ligand forms more stable Ln(tacn−TT) complexes than the corresponding Ln(tacn−CT) (8.1−11.4 kcal mol^{-1}) and Ln(tacn−CC) (17.2−20.7 kcal mol^{-1}) complexes as shown in Figure 6.6. Thus among all the complexes, Ln(tacn−TT) complexes are the most stable. In the present study we have mainly focused on the Ln(tacn−TT), Ln(tacn−CT) and Ln(tacn−CC) complexes.

All the studied Ln(tacn−CC) complexes are more stable in their staggered conformation (0.1−3.0 kcal mol^{-1}) as compared to the corresponding eclipsed conformation. Similarly for the Ln(tacn−TT) complexes, the staggered isomer is more stable (1.6−2.3 kcal mol^{-1}) than the corresponding eclipsed isomer. Same trend is observed for the Ln(tacn−CT) complexes. Therefore, in the current chapter we have discussed only staggered Ln(tacn−CC), Ln(tacn−CT) and Ln(tacn−TT) complexes (Figure 6.5).

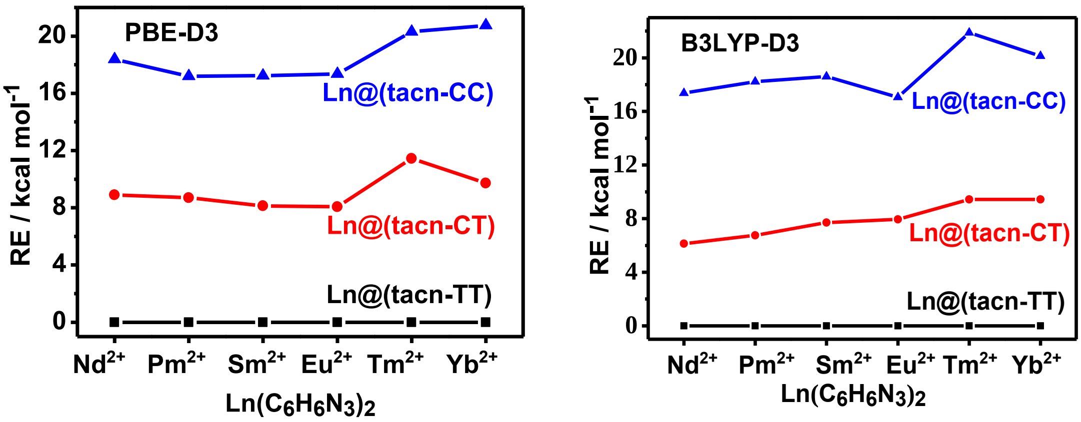

Figure 6.6: Relative energy (RE, in kcal mol^{-1}) plots of Ln(tacn−CC) and Ln(tacn−CT) complexes with respect to the corresponding Ln(tacn−TT) complexes.

The Ln(tacn−CC) complexes contain two η^9−coordinated ligands in linear sandwich arrangement with 180° centroid−Ln−centroid angle similar to that of the experimentally synthesized Ln(cnt−CC)[95] complexes. All the divalent lanthanides form iso−structural linear sandwich complexes. Among all the ions Tm(II) and Yb(II) forms strongest bonding with $C_6H_6N_3^-$ ligand with Ln−C and Ln−N bond distances in the range of 2.72−2.73 Å and 2.68−2.70 Å, respectively, while Eu(II) forms weakest Ln−C (2.83 Å) and Ln−N (2.81 Å) bonds (Table 6.2). However, it is interesting to note that the C−C (1.42 Å) and C−N (1.33 Å) bond distances are almost the same in all the lanthanide complexes.

Unlike in the linear Ln(tacn−CC) complexes, the centroid−Ln−centroid angle in Ln(tacn−TT) complexes is in the range of 162−167°. Here also Tm(II) and Yb(II) ions form strongest bonding (Ln−C = 2.61−2.97, Ln−C$_{avg}$ = 2.82 Å, Ln−N = 2.38−2.71, Ln−N$_{avg}$ = 2.59 Å) with the trans−ligands, while Eu(II) forms weakest Ln−C and Ln−N bonds (Ln−C$_{avg}$ =2.94 and Ln−N$_{avg}$ = 2.74). The C−C (1.41−1.45 Å) and C−N (1.32−1.36 Å) bond distances are almost the same in all the Ln(tacn−TT) complexes. It is to be noted that all the three N atoms of the cis−tacn ligand form almost equally strong bond with the Ln ion and same is observed with six carbon atoms, as all the N and C atoms are in the same chemical environment. Whereas in the trans-tacn ligand, the N atom which lie inside the tacn ring forms more strong bond with the Ln ion (by 0.28−0.33Å) as compared to the bond formed by the remaining two N atoms. Also the two C−C units directly connected with this inside ring N atom of trans ligand form significantly weaker bond with Ln ion (by 0.20−0.35, Å) as compared to that of the remaining two C atoms. In Eu(tacn−TT), the shortest Eu−N and Eu−C bond distance is 2.50 and 2.75Å, while the longest Eu−N and Eu−C distance is 2.84 and 3.02 Å, respectively. The shortest and longest (Ln−C and Ln−N) bond distances are reported in Table 6.2. Similar bonding trend is observed in the Ln(tacn−CT) complexes as shown in Table 6.2. Each trans ligands in Ln(tacn−TT) and Ln(tacn−CT) complexes form four relatively weak Ln−C and two relatively weak Ln−N bonds with an average Ln−C bond lengths in the range of 2.82−2.94 Å for the six Ln−C bonds and average Ln−N distances in the range of 2.54−2.67 Å for the three Ln−N bonds. The –C–C–C–C–, –N–C–C–N– and –C–C–N–C– dihedral angle in the trans $C_6H_6N_3^-$ ligand is deviated from the planarity by 5–17°, 10–12° and 4–11°, respectively, in the Ln(tacn–TT) complexes as compared to that in the free trans $C_6H_6N_3^-$ ligand.

It is noteworthy to mention that although the planarity of the ligands decreases in their Ln(tacn−TT) complexes but their HOMA value is slightly increased from 0.83 to 0.83−0.89. In addition the significantly high NICS values (in the range of −18 to −42) show that the aromaticity of these Ln(tacn−TT) complexes is significantly high similar to that observed in the $An(COT)_2$[244] complexes. The torsional angle between the two ligands in Ln(tacn−CC) complexes is calculated to be around 178−180 degree, while it is observed to be around 93−95 degree in Ln(tacn−TT) complexes. Among all the complexes the HOMO−LUMO gap is the highest for $Eu(tacn)_2$ and $Yb(tacn)_2$ complexes (Table 6.3). It is due to the half−filled (f^7) and fully filled (f^{14}) electronic configuration of Eu(II) and Yb(II) ions, respectively. Similar results are obtained using B3LYP and PBE0 functionals.

Table 6.2: Shortest and Longest Bond Lengths (in Å) in $Ln(C_6H_6N_3)_2$ Complexes Calculated using PBE−D3 Functional.

Complex	$R_{(Ln-C)}$	$R_{(Ln-N)}$	$R_{(C-C)}$	$R_{(C-N)}$
Nd(tacn–CC)	2.783–2.797	2.737–2.757	1.420–1.423	1.334–1.337
Pm(tacn–CC)	2.787–2.792	2.743–2.747	1.421	1.334
Sm(tacn–CC)	2.808–2.812	2.776–2.794	1.421–1.424	1.333–1.334
Eu(tacn–CC)	2.830–2.833	2.806–2.810	1.422	1.333
Tm(tacn–CC)	2.715–2.725	2.683–2.700	1.421–1.422	1.333
Yb(tacn–CC)	2.719–2.722	2.689–2.693	1.422	1.332–1.333
Nd(tacn–TT)	2.761–2.958	2.458–2.786	1.412–1.452	1.321–1.361
Pm(tacn–TT)	2.718–3.029	2.437–2.811	1.412–1.452	1.316–1.363
Sm(tacn–TT)	2.751–3.018	2.471–2.802	1.413–1.452	1.319–1.360
Eu(tacn–TT)	2.750–3.016	2.502–2.835	1.414–1.454	1.317–1.358
Tm(tacn–TT)	2.625–2.966	2.380–2.707	1.413–1.454	1.320–1.362
Yb(tacn–TT)	2.609–2.956	2.387–2.710	1.414–1.455	1.319–1.362
Nd(tacn–CT)	2.739–2.922	2.418–2.813	1.412–1.452	1.323–1.359
Pm(tacn–CT)	2.738–2.952	2.429–2.782	1.412–1.451	1.320–1.360
Sm(tacn–CT)	2.737–2.986	2.448–2.815	1.413–1.452	1.320–1.360
Eu(tacn–CT)	2.756–3.021	2.477–2.832	1.414–1.453	1.314–1.359
Tm(tacn–CT)	2.624–2.985	2.379–2.707	1.412–1.455	1.320–1.361
Yb(tacn–CT)	2.621–2.975	2.382–2.713	1.413–1.451	1.320–1.360

6.2.4 Binding energy estimation

The stability of all the complexes is analyzed by calculating their binding energy. The binding energy of the $Ln(C_6H_6N_3)_2$ and $Ln(C_9H_9)_2$ complexes has been calculated using the following given equations 6.2 and 6.4, respectively.

$$Ln^{2+} + 2*C_6H_6N_3^{-} \xrightarrow{\hspace{3em}} Ln@(C_6H_6N_3)_2 \tag{6.1}$$

$$BE = E[Ln(C_6H_6N_3)_2] - [E(Ln^{2+}) + 2*E(C_6H_6N_3^{-})] \tag{6.2}$$

$$Ln^{2+} + 2*C_9H_9^{-} \xrightarrow{\hspace{3em}} Ln@(C_9H_9)_2 \tag{6.3}$$

$$BE = E[Ln(C_9H_9)_2] - [E(Ln^{2+}) + 2*E(C_9H_9)] \tag{6.4}$$

The negative binding energy of Ln(tacn−CC) (−18.03 to −18.87 eV), Ln(tacn−CT) (−18.62 to −19.54 eV) and Ln (tacn−TT) (−19.14 to −20.14 eV) complexes demonstrate their high stability (Table 6.3). A slightly higher binding energy also indicate a higher stability of the Ln(tacn−TT) complexes as compared to the Ln(tacn−CC) and the Ln(tacn−CT) complexes. It is noteworthy to mention that the binding energy of the predicted $Ln(tacn)_2$ complexes is found to be only slightly less (1−2 eV) as compared to the corresponding experimentally observed $Ln(cnt)_2$ complexes[95] which indicate comparable stability of the predicted $Ln(tacn)_2$ complexes with the experimentally synthesized $Ln(cnt)_2$ complexes.

6.2.5 Natural population and spin population analyses

The natural population analysis (NPA)[166] derived positive charge on the divalent lanthanide ions in the Ln(tacn−CC), Ln(tacn−CT) and Ln(tacn−TT) complexes is slightly reduced to ~+1 e from their initial charge value (+2) (Table 6.3). It indicates a small amount of charge transfer from the ligand to the metal ion in these complexes. The magnitude of charge transfer is almost the same in all the studied Ln–complexes. It is noteworthy to mention that in all the $Ln(C_6H_6N_3)_2$ sandwich complexes, the spin population of valence ns, np, nd shell of Ln is zero, while spin population (N_S) in the 4f shell of lanthanides is very close to its atomic spins as shown in Table 6.3. The unquenched high spin density on the Ln(II) ion in $Ln(C_6H_6N_3)_2$ complexes also favors the application of these complexes in the design of single ion magnet. The zero spin population of Yb($C_6H_6N_3$)$_2$ complex is due to its singlet ground state.

Table 6.3: HOMO−LUMO Energy Gap (ΔE_{Gap}, in eV), Binding Energy (BE, in eV), NPA Charges on Ln, C, N (q_{Ln}, q_C and q_N, in e) Atoms, Spin Populations on Ln Ion (N_S) and Dipole Moment (μ, in Debye) of Ln($C_6H_6N_3$)$_2$ Complexes Obtained using PBE–D3 Functional.

Complex	ΔE_{Gap}	BE	q_{Ln}	q_N	q_C	N_S	μ
Nd(tacn–CC)	0.67	–18.35	1.11	–0.43	–0.08	3.65	0.00
Pm(tacn–CC)	0.62	–18.31	1.13	–0.43	–0.08	4.69	0.00
Sm(tacn–CC)	0.48	–18.18	1.14	–0.43	–0.08	5.83	0.00
Eu(tacn–CC)	1.20	−18.03	1.16	−0.43	−0.08	6.88	0.01
Tm(tacn–CC)	0.51	−18.89	1.07	−0.42	−0.08	1.06	0.00
Yb(tacn–CC)	1.19	−18.87	1.09	−0.42	−0.08	0.00	0.01
Nd(tacn–TT)	0.66	–19.51	1.11	–0.46	–0.07	3.58	3.22
Pm(tacn–TT)	0.40	–19.41	1.16	–0.46	–0.07	4.64	2.94
Sm(tacn–TT)	0.44	–19.23	1.18	–0.46	–0.07	5.76	2.82
Eu(tacn–TT)	1.02	−19.14	1.21	−0.46	−0.07	6.84	3.01
Tm(tacn–TT)	0.50	−20.13	1.14	−0.46	−0.06	1.13	3.02
Yb(tacn–TT)	1.15	−20.12	0.97	−0.46	−0.07	0.00	3.12
Nd(tacn–CT)	0.65	–18.94	1.12	–0.44	–0.08	3.62	2.76
Pm(tacn–CT)	0.53	–18.86	1.15	–0.44	–0.08	4.67	2.71
Sm(tacn–CT)	0.47	–18.75	1.15	–0.44	–0.08	5.79	2.33
Eu(tacn–CT)	1.07	−18.62	1.18	−0.44	−0.08	6.86	2.38
Tm(tacn–CT)	0.32	−19.40	1.13	−0.44	−0.08	1.11	2.50
Yb(tacn–CT)	1.00	−19.54	1.12	−0.44	−0.08	0.00	2.45

The zero dipole moment in Ln(tacn−CC) complexes confirms that the cis $C_6H_6N_3^-$ ligand forms a linear sandwich complexes, whereas nonzero dipole moment shows a deviation from the linearity of Ln(tacn−CT) and Ln(tacn−TT) complexes containing at least one trans $C_6H_6N_3^-$ ligand (Table 6.3). The dipole moment of all the $Ln(C_6H_6N_3)_2$ complexes is found to be in good agreement with their centroid−Ln−centroid angle.

6.2.6 Scalar relativistic and spin orbit calculations

Finally, to study the relativistic effect, we have optimized most of the Ln(tacn−CC) and Ln(tacn−TT) complexes using scalar relativistic and spin orbit ZORA approach at PBE−D3BJ/TZ2P level of theory. It is interesting to note that using relativistic effect the strongest bonding is also observed in Yb(II) complexes (Ln−C = 2.70−2.71 and Ln−N= 2.67−2.68 Å) and weakest bonding in Eu(II) complexes (Ln−C = 2.81 and Ln−N = 2.78 Å).

Unlike NPA analysis, the Voronoi deformation density (VDD) charges shows significant charge transfer from the ligand to the metal ion. The bond lengths calculated using relativistic scalar and spin orbit methods are almost the same, which indicate a negligible effect of spin orbit coupling (Table 6.4). However, the HOMO−LUMO energy gap is slightly lowered (0.01−0.35 eV) due to the spin orbit coupling (Table 6.4). It is to be noted that structural parameters as well as HOMO−LUMO energy gap, calculated using relativistic approaches (Table 6.4) are found to be in good agreement with the RECP based results (Table 6.2).

Among all the studied complexes, the divalent Pm, Sm, Eu sandwich complexes are the potential candidate for use as magnetic materials due to their larger spin population which might lead to large magnetic moment. It is noteworthy to mention that the highest occupied molecular spinor (HOMS) of Eu(tacn−CC) and Eu(tacn−TT) complexes shows a significant electronic delocalization in the metallic center orbitals, mainly from the 4f orbitals of Eu

(Figure 6.7). It is to be noted that the highest occupied molecular orbital (HOMO) as well as HOMO−1 to HOMO−5, each of which containing one unpaired electron have major contribution from the 4f orbital (> 93%) of Eu ion and a very small contribution from the ligand in Eu(tacn−CC) complex. Whereas, lowest unoccupied molecular spinor (LUMS) of Eu(tacn−CC) and Eu(tacn−TT) complexes shows a significant electronic delocalization in the ligand (Figure 6.7), which is in agreement with the lowest unoccupied molecular orbital (LUMO) which contains major contribution from the ligand (>95%) and a very small contribution from the Eu ion.

Table 6.4: Shortest and Longest Bond Lengths (in Å), HOMO–LUMO Gap (ΔE_{Gap}, in eV) and VDD Charge (q_{Ln}, q_N and q_C, in e) in $Ln(C_6H_6N_3)_2$ Complexes Obtained using PBE–D3BJ/TZ2P Method using Scalar Relativistic (Spin Orbit) ZORA Approach.

Complex	$R_{(Ln–C)}$	$R_{(Ln–N)}$	ΔE_{gap}	q_{Ln}	q_N	q_C
Sm(tacn–CC)	2.783–2.794	2.745–2.770	0.22	0.20	–0.16	–0.00
	(2.784–2.793)	(2.746–2.768)	(0.22)	(0.20)	(–0.16)	(–0.00)
Eu(tacn–CC)	2.810	2.785–2.786	1.09	0.21	–0.16	–0.00
	(2.810)	(2.784–2.785)	(0.79)	(0.21)	(–0.16)	(–0.00)
Yb(tacn–CC)	2.706–2.710	2.673–2.683	1.11	0.34	–0.16	–0.01
	(2.704)	(2.673)	(0.76)	(0.35)	(–0.16)	(–0.01)
Sm(tacn–TT)	2.726–2.978	2.452–2.760	0.25	0.24	–0.18	–0.00
	(2.726–2.974)	(2.457–2.759)	(0.24)	(0.24)	(–0.16)	(–0.00)
Eu(tacn–TT)	2.731–3.017	2.484–2.805	0.88	0.23	–0.18	–0.00
	(2.728–3.016)	(2.483–2.801)	(0.72)	(0.23)	(–0.15)	(–0.00)
Yb(tacn–TT)	2.595–2.924	2.370–2.683	0.93	0.35	–0.16	–0.01
	(2.590–2.919)	(2.364–2.676)	(0.64)	(0.36)	(–0.16)	(–0.01)

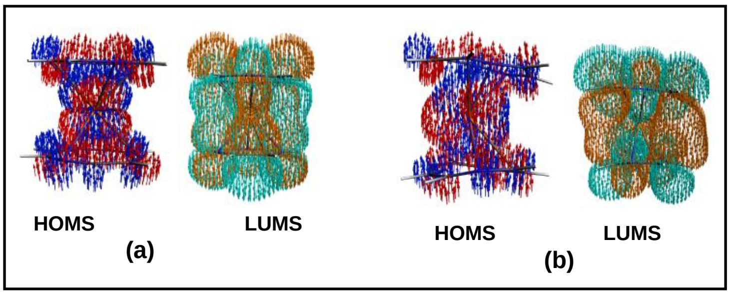

Figure 6.7: Spin magnetization density pictures of highest occupied molecular spinor (HOMS) and lowest unoccupied molecular spinor (LUMS) of a) Eu(tacn−CC) and b) Eu(tacn−TT) complexes at PBE–D3BJ/TZ2P level.

6.3 Conclusion

In summary, we have theoretically predicted a novel aromatic heterocyclic $C_6H_6N_3^-$ (tacn) ligand containing 10π electrons using dispersion−corrected density functional theory. The negative NICS value and 0.93 HOMA value of $C_6H_6N_3^-$ confirm the aromaticity of this ligand similar to that of the $C_9H_9^-$ ligand. The $C_6H_6N_3^-$ ligand forms stable Ln(tacn−CC), Ln(tacn−TT) and Ln(tacn−CT) sandwich complexes. Moreover, high spin population localized on the Ln ion in these studied sandwich complexes might be useful for their use as a single ion magnet. It is important here to mention that 1,4,7−triaza−2,5,8−cyclononatriene $C_6H_6(NR)_3$ neutral ligand[258-262] with 6π electrons and fully saturated 1,4,7−triazacyclononane[263-264] have been synthesized in the past. Although 1,4,7−triazacyclononane ligands are fully saturated, however, the unsaturated imino N can be introduced into the basic skeleton through photochemical reaction at ambient temperature condition.[265] Moreover, various monohetero C_8H_8X analogue of $C_9H_9^-$ have been studied computationally, among which C_8H_8NH and $C_8H_8N^-$ are predicted to be aromatic.[262]

Thus, prediction of new aromatic ligand and one to one correspondence in the studied properties of the predicted $Ln(tacn)_2$ complexes with the experimentally observed corresponding $Ln(cnt)_2$ complexes[95] will motivate experimentalists for the synthesis of the predicted $C_6H_6N_3^-$ ligand and its sandwich complexes with divalent lanthanides.

CHAPTER 7

High Coordination Behaviour of Lanthanide and Actinide Ions toward H_2 molecules

7.1 Introduction

In the previous chapters we have predicted highly stable lanthanide (Ln) and actinide (An) doped clusters, which have been found to follow 18– and 32–electron principles, and also the lanthanide sandwich complexes possessing high spin population. In all the studied Ln/An doped clusters or complexes the electronic and magnetic properties are governed by the f–orbitals of Ln and An elements as discussed in the previous chapters. However, in the present chapter, we are making use of large size of lanthanide and actinide ions for investigating highly coordinated lanthanide and actinide complexes. In recent years, actinides and lanthanides have attracted considerable research attention because of their unique and distinctive bonding behaviour as well as their ability to have very high coordination numbers (CNs). Werner defined the coordination number as the number of atoms directly connected to a metal atom/ion via coordinate or covalent bonds or the number of neighbouring atoms in the first coordination sphere of a metal atom/ion. However, with time this definition has been modified for different ligands such as ethene or cyclopentadienyl, which are considered to occupy one and three coordination sites, respectively. Though the high coordination numbers (CN = 12–16) of actinides in $[U(NO_3)_6]^{2-}$,[266] $[Th(NO_3)_6]^{2-}$,[267] $M(BH_4)_4$ (M = Th, Pa, U, Pu, Np),[268-271] and $[Th(H_3BNMe_2BH_3)]$,[272] and Cs in $Cs[H_2NB_2(C_6F_5)_6]$,[273] complexes are known, only recently Kaltsoyannis, for the first time, has reported seventeen–coordinated $Ac(He)_n^{3+}$, $Th(He)_n^{4+}$ and $Pa(He)_n^{4+}$ (n = 1–17) clusters theoretically where all the He atoms reside in the first coordination shell.[274] Earlier Schwerdtfeger and co–workers predicted the existence of $PbHe_{15}^{2+}$, with 15 He atoms in the first coordination sphere.[275] Recently, Ozama *et al.* showed a coordination number of 18 for Ac(III) in $Ac(He)_n^{3+}$ clusters using molecular dynamics simulation.[276]

Apart from the metal centered He clusters, hydrogen clusters have also attracted considerable attention because of their distinctive bonding behaviour. The most interesting bonding of H_2 molecule is its side on η^2 bonding with the metal ion that is 3–centered–2–electron (3c–2e) $M–\eta^2(H_2)$ bond in which strongly bonded electrons of H–H bond involves in bonding with the metal ion. This bond is known as Kubas type bond as it was first observed in dihydrogen complex by Kubas *et al.*[277] In 2004 Gagliardi and Pyykkö showed that a maximum of 12 H atoms can bind with a transition metal atom/ion through either M–H and $M–\eta^2(H_2)$ bonds or only $M–\eta^2(H_2)$ bonds in MH_{12} clusters.[278] Later Chandrakumar and Ghosh found that in the $M(H_2)_8$ cluster a maximum of 16 H atoms can bind with alkali metal ions via $M–\eta^2(H_2)$ bonds.[279] A recently performed combined experimental and theoretical study of $UH_4(H_2)_6$, $ThH_4(H_2)_x$ (x = 1–4), $MH_x(H_2)_y$ (M = La–Gd, n = 1–4, y = 0–6) and $MH_x(H_2)_y$ (M = Tb–Lu, n = 1–4, y = 0–3) systems shows the presence of both M–H and $M–\eta^2(H_2)$ bonds in these systems.[280-283] Very recently, in the experimentally observed $H@(H_2)_{12}^-$ system by Renzler *et al.*[284] as well as in theoretically investigated other atom/ion centered $X@(H_2)_{12}^-$ systems,[285] we found that only 12 H atoms can bind with the metal ion via 2c–2e $M–H_2$ bonds.[285] It is noteworthy to mention that in all the molecular/cluster systems reported until now not more than 16 H atoms can bind directly with a metal atom/ion in the first sphere of coordination.

Now interesting questions are: what can be the maximum number of H atoms that can directly bind to a metal ion in a molecular system? Is it possible for any lanthanide and actinide ion to bind with more than 16 H atoms in the gas phase? For these, we have investigated molecular hydrogen $(H_2)_n$ clusters containing actinide ions, namely, $Ac(H_2)_n^{3+}$ (n = 1–15), $Th(H_2)_{12}^{3+}$, $Th(H_2)_{12}^{4+}$, $Pa(H_2)_{12}^{4+}$ and $U(H_2)_{12}^{4+}$, using first–principles density functional theory (DFT). Various properties like structural, electronic, and energetic properties for all the clusters have been investigated systematically. Moreover, for comparison purposes, analogous $La(H_2)_n^{3+}$ (n = 1–15) clusters are investigated.

All the results discussed in this chapter have been obtained by using MP2, CCSD(T) and DFT–D3 methods[144, 146-149, 156-157] with def–TZVPP basis set along with a relativistic effective core potential (RECP) for heavier elements by using Turbomole[150], ADF[152-153], GAMESS−2018[286], MOLPRO2012[165] and Multiwfn[170] programs. Detail computational methodologies have been discussed in Chapter 2 of this thesis.

7.2 Results and discussions

7.2.1 Structural parameters of $M(H_2)_n^{3+}$ (n = 1–12) systems

To begin with, we have first optimized the $Ac(H_2)_n^{3+}$ (n = 1–3) systems using the CCSD(T) and MP2 methods. For comparison purposes, $Ac(H_2)_n^{3+}$ (n = 1–3) are also optimized with the PBE–D3, B3LYP–D3, PBE0–D3, TPSS–D3, TPSSH–D3 and BHLYP–D3 functionals using def–TZVPP basis set. The BHLYP–D3 results are found to be very close to the MP2 and CCSD(T) results (Table 7.1). Therefore, for all the $Ac(H_2)_n^{3+}$ and $La(H_2)_n^{3+}$ (n = 1–15) systems calculations have been performed using the BHLYP–D3/def–TZVPP method, and the corresponding results are discussed throughout this chapter unless otherwise mentioned. The optimized structure of the $M(H_2)_{12}^{3+}$ complex is depicted in Figure 7.1. In all the studied systems the hydrogen molecules are bonded with the metal ion by Kubas type 3c–2e side–on $M–\eta^2(H_2)$ bonds. We have found that a maximum of 24 H atoms can directly bind to the metal ion in $Ac(H_2)_{12}^{3+}$, $Th(H_2)_{12}^{3+}$, $Th(H_2)_{12}^{4+}$, $Pa(H_2)_{12}^{4+}$, $U(H_2)_{12}^{4+}$ and $La(H_2)_{12}^{3+}$ which is the highest reported number in the literature to date. It is to be noted that in the optimized structures of $M(H_2)_n^{3+}$ (M = Ac, La and n = 1–12) systems all the H atoms are positioned in the first coordination shell around the metal ion.

Table 7.1: Optimized Bond Lengths ($R_{(Ac–H)}$ and $R_{(H–H)}$, in Å) and Binding Energy (BE, in eV) of $Ac(H_2)_n^{3+}$(n = 1–3) Clusters.

Methods	$R_{min(Ac–H)}$	$R_{max(Ac–H)}$	$R_{min(H–H)}$	**BE**
		$Ac(H_2)^{3+}$		
PBE–D3	2.716	2.716	0.786	–0.94
B3LYP–D3	2.734	2.734	0.774	–0.84
TPSS–D3	2.701	2.701	0.776	–0.90
PBE0–D3	2.700	2.700	0.778	–0.89
TPSSH–D3	2.698	2.698	0.774	–0.88
BHLYP–D3	2.722	2.722	0.766	–0.81
MP2	2.722	2.722	0.766	–0.78
CCSD(T)	2.724	2.724	0.771	–0.78
		$Ac(H_2)_2^{3+}$		
PBE–D3	2.726	2.730	0.783	–1.80
B3LYP–D3	2.761	2.764	0.772	–1.63
TPSS–D3	2.704	2.719	0.774	–1.72
PBE0–D3	2.708	2.715	0.776	–1.71
TPSSH–D3	2.701	2.717	0.772	–1.69
BHLYP–D3	2.753	2.755	0.764	–1.56
MP2	2.727	2.733	0.764	–1.51
CCSD(T)	2.729	2.736	0.770	–1.52
		$Ac(H_2)_3^{3+}$		
PBE–D3	2.727	2.743	0.781	–2.61
B3LYP–D3	2.746	2.760	0.770	–2.35
TPSS–D3	2.711	2.724	0.772	–2.49
PBE0–D3	2.715	2.727	0.774	–2.48
TPSSH–D3	2.714	2.726	0.770	–2.45
BHLYP–D3	2.735	2.746	0.762	–2.27
MP2	2.737	2.744	0.763	–2.21
CCSD(T)	2.739	2.746	0.768	–2.22

However, for n = 13 or higher, we could not find the minimum energy structure where all H atoms reside in the first coordination sphere. The 13th, 14th and 15th H_2 molecules are present in the second coordination shell of the metal ion ($R_{M–H}$ > 4 Å). It is worthwhile to mention that we have also optimized the $Ac(H_2)_{12}^{3+}$ system containing only classical 2c–2e M–H_2 bonds in different high symmetries, namely, I_h, O_h, D_{3h}, and D_{5h}. All the I_h, O_h, D_{3h}, and D_{5h} structures of $Ac(H_2)_{12}^{3+}$ are optimized with imaginary frequencies and also found to be energetically less stable than the M–$\eta^2(H_2)$ bonded $Ac(H_2)_{12}^{3+}$ structure. To find the true minimum energy structure for the $Ac(H_2)_{12}^{3+}$ system, all the optimized I_h, O_h, D_{3h}, and D_{5h} structures are distorted along the imaginary frequency mode, and finally after optimization of each new structure, we got back the original optimized structure with only the M–$\eta^2(H_2)$ type of bonding, which indicates that side on M–$\eta^2(H_2)$ bonding is more favoured than 2c-2e M–H_2 bonding in the $Ac(H_2)_{12}^{3+}$ system.

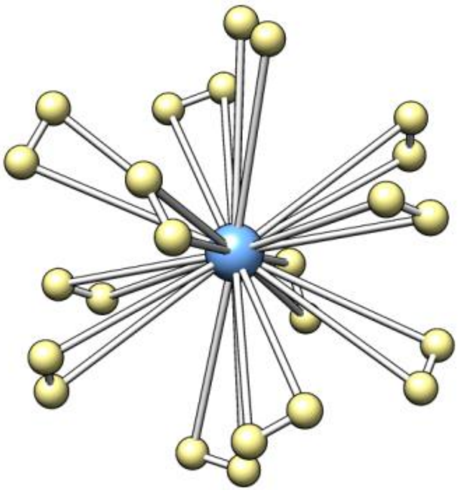

Figure 7.1: Optimized structure of $Ac(H_2)_{12}^{3+}$ cluster.

The optimized M–H and H–H bond lengths of all the $M(H_2)_{12}^{3+}$ systems are reported in Table 7.2. As expected, the M–H bond length in $M(H_2)_n^{3+}$ (n = 1–12) increases slightly (2.722 to 2.828 Å) with an increase in the number of H_2 molecules (from n = 1 to 12), while the opposite trend is found for the H–H bonds (0.766 to 0.750 Å). It is to be noted that in actinide centered $M(H_2)_{12}$ clusters the M–H distances are 2.815, 2.746, 2.644, 2.597, and 2.563 for M = Ac(III), Th(III), Th(IV), Pa(IV), and U(IV), respectively (Table 7.2). It indicates that the bonding strength increases from the Ac(III) ion to the U(IV) ion. In all the cases, the H–H distances (0.766 to 0.750 Å) are very close to the equilibrium bond length of a H_2 molecule (0.74 Å), indicating almost no activation of the H–H bond in the $M(H_2)_n^{3+}$ and $M(H_2)_n^{4+}$ complexes.

Table 7.2: Optimized Bond Lengths (in Å), HOMO−LUMO Energy Gap (ΔE_{Gap}, in eV), NPA Charges (q_M and q_H, in e) and BE/H_2 (in eV) of $M(H_2)_{12}^{3+/4+}$ Obtained using BHYLP−D3 Functional.

Cluster	$R_{min(M-H)}$	$R_{max(M-H)}$	ΔE_{Gap}	q_M	q_H	**BE/H_2**
$Ac(H_2)_{12}^{3+}$	2.815	2.828	12.98	1.93	0.04	–0.57
$Th(H_2)_{12}^{3+}$	2.746	2.774	5.73	1.33	0.07	–0.64
$Th(H_2)_{12}^{4+}$	2.644	2.654	10.82	1.41	0.11	–1.29
$Pa(H_2)_{12}^{4+}$	2.597	2.611	8.14	0.94	0.13	–1.37
$U(H_2)_{12}^{4+}$	2.563	2.581	8.20	0.85	0.13	–1.54
$La(H_2)_{12}^{3+}$	2.730	2.743	11.86	1.74	0.05	–0.62

We have also studied few species containing a mixture of radial M–H bonds and side–on M–$\eta^2(H_2)$ bonds, viz., $[Ac(H)_2(H_2)_y{}^{3+}]$ and $[Ac(H)_4(H_2)_y{}^{3+}]$, where y = 1, 2, 9, and 10 (Figure 7.2), and compared their stability with the corresponding $Ac(H_2)_n^{3+}$ systems containing only side–on M–$\eta^2(H_2)$ bonds with the same compositions. All the ionic species containing both the radial M–H bonds and side–on M–$\eta^2(H_2)$ bonds are significantly less stable (6–13 eV) with respect to the corresponding $Ac(H_2)_n^{3+}$ systems having only the side–on M–$\eta^2(H_2)$ bonds. The absence of one H_2 molecule in lieu of two H atoms in the mixed ionic species decreases the energy by 4.7 eV, and consequently mixed ionic species are higher in energy. We have also compared one of the experimentally observed neutral $UH_4(H_2)_6$[280] systems with the hypothetical $U(H_2)_8$ complex in the lowest energy spin state (triplet) and found that $UH_4(H_2)_6$ is more stable by 1.52 eV. This is due to the back donation from the metal orbital to the anti–bonding orbital of a H_2 molecule,[287] leading to breaking of a H–H bond in H_2 molecule favouring mixed M–H and M–$\eta^2(H_2)$ bonds in the neutral complex, with much shorter radial M–H bonds. However, such back donation is not possible in the ionic $M(H_2)_n^{3+}$ system, and hence mixed ionic structures containing radial M–H bonds and side–on M–$\eta^2(H_2)$ bonds are higher in energy than the corresponding $M(H_2)_n^{3+}$ structures containing only side–on M–$\eta^2(H_2)$ bonds.

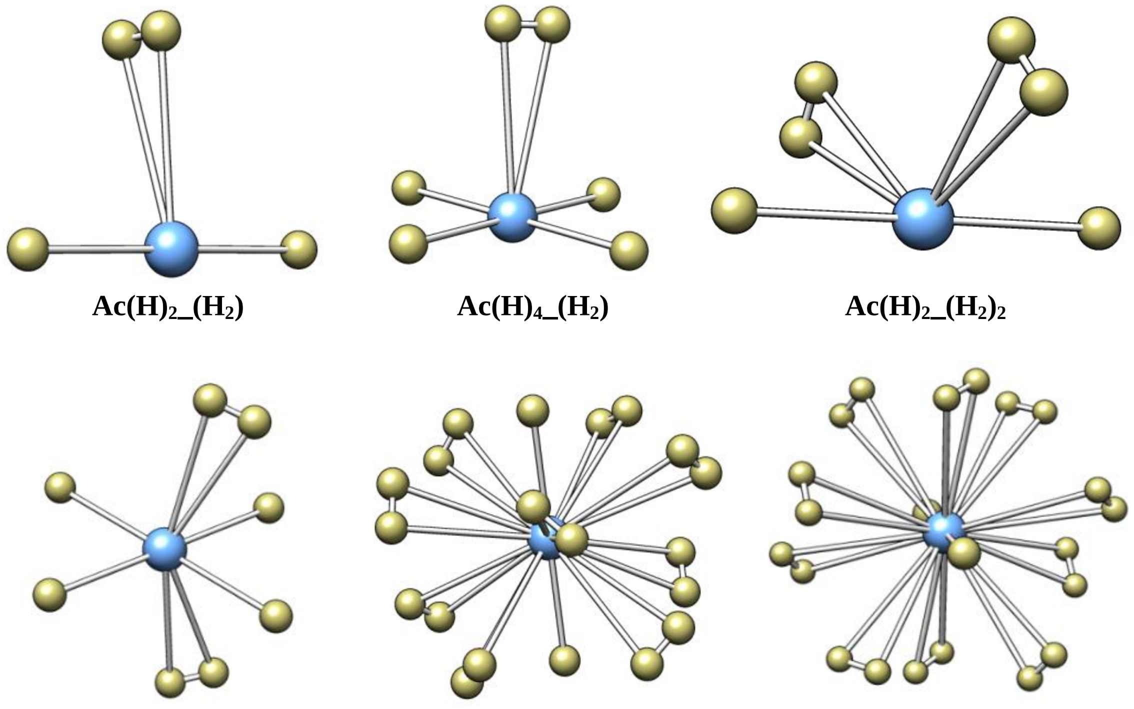

$Ac(H)_2\_(H_2)$ **$Ac(H)_4\_(H_2)$** **$Ac(H)_2\_(H_2)_2$**

$Ac(H)_4\_(H_2)_2$ **$Ac(H)_2\_(H_2)_9$** **$Ac(H)_2\_(H_2)_{10}$**

Figure 7.2: Optimized structures of $Ac(H)_2(H_2)_y^{3+}$ and $Ac(H)_4(H_2)_y^{3+}$ systems (where y = 1, 2, 9, 10) using BHLYP-D3 functional.

Furthermore, we have also studied the bonding of various other atom or ion (X = H^-, Be, Mg, B^{2-}, C^-, N^{3-}, P^{3-}, O^{2-}, S^{2-}, Se^{2-}, F^-, Cl^-, Br^-, Cu^-, Ag^-, Au^-, Zn, and Cd) with the H_2 molecules in $X@(H_2)_{12}$, $X@(H_2)_{32}$, $X@(H_2)_{44}$ clusters.[285] On comparison we found that unlike in the studied $M(H_2)_n^{3+/4+}$ systems, the central atom or ion in the $X@(H_2)_{12}$, $X@(H_2)_{32}$,

$X@(H_2)_{44}$ clusters form a 2–centre 2–electron (2c–2e) X–H_2 bond. Thus all the centre atom/ion in $X@(H_2)_{12}$, $X@(H_2)_{32}$, $X@(H_2)_{44}$ clusters are capable of forming a direct bond with only one H atom of each H_2 molecule. Therefore, unlike in $M(H_2)_n^{3+}$ (M = La/Ac), only 12 H atoms are present in the first coordination sphere of the central atom/ion in the $X@(H_2)_{12}$, $X@(H_2)_{32}$, $X@(H_2)_{44}$ clusters. This work has been extensively discussed in the reference 259.

7.2.2 Binding energy estimation

All the studied systems are energetically stable (Table 7.2) as the binding energy of all the systems is negative. The binding energy per H_2 molecule (BE/H_2) has been calculated using the following equation (7.1).

$$BE/H_2 = [E(M(H_2)_n) - n^*E(H_2) - E(M)]/n^*E(H_2) \qquad (7.1)$$

where, M = La^{3+}, Ac^{3+}, Th^{3+}, Th^{4+}, Pa^{4+}, U^{4+} and n = 1−12

The BE per H_2 molecule slightly decreases from −0.81 to −0.57 eV and −0.90 to −0.62 eV with an increase in the number of H_2 molecule for $Ac(H_2)_n^{3+}$ and $La(H_2)_n^{3+}$ (from n = 1 to 12), respectively. However, the BE/H_2 molecule increases from the Ac(III) to U(IV) containing $(H_2)_{12}$ clusters (−0.57 to −1.54) (Table 7.2). Moreover, the basis set superposition error (BSSE) for all the studied systems using the BHLYP–D3/def–TZVPP method is very small (0.001–0.025 eV).

Earlier theoretical studies have shown that the nuclear quantum effects (NQE) are important for species containing light hydrogen molecules, as reported by Gianturco and coworkers, who used the quantum path integral and diffusion Monte Carlo methods.[288] To investigate the NQE we have considered the nuclear–electronic orbital approach with MP2 (NEO–MP2) method using def2–TZVPP basis set for H and CRENBL basis set of Ac as implemented in GAMESS−2018 software.[289-290] Moreover, DZSPDN nuclear basis set is used for the quantum hydrogen as implemented in GAMESS−2018 software. In the NEO approach, specified nuclei are treated quantum mechanically at the same level as the electrons, and the mixed nuclear–electronic wavefunction is calculated with the molecular orbital method. The binding energies of $Ac(H_2)_n^{3+}$ (n = 1–7) systems with the NEO–MP2 approach are found to be only slightly increased as compared to the corresponding MP2 calculated results (Table 7.3). Moreover, ortho–para effects in a hydrogen molecule might also have a small influence, however, in order to consider the ortho–para effects, one needs to analyze the potential energy surface inclusive of internal rotation and vibration, which is left for future studies.

Table 7.3: Binding Energy (BE, in eV) and BE/H_2 (in eV) Calculated using MP2 and NEO–MP2 Methods.

System	**MP2**		**NEO–MP2**		**BE_Error/H₂**
	BE	**BE/H₂**	**BE**	**BE/H₂**	
$Ac(H_2)^{3+}$	–0.70	–0.70	–0.78	–0.78	0.09
$Ac(H_2)_2^{3+}$	–1.37	–0.68	–1.53	–0.76	0.08
$Ac(H_2)_3^{3+}$	–2.0	–0.67	–2.23	–0.74	0.08
$Ac(H_2)_4^{3+}$	–2.61	–0.65	–2.89	–0.72	0.07
$Ac(H_2)_5^{3+}$	–3.16	–0.63	–3.48	–0.70	0.07
$Ac(H_2)_6^{3+}$	–3.72	–0.62	–4.10	–0.68	0.06
$Ac(H_2)_7^{3+}$	–4.22	–0.60	–4.63	–0.66	0.06

We have also calculated the gain in the energy (EG, kJ mol^{-1}) of $M(H_2)_n^{3+}$ on the addition of hydrogen molecules in $M(H_2)_{n-1}^{3+}$ using the following equation (7.2).

$$EG = E[M(H_2)_n^{3+}] - E[M(H_2)_{n-1}^{3+}] - E(H_2) \qquad (7.2)$$

It can be seen from Figure 7.3 that the EG value decreases from $M(H_2)^{3+}$ to $M(H_2)_{11}^{3+}$ and increases at $M(H_2)_{12}^{3+}$ and again decreases significantly as we move from the $M(H_2)_{12}^{3+}$ to $M(H_2)_{13}^{3+}$ system, and remains almost the same for $M(H_2)_n^{3+}$ (n = 13–15) systems. The sharp dip in the EG of the $M(H_2)_{13}^{3+}$ cluster is caused by the disruption of the stable structure of the $M(H_2)_{12}^{3+}$ system. Similarly, the local maxima in EG were found for $Ac(He)_n^{3+}$ and $Pb(He)_n^{2+}$ systems[274–275] for n = 12. It is very interesting to note that in all the clusters the HOMO–LUMO energy gap (ΔE_{Gap}) is very large (Table 7.2). Among all the systems the ΔE_{Gap} is the largest in $M(H_2)_{12}^{3+}$ (ΔE_{Gap} = 12.98 and 11.86 eV, for M = Ac and La) followed by that in the $M(H_2)_9^{3+}$ (ΔE_{Gap} = 12.57 and 11.79 eV for M = Ac and La) system, which clearly shows the relatively high chemical stability of these two systems.

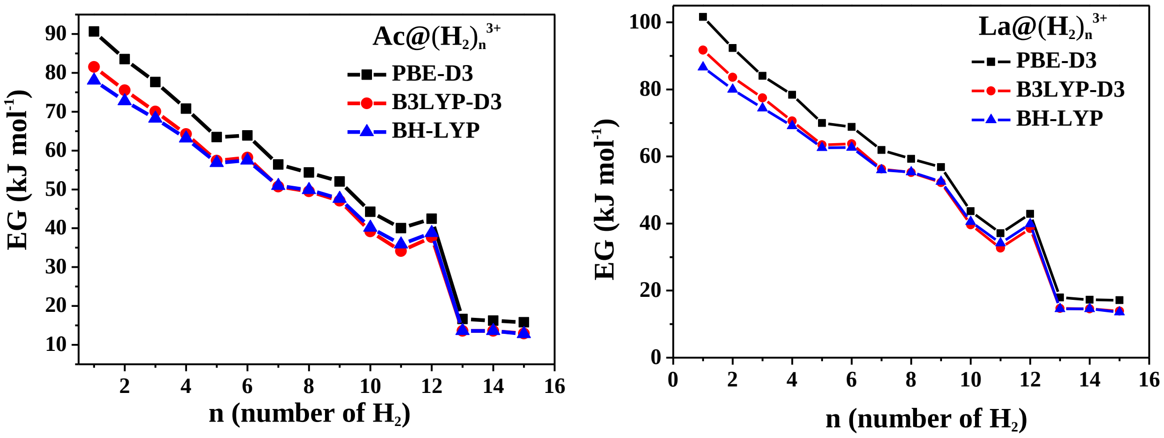

Figure 7.3: Energy Gain (EG, kJ mol^{-1}) of $M(H_2)_n^{3+}$ (M = Ac, La and n = 1–15) system on addition of hydrogen molecule in $M(H_2)_{n-1}^{3+}$ system using BHLYP-D3 functional.

7.2.3 Molecular orbital analysis

It is interesting to note that the $Ac(H_2)_n^{3+}$ systems (n = 9–12) satisfy the 18–electron rule corresponding to the fulfillment of $s^2p^6d^{10}$ configuration around Ac atom (Figures 7.4 and 7.5). It is in agreement with the $M@Pb_{12}^{+}$ and $M@Sn_{12}^{+}$ clusters (M=Ac and La) discussed in Chapter 3 of this thesis. However, $La(H_2)_n^{3+}$ system do not satisfy the 18–electron rule. It is because of the inability of H_2 molecules to perturb the highly stabilized energy levels of the La^{3+} ion in $La(H_2)_n$ systems as compared to that of the Ac^{3+} ion in the corresponding $Ac(H_2)_n$ systems.

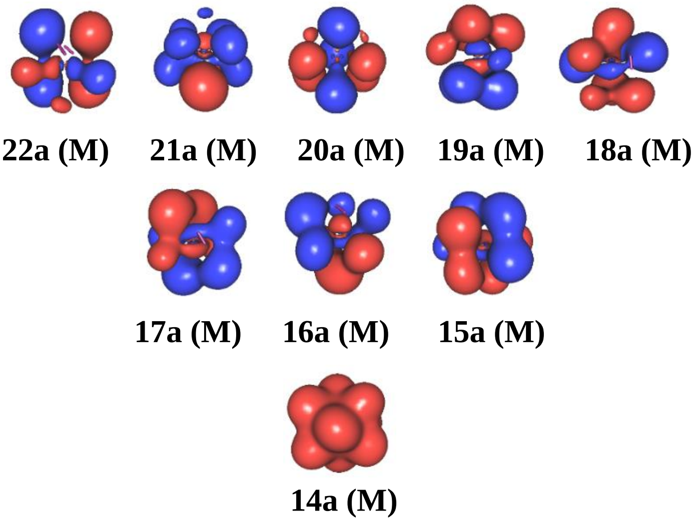

22a (M) 21a (M) 20a (M) 19a (M) 18a (M)

17a (M) 16a (M) 15a (M)

14a (M)

Figure 7.4: MO Pictures of $Ac(H_2)_9^{3+}$ cluster using BHLYP-D3 functional. Here, 'M' represent mixed Ac–$(H_2)_n$ atoms MOs.

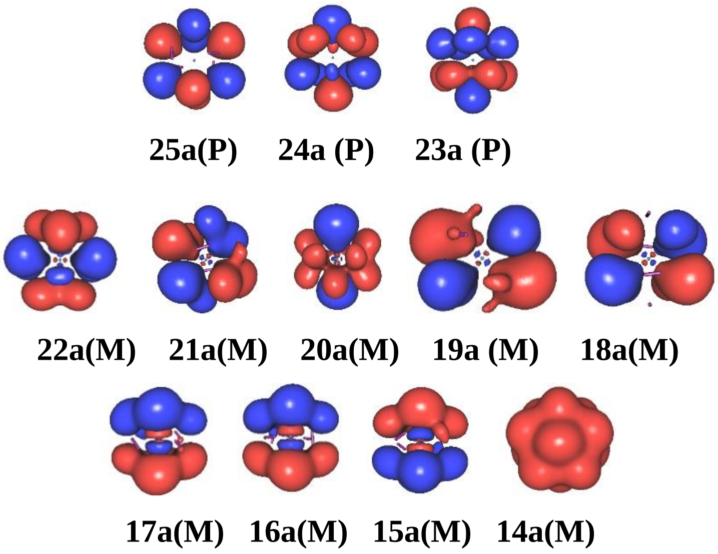

25a(P) 24a (P) 23a (P)

22a(M) 21a(M) 20a(M) 19a (M) 18a(M)

17a(M) 16a(M) 15a(M) 14a(M)

Figure 7.5: MO Pictures of $Ac(H_2)_{12}^{3+}$ cluster using BHLYP-D3 functional. Here 'P' represent Pure $(H_2)_n$ MOs and 'M' represent mixed Ac–$(H_2)_n$ atoms MOs.

7.2.4 Natural population analysis

To gain clear insight into the nature of bonding between the constituent atoms in the $Ac(H_2)_n^{3+}$ and $La(H_2)_n^{3+}$ (n = 1–12) systems, we have performed natural population analysis[166] (NPA). The initial charge (+3) on the metal ion is observed to decrease through transfer of electrons from the hydrogen molecules to the metal ion. As expected, the charge on the metal ion decreases (2.96–1.93 e) with the increase in the number of hydrogen molecules in $Ac(H_2)_n^{3+}$ (from n = 1 to 12). The presence of a very small positive charge on the hydrogen atoms in $Ac(H_2)_n^{3+}$ systems (0.02–0.04 e) implies an ion–induced dipole interaction in these systems. Similar trends are observed in $La(H_2)_n^{3+}$ (n = 1–12) complexes. We observe more charge transfer from H_2 molecules to other An (Th, Pa, U) ions due to the involvement of their f–orbitals in bonding (Table 7.2).

7.2.5 Analysis of topological properties

For further understanding the nature of bonding we have calculated the electron density at the bond critical point (BCP) of M–H and H–H bonds and other BCP properties like the Laplacian of the electron density ($\nabla^2\rho$), Lagrangian G(r), potential energy V(r), local energy density E(r) and G(r)/ρ. Using the Boggs criteria[169] of bonding we find that all the H–H bonds are strong covalent ($\rho > 0.1$ and $\nabla^2\rho < 0$) bonds, while M–H bonds are very weak covalent bonds of type D ($\nabla^2\rho > 0$, $|E(r)| < 0.0005$ and $G(r)/\rho < 1$) and contain major percent of ionic character. Again this shows the presence of ion–induced dipole interaction in M–H bonds in $M(H_2)_n^{3+}$ systems. The positions of the critical points between the metal ion and hydrogen molecules in Figure 7.6 clearly show the presence of side–on M–$\eta^2(H_2)$ bonds in the studied systems.

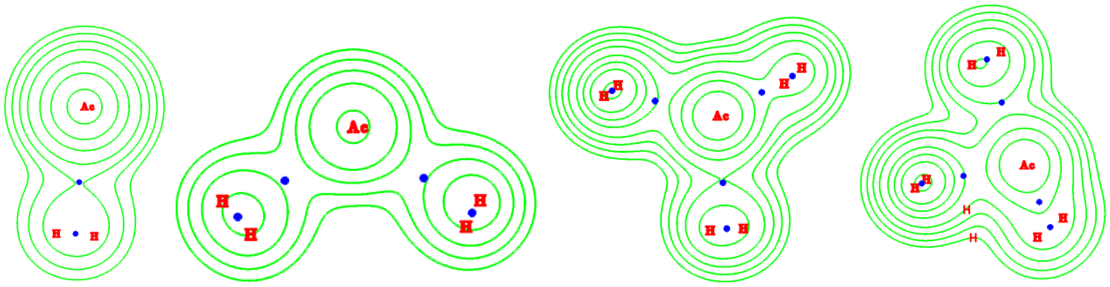

$Ac(H_2)^{3+}$ $Ac(H_2)_2^{3+}$ $Ac(H_2)_3^{3+}$ $Ac(H_2)_4^{3+}$

Figure 7.6: Electron density pictures of $Ac(H_2)_n^{3+}$ (n = 1–4) clusters using BHLYP-D3 functional.

7.2.6 Scalar relativistic effect

To study the relativistic effect, we have also optimized the systems using the zeroth order regular approximation (ZORA) approach with a 4f–frozen core as well as with an all–electron basis set using the PBE–D3BJ/TZ2P method (Table 7.4). Various properties like optimized structural parameters, binding energies, HOMO–LUMO energy gap and VDD charges[167] on metal ions calculated at the PBE–D3BJ/TZ2P level with the 4f frozen core show close similarity with the all electron basis set results (Table 7.4). Moreover, all the results calculated using the relativistic effect (Table 7.4) also show close similarity with the RECP (relativistic effective core potential) based results (Table 7.2).

Table 7.4: Optimized Bond Lengths (in Å), BE/H_2 (in eV), HOMO–LUMO Energy Gap ($\Delta E_{Gap,}$ in eV) and VDD Charge (q_M, in e) in $M(H_2)_{12}^{3+/4+}$ using Scalar Relativistic ZORA Approach at PBE–D3BJ/TZ2P Level of Theory.

System	$R_{min(M-H)}$	$R_{max(M-H)}$	$R_{(H-H)}$	**BE/H_2**	q_M	ΔE_{Gap}
			4f–Frozen Core			
$La(H_2)_{12}^{3+}$	2.714	2.721	0.769	–0.75	0.32	5.08
$Ac(H_2)_{12}^{3+}$	2.823	2.828	0.768	–0.66	0.32	7.92
$Th(H_2)_{12}^{3+}$	2.482	2.813	0.769	–0.76	0.12	0.56
$Th(H_2)_{12}^{4+}$	2.645	2.654	0.785	–1.46	0.38	4.85
$U(H_2)_{12}^{4+}$	2.550	2.584	0.789	–1.70	0.53	0.34
			All electron Basis Set			
$La(H_2)_{12}^{3+}$	2.710	2.717	0.770	–0.76	0.33	5.08
$Ac(H_2)_{12}^{3+}$	2.815	2.820	0.767	–0.66	0.32	7.98
$Th(H_2)_{12}^{3+}$	2.531	2.791	0.770	–0.77	0.10	0.57
$Th(H_2)_{12}^{4+}$	2.640	2.649	0.785	–1.47	0.38	4.71
$U(H_2)_{12}^{4+}$	2.551	2.578	0.789	–1.70	0.53	0.34

7.3 Conclusion

In summary, we have shown that An (Ac^{3+}, Th^{3+}, Th^{4+}, Pa^{4+}, U^{4+}) and La^{3+} ions form 3c–2e side–on $M–\eta^2(H_2)$ bonds with hydrogen molecules without any activation of the H–H bonds. The number of hydrogen atoms directly connected to the actinide/lanthanide ion in the predicted complexes is found to be higher than that in any of the alkali[279] or transition metal hydrogen complexes[278]. This is the highest ever reported number of hydrogen atoms (n = 24) bonded with any metal ion in the first coordination shell of a metal–hydrogen complex. Moreover, some of the predicted complexes, $Ac(H_2)_n^{3+}$ (n = 9–12), are found to satisfy the 18–electron rule. All the theoretical results presented here and the experimental preparations of various dihydrogen complexes mentioned here[280-283] indicate that it might be possible to prepare some of the $M(H_2)_{12}^{3+}$ (M = Ac and Th) and $M(H_2)_{12}^{4+}$ (M = Th, Pa and U) complexes experimentally. All these cationic $M(H_2)_{12}^{3+}$ systems could be prepared in the solid state in form of their salt. For this purpose very weakly coordinating anions can be used to minimize the effect of substitution of weakly bound H_2 molecules by anions in the first coordination sphere of the metal ion.

References

1. Jensen, W. B. The Positions of Lanthanum (Actinium) and Lutetium (Lawrencium) in the Periodic Table. *J. Chem. Educ.* **1982,** *59*, 634.
2. Jensen, W. B. Misapplying the Periodic Law. *J. Chem. Educ.* **2009,** *86*, 1186.
3. Lavelle, L. Lanthanum (La) and Actinium (Ac) Should Remain in the d-block. *J. Chem. Educ.* **2008,** *85*, 1482.
4. Lavelle, L. Response to “Misapplying the Periodic Law”. *J. Chem. Educ.* **2009,** *86*, 1187.
5. Lavelle, L. Response to "The Flyleaf Periodic Table". *J. Chem. Educ.* **2008,** *85*, 1491.
6. Xu, W.-H.; Pyykkö, P. Is the Chemistry of Lawrencium Peculiar? *Phys. Chem. Chem. Phys.* **2016,** *18*, 17351-17355.
7. Jemmis, E. D. Controversy Continues on the Position of Elements in the Periodic Table. *Current Science* **2018,** *114*, 2428-2429.
8. Lemonick, S. Rearranging the Table. *Chem. Engg. News.* **2019,** *97*, 26.
9. Kaltsoyannis, N.; Scott, P. The f Elements, 1 ed., Oxford University Press, Oxford **1999**.
10. Cotton, S. Lanthanide and Actinide Chemistry, 2nd ed.; Wiley, **2006**.
11. Kaltsoyannis, N. Recent Developments in Computational Actinide Chemistry. *Chem. Soc. Rev.* **2003,** *32*, 9-16.
12. Choppin, G. R. Comparative Solution Chemistry of the 4f and 5f Elements. *J. Alloys Compd.* **1995,** *223*, 174-179.
13. Kaltsoyannis, N. Does Covalency Increase or Decrease across the Actinide Series? Implications for Minor Actinide Partitioning. *Inorg. Chem.* **2013,** *52*, 3407-3413.
14. Nuclear power. https://en.wikipedia.org/wiki/Nuclear_power.

15. Magill, J.; Berthou, V.; Haas, D.; Galy, J.; Schenkel, R.; Wiese, H.-W.; Heusener, G.; Tommasi, J.; Youinou, G. Impact Limits of Partitioning and Transmutation Scenarios on the Radiotoxicity of Actinides in Radioactive Waste. *Nucl. Energy* **2003,** *42,* 263-277.
16. Nash, K. L. A Review of the Basic Chemistry and Recent Developments in Trivalent f-Elements Separations. *Solvent Extr. Ion Exch.* **1993,** *11,* 729-768.
17. Bhattacharyya, A.; Ghanty, T. K.; Mohapatra, P. K.; Manchanda, V. K. Selective Americium(III) Complexation by Dithiophosphinates: A Density Functional Theoretical Validation for Covalent Interactions Responsible for Unusual Separation Behavior from Trivalent Lanthanides. *Inorg. Chem.* **2011,** *50,* 3913-3921.
18. Bhattacharyya, A.; Mohapatra, M.; Mohapatra, P. K.; Gadly, T.; Ghosh, S. K.; Manna, D.; Ghanty, T. K.; Rawat, N.; Tomar, B. S. An Insight into the Complexation of Trivalent Americium Vis-à-Vis Lanthanides with Bis(1,2,4-triazinyl)bipyridine Derivatives. *Eur. J. Inorg. Chem.* **2017,** *2017,* 820-828.
19. Bhattacharyya, A.; Mohapatra, P. K.; Manchanda, V. K. Separation of Trivalent Actinides and Lanthanides Using a Flat Sheet Supported Liquid Membrane Containing Cyanex-301 as the Carrier. *Sep. Purif. Technol.* **2006,** *50,* 278-281.
20. Manna, D.; Ghanty, T. K. Complexation Behavior of Trivalent Actinides and Lanthanides with 1,10-Phenanthroline-2,9-Dicarboxylic Acid Based Ligands: Insight from Density Functional Theory. *Phys. Chem. Chem. Phys.* **2012,** *14,* 11060-11069.
21. Manna, D.; Mula, S.; Bhattacharyya, A.; Chattopadhyay, S.; Ghanty, T. K. Actinide Selectivity of 1,10-Phenanthroline-2,9-Dicarboxamide and its Derivatives: a Theoretical Prediction Followed by Experimental Validation. *Dalton Trans.* **2015,** *44,* 1332-1340.

22. Jansone-Popova, S.; Ivanov, A. S.; Bryantsev, V. S.; Sloop, F. V., Jr.; Custelcean, R.; Popovs, I.; Dekarske, M. M.; Moyer, B. A. Bis-lactam-1,10-Phenanthroline (BLPhen), a New Type of Preorganized Mixed N,O-Donor Ligand That Separates Am(III) over Eu(III) with Exceptionally High Efficiency. *Inorg. Chem.* **2017,** *56,* 5911-5917.
23. Sadhu, B.; Dolg, M. Enhancing Actinide(III) over Lanthanide(III) Selectivity through Hard-by-Soft Donor Substitution: Exploitation and Implication of Near-Degeneracy-Driven Covalency. *Inorg. Chem.* **2019,** *58,* 9738-9748.
24. Burns, J. H. Solvent-Extraction Complexes of the Uranyl ion. 2. Crystal and Molecular Structures of Catena- Bis(μ-di- n -butyl phosphato-*O,O'*)Dioxouranium(VI) and Bis(μ-di- n -butyl phosphato-*O,O'*)bis[(nitrato) (tri- n -butylphosphine oxide)Dioxouranium(VI)]. *Inorg. Chem.* **1983,** *22,* 1174-1178.
25. Horwitz, E. P.; Kalina, D. C.; Diamond, H.; Vandegrift, G. F.; Schulz, W. W. The Truex Process - a Process for the Extraction of the Tkansuranic Elements Erom Nitric Ac in Wastes Utilizing Modified Purex Solvent. *Solvent Extr. Ion Exch.* **1985,** *3,* 75-109.
26. Facchini, A.; Amato, L.; Modolo, G.; Nannicini, R.; Madic, C.; Baron, P. Transient- and Steady-State Concentration Profiles in a DIAMEX-like Countercurrent Process for An(III) + Ln(III) Separation. *Sep. Sci. Techol.* **2000,** *35,* 1055.
27. Hill, C.; Guillaneux, D.; Berthon, L.; Madic, C. Sanex-Btp Process Development Studies. *J. Nucl. Sci. Technol.* **2002,** *39,* 309-312.
28. Ruth, T. J.; Pate, B. D.; Robertson, R.; Porter, J. K. Radionuclide Production for the Biosciences. *Nucl. Med. Biol.* **1989,** *16,* 323-336.
29. Das, T.; Chakraborty, S.; Kallur, K. G.; Venkatesh, M.; Banerjee, S. Preparation of Patient Doses of ^{177}Lu-DOTA-TATE Using Indigenously Produced ^{177}Lu: The Indian Experience. *Cancer Biother. Radiopharm.* **2011,** *26,* 395-400.

30. Liu, S.; Edwards, D. S. Bifunctional Chelators for Therapeutic Lanthanide Radiopharmaceuticals. *Bioconjugate Chem.* **2001,** *12*, 7-34.

31. Wang, D.; van Gunsteren, W. F.; Chai, Z. Recent Advances in Computational Actinoid Chemistry. *Chem. Soc. Rev.* **2012,** *41*, 5836-5865.

32. Dognon, J.-P. Theoretical Insights into the Chemical Bonding in Actinide Complexes. *Coord. Chem. Rev.* **2014,** *266-267*, 110-122.

33. Seth, M.; Dolg, M.; Fulde, P.; Schwerdtfeger, P. Lanthanide and Actinide Contractions: Relativistic and Shell Structure Effects. *J. Am. Chem. Soc.* **1995,** *117*, 6597-6598.

34. Kroto, H. W.; Heath, J. R.; O'Brien, S. C.; Curl, R. F.; Smalley, R. E. C_{60}: Buckminsterfullerene. *Nature* **1985,** *318*, 162-163.

35. Stevenson, S.; Burbank, P.; Harich, K.; Sun, Z.; Dorn, H. C.; van Loosdrecht, P. H. M.; deVries, M. S.; Salem, J. R.; Kiang, C.-H.; Johnson, R. D.; Bethune, D. S. $La_2@C_{72}$: Metal-Mediated Stabilization of a Carbon Cage. *J. Phys. Chem. A* **1998,** *102*, 2833-2837.

36. Kuran, P.; Krause, M.; Bartl, A.; Dunsch, L. Preparation, Isolation and Characterisation of $Eu@C_{74}$: the First Isolated Europium Endohedral Fullerene. *Chem. Phys. Lett.* **1998,** *292*, 580-586.

37. Gao, Y.; Dai, X.; Kang, S.; Jimenez-Cruz, C. A.; Xin, M.; Meng, Y.; Han, J.; Wang, Z.; Zhou, R. Structural and Electronic Properties of Uranium-Encapsulated Au_{14} Cage. *Sci. Rep.* **2014,** *4*, 5862.

38. Rocha, A. R.; García-suárez, V. M.; Bailey, S. W.; Lambert, C. J.; Ferrer, J.; Sanvito, S. Towards Molecular Spintronics. *Nat. Mater.* **2005,** *4*, 335-339.

39. Affronte, M. Molecular Nanomagnets for Information Technologies. *J. Mater. Chem.* **2009,** *19*, 1731-1737.

40. Leuenberger, M. N.; Loss, D. Quantum Computing in Molecular Magnets. *Nature* **2001,** *410*, 789-793.

41. Ardavan, A.; Rival, O.; Morton, J. J. L.; Blundell, S. J.; Tyryshkin, A. M.; Timco, G. A.; Winpenny, R. E. P. Will Spin-Relaxation Times in Molecular Magnets Permit Quantum Information Processing? *Phys. Rev. Lett.* **2007,** *98*, 057201.

42. Stamp, P. C. E.; Gaita-Ariño, A. Spin-Based Quantum Computers Made by Chemistry: Hows and Whys. *J. Mater. Chem.* **2009,** *19*, 1718-1730.

43. Rinehart, J. D.; Long, J. R. Exploiting Single-Ion Anisotropy in the Design of f-Element Single-Molecule Magnets. *Chem. Sci.* **2011,** *2*, 2078-2085.

44. Gatteschi, D.; Sessoli, R. Quantum Tunneling of Magnetization and Related Phenomena in Molecular Materials. *Angew. Chem., Int. Ed.* **2003,** *42*, 268-297.

45. Antunes, M. A.; Pereira, L. C. J.; Santos, I. C.; Mazzanti, M.; Marçalo, J.; Almeida, M. $[U(TpMe_2)_2(bipy)]^+$: A Cationic Uranium(III) Complex with Single-Molecule-Magnet Behavior. *Inorg. Chem.* **2011,** *50*, 9915-9917.

46. Ishikawa, N.; Sugita, M.; Wernsdorfer, W. Quantum Tunneling of Magnetization in Lanthanide Single-Molecule Magnets: Bis(phthalocyaninato)terbium and Bis(phthalocyaninato)dysprosium Anions. *Angew. Chem., Int. Ed.* **2005,** *44*, 2931-2935.

47. Pugh, T.; Chilton, N. F.; Layfield, R. A. A Low-Symmetry Dysprosium Metallocene Single-Molecule Magnet with a High Anisotropy Barrier. *Angew. Chem., Int. Ed.* **2016,** *55*, 11082-11085.

48. Day, B. M.; Guo, F.-S.; Layfield, R. A. Cyclopentadienyl Ligands in Lanthanide Single-Molecule Magnets: One Ring To Rule Them All? *Acc. Chem. Res.* **2018,** *51*, 1880-1889.

49. Hong, K. The Development of Hydrogen Storage Alloys and the Progress of Nickel Hydride Batteries. *J. Alloys Compd.* **2001,** *321*, 307–313.

50. Young, K.-H.; Nei, J. The Current Status of Hydrogen Storage Alloy Development for Electrochemical Applications. *Materials* **2013,** *6*, 4574-4608.

51. McCallum, R. W.; Lewis, L. H.; Skomski, R.; Kramer, M. J.; Anderson, I. E. Practical Aspects of Modern and Future Permanent Magnets. *Annu. Rev. Mater. Res.* **2014,** *44*, 451–477.

52. Sprecher, B.; Xiao, Y.; Walton, A.; Speight, J.; Harris, R.; Kleijn, R.; Visser, G.; Kramer, G. J. Life Cycle Inventory of the Production of Rare Earths and the Subsequent Production of NdFeB Rare Earth Permanent Magnets. *Environ. Sci. Technol.* **2014,** *48*, 3951−3958.

53. Pyrhönen, J.; Nerg, J.; Kurronen, P.; Puranen, J.; Haavisto, M. Permanent Magnet Technology in Wind Power Generators. *XIX International Conference on Electrical Machines-ICEM 2010, Rome* **2010**, 1-6.

54. Binnemans, K.; Jones, P. T.; Müller, T.; Yurramendi, L. Rare Earths and the Balance Problem: How to Deal with Changing Markets ? *J. Sustain. Metall.* **2018,** *4*, 126–146.

55. Kruck, C.; Nazari, P.; Dee, C.; Richards, B. S.; Turshatov, A.; Seitz, M. Efficient Ytterbium Near-Infrared Luminophore Based on a Nondeuterated Ligand. *Inorg. Chem.* **2019,** *58*, 6959−6965.

56. Bünzli, J.-C. G.; Eliseeva, S. V. Lanthanide NIR Luminescence for Telecommunications, Bioanalyses and Solar Energy Conversion. *J. Rare Earths* **2010,** *28*, 824-842.

57. Montgomery, C. P.; Murray, B. S.; New, E. J.; Pal, R.; Parker, D. Cell-Penetrating Metal Complex Optical Probes: Targeted and Responsive Systems Based on Lanthanide Luminescence. *Acc. Chem. Res.* **2009,** *42*, 925–937.

58. Moore, E. G.; Samuel, A. P. S.; Raymond, K. N. From Antenna to Assay: Lessons Learned in Lanthanide Luminescence. *Chem. Rev. Acc. Chem. Res.* **2009,** *42*, 542–552.

59. Bünzli, J.-C. G. Lanthanide Luminescence for Biomedical Analyses and Imaging. *Chem. Rev.* **2010,** *110*, 2729–2755.

60. Li, H.; Wang, X.; Huang, D.; Chen, G. Recent Advances of Lanthanide-Doped Upconversion Nanoparticles for Biological Applications. *Nanotechnology* **2020,** *31*, 072001.

61. Huang, K.; Idris, N. M.; Zhang, Y. Engineering of Lanthanide-Doped Upconversion Nanoparticles for Optical Encoding. *small* **2016,** *12*, 836–852.

62. Cui, L.-F.; Huang, X.; Wang, L.-M.; Zubarev, D. Y.; Boldyrev, A. I.; Li, J.; Wang, L.-S. Sn_{12}^{2-}: Stannaspherene. *J. Am. Chem. Soc.* **2006,** *128*, 8390-8391.

63. Cui, L.-F.; Huang, X.; Wang, L.-M.; Li, J.; Wang, L.-S. Pb_{12}^{2-}: Plumbaspherene. *J. Phys. Chem. A* **2006,** *110*, 10169-10172.

64. Dunk, P. W.; Kaiser, N. K.; Mulet-Gas, M.; Rodríguez-Fortea, A.; Poblet, J. M.; Shinohara, H.; Hendrickson, C. L.; Marshall, A. G.; Kroto, H. W. The Smallest Stable Fullerene, $M@C_{28}$ (M = Ti, Zr, U): Stabilization and Growth from Carbon Vapor. *J. Am. Chem. Soc.* **2012,** *134*, 9380-9389.

65. Cui, L. F.; Huang, X.; Wang, L. M.; Li, J.; Wang, L. S. Endohedral Stannaspherenes $M@Sn_{12}^{-}$: A Rich Class of Stable Molecular Cage Clusters. *Angew. Chem., Int. Ed.* **2007,** *46*, 742-745.

66. Atobe, J.; Koyasu, K.; Furuse, S.; Nakajima, A. Anion Photoelectron Spectroscopy of Germanium and Tin Clusters Containing a Transition- or Lanthanide-Metal Atom; MGe_n^{-} (n = 8-20) and MSn_n^{-} (n = 15-17) (M = Sc-V, Y-Nb, and Lu-Ta). *Phys. Chem. Chem. Phys.* **2012,** *14*, 9403-9410.

67. Koyasu, K.; Atobe, J.; Furuse, S.; Nakajima, A. Anion Photoelectron Spectroscopy of Transition Metal- and Lanthanide Metal-Silicon Clusters: MSi_n^- (n = 6-20). *J. Chem. Phys.* **2008,** *129*, 214301.

68. Furuse, S.; Koyasu, K.; Atobe, J.; Nakajima, A. Experimental and Theoretical Characterization of MSi_{16}^-, MGe_{16}^-, MSn_{16}^-, and MPb_{16}^- (M = Ti, Zr, and Hf): The Role of Cage Aromaticity. *J. Chem. Phys.* **2008,** *129*, 064311.

69. Heiles, S.; Johnston, R. L.; Schäfer, R. Bismuth-Doped Tin Clusters: Experimental and Theoretical Studies of Neutral Zintl Analogues. *J. Phys. Chem. A* **2012,** *116*, 7756-7764.

70. Rohrmann, U.; Schwerdtfeger, P.; Schäfer, R. Atomic Domain Magnetic Nanoalloys: Interplay between Molecular Structure and Temperature Dependent Magnetic and Dielectric Properties in Manganese Doped Tin Clusters. *Phys. Chem. Chem. Phys.* **2014,** *16*, 23952-23966.

71. Rohrmann, U.; Schäfer, R. Stern-Gerlach Experiments on $Fe@Sn_{12}$: Magnetic Response of a Jahn-Teller Distorted Endohedrally Doped Molecular Cage Cluster. *J. Phys. Chem. C* **2015,** *119*, 10958-10961.

72. Gleditzsch, M.; Pašteka, L. F.; Götz, D. A.; Shayeghi, A.; Johnston, R. L.; Schäfer, R. Gold Doping of Tin Clusters: Exo- vs. Endohedral Complexes. *Nanoscale* **2019,** *11*, 12878-12888.

73. Pitochelli, A. R.; Hawthorne, F. M. The Isolation of the Icosahedral $B_{12}H_{12}^{-2}$ Ion. *J. Am. Chem. Soc.* **1960,** *82*, 3228-3229.

74. Charkin, O. P. Theoretical Modeling of the Structure of Complexes of the Dodecaalane Anion $Al_{12}H_{12}^{2-}$ with Borane, Alane, Diborane, and Dialane Molecules. *Russ. J. Inorg. Chem.* **2019,** *64*, 478-487.

75. Charkin, O. P.; Klimenko, N. M.; Moran, D.; Mebel, A. M.; Charkin, D. O.; Schleyer, P. v. R. Theoretical Study of Icosahedral closo-Borane, -Alane, and Gallane Dianions ($A_{12}H_{12}^{2-}$; A = B, Al, Ga) with Endohedral Noble Gas Atoms (Ng = He, Ne, Ar, and Kr) and their Lithium Salts ($Li[Ng@A_{12}H_{12}]^{-}$ and $Li_2[Ng@A_{12}H_{12}]$). *Inorg. Chem.* **2001,** *40*, 6913-6922.

76. Charkin, O. P.; Charkin, D. O.; Klimenko, N. M.; Mebel, A. M. A Theoretical Study of Isomerism in Doped Aluminum MAl_{12} and $MAl_{12}X_{12}$ Clusters with 40 and 50 Valence Electrons. *Faraday Discuss.* **2003,** *124*, 215-237.

77. Ababei, R.; Massa, W.; Weinert, B.; Pollak, P.; Xie, X.; Clérac, R.; Weigend, F.; Dehnen, S. Ionic-Radius-Driven Selection of the Main-Group-Metal Cage for Intermetalloid Clusters $[Ln@Pb_xBi_{14-x}]^{q-}$ and $[Ln@Pb_yBi_{13-y}]^{q-}$ (x/q= 7/4, 6/3; y/q= 4/4, 3/3). *Chem. Euro. J.* **2015,** *21*, 386-394.

78. Lichtenberger, N.; Wilson, R. J.; Eulenstein, A. R.; Massa, W.; Clérac, R.; Weigend, F.; Dehnen, S. Main Group Metal-Actinide Magnetic Coupling and Structural Response Upon U^{4+} Inclusion into Bi, Tl/Bi, or Pb/Bi Cages. *J. Am. Chem. Soc.* **2016,** *138*, 9033-9036.

79. Min, X.; Popov, I. A.; Pan, F. X.; Li, L. J.; Matito, E.; Sun, Z. M.; Wang, L. S.; Boldyrev, A. I. All-Metal Antiaromaticity in Sb_4-Type Lanthanocene Anions. *Angew. Chem., Int. Ed.* **2016,** *55*, 5531-5535.

80. Streitwieser, A., Jr.; Mueller-Westerhoff, U. Bis(cyclooctatetraenyl)Uranium (Uranocene). A New Class of Sandwich Complexes that Utilize Atomic f Orbitals. *J Am. Chem. Soc.* **1968,** *90,* 7364-7364.

81. Zalkin, A.; Raymond, K. N. Structure of Di-.Pi.-Cyclooctatetraeneuranium (Uranocene). *J. Am. Chem. Soc.* **1969,** *91,* 5667-5668.

82. Karraker, D. G.; Stone, J. A.; Jones, E. R., Jr.; Edelstein, N. Bis(cyclooctatetraenyl)neptunium(IV) and Bis(cyclooctatetraenyl)plutonium(IV). *J. Am. Chem. Soc.* **1970,** *92*, 4841-4845.

83. Raymond, K. N.; Eigenbrot, C. W., Jr. Structural Criteria for the Mode of Bonding of Organoactinides and -Lanthanides and Related Compounds. *Acc. Chem. Res.* **1980,** *13*, 276-283.

84. Kinsley, S. A.; Streitwieser, A.; Zalkin, A. Dipotassium Bis([8]annulene)ytterbate(II) and -Calcate(II). *Organometallics* **1985,** *4*, 52-57.

85. Evans, W. J.; Shreeve, J. L.; Ziller, J. W. Synthesis and Structure of Inverse Cyclooctatetraenyl Sandwich Complexes of Europium(II): $[(C_5Me_5)(THF)_2Eu]_2(\mu\text{-}C_8H_8$ and $[(THF)_3K(\mu\text{-}C_8H_8)]_2Eu$. *Polyhedron* **1995,** *14*, 2945-2951.

86. Kurikawa, T.; Negishi, Y.; Hayakawa, F.; Nagao, S.; Miyajima, K.; Nakajima, A.; Kaya, K. Multiple-Decker Sandwich Complexes of Lanthanide-1,3,5,7-Cyclooctatetraene $[Ln_n(C_8H_8)_m]$ (Ln = Ce, Nd, Eu, Ho, and Yb); Localized Ionic Bonding Structure. *J. Am. Chem. Soc.* **1998,** *120*, 11766-11772.

87. Guo, F. S.; Tsoureas, N.; Huang, G. Z.; Tong, M. L.; Mansikkamäki, A.; Layfield, R. A. Isolation of a Perfectly Linear Uranium(II) Metallocene. *Angew. Chem., Int. Ed.* **2020,** *59*, 2299-2303.

88. Zhang, P.; Zhang, L.; Tang, J. Lanthanide Single Molecule Magnets: Progress and Perspective. *Dalton Trans.* **2015,** *44*, 3923-3929.

89. Guo, F. S.; Day, B. M.; Chen, Y. C.; Tong, M. L.; Mansikkamäki, A.; Layfield, R. A. A Dysprosium Metallocene Single-Molecule Magnet Functioning at the Axial Limit. *Angew. Chem., Int. Ed.* **2017,** *56*, 11445-11449.

90. Goodwin, C. A. P.; Ortu, F.; Reta, D.; Chilton, N. F.; Mills, D. P. Molecular Magnetic Hysteresis at 60 Kelvin in Dysprosocenium. *Nature* **2017,** *548*, 439-442.

91. Guo, F.-S.; Day, B. M.; Chen, Y.-C.; Tong, M.-L.; Mansikkamäki, A.; Layfield, R. A. Magnetic Hysteresis up to 80 Kelvin in a Dysprosium Metallocene Single-Molecule Magnet. *Science* **2018,** *362*, 1400-1403.
92. Kealy, T. J.; Pauson, P. L. A New Type of Organo-Iron Compound. *Nature* **1951,** *168,* 1039.
93. Levy, D. A.; Orgel, L. E. Electronic Structure and Spectra of $[Cr(C_6H_6)_2]^+$ and $[Fe(C_5H_5)_2]^+$. *Mol. Phys.* **1961,** *4*, 93-94.
94. Walter, M. D.; Wolmershäuser, G.; Sitzmann, H. Calcium, Strontium, Barium, and Ytterbium Complexes with Cyclooctatetraenyl or Cyclononatetraenyl Ligands. *J. Am. Chem. Soc.* **2005,** *127*, 17494-17503.
95. Xémard, M.; Zimmer, S.; Cordier, M.; Goudy, V.; Ricard, L.; Clavaguéra, C.; Nocton, G. Lanthanidocenes: Synthesis, Structure, and Bonding of Linear Sandwich Complexes of Lanthanides. *J. Am. Chem. Soc.* **2018,** *140*, 14433-14439.
96. Münzfeld, L.; Schoo, C.; Bestgen, S.; Moreno-Pineda, E.; Köppe, R.; Ruben, M.; Roesky, P. W. Synthesis, Structures and Magnetic Properties of $[(\eta^9\text{-}C_9H_9)Ln(\eta^8\text{-}C_8H_8)]$ Super Sandwich Complexes. *Nat Commun.* **2019,** *10*, 3135.
97. Lewis, G. N. The Atom and the Molecule. *J. Am. Chem. Soc.* **1916,** *38*, 762-785.
98. Langmuir, I. The Arrangement of Electrons in Atoms and Molecules. *J. Am. Chem. Soc.* **1919,** *41*, 868-934.
99. Langmuir, I. Types of Valence. *Science* **1921,** *54,* 59-67.
100. Jensen, W. B. The Origin of the 18-Electron Rule. *J. Chem. Educ.* **2005,** *82*, 28.
101. Dognon, J. P.; Clavaguéra, C.; Pyykkö, P. Towards a 32-Electron Principle: $Pu@Pb_{12}$ and Related Systems. *Angew. Chem., Int. Ed.* **2007,** *46*, 1427-1430.
102. de Heer, W. A. The Physics of Simple Metal Clusters: Experimental Aspects and Simple Models. *Rev. Mod. Phys.* **1993,** *65*, 611.

103. Hirsch, A.; Chen, Z.; Jiao, H. Spherical Aromaticity in I_h Symmetrical Fullerenes: The $2(N+1)^2$ Rule. *Angew. Chem., Int. Ed.* **2000,** *39*, 3915-3917.

104. Neukermans, S.; Janssens, E.; Chen, Z. F.; Silverans, R. E.; Schleyer, P. v. R.; Lievens, P. Extremely Stable Metal-Encapsulated $AlPb_{10}^+$ and $AlPb_{12}^+$ Clusters: Mass-Spectrometric Discovery and Density Functional Theory Study. *Phys. Rev. Lett.* **2004,** *92*, 163401.

105. Pyykkö, P.; Runeberg, N. Icosahedral WAu_{12}: A Predicted Closed-Shell Species, Stabilized by Aurophilic Attraction and Relativity and in Accord with the 18-Electron Rule. *Angew. Chem., Int. Ed.* **2002,** *41*, 2174-2176.

106. Li, X.; Kiran, B.; Li, J.; Zhai, H. J.; Wang, L. S. Experimental Observation and Confirmation of Icosahedral $W@Au_{12}$ and $Mo@Au_{12}$ Molecules. *Angew. Chem., Int. Ed.* **2002,** *41*, 4786-4789.

107. Cao, G.-J.; Schwarz, W. H. E.; Li, J. An 18-Electron System Containing a Superheavy Element: Theoretical Studies of $Sg@Au_{12}$. *Inorg. Chem.* **2015,** *54*, 3695-3701.

108. Dognon, J.-P.; Clavaguéra, C.; Pyykkö, P. Predicted Organometallic Series Following a 32-Electron Principle: $An@C_{28}$ (An = Th, Pa^+, U^{2+}, Pu^{4+}). *J. Am. Chem. Soc.* **2009,** *131*, 238-245.

109. Guo, T.; Diener, M. D.; Chai, Y.; Alford, M. J.; Haufler, R. E.; McClure, S. M.; Ohno, T.; Weaver, J. H.; Scuseria, G. E.; Smalley, R. E. Uranium Stabilization of C_{28}: A Tetravalent Fullerene. *Science* **1992,** *257*, 1661-1664.

110. Dai, X.; Gao, Y.; Jiang, W.; Lei, Y.; Wang, Z. $U@C_{28}$: the Electronic Structure Induced by the 32-Electron Principle. *Phys. Chem. Chem. Phys.* **2015,** *17*, 23308-23311.

111. Dognon, J.-P.; Clavaguéra, C.; Pyykkö, P. A New, Centered 32-Electron System: the Predicted $[U@Si_{20}]^{6-}$-Like Isoelectronic Series. *Chem. Sci.* **2012,** *3*, 2843-2848.

112. Manna, D.; Sirohiwal, A.; Ghanty, T. K. Pu@C_{24}: A New Example Satisfying the 32-Electron Principle. *J. Phys. Chem. C* **2014,** *118*, 7211-7221.

113. Manna, D.; Ghanty, T. K. Prediction of a New Series of Thermodynamically Stable Actinide Encapsulated Fullerene Systems Fulfilling the 32-Electron Principle. *J. Phys. Chem. C* **2012,** *116*, 25630-25641.

114. Gao, Y.; Liu, X.; Wang, Z. Ce@Au_{14}: A Bimetallic Superatom Cluster with 18-Electron Rule. *J. Electron. Mater.* **2017,** *46*, 3899-3903.

115. Jemmis, E. D.; Balakrishnarajan, M. M.; Pancharatna, P. D. Electronic Requirements for Macropolyhedral Boranes. *Chem. Rev.* **2002,** *102*, 93-144.

116. Wade, K. Structural and Bonding Patterns in Cluster Chemistry. *Adv. Inorg. Chem. Radiochem.* **1976,** *18*, 1-66.

117. Mingos, D. M. P. Polyhedral Skeletal Electron Pair Approach. *Acc. Chem. Res.* **1984,** *17*, 311-319.

118. Jemmis, E. D.; Balakrishnarajan, M. M.; Pancharatna, P. D. A Unifying Electron-Counting Rule for Macropolyhedral Boranes, Metallaboranes, and Metallocenes. *J. Am. Chem. Soc.* **2001,** *123*, 4313-4323.

119. Kang, S.; Zhou, G.; Yang, P.; Liu, Y.; Sun, B.; Huynh, T.; Meng, H.; Zhao, L.; Xing, G.; Chen, C.; Zhao, Y.; Zhou, R. Molecular Mechanism of Pancreatic Tumor Metastasis Inhibition by Gd@$C_{82}(OH)_{22}$ and its Implication for de Novo Design of Nanomedicine. *Proc. Natl. Acad. Sci. USA.* **2012,** *109*, 15431-15436.

120. Kang, S.; Huynh, T.; Zhou, R. Metallofullerenol Gd@$C_{82}(OH)_{22}$ Distracts the Proline-Rich-Motif from Putative Binding on the SH_3 Domain. *Nanoscale* **2013,** *5*, 2703-2712.

121. Kang, S.; Huynh, T.; Zhou, R. Non-destructive Inhibition of Metallofullerenol Gd@$C_{82}(OH)_{22}$ on WW domain: Implication on Signal Transduction Pathway. *Sci. Rep.* **2012,** *2*, 957.

122. Brewer, L. Energies of the Electronic Configurations of the Lanthanide and Actinide Neutral Atoms. *J. Opt. Soc. Am.* **1971,** *61*, 1101-1111.

123. Desclaux, J. P.; Fricke, B. Relativistic Prediction of the Ground State of Atomic Lawrencium. *J. Phys.* **1980,** *41*, 943-946.

124. Fritzsche, S.; Dong, C. Z.; Koike, F.; Uvarov, A. The Low-Lying Level Structure of Atomic Lawrencium (Z = 103): Energies and Absorption Rates. *Eur. Phys. J. D.* **2007,** *45*, 107-113.

125. Sato, T. K.; Asai, M.; Borschevsky, A.; Stora, T.; Sato, N.; Kaneya, Y.; Tsukada, K.; Düllmann, C. E.; Eberhardt, K.; Eliav, E.; Ichikawa, S.; Kaldor, U.; Kratz, J. V.; Miyashita, S.; Nagame, Y.; Ooe, K.; Osa, A.; Renisch, D.; Runke, J.; Schädel, M.; Thörle-Pospiech, P.; Toyoshima, A.; Trautmann, N. Measurement of the First Ionization Potential of Lawrencium, Element 103. *Nature* **2015,** *520,* 209-211.

126. Srivastava, A. K.; Pandey, S. K.; Misra, N. Encapsulation of Lawrencium into C_{60} Fullerene: Lr@C_{60} versus Li@C_{60}. *Mater. Chem. Phys.* **2016,** *177,* 437-441.

127. Nagame, Y. Lawrencium's Place at the Table. *Nat. Chem.* **2016,** *8,* 282.

128. Szabo, A.; Ostlund, N. S. Modern Quantum Chemistry: Introduction to Advanced Electronic Structure Theory, McGraw-Hill, New York **1989**.

129. Cramer, C. J. Essentials of Computational Chemistry -Theories and Models, 2 edn., John Wiley & Sons Ltd, London **2005**.

130. Parr, R. G.; Yang, W. Density Functional Theory of Atoms and Molecules, Oxford University Press, New York, USA **1989**.

131. Slater, J. C. Atomic Shielding Constants. *Phys. Rev.* **1930,** *36,* 57.

132. Gill, P. M. W. Molecular integrals Over Gaussian Basis Functions. *Adv. Quantum Chem.* **1994,** *25*, 141-205.

133. Hehre, W. J.; Stewart, R. F.; Pople, J. A. Self-Consistent Molecular-Orbital Methods. I. Use of Gaussian Expansions of Slater-Type Atomic Orbitals. *J. Chem. Phys.* **1969,** *59*, 2657.

134. Schrödinger, E. Quantisierung als Eigenwertproblem. *Annalen der Physik* **1926,** *385*, 437-490.

135. Born, M.; Oppenheimer, R. Zur Quantentheorie der Molekeln. *Ann. Phys. (Leipzif)* **1927,** *84*, 457-484.

136. Hartree, D. R. The Wave Mechanics of an Atom with a Non-Coulomb Central Field. Part I. Theory and Methods. *Math. Proc. Camb. Philos. Soc.* **1928,** *24*, 89-110.

137. Slater, J. C. A Simplification of the Hartree-Fock Method. *Phys. Rev.* **1951,** *81*, 385.

138. Møller, C.; Plesset, M. S. Note on an Approximation Treatment for Many-Electron Systems. *Phys. Rev.* **1934,** *46*, 618.

139. Čížek, J. On the Correlation Problem in Atomic and Molecular Systems. Calculation of Wavefunction Components in Ursell-Type Expansion Using Quantum-Field Theoretical Methods. *J. Chem. Phys.* **1966,** *45*, 4256.

140. Thomas, L. H. The Calculation of Atomic Fields. *Math. Proc. Camb. Philos. Soc.* **1927,** *23*, 542-548.

141. Fermi, E. Statistical Method to Determine Some Properties of Atoms. *Rend. Accad. Naz. Lincei* **1927,** *6*, 602-607.

142. Hohenberg, P.; Kohn, W. Inhomogeneous Electron Gas. *Phys. Rev.* **1964,** *136*, B864.

143. Kohn, W.; Sham, L. J. Self-Consistent Equations Including Exchange and Correlation Effects. *Phys. Rev.* **1965,** *140*, A1133.

144. Perdew, J. P.; Burke, K.; Ernzerhof, M. Generalized Gradient Approximation Made Simple. *Phys. Rev. Lett.* **1996,** *77*, 3865.

145. Zhao, Y.; Truhlar, D. G. The M06 Suite of Density Functionals for Main Group Thermochemistry, Thermochemical Kinetics, Noncovalent Interactions, Excited States, and Transition Elements: Two New Functionals and Systematic Testing of Four M06-Class Functionals and 12 Other Functionals. *Theor. Chem. Acc.* **2008,** *120*, 215-241.

146. Becke, A. D. A New mixing of Hartree-Fock and Local Density-Functional Theories. *J. Chem. Phys.* **1993,** *98*, 1372.

147. Lee, C.; Yang, W.; Parr, R. G. Development of the Colle-Salvetti Correlation-Energy Formula into a Functional of the Electron Density. *Phys. Rev. B* **1988,** *37*, 785.

148. Adamo, C. Toward Reliable Density Functional Methods Without Adjustable Aarameters: The PBE0 Model. *J. Chem. Phys.* **1999,** *110*, 6158.

149. Perdew, J. P.; Ernzerhof, M. Rationale for Mixing Exact Exchange with Density Functional Approximations. *J. Chem. Phys.* **1996,** *105*, 9982.

150. Ahlrichs, R.; Bär, M.; Häser, M.; Horn, H.; Kölmel, C. TURBOMOLE is program package developed by the Quantum Chemistry Group at the University of Karlsruhe, Germany, 1988. *Chem. Phys. Lett.* **1989,** *162*, 165.

151. ADF2016; SCM, Theoretical Chemistry, Vrije Universiteit: Amsterdam, The Netherlands. http://www.scm.com.

152. ADF2017; SCM, Theoretical Chemistry, Vrije Universiteit: Amsterdam, The Netherlands. http://www.scm.com.

153. Velde, G. T.; Bickelhaupt, F. M.; Baerends, E. J.; Guerra, C. F.; Van Gisbergen, S. J. A.; Snijders, J. G.; Ziegler, T. Chemistry with ADF. *J. Comput. Chem.* **2001,** *22*, 931-967.

154. Tao, J.; Perdew, J. P.; Staroverov, V. N.; Scuseria, G. E. Climbing the Density Functional Ladder: Nonempirical Meta-Generalized Gradient Approximation Designed for Molecules and Solids. *Phys. Rev. Lett.* **2003,** *91*, 146401.

155. Becke, A. D. Density-Functional Exchange-Energy Approximation with Correct Asymptotic Behavior. *Phys. Rev. A* **1988,** *38*, 3098-3100.

156. Grimme, S.; Antony, J.; Ehrlich, S.; Krieg, H. A Consistent and Accurate Ab Initio Parametrization of Density Functional Dispersion Correction (DFT-D) for the 94 Elements H-Pu. *J. Chem. Phys.* **2010,** *132*, 154104.

157. Grimme, S.; Hansen, A.; Brandenburg, J. G.; Bannwarth, C. Dispersion-Corrected Mean-Field Electronic Structure Methods. *Chem. Rev.* **2016,** *116*, 5105-5154.

158. Frisch, M. J.; Head-Gordon, M.; Pople, J. A. A Direct MP2 Gradient Method. *Chem. Phys. Lett.* **1990,** *166*, 275-280.

159. Hampel, C.; Peterson, K. A.; Werner, H.-J. A Comparison of the Efficiency and Accuracy of the Quadratic Configuration Interaction (QCISD), Coupled Cluster (CCSD) and Brueckner Couple Cluster (BCCD) Methods. *Chem. Phys. Lett.* **1992,** *190,* 1-12.

160. Weigend, F.; Ahlrichs, R. Balanced Basis Sets of Split Valence, Triple Zeta Valence and Quadruple Zeta Valence Quality for H To Rn: Design and Assessment of Accuracy. *Phys. Chem. Chem. Phys.* **2005,** *7*, 3297-3305.

161. Cao, X.; Dolg, M. Valence Basis Sets for Relativistic Energy-Consistent Small-Core Lanthanide Pseudopotentials. *J. Chem. Phys.* **2001,** *115,* 7348-7355.

162. Cao, X.; Dolg, M.; Stoll, H. Valence Basis Sets for Relativistic Energy-Consistent Small-Core Actinide Pseudopotentials. *J. Chem. Phys.* **2003,** *118,* 487-496.

163. Bergner, A.; Dolg, M.; Küchle, W.; Stoll, H.; Preuß, H. Ab Initio Energy-Adjusted Pseudopotentials for Elements of Groups 13-17. *Mol. Phys.* **1993,** *80,* 1431-1441.

164. Dolg, M.; Stoll, H.; Preuss, H. Energy-Adjusted ab initio Pseudopotentials for the Rare Earth Elements. *J. Chem. Phys.* **1989,** *90*, 1730-1734.

165. Werner, H.-J.; Knowles, P. J.; Knizia, G.; Manby, F. R.; Schützet, M.; Celani, P.; Korona, T.; Lindh, R.; Mitrushenkov, A.; Rauhut, G., et al. MOLPRO, version 2012.1, a Package of ab initio Programs, 2012; see http://www.molpro.net.

166. Reed, A. E.; Weinstock, R. B.; Weinhold, F. Natural Population Analysis. *J. Chem. Phys.* **1985,** *83*, 735.

167. Guerra, C. F.; Handgraaf, J. W.; Baerends, E. J.; Bickelhaupt, F. M. Deformation Density (VDD) Charges: Assessment of the Mulliken, Bader, Hirshfeld, Weinhold, and VDD Methods for Charge Analysis. *J. Comput. Chem.* **2004,** *25*, 189-210.

168. Bader, R. F. W. Atoms in Molecules-A Quantum Theory; Oxford University Press: Oxford, U.K. **1990**.

169. Zou, W.; Nori-Shargh, D.; Boggs, J. E. On the Covalent Character of Rare Gas Bonding Interactions: A New Kind of Weak Interaction. *J. Phys. Chem. A* **2013,** *117*, 207-212.

170. Lu, T.; Chen, F. Multiwfn: A Multifunctional Wavefunction Analyzer. *J. Comput. Chem.* **2012,** *33*, 580-592.

171. Becke, A. D.; Edgecombe, K. E. A Simple Measure of Electron Localization in Atomic and Molecular Systems. *J. Chem. Phys.* **1990,** *92*, 5397.

172. Keith, T. A.; Frisch, M. J. Subshell Fitting of Relativistic Atomic Core Electron Densities for Use in QTAIM Analyses of ECP-Based Wave Functions. *J. Phys. Chem. A* **2011,** *115*, 12879-12894.

173. Ziegler, T.; Rauk, A. On the Calculation of Bonding Energies by the Hartree-Fock-Slater Method-I. The Transition State Method. *Theor. Chim. Acta.* **1977,** *46*, 1-10.

174. Bickelhaupt, F. M.; Baerends, E. J. "Kohn-Sham Density Functional Theory: Predicting and Understanding Chemistry" Lipkowitz, K. B.; Boyd, D. B. (Eds.). *Rev. Comput. Chem.* **2007,** *15*, 1-86.

175. Kitaura, K.; Morokuma, K. A New Energy Decomposition Scheme for Molecular Interactions within the Hartree-Fock Approximation. *Int. J. Quantum Chem* **1976,** *10,* 325-340.

176. van Lenthe, E.; Baerends, E. J.; Snijders, J. G. Relativistic Total Energy using Regular Approximations. *J. Chem. Phys.* **1994,** *101*, 9783-9792.

177. van Lenthe, E.; Ehlers, A.; Baerends, E.-J. Geometry Optimization in the Zero Order Regular Approximation for Relativistic Effects. *J. Chem. Phys.* **1999,** *110,* 8943-8953.

178. van Lenthe, E.; Baerends, E. J. Optimized Slater-Type Basis Sets for the Elements 1-118. *J. Comput. Chem.* **2003,** *24*, 1142-1156.

179. van Lenthe, E.; Snijders, J. G.; Baerends, E. J. The Zero-Order Regular Approximation for Relativistic Effects: The Effect of Spin-Orbit Coupling in Closed Shell Molecules. *J. Chem. Phys.* **1996,** *105*, 6505-6516.

180. Grochala, W. The Generalized Maximum Hardness Principle Revisited and Applied to Solids (Part 2). *Phys. Chem. Chem. Phys.* **2017,** *19,* 30984-31006.

181. Schwerdtfeger, P.; Nagle, J. K. 2018 Table of Static Dipole Polarizabilities of the Neutral Elements in the Periodic Table *Mol. Phys.* **2019**, 1-50.

182. Scerri, E. R. The Dual Sense of the Term “Element,” Attempts to Derive the Madelung Rule, and the Optimal Form of the Periodic Table, If Any. *Int. J. Quantum Chem.* **2009,** *109,* 959 –971.

183. Scerri, E. R. Periodic Change. *Chem. World* **2009,** *3,* 46–49.

184. Scerri, E. R. The Periodic Table and the Turn to Practice. *Stud Hist Philos Sci Part A* **2020,** *79,* 87-93.

185. Scerri, E. R. The Periodic Table: Its Story and Its Significance. *Oxford University Press, Oxford* **2006**.

186. Scerri, E. The Role of Triads in the Evolution of the Periodic Table: Past and Present. *J. Chem. Educ.* **2008,** *85*, 585.

187. Jensen, W. B. The Positions of Lanthanum (Actinium) and Lutetium (Lawrencium) in the Periodic Table: an Update. *Found Chem.* **2015,** *17*, 23–31.

188. Cao, C.-S.; Hu, H.-S.; Li, J.; Schwarz, W. H. E. Physical Origin of Chemical Periodicities in the System of Elements. *Pure Appl. Chem.* **2019,** *91*, 1969–1999.

189. Grochala, W. On the Position of Helium and Neon in the Periodic Table of Elements. *Found. Chem.* **2018,** *20*, 191–207.

190. IUPAC, iupac.org/what−we−do/periodic−table−of−elements/, Downloaded **2016**.

191. Esenturk, E. N.; Fettinger, J.; Eichhorn, B. The Closo-Pb_{10}^{2-} Zintl Ion in the $[Ni@Pb_{10}]^{2-}$ Cluster. *Chem. Commun.* **2005**, 247-249.

192. Esenturk, E. N.; Fettinger, J.; Eichhorn, B. The Pb_{12}^{2-} and Pb_{10}^{2-} Zintl Ions and the $M@Pb_{12}^{2-}$ and $M@Pb_{10}^{2-}$ Cluster Series Where M = Ni, Pd, Pt. *J. Am. Chem. Soc.* **2006,** *128*, 9178-9186.

193. Esenturk, E. N.; Fettinger, J.; Lam, Y. F.; Eichhorn, B. $[Pt@Pb_{12}]^{2-}$. *Angew. Chem., Int. Ed.* **2004,** *43*, 2132-2134.

194. Cao, T.-T.; Zhao, L.-X.; Feng, X.-J.; Lei, Y.-M.; Luo, Y.-H. Structural and Electronic Properties of $LuSi_n$ (n = 1-12) Clusters: A Density Functional Theory Investigation. *J. Mol. Struct. TheoChem.* **2009,** *895*, 148-155.

195. Mitzinger, S.; Broeckaert, L.; Massa, W.; Weigend, F.; Dehnen, S. Understanding of Multimetallic Cluster Growth. *Nat. Commun.* **2016,** *7*, 10480.

196. Bals, S.; Van Aert, S.; Romero, C. P.; Lauwaet, K.; Van Bael, M. J.; Schoeters, B.; Partoens, B.; Yücelen, E.; Lievens, P.; Van Tendeloo, G. Atomic Scale Dynamics of Ultrasmall Germanium Clusters. *Nat. Commun.* **2012,** *3*, 897.

197. Fässler, T. F.; Hoffmann, S. D. Endohedral Zintl Ions: Intermetalloid Clusters. *Angew. Chem., Int. Ed.* **2004,** *43*, 6242-6247.

198. Schnöckel, H. Formation, Structure and Bonding of Metalloid Al and Ga Clusters. A Challenge for Chemical Efforts in Nanosciences. *Dalton Trans.* **2008**, 4344-4362.

199. Wang, J. Q.; Stegmaier, S.; Fässler, T. F. $[Co@Ge_{10}]^{3-}$: An Intermetalloid Cluster with Archimedean Pentagonal Prismatic Structure. *Angew. Chem., Int. Ed.* **2009,** *48*, 1998-2002.

200. Zhou, B.; Denning, M. S.; Kays, D. L.; Goicoechea, J. M. Synthesis and Isolation of $[Fe@Ge_{10}]^{3-}$: A Pentagonal Prismatic Zintl Ion Cage Encapsulating an Interstitial Iron Atom. *J. Am. Chem. Soc.* **2009,** *131*, 2802-2803.

201. Goicoechea, J. M.; Sevov, S. C. $[Zn_9Bi_{11}]^{5-}$: A Ligand-Free Intermetalloid Cluster. *Angew. Chem., Int. Ed.* **2006,** *45*, 5147-5150.

202. Moses, M. J.; Fettinger, J. C.; Eichhorn, B. W. Interpenetrating As_{20} Fullerene and Ni_{12} Icosahedra in the Onion-Skin $[As@Ni_{12}@As_{20}]^{3-}$ Ion. *Science* **2003,** *300*, 778-780.

203. Grubisic, A.; Ko, Y. J.; Wang, H.; Bowen, K. H. Photoelectron Spectroscopy of Lanthanide- Silicon Cluster Anions $LnSi_n^-$ ($3 \leq n \leq 13$; Ln=Ho, Gd, Pr, Sm,Eu, Yb): Prospect for Magnetic Silicon-Based Clusters. *J. Am. Chem. Soc.* **2009,** *131*, 10783-10790.

204. Lips, F.; Clérac, R.; Dehnen, S. $[Eu@Sn_6Bi_8]^{4-}$: A Mini-Fullerane-Type Zintl Anion Containing a Lanthanide ion. *Angew. Chem., Int. Ed.* **2011,** *50*, 960-964.

205. Lips, F.; Hołyńska, M.; Clérac, R.; Linne, U.; Schellenberg, I.; Pöttgen, R.; Weigend, F.; Dehnen, S. Doped Semimetal Clusters: Ternary, Intermetalloid Anions $[Ln@Sn_7Bi_7]^{4-}$ and $[Ln@Sn_4Bi_9]^{4-}$ (Ln=La, Ce) with Adjustable Magnetic Properties. *J. Am. Chem. Soc.* **2012,** *134*, 1181-1191.

206. Rookes, T. M.; Wildman, E. P.; Balázs, G.; Gardner, B. M.; Wooles, A. J.; Gregson, M.; Tuna, F.; Scheer, M.; Liddle, S. T. Actinide-Pnictide (An−Pn) Bonds Spanning Non-Metal, Metalloid, and Metal Combinations (An = U, Th; Pn = P, As, Sb, Bi). *Angew. Chem., Int. Ed.* **2018,** *57*, 1332-1336.

207. Liu, C.; Popov, I. A.; Chen, Z.; Boldyrev, A. I.; Sun, Z. M. Aromaticity and Antiaromaticity in Zintl Clusters. *Chem. Eur. J.* **2018,** *24*, 14583-14597.

208. Critchlow, S. C.; Corbett, J. D. Homopolyatomic Anions of the Post Transition Elements. Synthesis and Structure of Potassium-crypt Salts of the Tetraantimonide(2-) and Heptaantimonide(3-) Anions, Sb_4^{2-} and Sb_7^{3-}. *Inorg. Chem.* **1984,** *23*, 770-774.

209. Cisar, A.; Corbett, J. D. Polybismuth Anions. Synthesis and Crystal Structure of a Salt of the Tetrabismuthide (2-) ion, Bi_4^{2-}. A Basis for the Interpretation of the Structure of Some Complex Intermetallic Phases. *Inorg. Chem.* **1977,** *16*, 2482-2487.

210. Lohr, L. L., Jr.; Pyykkö, P. Relativistically Parameterized Extended Hückel Theory. *Chem. Phys. Lett.* **1979,** *62*, 333-338.

211. Feller, D. The Role of Databases in Support of Computational Chemistry Calculations. *J. Comp. Chem.* **1996,** *17*, 1571-1586.

212. http://www.tc.uni–koeln.de/PP/index.en.html.

213. Hosmane, N. S.; Maguire, J. A.; Zhu, Y.; Takagaki, M. Boron and Gadolinium Neutron Capture Therapy for Cancer Treatment, 1st ed. (World Scientific Publishing Company, Singapore; Hackensack). 2012.

214. Tutusaus, O.; Mohtadi, R.; Arthur, T. S.; Mizuno, F.; Nelson, E. G.; Sevryugina, Y. V. An Efficient Halogen-Free Electrolyte for Use in Rechargeable Magnesium Batteries. *Angew. Chem., Int. Ed.* **2015,** *54*, 7900-7904.

215. Zhao, H.; Zhou, J.; Jena, P. Stability of $B_{12}(CN)_{12}^{2-}$: Implications for Lithium and Magnesium Ion Batteries. *Angew. Chem., Int. Ed.* **2016,** *55*, 3704-3708.

216. Joshi, M.; Ghanty, T. K. Hybrid Organic-Inorganic Functionalized Dodecaboranes and their Potential Role in Lithium and Magnesium Ion Batteries. *J. Phys. Chem. C* **2018,** *122*, 27947-27954.

217. Weiser, V.; Eisenreich, N.; Koleczko, A.; Roth, E. On the Oxidation and Combustion of AlH_3 a Potential Fuel for Rocket Propellants and Gas Generators. *Prop. Explos. Pyrotech.* **2007,** *32*, 213-221.

218. Zidan, R.; Garcia-Diaz, B. L.; Fewox, C. S.; Stowe, A. C.; Gray, J. R.; Harter, A. G. Aluminium Hydride: A Reversible Material for Hydrogen Storage. *Chem. Commun.* **2009**, 3717-3719.

219. Hiller, W.; Klinkhammer, K. W.; Uhl, W.; Wagner, J. $K_2[Al_{12}iBu_{12}]$ mit Al_{12}-Ikosaeder. *Angew. Chem.* **1991,** *103*, 182.

220. Wang, L.; Zhao, J.; Zhou, Z.; Zhang, S. B.; Chen, Z. First–Principle Study of Molecular Hydrogen Dissociation on Doped $Al_{12}X$ (X = B, Al, C, Si, P, Mg and Ca) Clusters. *J. Comp. Chem.* **2009,** *30*, 2509-2514.

221. Lu, Q. L.; Wan, J. G. Sc-Coated $Si@Al_{12}$ as High-Capacity Hydrogen Storage Medium. *J. Chem. Phys.* **2010,** *132*, 224308.

222. Hua, Y.; Liu, Y.; Jiang, G.; Du, J.; Chen, J. Geometric transition and Electronic Properties of Titanium-doped Aluminium Clusters: Al_nTi (n = 2-24). *J. Phys. Chem. A* **2013,** *117*, 2590-2597.

223. Molina, B.; Soto, J. R.; Castro, J. J. Stability and Nonadiabatic Effects of the Endohedral Clusters $X@Al_{12}$ (X = B, C, N, Al, Si, P) with 39, 40, and 41 Valence Electrons. *J. Phys. Chem. C* **2012,** *116*, 9290-9299.

224. Popov, I. A.; Li, W.-L.; Piazza, Z. A.; Boldyrev, A. I.; Wang, L.-S. Complexes between Planar Boron Clusters and Transition Metals: A Photoelectron Spectroscopy and Ab Initio Study of CoB_{12}^- and RhB_{12}^-. *J. Phys. Chem. A* **2014,** *118*, 8098-8105.

225. Li, W.-L.; Romanescu, C.; Galeev, T. R.; Piazza, Z. A.; Boldyrev, A. I.; Wang, L.-S. Transition-Metal-Centered Nine-Membered Boron Rings: M©B_9 and M©B_9^- (M = Rh, Ir). *J. Am. Chem. Soc.* **2012,** *134*, 165-168.

226. Popov, I. A.; Jian, T.; Lopez, G. V.; Boldyrev, A. I.; Wang, L.-S. Cobalt-Centred Boron Molecular Drums with the Highest Coordination Number in the CoB_{16}^- Cluster. *Nat. Commun.* **2015,** *6*, 8654.

227. Lu, Q. L.; Luo, Q. Q.; Jalbout, A. F.; Wan, J. G.; Wang, G. H. The Structure and Stability of Si@$Al_{12}H_n$ (n = 1-14) Clusters. *Eur. Phys. J. D.* **2009,** *51*, 219-223.

228. Liu, J.; Yu, J.; Ge, Q. Transition-Metal-Doped Aluminum Hydrides as Building Blocks for Supramolecular Assemblies. *J. Phys. Chem. A* **2010,** *114*, 12318-12322.

229. Charkin, O. P.; Charkin, D. O.; Klimenko, N. M.; Mebel, A. M. Theoretical Study of Isomerism in Doped Aluminum XAl_{12} Clusters (X = B, Al, Ga, C, Si, Ge) with 40 Valence Electrons. *Chem. Phys. Lett.* **2002,** *365*, 494-504.

230. Charkin, O. P.; Klimenko, N. M.; Charkin, D. O.; Mebel, A. M.; Schleyer, P. v. R. Theoretical Study of Isomerism in Alanes $LAl_{12}H_{12}$ with Metal Cations Inside and Outside of the Icosahedral Anion $Al_{12}H_{12}^{2-}$. *Russ. J. Inorg. Chem.* **2004,** *49*, 1536-1546.

231. De Vlugt, I. J. S.; Lecours, M. J.; Carr, P. J. J.; Anwar, A.; Marta, R. A.; Fillion, E.; Steinmetz, V.; Hopkins, W. S. Infrared-Driven Charge-Transfer in Transition Metal-Containing $B_{12}X_{12}^{2-}$ (X = H, F) Clusters. *J. Phys. Chem. A* **2018,** *122*, 7051-7061.

232. Boys, S. F.; Bernardi, F. The Calculation of Small Molecular Interactions by the Differences of Separate Total Energies. Some Procedures with Reduced Errors. *Mol. Phys.* **1970,** *19*, 553-566.

233. Grochala, W.; Edwards, P. P. Thermal Decomposition of the Non-Interstitial Hydrides for the Storage and Production of Hydrogen. *Chem. Rev.* **2004,** *104*, 1283-1316.

234. Starobrat, A.; Tyszkiewicz, M. J.; Wegner, W.; Pancerz, D.; Orłowski, P. A.; Leszczyński, P. J.; Fijalkowski, K. J.; Jaroń, T.; Grochala, W. Salts of Highly Fluorinated Weakly Coordinating Anions as Versatile Precursors Towards Hydrogen Storage Materials. *Dalton Trans.* **2015,** *44*, 19469-19477.

235. Wegner, W.; Jaroń, T.; Grochala, W. Preparation of a Series of Lanthanide Borohydrides and their Thermal Decomposition to Refractory Lanthanide Borides. *J. Alloys Compd.* **2018,** *744*, 57-63.

236. Kawasaki, K.; Sugiyama, R.; Tsuji, T.; Iwasa, T.; Tsunoyama, H.; Mizuhata, Y.; Tokitoh, N.; Nakajima, A. A Designer Ligand Field for Blue-Green Luminescence of Organoeuropium (II) Sandwich Complexes with Cyclononatetraenyl Ligands. *Chem. Commun.* **2017,** *53*, 6557-6560.

237. Molander, G. A.; Romero, J. A. C. Lanthanocene Catalysts in Selective Organic Synthesis. *Chem. Rev.* **2002,** *102*, 2161-2186.

238. Demir, S.; Gonzalez, M. I.; Darago, L. E.; Evans, W. J.; Long, J. R. Giant Coercivity and High Magnetic Blocking Temperatures for N_2^{3-} Radical-Bridged Dilanthanide Complexes Upon Ligand Dissociation. *Nat. Comm.* **2017,** *8*, 2144.

239. Fischer, E. O.; Pfab, W. Cyclopentadien-Metallkomplexe, ein neuer Typ metallorganischer Verbindungen. Z. Naturforsch. *B: J. Chem. Sci.* **1952,** *7*, 377-379.

240. Murahashi, T.; Inoue, R.; Usui, K.; Ogoshi, S. Square Tetrapalladium Sheet Sandwich Complexes: Cyclononatetraenyl as a Versatile Face-Capping Ligand. *J. Am. Chem. Soc.* **2009,** *131*, 9888-9889.

241. Hosoya, N.; Takegami, R.; Suzumura, J.-I.; Yada, K.; Miyajima, K.; Mitsui, M.; Knickelbein, M. B.; Yabushita, S.; Nakajima, A. Formation and Electronic Structures of Organoeuropium Sandwich Nanowires. *J. Phys. Chem. A* **2014,** *118*, 8298-8308.

242. LaLancette, E. A.; Benson, R. E. A Ten-π-Electron Aromatic System. *J. Am. Chem. Soc.* **1965,** *87*, 1941-1946.

243. Katz, T. J.; Garratt, P. J. The Cyclononatetraenyl Anion. *J. Am. Chem. Soc.* **1963,** *85*, 2852-2853.

244. Páez-Hernández, D.; Murillo-López, J. A.; Arratia-Pérez, R. Bonding Nature and Electron Delocalization of An(COT)$_2$, An = Th, Pa, U. *J. Phys. Chem. A* **2011,** *115*, 8997-9003.

245. Evans, W. J. Tutorial on the Role of Cyclopentadienyl Ligands in the Discovery of Molecular Complexes of the Rare-Earth and Actinide Metals in New Oxidation States. *Organometallics* **2016,** *35*, 3088-3100.

246. Day, B. M.; Guo, F. S.; Giblin, S. R.; Sekiguchi, A.; Mansikkamäki, A.; Layfield, R. A. Rare-Earth Cyclobutadienyl Sandwich Complexes: Synthesis, Structure and Dynamic Magnetic Properties. *Chem. Eur. J.* **2018,** *24*, 16779-16782.

247. Sroor, F. M.; Vendier, L.; Etienne, M. Cyclooctatetraenyl Calcium and Strontium Amido Complexes. *Dalton Trans.* **2018,** *47*, 12587-12595.

248. Edelmann, A.; Hrib, C. G.; Blaurock, S.; Edelmann, F. T. New Sandwich Complexes of Di- and Trivalent Ytterbium: Reduction of Yb(3+) by a Bulky Cyclooctatetraenyl Dianion. *J. Organomet. Chem.* **2010,** *695*, 2732-2737.

249. Bochkarev, M. N. Molecular Compounds of "New" Divalent Lanthanides. *Coordin. Chem. Rev.* **2004,** *248*, 835-851.

250. Nief, F. Non-Classical Divalent Lanthanide Complexes. *Dalton Trans.* **2010,** *39*, 6589-6598.

251. Anastassiou, A. G. Heteronins. *Acc. Chem. Res.* **1972,** *5*, 281-288.

252. Vitaku, E.; Smith, D. T.; Njardarson, J. T. Analysis of the Structural Diversity, Substitution Patterns, and Frequency of Nitrogen Heterocycles among U.S. FDA Approved Pharmaceuticals. *J. Med. Chem.* **2014,** *57*, 10257-10274.

253. Gajera, S. B.; Mehta, J. V.; Thakor, P.; Thakkar, V. R.; Chudasama, P. C.; Patel, J. S.; Patel, M. N. Half-Sandwich IridiumIII Complexes with Pyrazole-Substituted Heterocyclic Frameworks and their Biological Applications. *New J. Chem.* **2016,** *40*, 9968-9980.

254. Guo, L.; Zhang, H.; Tian, M.; Tian, Z.; Xu, Y.; Yang, Y.; Peng, H.; Liu, P.; Liu, Z. Electronic Effects on Reactivity and Anticancer Activity by Half-Sandwich N,N-Chelated Iridium(III) Complexes. *New J. Chem.* **2018,** *42*, 16183-16192.

255. Yang, Y.; Guo, L.; Tian, Z.; Gong, Y.; Zheng, H.; Zhang, S.; Xu, Z.; Ge, X.; Liu, Z. Novel and Versatile Imine-N-Heterocyclic Carbene Half Sandwich Iridium(III) Complexes as Lysosome-Targeted Anticancer Agents. *Inorg. Chem.* **2018,** *57*, 11087-11098.

256. Urnėžius, E.; Brennessel, W. W.; Cramer, C. J.; Ellis, J. E.; Schleyer, P. v. R. A Carbon-Free Sandwich Complex $[(P_5)_2Ti]^{2-}$. *Science* **2002,** *295*, 832-834.

257. Ashe, A. J., III. Aromatic Borataheterocycles: Surrogates for Cyclopentadienyl in Transition-Metal Complexes. *Organometallics* **2009,** *28*, 4236-4248.

258. Prinzbach, H.; Schwesinger, R.; Breuninger, M.; Gallenkamp, B.; Hunkler, D. Chemistry of Cis-Triazatris-σ-homobenzene. 3σ→3π Isomerization to the 1,4,7,-Triaza-2,5,8-Cyclononatriene System. *Angew. Chem., Int. Ed.* **1975,** *14*, 347-348.

259. Schleyer, P. v. R.; Nyulászi, L.; Kárpáti, T. To What Extent Can Nine-Membered Monocycles Be Aromatic? *Eur. J. Org. Chem.* **2003**, 1923-1930.

260. Anastassiou, A. G.; Kasmai, H. S. Medium-Large and Large π-Excessive Heteroannulenes. *Adv. Heterocycl. Chem.* **1978,** *23*, 55-102.

261. Anastassiou, A. G.; Gebrian, J. H. N-Ethoxycarbonyl-1-Azacyclonona-2,4,6,8-Tetraene. *J. Am. Chem. Soc.* **1969,** *91*, 4011-4012.

262. Elango, M.; Subramanian, V. Density Functional Theoretical Investigation on Influence of Heterosubstitution and Benzannelation on the Thermal 6π Electrocyclization of Cis–Cyclononatetraene. *J. Phys. Chem. A* **2005,** *109*, 11870-11877.

263. Huang, Y.; Liu, Y.; Liu, S.; Wu, R.; Wu, Z. An Efficient Synthesis of N,N,N-Substituted 1,4,7- Triazacyclononane. *Eur. J. Org. Chem.* **2018**, 1546-1551.

264. Warden, A.; Graham, B.; Hearn, M. T. W.; Spiccia, L. Synthesis of Novel Derivatives of 1,4,7-Triazacyclononane. *Org. Lett.* **2001,** *3*, 2855-2858.

265. Bangal, P. R.; Patra, G. K.; Datta, D. Insertion of Unsaturations into the 1,4,7-Triazacyclononane Skeleton. Photochemical Reaction between Benzil and Diethylenetriamine: Synthesis and Properties of 2,3-Diphenyl-1,4,7-Triazacyclonona-1,3-Diene. *New J. Chem.* **2000,** *24*, 719-723.

266. Rebizant, J.; Apostolidis, C.; Spirlet, M. R.; Andreetti, G. D.; Kanellakopulos, B. Structure of Bis(Tetraethylammonium) Hexanitratouranium(IV). *Acta Crystallogr. Sect. C* **1988,** *C44*, 2098-2101.

267. Abram, U.; Bonfada, E.; Lang, E. S. Bis{2-[1-(thiosemicarbazono)ethyl]pyridinium} Hexakis(nitrato-O,O')thorate(IV) Tetramethanol Solvate. *Acta Cryst.* **1999,** *C55*, 1479-1482.

268. Hoekstra, H. R.; Katz, J. J. The Preparation and Properties of the Group IV–B Metal Borohydrides. *J. Am. Chem. Soc.* **1949,** *71*, 2488-2492.

269. Schlesinger, H. I.; Brown, H. C. Uranium(IV) Borohydride. *J. Am. Chem. Soc.* **1953,** *75*, 219-221.

270. Bernstein, E. R.; Hamilton, W. C.; Keiderling, T. A.; La Placa, S. J.; Lippard, S. J.; Mayerle, J. J. 14-Coordinate Uranium(IV). Structure of Uranium Borohydride by Single-Crystal Neutron Diffraction. *Inorg. Chem.* **1972,** *11*, 3009-3016.

271. Banks, R. H.; Edelstein, N. M.; Rietz, R. R.; Templeton, D. H.; Zalkin, A. Preparation and Properties of the Actinide Borohydrides: Protactinium(IV), Neptunium(IV), and Plutonium(IV) Borohydrides. *J. Am. Chem. Soc.* **1978,** *100*, 1957-1958.

272. Daly, S. R.; Piccoli, P. M. B.; Schultz, A. J.; Todorova, T. K.; Gagliardi, L.; Girolami, G. S. Synthesis and Properties of a Fifteen-Coordinate Complex: The Thorium Aminodiboranate [$Th(H_3BNMe_2BH_3)_4$]. *Angew. Chem., Int. Ed.* **2010,** *49*, 3379-3381.

273. Pollak, D.; Goddard, R.; Pörschke, K.-R. $Cs[H_2NB_2(C_6F_5)_6]$ Featuring an Unequivocal 16-Coordinate Cation. *J. Am. Chem. Soc.* **2016,** *138*, 9444-9451.

274. Kaltsoyannis, N. Seventeen-Coordinate Actinide Helium Complexes. *Angew. Chem., Int. Ed.* **2017,** *56*, 7066-7069.

275. Hermann, A.; Lein, M.; Schwerdtfeger, P. The Search for the Species with the Highest Coordination Number. *Angew. Chem., Int. Ed.* **2007,** *46*, 2444-2447.

276. Ozama, E.; Adachi, S.; Takayanagi, T.; Shiga, M. Quantum Simulation Verifies the Stability of an 18-Coordinated Actinium-Helium Complex. *Chem. Eur. J.* **2018,** *24*, 12716.

277. Kubas, G. J.; Ryan, R. R.; Swanson, B. I.; Vergamini, P. J.; Wasserman, H. J. Characterization of the First Examples of Isolable Molecular Hydrogen Complexes, $M(CO)_3(PR_3)_2(H_2)$ (M = Molybdenum or Tungsten; R = Cy or Isopropyl). Evidence for a Side-on Bonded Dihydrogen Ligand. *J. Am. Chem. Soc.* **1984,** *106*, 451-452.

278. Gagliardi, L.; Pyykkö, P. How Many Hydrogen Atoms Can Be Bound to a Metal? Predicted MH_{12} Species. *J. Am. Chem. Soc.* **2004,** *126*, 15014-15015.

279. Chandrakumar, K. R. S.; Ghosh, S. K. Electrostatics Driven Interaction of Dihydrogen with s-Block Metal Cations: Theoretical Prediction of Stable MH_{16} Complex. *Chem. Phys. Lett.* **2007,** *447,* 208-214.

280. Raab, J.; Lindh, R. H.; Wang, X.; Andrews, L.; Gagliardi, L. A Combined Experimental and Theoretical Study of Uranium Polyhydrides with New Evidence for the Large Complex $UH_4(H_2)_6$. *J. Phys. Chem. A* **2007,** *111,* 6383-6387.

281. Infante, I.; Gagliardi, L.; Wang, X.; Andrews, L. Binding Motifs for Lanthanide Hydrides: A Combined Experimental and Theoretical Study of the $MH_x(H_2)_y$ Species (M = La-Gd; x = 1-4; y = 0-6). *J. Phys. Chem. A* **2009,** *113,* 2446-2455.

282. Wang, X.; Andrews, L.; Infante, I.; Gagliardi, L. Matrix Infrared Spectroscopic and Computational Investigation of Late Lanthanide Metal Hydride Species $MH_x(H_2)_y$ (M = Tb-Lu, x = 1-4, y = 0-3). *J. Phys. Chem. A* **2009,** *113,* 12566-12572.

283. Wang, X.; Andrews, L.; Gagliardi, L. Infrared Spectra of ThH_2, ThH_4, and the Hydride Bridging $ThH_4(H_2)_x$ (x = 1-4) Complexes in Solid Neon and Hydrogen. *J. Phys. Chem. A* **2008,** *112,* 1754-1761.

284. Renzler, M.; Kuhn, M.; Mauracher, A.; Lindinger, A.; Scheier, P.; Ellis, A. M. Anionic Hydrogen Cluster Ions as a New Form of Condensed Hydrogen. *Phys. Rev. Lett.* **2016,** *117,* 273001.

285. Joshi, M.; Ghosh, A.; Ghanty, T. K. Atom- and Ion-Centered Icosahedral Shaped Subnanometer-Sized Clusters of Molecular Hydrogen. *J. Phys. Chem. C* **2017,** *121,* 15036-15048.

286. Schmidt, M. W.; Baldridge, K. K.; Boatz, J. A.; Elbert, S. T.; Gordon, M. S.; Jensen, J. H.; Koseki, S.; Matsunaga, N.; Nguyen, K. A.; Su, S.; Windus, T. L.; Dupuis, M.; Montgomery, J. A., Jr. General Atomic and Molecular Electronic Structure System. *J. Comput. Chem.* **1993,** *14,* 1347-1363.

287. Kubas, G. J. Dihydrogen Complexes as Prototypes for the Coordination Chemistry of Saturated Molecules. *Proc. Natl. Acad. Sci. U. S. A.* **2007,** *104*, 6901-6907.

288. Sebastianelli, F.; Baccarelli, I.; Paola, C. D.; Gianturco, F. A. Structural and Quantum Effects from Anionic Centers in Rare Gas clusters: The $(Ne)_nH^-$ and $(Ne)_{n+1}$ Systems. *J. Chem. Phys.* **2003,** *119*, 5570.

289. Swalina, C.; Hammes-Schiffer, S. Impact of Nuclear Quantum Effects on the Molecular Structure of Bihalides and the Hydrogen Fluoride Dimer. *J. Phys. Chem. A* **2005,** *109*, 10410-10417.

290. Swalina, C.; Pak, M. V.; Hammes-Schiffer, S. Alternative Formulation of Many-Body Perturbation Theory for Electron-Proton Correlation. *Chem. Phys. Lett.* **2005,** *404*, 394-399.

Thesis Highlight

Name of the Student: Ms. Meenakshi Joshi

Name of the CI: Bhabha Atomic Research Centre Enrolment No.: CHEM01201504005

Thesis Title: Electronic Structure and Chemical Bonding in Novel Lanthanide and Actinide Compounds: A Comprehensive Theoretical Study

Discipline: Chemical Sciences Sub-Area of Discipline: Computational Chemistry

Date of viva voce: 14th September, 2020

Lanthanide (Ln) and actinide (An) compounds show interesting electronic, magnetic and bonding properties due to their hyperactive valence electrons. Moreover, sandwich compounds of lanthanides are used in the construction of single−molecule magnets (SMMs) or single−ion magnets (SIMs), which have received considerable attention of scientists due to their slow magnetic relaxation behaviour and their application in switchable molecular−scale devices and quantum computing. Furthermore, the applications of lanthanide encapsulated fullerenes in nanomaterials and nanomedicine have stimulated a new field of f−block element doped compounds. Therefore, in the present thesis, we have investigated the electronic structure and chemical bonding in the different Ln and An atom or ion doped clusters by using various *ab initio* quantum chemical computational techniques. Moreover, motivated by the high coordination behaviour of Ln and An ion, we have studied their coordination behaviour toward the smallest and simplest H_2 molecules known in the universe.

In the present thesis, we have designed various novel Ln/An doped Pb_{12}^{2-}, Sn_{12}^{2-}, $(Bi_4^{2-})_3$, $(Sb_4^{2-})_3$, $B_{12}H_{12}^{2-}$ and $Al_{12}H_{12}^{2-}$ clusters as well as lanthanide sandwich complexes. We have also made an attempt to settle down the ongoing debate on the position of La, Ac, Lr and Lu elements in the periodic table based on the encapsulation of these four elements (in their various oxidation states) into the Pb_{12}^{2-} and Sn_{12}^{2-} cages. Considering the similarity in electronic configurations, energetic aspects and geometric behavior, we have advocated the placement of all these four elements (La, Ac, Lu and Lr) in the 15-elements f-block, as suggested and followed by IUPAC.

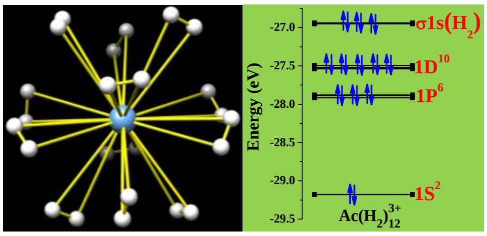

Figure 1:*First ever report showing a maximum of 24 hydrogen atoms can directly bind to actinide ions in M^{3+}-(η^2-H_2)$_{12}$ complexes.*

In addition, we have predicted very stable $M@(E_4^{2-})_3$ (M = La^{3+}, Th^{4+}) and $M@(E_4^{2-})_3$ (M = Pa^{5+}, U^{6+}, Np^{7+}; E = Sb, Bi) clusters which follow 26−electron and 32−electron principles, respectively. Moreover, we have investigated the magnetic $M@B_{12}H_{12}^{2-}$ and $M@Al_{12}H_{12}^{2-}$ (M = Pm^+, Sm^{2+}, Eu^{3+}; Np^+, Pu^{2+}, Am^{3+}) clusters possessing high magnetic moment. In addition, we have designed novel nine membered 1,4,7−triazacyclononatetraenyl ligand and its magnetic sandwich complexes with divalent lanthanide (Ln = Nd(II), Pm(II), Sm(II), Eu(II), Tm(II), and Yb(II)). Moreover, we have shown high coordination behaviour of Ln/An ion toward the hydrogen molecule where Ln (La^{3+}) and An (Ac^{3+}, Th^{3+}, Th^{4+}, Pa^{4+}, U^{4+}) ion can hold a maximum of 24 hydrogen atoms in its first coordination sphere in $M(H_2)_{12}^{3+/4+}$ (M = La, An) clusters, which is the highest recorded coordination number till date. It is interesting to note that $An@(H_2)_n$ (n = 9-12) clusters follow 18-electron rule corresponding to $s^2p^6d^{10}$ configuration around the Ac ion (Figure 1).